Vloeistof-wand interactie in bloedvaten

Fluid-Structure Interaction of Blood Vessels

Lieve Lanoye

UNIVERSITEIT
GENT

Supervisors:

Prof. dr. ir. Pascal Verdonck
Prof. dr. ir. Jan Vierendeels

Research facility:

Institute Biomedical Technology
Heymans Campus - Building B - 5th floor
De Pintelaan 185
B-9000 Gent

Members of the exam committee:

Prof. dr. ir. Ronny Verhoeven	(chairman, Faculty of Engineering, UGent)
Prof. dr. ir. Patrick Segers	(secretary, Faculty of Engineering, UGent)
Prof. dr. ir. Valérie Deplano	(Université de Marseilles, France)
Prof. dr. Stanislas Sys	(Faculty of Veterinary Medecine, UGent)
Prof. dr. ir. Pascal Verdonck	(supervisor, Faculty of Engineering, UGent)
Prof. dr. ir. Peter Van Ransbeeck	(Faculty of Applied Engineering, HoGent)
Prof. dr. ir. Benedict Verhegghe	(Faculty of Engineering, UGent)
Prof. dr. ir. Jan Vierendeels	(supervisor, Faculty of Engineering, UGent)

Acknowledgments

I am sitting at my desk at home, it is raining cats and dogs outside and my CD-player just started the John Dunbar theme from "Dances with wolves". And all of a sudden I realize that my PhD is almost over. The last months were so jammed and busy that I forgot what the work is all about. It is like reading a very thrilling book. You want to know so badly how things are going to end, so you read and read and read. And all of a sudden you are starting the last chapter, sadly realizing that the book, inevitably, is going to end at some point.

It started with biomechanics. Even though I was an engineer, so I thought I knew something about solid and fluid mechanics, I soon found out that in biomechanics, nothing is like it seems. Everything is non-linear, has large deformations, in short behaves like in an engineers worst nightmare. Thus, you start by studying what you thought you knew all over again. And gradually the formula's you see are not just derivatives and integrands, but you can see right through them as the physic process they represent, a viscosity influence or a volume change for example.

Next you start the constructive work, in my case the construction of a fluid-structure interaction program. Which feels like you are on a roller coaster, when the program works you are happy and when it does not you feel despaired. After a while however there are more ups than downs and things start to look good, luckily because you are almost four years far. So you start writing and each chapter you write brings you closer to the end. And with the end of the PhD, comes the beginning of new opportunities, exiting prospects and a real (!) job.

It is only at the end that one realizes how important some choices are at the beginning. Thanks to Prof. Pascal Verdonck I had the opportunity to start a PhD four years ago in a place where I would feel right at home. Thank you for the general vision.

Prof. Jan Vierendeels also played a very important part in the realization of this PhD. The discussion we had were very enlighting and your wide view of fluid-structure interaction mechanics really helped me to put things in perspective.

Also Prof. Patrick Segers needs a big thank you for the guidance, scientific and personal. It is very refreshing to be able to discuss about anything, from music for kids to American politics. Thank you for the listening ear and the opinion.

Very important are the colleagues you end up with. And the ones I ended up

We shall not cease from exploration
And the end of all our exploring
Will be to arrive where we started
And know the place for the first time.
Through the unknown, unremembered gate
When the last to discover
Is that which was the beginning;

Little Gidding - T.S. Eliot

Table of Contents

Research is the process of going up alleys
to see if they are blind

Marston Bates

Nederlandse samenvatting
–Summary in Dutch–

In de ingenieurswetenschap worden numerieke technieken voor het kwantificeren van stromingsvelden of het berekenen van vervormingen van continue media vaak gebruikt. Deze technieken kunnen niet alleen toegepast worden op de klassieke ingenieursdisciplines, maar zijn in een veel ruimer gebied inzetbaar. Numerieke biomechanische simulaties hebben in de medische wereld al enige tijd hun plaats verworven.

Naast de meer klassieke technieken zoals medische beeldvorming en het empirisch doktersonderzoek bieden ze bijkomende informatie en inzicht aan de arts. Ook kunnen ze aangewend worden om het ontwerpproces van biomedische apparaten te versnellen. Zo kan het gedrag van een hartklep of een stent getest worden vóór een prototype werd gemaakt. Aanpassingen zijn dan reeds mogelijk en het aantal (dure) prototypes dat dient geproduceerd te worden kan zo worden verminderd.

Uiteraard is het cruciaal dat deze numerieke tests zo waarheidsgetrouw mogelijk gebeuren. In vasculaire stromingsberekeningen speelt de interactie tussen het bloed en de vaatwand een grote rol. Wanneer de druk in het bloed lokaal verhoogt, zal de vaatwand uitzetten en met die uitzetting de bloedstroming terug beïnvloeden. Deze interactie kan niet verwaarloosd worden wanneer numerieke technieken worden toegepast om bloedstromingsberekeningen te kwantificeren.

Een manier ontwikkelen om deze interactie, de vloeistof-structuur interactie (Fluid-Structure Interaction - FSI), in rekening te brengen in vasculaire berekeningen is het centrale doel van dit doctoraatsonderzoek. Het werk is ingedeeld in acht hoofdstukken. Er wordt begonnen met een inleiding, van zowel de anatomie, fysiologie en pathofysiologie van het cardiovasculair systeem (hoofdstuk 1) als van de reeds bestaande technieken om FSI in rekening te brengen (hoofdstuk 2). Vervolgens wordt de implementatie van de numerieke FSI code behandeld die in het kader van dit doctoraatsonderzoek gerealiseerd werd (hoofdstuk 3), alsook twee toepassingen van de code (hoofdstukken 4 en 5). Een volgende studie behandelt een eendimensionale golfreflectietheorie die geïllustreerd wordt met resultaten van een ventriculair FSI-model (hoofdstuk 6). In een volgend hoofdstuk (hoofdstuk 7) worden de beperkingen van een louter mechanische aanpak geïllustreerd aan de hand van een diermodel van reperfusiegeïnduceerde kwetsuren in de hartspierwand. Tenslotte worden conclusies getrokken en toekomstperspectieven geformuleerd (hoofdstuk 8).

Hoofdstuk 1 - Hart en bloedvaten   In dit hoofdstuk worden alle medische termen en inzichten aangereikt die in verdere hoofdstukken aan bod zullen komen. Er wordt begonnen met een overzicht van de hartwerking, de anatomie en fysiologie. Daarbij wordt het conductief systeem van het hart naderbij bekeken met de actiepotentiaal, de de- en repolarisatie van de hartspiercellen en de daaruit volgende vorm van het elektrocardiogram. Ook het verloop van de drukken en volumes van de kamers in het hart worden beschreven. Nu de werking van het hart beschreven is, wordt naar de bloedvaten gekeken. Hierbij wordt een onderscheid gemaakt tussen slagaders, aders en haarvaatjes. De opbouw van de vaatwand wordt van naderbij bekeken. Daarna wordt een onderscheid gemaakt tussen de verschillende functies van de bloedvaten in het vasculaire netwerk. Vervolgens wordt de interactie tussen het hart en de bloedvaten bestudeerd. Daarbij worden begrippen zoals het slagvolume (stroke volume - SV) en het hartminuutvolume (cardiac output - CO) gedefinieerd en worden de bepalende factoren van deze parameters van naderbij bekeken. Ook de druk-volume lus die het werkingsregime van het hart beschrijft wordt bekeken. Tenslotte wordt aandacht besteed aan enkele pathologieën die in dit werk zullen worden behandeld. Als vasculaire pathologiën wordt slagaderverkalking beschreven met in een later stadium vernauwingen (stenoses) van de slagaders. Ook aneurysma's, een pathologisch, ballonachtig uitzetten van een slagader, worden beschreven. Daarna wordt congestief hartfalen beschreven met aandacht voor de prevalentie en de maatschappelijke gevolgen. Tenslotte worden de doelstellingen geformuleerd zoals ze in de inleiding van deze sectie werden verwoord.

Hoofdstuk 2 - Modelleren met numerieke methodes   De verschillende technieken die aangewend worden om op numerieke wijze het bloedstromingsveld en het wandvervormingsveld te berekenen worden in dit hoofdstuk beschreven, alsook verschillende bestaande technieken om de interactie tussen beide disciplines in rekening te brengen. Dit hoofdstuk is dan ook opgedeeld in drie grote stukken. Eerst worden numerieke stromingstechnieken (computational fluid mechanics - CFD) behandeld, waarna numerieke mechanica van continue media (computational solid mechanics - CSM) wordt beschreven. Beide vormen de basis van vloeistof-structuur interactie berekeningen, dus een grondige basiskennis van de begrippen, technieken en vergelijkingen uit de beide mechanica takken zijn onontbeerlijk voor een goed begrip van vloeistof-structuur interactie benaderingen. Die vloeistof-structuur interactie benaderingen worden in een derde deel besproken.

Na het verschil te hebben belicht tussen een Euleriaanse en Lagrangiaanse manier om mechanica te beschrijven, begint het hoofdstuk met een sectie over numerieke stromingsmechanica. Om inzicht te verwerven in de verschillende termen van de Navier-Stokes vergelijkingen wordt eerst de eendimensionale stromingsvergelijking van een incompressibele, niet-visceuze vloeistof door een rechte, compliante buis beschreven. Vervolgens wordt het geval uitgebreid naar compressibele, visceuze, driedimensionale stromingen. De Navier-Stokes vergelijkingen worden in differentiaalvorm en integraalvorm gegeven. Er wordt aandacht besteed aan

de kinematische decompositie van het stromingsveld en aan het begrip viscositeit. Ook wordt de differentiaalvorm geformuleerd in een bewegend rooster. De numerieke discretisatie van de vergelijkingen wordt besproken. Zo worden drie discretisatiemethoden vergeleken: de eindige differentie methode, de eindige volumes methode en de eindige elementen methode. Tenslotte worden de details van het CFD-pakket Fluent (ANSYS, Inc.) besproken.

In een tweede deel worden de technieken besproken die numerieke mechanica van continue media mogelijk maken. Hier worden eerst manieren aangereikt om rek en vervormingen te beschrijven. Vervolgens worden enkele spanningsdefinities gegeven en worden de regerende continuïteitsvergelijkingen afgeleid. Waarna de mechanica van kleine vervormingen wordt besproken, deze biedt immers het meeste inzicht. Bronnen van niet-lineariteiten in berekeningen worden bekeken. De zwakke, variationele formulering van de vergelijkingen wordt afgeleid. Een uitbreiding naar grote verplaatsingen en/of vervormingen wordt behandeld, waarna de eindige elementen discretisatietechniek wordt geïllustreerd. Tenslotte wordt het CSM-pakket Abaqus (Simulia, Inc.) van dichterbij bekeken.

In het laatste deel worden de reeds bestaande vloeistof-wand interactie benaderingen beschreven. Dit onderdeel begint met een paragraaf die de mogelijkheden bespreekt om de Euleriaanse vloeistofstromingsformulering te verzoenen met de Lagrangiaanse continue media mechanica formulering. Twee grote aanpakken worden vergeleken : de benadering van de vaste roosters en de arbitraire Lagrangiaanse-Euleriaanse benadering (ALE). Vervolgens wordt de monolitische aanpak, waarbij alle vergelijkingen samen worden opgelost, vergeleken met de gepartitioneerde aanpak, waarbij het stromingprobleem en het vervormingsprobleem apart worden opgelost en een derde programma zich bezig houdt met de koppeling. De commercieel beschikbare FSI-pakketten worden besproken volgens hun aanpak. Daarna worden enkele koppelingsalgoritmes besproken. Als afsluiter wordt de transfer van data tussen de twee solvers in een gepartitioneerde benadering besproken, waarbij de nadruk ligt op het conserveren van virtuele energie aan de interface.

Hoofdstuk 3 - Implementatie en validatie van de vloeistof-structuur interactie
In hoofdstuk 3 wordt de aanpak uiteen gezet die opgesteld werd in het kader van dit doctoraat. Eerst wordt, op basis van de mogelijke aanpakken die in het vorige hoofdstuk besproken werden, een overzicht gegeven van de keuzes. Er wordt voor een gepartitioneerde aanpak gekozen waarbij de CFD-solver en de CSM-solver commercieel beschikbare software zijn, het pakket Fluent (ANSYS, Inc.) en het pakket Abaqus (Simulia, Inc.), respectievelijk. Er werd een eigen iteratieve procedure geschreven die beide pakketten aan elkaar koppelt. Hierbij wordt de arbitraire Lagrangiaanse-Euleriaanse formulering gebruikt om de twee mechanica beschrijvingen van de vloeistofsolver en de structuursolver met elkaar in overeenstemming te brengen.

Een eerste grote paragraaf handelt over de algemene koppeling. Hier wordt de constructie van het rekendomein besproken. Er wordt besproken welk interpola-

tieschema wordt gebruikt voor de verplaatsings- en krachtkoppeling tussen beide solvers. De krachtkoppeling dient daarbij de kracht aan de interface op te splitsen in een krachtcomponent loodrecht en een component parallel aan het oppervlak van de beschouwde rekencel. Ook het convergentiecriterium wordt geëxpliciteerd, samen met de gegenereerde data voor mogelijke naverwerking. Tenslotte worden de beperkingen van de aanpak en de keuzes bepaald.

In de tweede grote sectie in dit hoofdstuk wordt de stabilisatieprocedure in de koppeling uiteen gezet. De procedure stelt tijdens de iteraties een gereduceerde orde model van de commerciële solver op om de werking van de solver op een toegankelijke matrixvergelijking-vormige wijze te benaderen. Het gereduceerde model van de solver wordt opgesteld aan de hand van gekende input-output-koppels van de solver. Hoe meer koppels in rekening gebracht worden, hoe beter het gereduceerde orde model het gedrag van de solver nabootst. Op die manier wordt de ontoegankelijkheid van de commerciële solver omzeild. Twee mogelijkheden worden onderzocht. Indien enkel een commercieel vloeistofstromingpakket wordt gebruikt, kan een gereduceerde orde model ervan worden opgesteld, dat dan als dynamische randvoorwaarde gebruikt wordt in de toegankelijke niet-commerciële structuursolver. Indien beide solvers ontoegankelijk zijn kunnen ze beide benaderd worden door een gereduceerd orde model, waarna de beide gereduceerde orde modellen gelijktijdig worden opgelost. De wiskundige ondersteuning van de aanpak wordt in deze sectie gegeven.

De volgende twee secties bevatten de validatieberekeningen van de nieuw opgestelde solver. Een eerste berekening behelst de golfvoortplanting in een rechte buis. De theoretische waarde van de golfvoortplantingssnelheid kan bepaald worden met gekende formules. Uit de vloeistof-wand interactie berekening kan ook een golfvoortplantingssnelheid bepaald worden uit de eindige voortplantingssnelheid van een storing. Beide snelheden verschillen minder dan 1%, wat de accuraatheid van de methode illustreert. Bovendien werd bij deze berekening de computationele kost vergeleken met een andere methode die gestoeld is op de Aitken acceleratie.

Een tweede validatieberekening is de berekening van de uitwijking van een flexibele elastische vin, stroomafwaarts aan een vaste cilinder gefixeerd, die ondergedompeld is in een stroming. Van dit voorbeeld zijn in de literatuur uitgebreide resultaatverslagen beschikbaar, zodat het kan gebruikt worden als een goede validatie. Het probleem is opgesplitst in drie deelproblemen. Eerst wordt de stromingberekening gevalideerd door de vin onbeweeglijk te onderstellen. De geïntegreerde krachtcomponenten op de vin en cilinder zijn gegeven, de berekende waarden wijken er slechts een weinig van af in een voldoende verfijnd rooster. In een tweede luik wordt de accuraatheid van de numerieke continue mechanica solver geanalyseerd aan de hand van de uitwijking van de vin door een opgelegde zwaartekracht, berekend zonder vloeistof-wand interactie. Ook hier komen de resultaten zeer goed overeen met de literatuur. Tenslotte wordt een vloeistof-structuur probleem uitgerekend, waarbij de vin uitwijkt door de krachten die de stroming op de vin uitoefenen, in een volledig gekoppelde omgeving. Hier wijkt de oplossing in het slechtste geval 3% af van de opgegeven literatuurwaarde. Het verschil met de meer

accurate berekening in het golfvoortplantingsprobleem komt voort uit het feit dat de viscositeit in het vin-probleem een grotere rol speelt, waardoor de accuraatheid van de krachten op de vin wordt beperkt door minder accuraat berekende snelheidsgradiënten.

Hoofdstuk 4 - Vloeistof-structuur interactie model van de menselijke aorta
In dit hoofdstuk wordt de eerste toepassing besproken. Hier wordt het reflectiepatroon van de eerste $20cm$ aorta bestudeerd. De aorta is een gradueel vernauwende buis. Door die graduele vernauwing ontstaan overal reflecties, ook op plaatsen waar geen zijtakken of plotse diameterveranderingen optreden. Het materiaalmodel voor de aortawand werd uit druk-diameterrelaties gehaald die beschikbaar zijn in de vakliteratuur. Een hyperelastisch, isotroop materiaalmodel met een polynomiale rek-energiefunctie werd gefit aan de beschikbare data via een kleinste kwadraten methode om de parameters van het materiaalmodel te bepalen. De geometrie werd zodanig bepaald dat op de diastolische bloeddruk de geometrie verkregen werd van een in vitro model van een menselijke arteriële boom beschikbaar in het labo. Met die arteriële boom werden ook de opwaartse en afwaartse randvoorwaarden bepaald voor het stromingprobleem. De randvoorwaarden voor het structuurprobleem, de opgelegde axiale rek, werden uit literatuur gehaald. Twee hartcycli werden doorgerekend om eventuele invloeden van de initialisatie-keuze teniet te doen.

In het vorige hoofdstuk werd de studie van golfpropagatie in een bloedvat gebruikt ter validatie van de vloeistof-structuur benadering. Aangezien echter een vergelijking met de theorie werd beoogd, werden niet-fysiologische randvoorwaarden gebruikt. Het gebruikte inlaatprofiel had een kleine amplitude, de wandschuifspanning was nul verondersteld en een niet-reflectieve uitlaatrandvoorwaarde garandeerde enkel voorwaartse druk en snelheidsgolven. In dit hoofdstuk wordt een fysiologisch model van de thoracale aorta opgebouwd, zodat golfreflecties er kunnen bestudeerd worden. De thoracale aorta is een taps bloedvat, de diameter verkleint gradueel stroomafwaarts vanaf de aorta klep. Door die continue verandering in diameter wordt een voorwaartse golf continu gereflecteerd, zelfs bij afwezigheid van vertakkingen.

Met deze gegevens wordt een tweedimensionaal, axisymmetrisch vloeistofstructuur interactiemodel geconstrueerd, alsook een eendimensionaal model, zodat de resultaten van beide benaderingen kunnen vergeleken worden. De druk- en debietgolven worden geanalyseerd gebruik makend van twee technieken, een impedantieanalyse in het frequentiedomein en een golfintensiteitsanalyse in the tijdsdomein. De bekomen druk en debietgolven via de twee- en eendimensionale benadering vertonen een goede overeenkomst. Bovendien wordt voor beide resultaten een fysiologisch golfintensiteitsprofiel gezien. De impedantieanalyse toont een impedantiespectrum waarbij fase en modulus gelijkaardige patronen tonen voor de beide resultaten. Gezien de eendimensional benadering een vereenvoudigde druk-diameterrelatie gebruikt, is een verschil in golfsnelheid zichtbaar, waardoor de timing van de voorwaartse en achterwaartse golven lichtjes afwijkt van de twee-

dimensionale benadering. Daarnaast is de attenuatie van de golven verschillend in beide gevallen, de golven in de eendimensionale berekening worden veel minder sterk gedempt dan de golven in de tweedimensionale berekening, deels door de vereenvoudigde manier waarop het eendimensionale model de vloeistofviscositeit incorporeert.

Wanneer men golfpropagatie wil bestuderen in de arteriële boom zijn eendimensionale modellen bijzonder nuttig, aangezien de vereiste rekenkracht zeer beperkt is. Wanneer uiteraard gedetailleerde kennis nodig is van het druk- en snelheidsveld is een meerdimensionale benadering onontbeerlijk. Beide benaderingen zijn dus complementair. De keuze van een gepaste druk-diameterfunctie is cruciaal wil met physiologisch relevante resultaten bekomen. Daarnaast werd aangetoond dat de voet-methode en de dU-dp-curve methode ter bepaling van de golfsnelheid afwijkende resultaten opleveren. Dit is te verklaren doordat beide methodes onderstellen dat bij het begin van de systole geen reflecties aanwezig zijn in het systeem. In de gesimuleerde aorta echter werden sterke reflecties waargenomen, waardoor die onderstelling niet voldaan is.

Hoofdstuk 5 - Vloeistof-structuur interactie model van een abdominaal aorta aneurysma   Een tweede probleem dat werd bestudeerd aan de hand van de ontwikkelde vloeistof-structuurinteractie code is de wandspanningsverdeling van een abdominaal aorta aneurysma (AAA), een pathologische dilatatie van de aorta in de buikholte. Wanneer de wandspanning van het aneurysma de breukspanning overschrijdt, breekt het aneurysma met een zware, in 90% van de gevallen fatale, inwendige bloeding als gevolg. Aneurysma's kunnen behandeld worden, maar de behandeling brengt eveneens een risico met zich mee. Hierdoor is er nood aan een duidelijk criterium om te bepalen of een aneurysma een substantieel breukrisico heeft. Momenteel worden twee criteria gebruikt die elkaar aanvullen, maar die zijn niet sluitend.

In deze studie worden verschillende manieren vergeleken waarop in de literatuur de spanningsverdeling in de aneurysmawand wordt gekwantificeerd. De ontwikkelde vloeistof-structuurinteractie code wordt gebruikt om de wandspanningen als functie van de tijd te berekenen. De gevonden piekspanning wordt vergeleken met (i) de piekspanning uit een statische vloeistof-structuurberekening; (ii) de piekspanning uit een ontkoppelde berekening, waarbij de druk verkregen uit een statische vloeistofstromingsberekening wordt gebruikt als niet-uniforme drukverdelingsrandvoorwaarde in een vervormingsberekening; en (iii) de piekspanning uit een vervormingsberekening met een homogene drukrandvoorwaarde.

Een vereenvoudigde, axisymmetrische geometrie werd gebruikt. Twee situaties werden vergeleken, een situatie waarbij het aneurysma volledig gevuld is met bloed en een situatie waarbij het aneurysma volledig gevuld is met thrombus. De wand werd gemodelleerd met een hyperelastisch, isotroop materiaalmodel uit de literatuur, terwijl de thrombus gemodelleerd werd met een lineair materiaalmodel, eveneens uit de literatuur. Beide modellen zijn gebaseerd op populatiestudies. De randvoorwaarden voor beide gevallen werden bepaald via een eendimensionaal

parametermodel. Bij de transiënte berekening werden twee cycli doorgerekend, waarbij de tweede cyclus werd gebruikt voor analyse zodat de keuze van beginvoorwaarden geen invloed heeft op de resultaten.

De resultaten toonden aan dat de benaderingen kwalitatief en kwantitatief dezelfde oplossing gaven als de meer tijdrovende FSI berekening. De ontkoppelde benadering en de statische vloeistof-structuurberekening gaven dus geen extra nauwkeurigheid ten opzichte van de zuivere structuurberekening, terwijl die laatste computationeel veel minder duur is. De resultaten wezen ook op een mogelijk gunstig effect van de aanwezigheid van een thrombus op het scheurrisico van het aneurysma, hoewel het zelf leidt tot een verhoogd risico op embolie van een beenslagader. Tenslotte toonde de studie ook aan dat wanneer het mogelijk positieve effect van een thrombus wordt bestudeerd, de randvoorwaarden dienen te worden in acht genomen die rekening houden met de gewijzigde compliantie van de abdominale aorta en de bloeddistributie die daarbij hoort. Door de verhoogde relatieve stijfheid van een thrombusgevuld aneurysma gaat minder debiet naar het aneurysma in vergelijking met een thrombus-vrij aneurysma. Dit verschil in randvoorwaarden moet meegenomen worden in de berekingen.

Hoofdstuk 6 - Golfintensiteitsanalyse van het linker ventrikel tijdens diastole
In vorige hoofdstukken werden reflecties en propagaties van golven bestudeerd om een inzicht te verwerven in de fysiologie van het vasculair stelsel. Daarbij kijkt men naar de bloedstroming als een eendimensionale stroming en wordt de wandvervorming direct ingebracht in de vergelijkingen, zoals gedaan werd aan het begin van hoofdstuk 2.

Golfintensiteitsanalyse (wave intensity analysis - WIA) is een krachtige techniek om in het tijdsdomein te kijken naar druk en snelheidsgolven in het vasculair netwerk. De techniek is gebaseerd op de analyse van de door de golf getransporteerde energie via berekening van de golfintensiteit $dI = dPdU$ waarbij dP en dU een verandering per tijdsinterval voorstellen van respectievelijk de druk en snelheid.

In deze studie wordt een aanpassing van de golfintensiteitsanalyse voorgesteld, zodat ze toepasbaar is in de golfstudie waarbij de wand tijdsafhankelijke elasticiteitseigenschappen heeft, zoals het geval is in het linkerventrikel tijdens diastole. Op die manier kan de techniek bijdragen om de processen die diastolisch hartfalen in de hand werken te begrijpen. De benadering wordt eerst analytisch onderbouwd met een eendimensionaal elastisch buismodel van het linker ventrikel met een tijdsafhankelijke druk-diameter relatie. Daarna wordt de techniek geïllustreerd met data die verkregen werd met een gevalideerd quasi-driedimensionaal axisymmetrisch numeriek vloeistof-wand interactiemodel van het linker ventrikel.

De nieuwe benadering werd vergeleken met de oude techniek voor curves langs de basis-apex as, dicht bij de mitraalklep. Net na klepopening wordt het grootste verschil waargenomen tussen de nieuw voorgestelde en de bestaande techniek. Waar de standaard golfintensiteitsanalyse een achterwaartse expansiegolf toont, ziet men bij de aangepaste techniek een voorwaartse compressiegolf. De

voorgestelde aanpassing dient meegenomen te worden in elke golfintensiteitsanalyse waarbij de wandelasticiteit verandert met de tijd. Het toont immers een substantiële invloed op de resultaten.

Hoofdstuk 7 - Diermodel van coronaire ischemie-reperfusie   In alle voorgaande hoofdstukken werd gekeken naar het louter mechanisch aspect van bloedstroming en wandvervorming van bloedvaten. Echter, in het cardiovasculair systeem is het belangrijk een algemener beeld te behouden. Het is cruciaal het celniveau niet uit het oog te verliezen, meer bepaald de metabolische veranderingen die een veranderde bloedstroming kan induceren. In dit hoofdstuk wordt een voorbeeld gegeven van zo'n interactie die waargenomen wordt nadat bloedstroming in de kransslagaders is hersteld een uur nadat een kransslagader werd afgeknepen.

Alhoewel reperfusie na een kransslagaderblokkade cruciaal is om de overlevingskansen van de hartspiercellen te optimalizeren, kan de reperfusie een waterval aan hartspiercelbeschadigingen veroorzaken die de beschadigingen door de ischemie nog versterken. De invloed van reperfusie op de linkerventrikelfunctie en de ventriculo-arteriële koppeling werd onderzocht in varkens. Door het afklemmen van een kransslagader werd coronaire ischemie geïnduceerd, waarna de klem werd verwijderd om de gevolgen van de reperfusie te kunnen bekijken. Zes dieren werden opgenomen in de studie, waarbij metingen werden gedaan ter evaluatie van de cardiovasculaire functie voor het aanbrengen van de klem (baseline - BL), een uur na het aanbrengen van de klem ($T60$), twee uur na het verwijderen van de klem ($T180$) en vier uur na het verwijderen van de klem ($T300$). Ventriculo-arteriële koppeling werd geëvalueerd via een ventriculo-arteriële elastantie, alsook via een stijfheidskoppelingsindex en een temporele koppelingsindex.

Er werd aangetoond dat ischemie gevolgd door reperfusie ($T180$-metingen tegenover $T60$-metingen) een progressieve verslechtering in cardiovasculaire functie veroorzaakte. Dit werd naar voor gebracht door een daling van de gemiddelde arteriële bloeddruk, het hartminuutvolume en het ejectiepercentage, waarbij de daling niet hersteld bleek bij de $T300$-metingen. Hoewel de reperfusie een verhoging van de helling van de eind-diastolische druk-volume relatie teweegbracht, werd tegelijkertijd ook een verschuiving van deze relatie naar rechts waargenomen, geassocieerd met een vermindering van de contractiele functie van het hart. Histologisch onderzoek toonde aan dat na vier uur reperfusie het hartspierweefsel onherstelbaar beschadigd was.

Globaal kan men stellen dat na reperfusie de cardiovasculaire functie niet hersteld wordt, maar in tegendeel verder achteruitgaat. Het is onwaarschijnlijk dat deze geobserveerde veranderingen enkel te wijten zijn aan ischemische beschadiging van de hartspiercellen. Dit voorbeeld toont bovendien aan dat wanneer men enkel naar de mechanische aspecten kijkt van bloedstroming, zoals in voorgaande hoofdstukken, de resultaten potentieel sterk kunnen verschillen van het werkelijke cardiovasculaire gedrag.

Hoofdstuk 8 - Conclusie en toekomstperspectieven In dit werk werd een manier voorgesteld om stromingberekeningen te doen waarbij de interactie tussen het bloed en de vaatwand in rekening wordt gebracht. Hiervoor werd gebruik gemaakt van een commercieel beschikbare vloeistof- en structuursolver en werd zelf een koppelingsalgoritme uitgewerkt. De stabilisatiekoppeling bestond erin om matrixbenaderingen op te stellen van de vloeistof- en structuursolver en om die te koppelen. De code werd gevalideerd en toegepast op twee voorbeelden, de studie van reflecties in de aorta en de begroting van wandspanningen in een aneurysma. Daarnaast werden de resultaten van een ventriculair FSI-model gebruikt om een voorgestelde aanpassing van de golfintensiteitsanalyse te illustreren. Tenslotte werd aangetoond dat een louter mechanische studie van bloedstroming tot foute conclusies kan leiden, wat geïllustreerd werd met een studie die het reperfusiegedrag van de hartspiercellen bekijkt nadat een afgeklemde kransslagader opnieuw doorstroomd wordt.

De voorgestelde techniek geeft accurate resultaten bij vloeistof-wand interactie berekeningen. De aanpak is stabiel en aangepast aan de biomechanische situatie. Evenwel is de aanpak niet zaligmakend. Zo dient steeds met een bredere visie naar de resultaten gekeken worden en wanneer sterke (biologische) feedback-mechanismen aanwezig zijn, zoals bij de reperfusie van een kransslagader na afklemming, kan de techniek weinig uitsluitsel bieden.

Naar de toekomst toe kan het algoritme nog verder aangepast worden. Zo dient het interpolatieschema aangepast te worden zodat ook roosters waarvan de knopen op de natte en droge kant van de interface niet samenvallen, kunnen bestudeerd worden. Ook verdere optimalisaties zijn mogelijk wanneer bijvoorbeeld de vloeistofsolver niet elke keer herstart moet worden, maar waarbij de vloeistofsolver kan verderwerken met de oplossing van de vorige iteratie. Tenslotte dient een eendimensionaal, vereenvoudigd model te worden opgesteld om effectief uitsluitsel te bieden of de instabiliteiten die gevonden werden tijdens tijdsafhankelijke berekeningen het gevolg zijn van een verschil in tijdsdiscretisatie tussen de vloeistofsolver en de structurele solver of niet.

English summary

Numerical methods, like computational fluid mechanics (CFD) and computational solid mechanics (CSM), are frequently used in engineering sciences . These techniques are not limited to the classic engineering sciences, however, but are also applicable to biomechanics. Numerical biomechanical simulations are already indispensable in the medical world. Next to medical imaging techniques and observation by the physician, they offer additional diagnostic information.

The numerical methods can also be used to enhance the design process of medical devices. Using numerical simulations one can already predict the behavior of the device, e.g. a heart valve or a stent, before the first prototype is made. Adaptations are possible and the number of necessary (expensive) prototypes can be hugely diminished.

Obviously, it is crucial to perform these numerical test as realistic as possible. In vascular flow computations the interaction between the blood flow and the vessel wall is very important. This fluid-structure interaction (FSI) cannot be neglected when using numerical techniques to perform flow calculations. The aim of the research presented in this work was to implement a method to enable numerical calculations where this fluid-structure interaction (FSI) was taken into account.

The dissertation is divided in eight chapters. It starts with an introduction of the anatomy, physiology and pathophysiology of the cardiovascular system (chapter 1) as well as an overview of the existing techniques to model fluid-structure interaction (chapter 2). Next the approach of the numerical FSI code which was implemented during this research is highlighted (chapter 3), as well as two applications (chapter 4 and 5). In a next chapter a ventricular FSI-model is used to illustrate a proposed adaptation in wave intensity analysis theory (chapter 6). A next chapter illustrates the limitations of a purely mechanical approach by studying reperfusion injuries, injuries that occur in the vessel wall after lifting a blockage on a coronary artery (chapter 7). Finally some general conclusions and propositions for future work are given (chapter 8).

Chapter 1 - Heart and circulation In this chapter all medical terms that will be used in later chapters are introduced. The chapter starts with an overview of the heart's function, the anatomy and physiology. The conductive system is described, with the action potential, the de- and repolarisation of the heart muscle cells and the shape of the electrocardiogram curve that is a consequence of it. The variation of the ventricular pressure and volume throughout the cardiac cycle is

described. After the description of the heart, the vessels are the next subject to focus on. A distinction is made between arteries, veins and capillaries. The different layers in the vessel wall are described and an overview is given of the different functions of vessels in the cardiovascular system. Next, the interaction between the heart and blood vessels is described. Parameters such as the cardiac output, stroke volume and stroke work are described and the parameters influencing them are given. The pressure-volume loop, describing the working regime of the heart, is discussed. Finally some pathologies are treated that will be studied in the next chapters. Atherosclerosis and stenosis, aneurysms and congestive heart failure are described.

Chapter 2 - Modeling with computational methods   The different techniques used to separately study the blood flow and the vessel wall deformation are described in this chapter, together with the possible techniques to account for the interaction between both. Hence this chapter is divided in three parts. In the first part computational fluid dynamics (CFD) are described, and in the second part computational solid mechanics (CSM) are treated. Both disciplines form the basis of fluid-structure interaction, so a profound knowledge of the techniques is essential to understand FSI. The techniques for fluid-structure interaction are described in the last section of this chapter.

After having explained the difference between an Eulerian and Lagrangian way to look at motion, the chapter starts with computational fluid mechanics. To gain insight in the physical processes behind the different terms in the Navier-Stokes equations, first the inviscid flow in a one-dimensional, compliant tube is considered. Afterward the equations are generalized to the Navier-Stokes equations for a three-dimensional, compressible, viscid flow. The equations are given in differential and integral form, and attention is given to the kinematic decomposition of the flow field and to the viscosity. The integral formulation is also generalized to a moving grid formulation. Finally the numerical discretization of the equations is given. Three discretization methods are compared: the finite difference, finite volume and finite element method. The commercial CFD software package Fluent (ANSYS, Inc.) is described.

In the second part of the chapter, techniques are given to study computational solid mechanics. First the definitions of deformation, strain and stress are given and the continuum equations are described. Small deformation mechanics are described, as they offer the best insight, and a generalization toward large displacement and deformation theory is given. Possible sources of non-linearity are described. Finally the discretization methods are described and Abaqus (Simulia, Inc.) is described as a commercially available finite element software package.

In a last section the existing fluid-structure interaction methods are given. First, possible ways to match the Eulerian description of the flow equations with the Lagrangian description of solid mechanics are discussed : the fixed grid approaches and the arbitrary Lagrangian-Eulerian approach. Next the monolithic approach, solving both the fluid and solid equations as one set of equations, is compared

to the partitioned solver approach, where the fluid and solid equations are solved separately after which the solutions are coupled in a third program. Commercially available FSI-codes are described with their approach, after which possible partitioned coupling methods are given. Finally the data transfer in a partitioned approach is studied in more detail.

Chapter 3 - Implementation and validation of fluid-structure interaction   In chapter 3 the FSI-approach that was implemented during this research is explained. First an overview of the choices is given, based on the possibilities given in the previous chapter. A partitioned approach is chosen where the solid solver is the commercially available Abaqus software (Simulia, Inc.) and the fluid solver is Fluent software (ANSYS, Inc.). An own written iterative coupling program was designed, using both software packages, to obtain fluid-structure interaction. The arbitrary Lagrangian-Eulerian approach was used to match the fluid solver's and the solid solver's description of motion.

A first paragraph deals with the general coupling. The construction of the computational domain is given and the transport procedure at the interface is described. The interpolation scheme between the fluid and the solid side of the interface is given. The forces need to be split in tangential and normal components compared to the interface face they work on. The convergence criterion is written down and the limitations of the approach are discussed.

In the second section of this chapter the stabilization procedure is described. The approach constructs reduced order models of the commercial solvers in order to approach the solver by accessible matrix equations. The reduced order model is built up using known pairs of input and associated ouput generated by the solver. The more pairs taken into account, the more accurately the reduced order model will mimic the behavior of the commercial solver. Two possible approaches are given. If the solid solver is an open source solver, only a reduced order model of the fluid solver is needed, which can be inserted into the solid solver as a dynamic boundary condition at the interface. If both the fluid and the solid solver are inaccessible, two reduced order models are constructed, one for each solver, and the reduced order models are solved as one big set of equations. The mathematical groundwork for this approach is given in this section.

The last two sections contain the validations of the approach. As a first validation wave propagation in a straight tube is studied. The theoretical value of the wave speed can be assessed using the Bramwell-Hill equation. On the other hand, from the fluid-structure interaction calculation the wave speed can be assessed from the propagation behavior of a disturbance in flow velocity or pressure. Both values for the wave speed differ less than 1%, illustrating the accuracy of the method. In this validation the computational efficiency of the reduced order model approach was compared to that of the Aitken acceleration method, showing that the reduced order model approach was considerably faster.

A second validation calculation studies the displacement of a two-dimensional flexible slab, downstream fixed to a fixed cylinder, submerged in a fluid flow. The

expected results from this example are frequently described in literature, making it a good validation case. The problem is separated into three parts. First the CFD-part is validated, considering the slab fixed and calculating the drag and lift forces working on the slab and cylinder. The obtained values do not differ for a sufficiently refined mesh. In a second part the CSM-part is validated, only considering the slab and studying the displacement induced by an imposed gravity. The results follow the results from literature. In a third part the interaction between fluid flow and the solid deformation is taken into account. Here the solution differs less than 3% from the results found in literature. The explanation of the more elevated difference compared to the more accurate results from the previous calculation is found in the fact that in this calculation the viscosity forces are playing a bigger role, so the accuracy is limited due to the limited accuracy of the interpolated velocity gradients.

Chapter 4 - Fluid-structure interaction model of the human aorta   In the previous chapter, wave propagation in an artery is used to validate the FSI-approach. However, as a comparison with the theoretical, one-dimensional wave speed was required, the boundary conditions in the validation study were non-physiological. The imposed inlet velocity was very small, slip at the fluid-structure interface was allowed and a non-reflecting outlet boundary condition was used. In this chapter a physiological numerical model of the thoracic aorta is constructed to study wave reflections.

The aorta is a tapered tube, hence due to this gradual narrowing a forward wave is continuously reflected, even if no side branches are present. The material model used is obtained from pressure-area relations found in literature. A hyperelastic, isotropic material law with a polynomial strain energy function is used to fit to the pressure-area data using a least square method in order to establish the material parameters. The geometry, with length $20cm$, is designed in such a way that at diastolic pressure the aorta has the geometry of an in vitro model of the arterial tree present in our research facility.

A two-dimensional axisymmetrical fluid-structure interaction model is constructed, as well as a one-dimensional compliant-tube model in order to allow comparison of the results obtained with the two approaches. The one-dimensional model uses the solver developed by Stergiopulos et al. [1]. The pressure and flow waves are analyzed using two techniques, impedance analysis in the frequency domain and wave intensity analysis in the time domain. The obtained pressure and flow waves show good resemblance. Both approaches yield a physiological wave intensity analysis pattern with two forward and one backward wave peak throughout the aorta. Impedance analysis shows similar patterns for the modulus and the phase of the impedance for both approaches.

One-dimensional models are useful when studying wave propagation in the vascular tree, as they do not require huge numerical resources. However, when flow velocity and pressure fields are required, for example when one wants to assess wall shear stress distributions, a two-dimensional axisymmetrical approach

is vital. Hence both approaches are complementary. However, the pressure-area-relationship used in the one-dimensional case needs to be chosen with care, as oversimplification of the relation can yield a wrong wave speed, which will result in incorrect wave propagation simulations. The study highlighted that, when strong reflections are present, the foot-to-foot method and the dU-dp-curve method to assess the pulse wave velocity yield deviating values, due to the fact that the no-reflections requirement is not fulfilled anywhere during the cardiac cycle.

Chapter 5 - Fluid-structure interaction model of an abdominal aortic aneurysm The second application, which is described in this chapter, considers an abdominal aortic aneurysm (AAA), a pathological dilatation of the abdominal aorta. When the local wall stress in the aneurysm exceeds the local failure strength, the aneurysm ruptures inducing a heavy and in 90% of the cases fatal internal bleeding. Aneurysms can be treated but the treatment holds some risk itself. Therefore a good criterion is needed to establish the potential rupture risk. The currently used diameter criterion, however, is insufficient.

In literature several approaches to establish a patient-specific wall stress distribution are mentioned. In this study the results of four different approaches are compared: (i) a fully coupled transient fluid-structure interaction approach, (ii) a fully coupled static FSI-approach, (iii) a decoupled approach, where the pressure distribution from a static flow computation is used as a non-uniform pressure load for the solid computation, and (iv) a pure solid mechanics approach with uniform pressure load.

A simplified, axisymmetrical geometry is used, once computed without thrombus and once computed with an intraluminal thrombus (ILT) filling the aneurysmal sac. The wall of the aneurysm is modeled as a hyperelastic, isotropic material model, while the thrombus is modeled as a linear elastic material. Both material models were obtained from population studies in literature. Boundary conditions are assessed using a non-linear one-dimensional model of the systemic circulation.

Results showed that a decoupled or a static FSI-approach do not necessarily provide results closer to the transient FSI results as compared to the computational solid mechanics approach, even though they are computationally more expensive. Finally we show that when comparing the stress distribution with and without ILT, the change of blood flow through the aneurysm needs to be taken into account in the imposed boundary conditions. This redistribution of blood is caused by the thrombus-related change in resistance and compliance in the abdominal region.

Chapter 6 - Wave Intensity Analysis of the left ventricle using a ventricular FSI-model In previous chapters wave reflection and propagation behavior was studied, which helped to gain insight in the physiology of the vascular system. In these wave reflection and propagation studies one considers blood flow to be a one-dimensional flow, where the vessel wall interaction is inserted directly into the Navier-Stokes equations, as was done at the beginning of chapter 2.

Wave intensity analysis (WIA) is a powerful technique to study pressure and flow velocity waves in the time domain in vascular networks. The method is based on the analysis of energy transported by the wave through computation of the wave intensity $dI = dPdU$, where dP and dU denote pressure and flow velocity changes per time interval respectively.

In this study we propose an analytical modification to the WIA so that it can be used to study waves in conditions of time varying elastic properties, as in the left ventricle (LV) during diastole. This may help to unravel the processes leading to diastolic heart failure. The approach is first analytically elaborated for a one-dimensional elastic tube-model of the left ventricle with a time-dependent pressure-area relationship.

Data obtained with a validated quasi-three dimensional axisymmetrical fluid-structure interaction model of the left ventricle are employed to demonstrate this new approach. Along the base-apex axis close to the base wave intensity curves are obtained, both using the standard method and the newly proposed modified method. The main difference between the standard and modified wave intensity pattern occurs immediately after the opening of the mitral valve. Where the standard WIA shows a backward expansion wave, the modified analysis shows a forward compression wave. The proposed modification needs to be taken into account when studying left ventricular relaxation, as it affects the wave type.

Chapter 7 - Porcine model of coronary ischaemia-reperfusion In previous chapters the research was focused purely on the numerical simulation of blood flow and wall deformation in the cardiovascular system. However, when one is looking at the cardiovascular system, a wider look is imperative. It is important that one does not forget to consider the cell level and the metabolic changes blood flow alternations can induce. In this chapter such an interaction between blood flow and cell metabolism is illustrated, observed after blood flow is restored an hour after onset of clamping the left anterior descending coronary artery.

Although reperfusion after coronary occlusion is mandatory for myocardial salvage, reperfusion may trigger a cascade of harmful events (reperfusion injury) adding to myocardial injury. We investigated effects of reperfusion on left ventricular (LV) haemodynamics and ventriculo-arterial (VA) coupling in pigs following acute myocardial ischaemia induced by coronary artery occlusion. Experiments were performed in six animals, with measurements of cardiac and arterial function at baseline, after 60 min of ischaemia ($T60$) and after 2 ($T180$) and 4 h of reperfusion ($T300$). Ventriculo-arterial coupling was assessed using the ventriculo-arterial elastance ratio (E_{es}/E_a; E_a : effective arterial elastance; E_{es} : ventricular end-systolic stiffness) , as well as using a 'stiffness coupling' and 'temporal coupling' index.

Reperfusion following ischaemia ($T180$ versus $T60$) induced a progressive decline in cardiovascular function, evidenced by a decrease in mean arterial blood pressure, cardiac output and ejection fraction which was not restored at $T300$. Although reperfusion also induced an increase in slope of the end-systolic pressure-

volume relationship ($ESPVR$), the $ESPVR$ curve shifted to the right, associated with a depression of contractile function. Histology demonstrated irreversible myocardial damage at $T300$. The ventriculo-arterial elastance ratio and the 'stiffness coupling' index were unaffected throughout the protocol, but the 'temporal coupling' parameter indicated a relative shift between heart period and the time constant of the arterial system.

It is seen that the cardiovascular function is not restored, but that the situation is further worsened by the reperfusion. It is unlikely that these alterations are attributable to ischaemic injury alone. This example illustrates that when one is only looking at the heart as a pump and a set of tubes, as done in the previous chapters, the findings of computer models can be far from the actual cardiovascular response.

Chapter 8 - Overall Conclusion and future work   In this work a method was proposed to perform vascular flow calculations where the interaction between the blood flow and the vessel wall is taken into account. To achieve this, commercially available fluid and structural solvers were embedded in an own-written coupling program. Stabilizing the coupling was obtained by coupling reduced order models, matrix representations of the fluid and solid solver. The approach was validated and was applied to two cases, the study of reflections in the aorta and the quantification of wall stresses in an abdominal aortic aneurysm. In chapter 6 fluid-structure interaction was used to illustrate a proposed modification to the wave intensity analysis theory when studying the left ventricle flow. A last chapter illustrated the limitations of pure mechanical approaches by studying the reperfusion injuries after occlusion and reperfusion of coronary arteries.

The proposed method delivers accurate results when performing FSI-calculations. The approach is stable and is applicable to biomechanical cases. However the approach is not flawless as was illustrated in the last chapter. A wide vision is needed when performing FSI-calculations and a healthy portion of skepticism is required. Especially when strong feedback mechanisms are present, as is seen after reperfusion of a coronary artery, the mechanical FSI-approach reaches its limits.

The algorithm can be further improved. The interpolation method to match the results from the wet and dry side of the interface has to be improved in such a way that also meshes can be used where the nodes do not match. Secondly, the code can be strongly optimized if a way was found so that the fluid solver does not have to be restarted each iteration, and where the new solution can be calculated starting from the solution in the previous iteration. This will hugely enhance the profit that can be made by parallelizing the code. Finally a simplified one-dimensional model is needed to study the instability due to the difference in time discretization approach between the fluid and the solid solver.

1

Heart and circulation

The cardiovascular system fulfills a wide range of functions. Through the cardiovascular system oxygen, glucose, hormones, drugs, vitamins, water and many other essentials for cell metabolism are transported to the cells of the body. On the other hand it serves to efficiently wash out waste products, such as carbon dioxide and urea. Although transport of blood to a distance from the cells at which exchange by diffusion is possible is its most obvious function, the cardiovascular system has many other functions, amongst which temperature regulation.

The human heart is one of the most mind-blowing organs, weighing about $300g$ but beating about 2 000 000 000 times by the time we are 60 years old. However, the heart can not do its job without the vessels, the "tubes" that bring the blood to where it needs to be. The interaction between the heart and the vessels is very refined, making healthy vessels a key part of a healthy circulation. In this chapter I will try to highlight this interaction of the heart with the vessels.

First, the anatomy and physiology of the heart will be described. Second we will take a closer look at the blood vessels, both arteries and veins. In a third section the interaction between the heart and vessels will be described, explaining the subtleties which determine e.g., blood pressure. After that section cardiac and vascular pathologies will be described and in a last section the role of computational models is emphasized.

1 The heart

1.1 Anatomy and physiology

The heart is a hollow muscle about the size of a fist, which acts like a volumetric pump. It has two separate parts, a left and right one, both consisting of an atrium and a ventricle, separated by a septum, as shown in Fig. 1.1. Oxygen-rich blood coming from the lungs (pulmonary circulation) is collected in the left atrium (2) and pumped through the left ventricle (9) to the other organs (systemic circulation). Oxygen-poor blood is collected in the right atrium (1) and pumped through the right ventricle (10) to the lungs for reoxygenation.
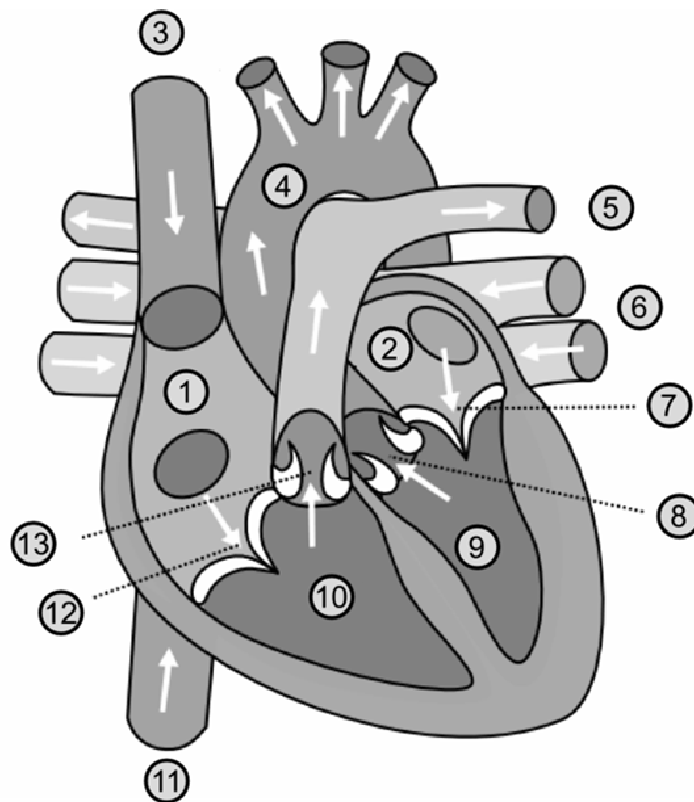
Figure 1.1: Section of the heart; anterior side. 1. Right atrium, 2. Left atrium, 3. Vena cava superior, 4. Aorta, 5. Pulmonary artery, 6. Pulmonary vein, 7. Mitral valve, 8. Aortic valve, 9. Left ventricle, 10. Right ventricle, 11. Vena cava inferior, 12. Tricuspid valve, 13. Pulmonary valve. [2].

In the heart, the blood flows from atrium through ventricle to the other organs.

To avoid backward flow four valves are present which are situated in one plane, the annulus fibrosus, a fibrotic separation between the atria and ventricles. Two valves are positioned between the atria and the ventricles, the tricuspid valve (12) between the right atrium and ventricle and the mitral valve (7) between the left atrium and ventricle. The two other valves are situated between the ventricles and the arteries, the aortic valve (8) between the left ventricle and the aorta, and the pulmonary valve (13) between the pulmonary artery and the right ventricle. The atrial-ventricular valves are attached to the chordae tendineae which are attached to the papillary muscles. As such, the valve can withstand high atrio-ventricluar pressure gradients without slipping through. The valves make sure the heart is an efficient pump and deficiency of one of the valves causes major complications due to a significantly deteriorated performance, ultimately resulting in a shortage of oxygen at organ level.

1.2   The conductive system
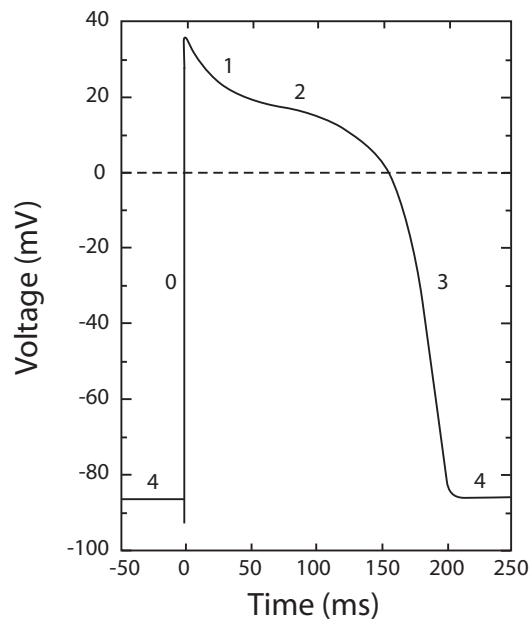
Figure 1.2: A typical ventricular action potential with the rest potential (4), the depolarisation (0) and the repolarisation (1-3). Adapted from [3].

The heart is a muscle, built up of a lot of muscle cells (myocytes). For efficient pumping, the timing of each muscle cell's contraction is essential. Muscle cells have a rest potential, a potential difference of about 50 to $100mV$ over the

cell membrane. This potential is defined negative because the cell interior has a lower potential than the surroundings. Muscle cells contract when they are activated, e.g., by neuron stimulation. When a myocyte is activated the muscle cell's membrane potential becomes positive (action potential), due to a depolarisation of the membrane, and then drops again due to a repolarisation (Fig. 1.2).
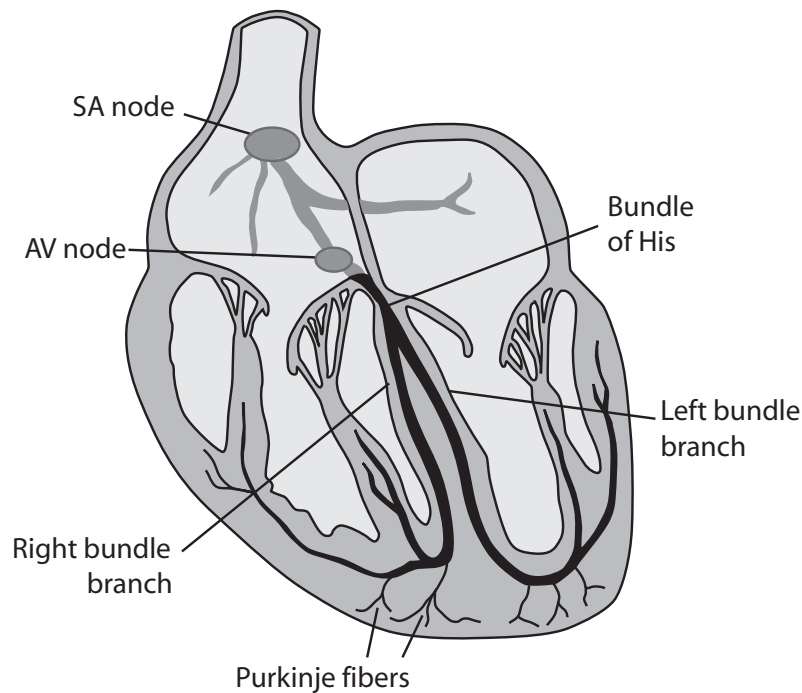
Figure 1.3: The conductive system in the human heart. Adapted from [4].

Some of the muscle cells, called pacemaker cells, have the ability to start an action potential without any external activation. They do not have a stable rest potential, but show a slow spontaneous depolarisation. They generate a regular pulse of which the frequency is determined by the slope of the depolarisation. The group of pacemaker cells situated in the right atrial wall are called the sino-atrial node (SA-node, Fig. 1.3). This sino-atrial node generates a periodic depolarisation, which propagates from muscle cell to muscle cell over the atrium. The depolarisation propagates to the ventricle through a group of cells called the atrial-ventricular node (AV-node, Fig. 1.3). This is the only electrical connection between atrium and ventricle, as the annulus fibrosus electrically isolates the upper and lower heart halves. From the atrial-ventricular node, the depolarisation propagates through the bundle of His and the left and right bundle branch onto the myocytes of the ventri-

cles.

The propagation of the depolarisation and subsequent repolarisation occurs at a limited speed. Due to this limited propagation velocity, the heart acts like a dipole during the process, inducing an electrical field. The changes in voltage induced by this field can be measured at skin level, producing the electro-cardiogram (ECG). An ECG (Fig. 1.4, top panel) is taken by at least three electrodes, one on each wrist and one on the left ankle; a galvanometer is used to measure the voltage differences between the electrodes. The ECG-curve typically consists of four characteristic complexes. The *P-wave* is associated with atrial depolarisation, induced by a pulse from the sino-atrial node. Next, the *QRS-complex* is seen, which is associated with ventricular depolarisation which creates a rotating dipole, starting from the septum-right ventricle orientation rotating counterclockwise. This results in the two small negative peaks and a large positive peak. The last complex is the *T-wave* associated with repolarisation of the ventricular myocytes.

1.3 The cardiac cycle

The cardiac cycle consists of two main phases, the systole and the diastole, as, for the left heart, represented in Fig. 1.4. The systole starts with an isovolumic contraction phase. The ventricles are filled with blood and start contracting, closing the mitral valve. When the left ventricular pressure exceeds the pressure in the aorta, the aortic valve opens and the ejection phase starts. At the end of the ejection phase the aortic valve will close and the diastole starts with an isovolumic relaxation phase, where all four cardiac valves are closed. The mitral valve opens when the left ventricular pressure is lower than the atrial pressure, starting the filling phase. The filling of the left ventricle is divided in three waves: the E-wave, where the atrium acts as a reservoir, the L-wave (if present), where the atrium acts as a prolongation of the venae cavae and finally the A-wave, where the atrium actively contracts. If the pressure in the ventricle rises higher than the pressure in the atrium the valves close again, starting the isovolumic compression.

2 The systemic circulation

Oxygen-rich blood leaves the heart trough the aorta, the main artery in the human body. The aorta divides into smaller arteries and more distal into arterioles. The arterioles divide into capillaries, very small blood vessels with thin walls, which allow diffusive metabolic exchanges with cells. The capillaries regroup into venulas and veins. The main veins are the superior and inferior venae cavae, which collect blood straight into the right atrium. A similarly branched structure is seen in the pulmonary circulation. Our main interest, however, goes to the systemic circulation.
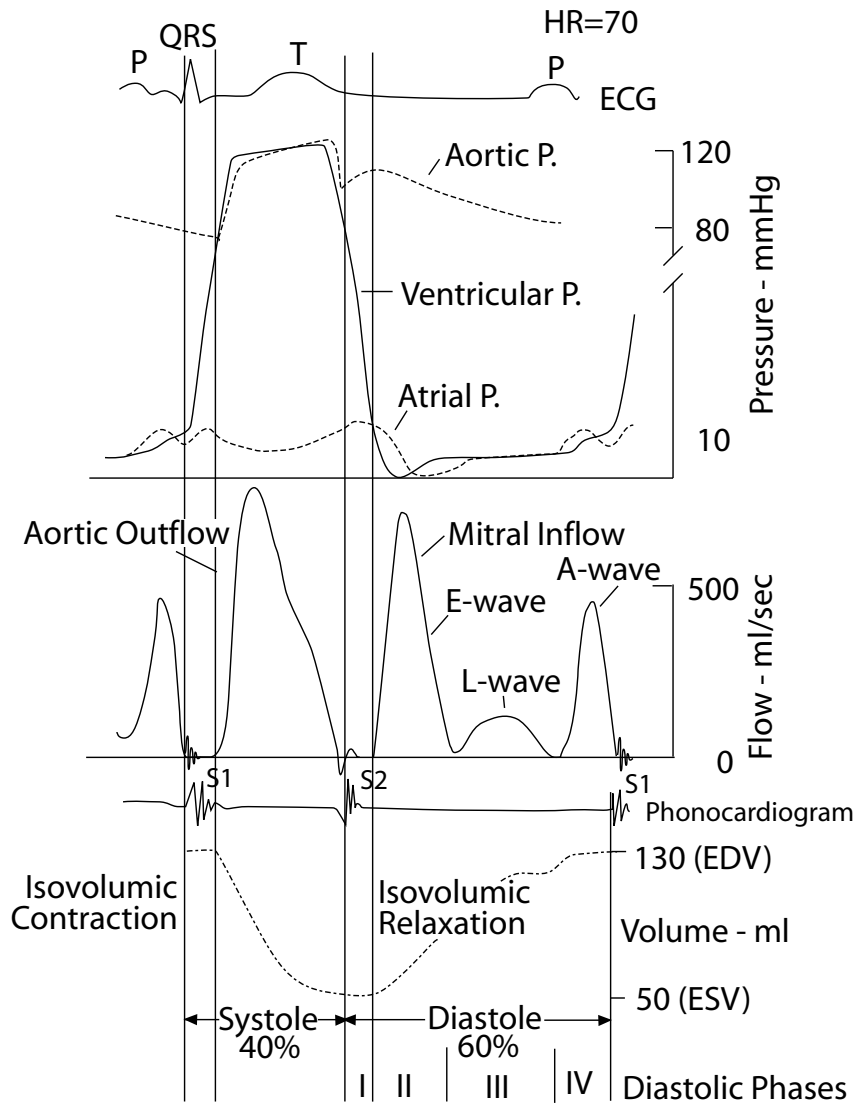
Figure 1.4: Evolution of ECG and some main cardiovascular pressures and flows and the ventricular volume during one cardiac cycle in the left heart. Adapted from [5].

Vessel	Number	Length (mm)	Diameter (mm)	Total cross-sectional area (mm^2)	Volume (% of total)
Main artery	1	60	3	7	2.5
Arterioles/smallest arteries	1 380 000	1.5-2	0.024-0.031	739	8.1
Capillaries	47 300 000	0.4	0.008	2378	5.7
Venules	2 100 000	1.0	0.026	1151	6.9
Small veins	180 000	1-14	0.075-0.28	1019	21.3
Large veins	61	39-60	1.5-6	174	46.7

Table 1.1: Dimensions of blood vessels in dog mesentery [6].

In table 1.1 the diameter and total cross-sectional area of vessels from a dog mesentery are given. One can see that the capillaries have a much smaller diameter compared to the main artery. However, the total cross-sectional area is much larger. Due to this elevated cross-sectional area the blood velocity will decrease firmly, allowing exchange between the blood and the surrounding tissue. The vessel wall, except the wall of capillaries, consists of three layers, the tunica intima, the tunica media and the tunica adventitia, as shown in Fig. 1.5. The tunica intima is the thin layer closest to the lumen, built up of a single layer of endothelial cells on a layer of connective tissue. The layer of endothelial cells forms a boundary between the blood and the vessel wall. It acts as a receptor-effector organ and reacts on each stimulus with the release of the appropriate vasoactive products in order to maintain the vasomotoric balance [7]. The tunica media consists of smooth muscle cells surrounded by a matrix of elastin and collagen fibers. It supplies mechanical strength to the intimal layer. The function of the contractile ability of this layer will be discussed in the next section. The outermost layer, the tunica adventitia, forms a protective layer around the vessel. It consists of connective tissue and elastin and collagen fibers.

2.1 Functions

Vessels bring the blood from the heart to the organs. However, vessels fulfill also other tasks besides the basic transport of blood. These other functions are described in this paragraph.

Elastic arteries The heart contracts and relaxes in a cyclic way, which means that the generated blood flow is not constant but pulsatile: the blood flow in the aorta falls back to zero during diastole. Organs however require an almost constant flow. To convert the pulsatile flow of the heart into a more constant flow, the main
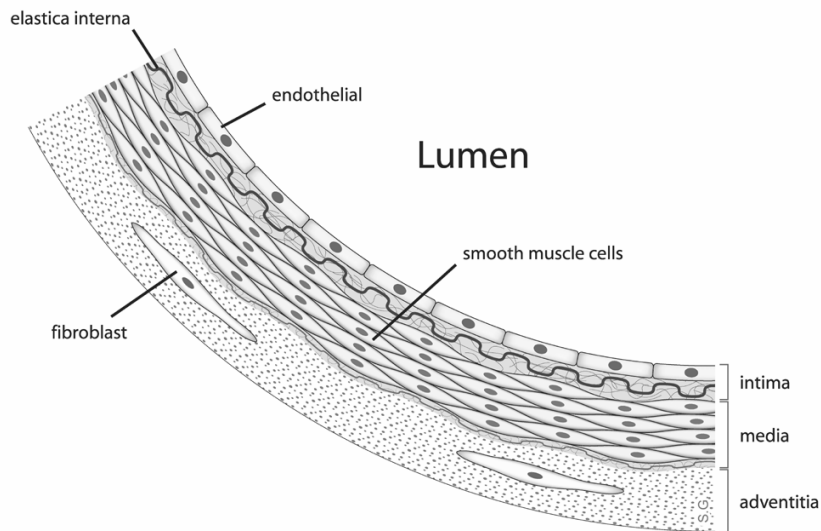
Figure 1.5: The layers in an arterial vessel wall [8].

arteries close to the heart, such as the pulmonary artery and the aorta, have a highly elastic vessel wall. The tunica media of these vessels consists of a high level of elastin, allowing the vessels to expand during the ejection phase of the heart, acting as a buffer. During diastole the heart does not eject flow anymore, but now the buffered blood in the expanded arteries flows to the organs, thus providing blood to the organs during the filling phase of the heart.

Resistance vessels   Resistance vessels control the blood distribution over the different organs. By contracting (vasocontraction) they increase their hydraulic resistance, thus diminishing the flow to the capillaries downstream. When they dilate (vasodilatation) more blood will flow to the capillaries. This way the blood distribution over the different organs is regulated. The bigger arteries, sometimes called muscle arteries, can contract in life-threatening situations, for example after loss of limb due to a car accident. By contracting they prevent blood loss and increase the chance of survival.

Exchange vessels   The exchange vessels are the capillaries and the arteries and venules close to the capillaries. Their vessel wall is very thin, consisting only of one layer of endothelial cells. There are a lot of capillaries, in such a way that only few cells have a distance of more than $10 \mu m$ to a capillary [6]. The thin wall and

the small distance to the cells allow e.g. oxygen exchange through diffusion. The fact that, due to the elevated total cross sectional area (Tab. 1.1), the blood flow velocity decreases, aids to an efficient exchange process of for example CO_2 and O_2.

Capacitance vessels   The venules and veins have a rather large diameter, compared to their arterial counterpart. This allows blood to flow through the veins very easily, only a pressure difference of about $10 - 15mmHg$ is sufficient to let blood flow from the venules to the venae cavae. Due to this high diameter about 2/3 of the total blood volume is situated in the veins and venules, thus acting as a reservoir for blood. The reservoir is variable, as many veins can contract in times of stress, hence forcing more blood to the heart and arterial system.

3   Cardiovascular interaction

In the previous sections the anatomy and physiology of the heart and the vessels were highlighted. The interaction between the heart and the vessels will be the subject of this section. It's this interaction that defines the heart's working regime. By explaining a number of parameters such as cardiac output and stroke work this interaction will be highlighted.

3.1   Cardiac output and stroke volume

The cardiac output (CO), the blood volume per minute that is ejected into the aorta, is one of the key parameters when cardiovascular function is evaluated. It is the product of the heart rate (HR), the number of beats per minute, and the stroke volume (SV), the volume ejected by the ventricle in one beat. SV is influenced by the energy with which the myocytes contract and by the arterial pressure against which needs to be ejected. These important factors will be discussed in this section.

   The contractile energy of the myocytes is determined by the stretch of the myocytes at the end of ventricular filling, also called the *preload*. This principle is called *Starling's law of the heart* and is a consequence of the laminated actin-myosin structure. Parker et al. [9] showed that for in situ human hearts the stroke volume index (stroke volume per unit body surface area) is strongly correlated with left ventricular end-diastolic pressure ($LVEDP$) up to $10mmHg$. For $LVEDP$ above $10mmHg$ a plateau is reached. The preload is also influenced by other parameters, such as the strength of atrial contraction or the flow resistance of the mitral valve. Evidently the nervous system also influences the contractility (inotropism) of the cardiac muscle cells.

For constant left ventricular end-diastolic volume ($LVEDV$), the stroke volume will decrease with increasing *afterload*. Afterload is the tension that the left ventricular wall needs to generate during systole to open the aortic valve and to start the ejection phase. Afterload is mainly determined by mean arterial pressure. Indeed, when the arterial pressure increases, the ventricular pressure at which the aortic valve opens will increase. For this reason, more energy will be needed for the isovolumic contraction so that less is left for the ejection of the blood. This arterial pressure is influenced by the total peripheral resistance, which can be changed by vasoconstriction or vasodilatation.

3.2   The pressure-volume loop
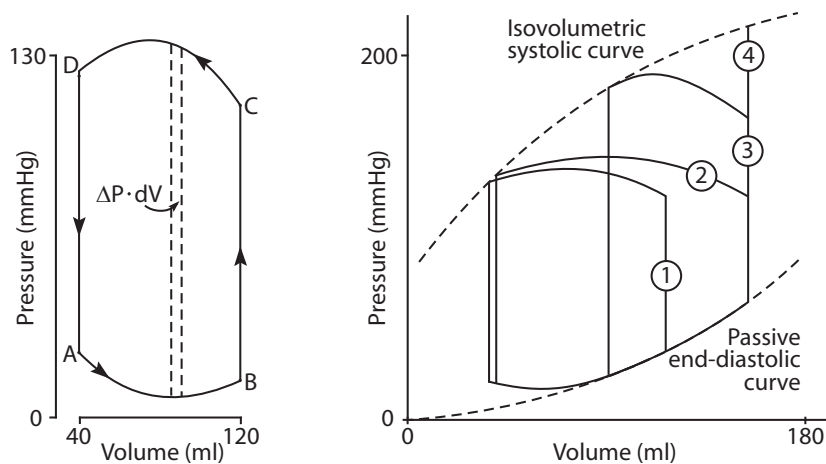
Figure 1.6: Left panel : Simplified left ventricular pressure-volume relation during the cardiac cycle; AB : filling phase; BC : isovolumic contraction phase; CD : ejection phase; DA : isovolumic relaxation phase. Right panel : Factors influencing the pressure-volume cycle. Loop 1 : control state; Loop 2 : increasing end-diastolic volume with steady arterial pressure; Loop 3 : starting from loop 2, increasing arterial pressure with steady end-diastolic volume; Loop 4 : purely isovolumic contraction. Adapted from [6].

The stroke volume and cardiac output are important parameters when it comes to evaluating cardiac function. However, beside the volume that is pumped into the aorta, it is essential that the pressure at which this pumping is done is not too elevated. A pressure-volume graph, as shown in Fig. 1.6, combines pressure information with volumetric information. When plotting the ventricular pressure as a function of the ventricular volume at every instant during the cardiac cycle

one obtains a closed loop, the pressure-volume loop. The four phases from Fig. 1.4 can be recognized here as well, as indicated on the figure.

The pressure-volume loop is bound in the down-right corner by the passive end-diastolic curve of the fully relaxed ventricle. The upper-left corner of the curve is bound by the end-systolic pressure-volume curve. This curve gives the pressure that would be reached in a fully isovolumic contraction from a certain end-diastolic volume (curve 4, Fig. 1.6, left panel).

The right panel of Fig. 1.6 shows how changes in preload and afterload affect the pressure-volume curve. When starting at the given PV-loop 1, one can increase the preload, which will increase the contractile force of the ventricle. If the afterload does not change, curve 2 is followed, with an increased stroke volume and a virtually unchanged pressure. If the induced rise in afterload is not prevented, the aortic valve will open at much higher pressure and curve 3 is followed. In this case the ventricular pressure rises and the stroke volume is reduced.

3.3 Stroke work

The pressure-volume loop is also interesting when one tries to quantify the energy that is used during one cardiac cycle. A part of this energy goes into heat and the other part goes into mechanical work. The mechanical work performed during one heart beat is called stroke work (SW). It is quantified as the pressure gain ΔP needed for the induced volume change ΔV. However in a cardiac cycle the pressure differences vary with time, meaning an integration is needed. Thus, the stroke work, the mechanical work performed by the heart in one heart beat, is the total area within the pressure-volume loop.
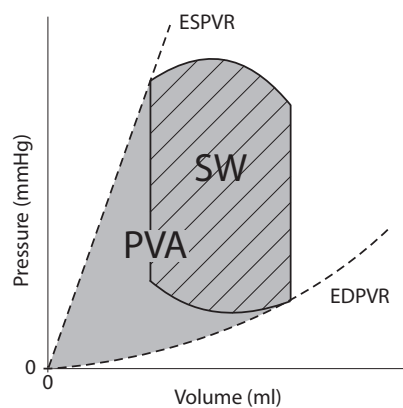
Figure 1.7: The pressure-volume loop with indication of the pressure-volume area (PVA) in gray. $EDPVR$: end-diastolic pressure volume relationship; $ESPVR$: end-systolic pressure-volume relationship.

Stroke work is the useful amount of work, but as stated earlier some of the energy is lost for example in order to overcome the viscoelastic properties of the myocardium itself. Denslow [10] showed that the pressure-volume area (PVA), the area between the end-systolic pressure-volume curve, the end-diastolic pressure-volume curve and the systolic segment of the pressure-volume loop, is correlated to the oxygen consumption of the myocytes. The PVA is also indicated on in Fig. 1.7 as the gray area. As such PVA is a measure of the total energy required by the myocytes and the difference in area between PVA and SW can be seen as the amount of energy that is lost due to the viscoelasticity of a cell. Hence one can define stroke efficiency as SW/PVA.

When looking again at the three cases in the right panel of Fig. 1.6, one can see that curve 2 will result in an increase in SW, and the efficiency SW/PVA will increase with respect to curve 1. Curve 3, however, results in an increase in SW, a decrease in SV and a very strong increase in PVA, overall a less efficient situation. These concepts will prove very useful in chapter 7.

4   Pathologies

In the previous sections the healthy cardiovascular system was described. However a lot can go wrong with this finely tuned system. In this section a small selection of pathologies relevant for the next chapters will be described.

4.1   Vascular pathologies

4.1.1   Atherosclerosis and stenosis

Atherosclerosis is an inflammatory vascular pathology where the immunity system interacts with metabolic factors and induces vessel wall damage. Central in atherogenesis, the development of atherosclerosis, stands the development of an atheromatous plaque, a fatty fibrotic sedimentation potentially with calcified parts, found between the tunica intima and media. It's mainly since the work done by Ross [11] that atherosclerosis is no longer seen as a simple accumulation of cholesterol but as a complex inflammatory process.

The molecular mechanism leading to atherosclerosis is not yet fully understood. However, it is known that the endothelial layer, through cytokines, plays a central role in each phase of the atherogenesis [12]. The development of a plaque starts with a dysfunction of the endothelial wall [7]. More exactly the permeability of the endothelial layer for active proteins, such as low density lipoprotein (LDL), changes. LDL is useful, it is the transport medium of cholesterol and necessary for the metabolism of the muscle cells in the tunica media. However this increase in permeability of LDL causes an accumulation of LDL between the tunica intima and media.

Things start to go wrong when part of this LDL oxidizes. The presence of oxidized LDL is directly correlated with the presence of plaques [13]. The oxidation of LDL also triggers the release of phospholipids, which further activates the endothelial cells. In a complex process (details can be found in the paper of Tedgui and Mallat [14]) macrophages migrate through the endothelial layer to the tunica media. The presence of the macrophages starts a cascade process resulting in migration of smooth muscle cells and development of a fibrotic collagen cap around the plaque. In a next stage the blood coagulation is activated. The vessel wall tries to compensate for the presence of a plaque by vascular remodeling. Initially the exterior of the vessel grows, without narrowing of the lumen. However, in an advanced stage a considerable reduction of the lumen is seen. Such a narrowing of the lumen is called a stenosis [15].

Atherosclerosis is one of the main causes of death in the western world. Indeed, a considerable narrowing of the lumen of a stenosed vessel may induce oxygen shortage in all downstream organs and tissues, especially in the heart or the brain. An other serious situations occurs when a part of the plaque breaks loose and blocks a downstream vessel, called an embolism. In a cerebral artery this can lead to a stroke, in a coronary artery this can lead to a heart attack. But even without local obstruction of an artery atherosclerosis causes problems. As atherosclerosis results in much stiffer vessels it will require an extra effort from the heart to eject blood in the cardiovascular system.

Risk factors of atherosclerosis include smoking, high blood pressure and diabetes [16]. These are risk factors that affect the health of the entire vascular tree. As atherosclerosis results in much stiffer vessels, the compliance of a vessel, the inverse of the elastance, will decrease. This will induce an increase in pulse wave velocity, the velocity at which an increase or decrease in pressure or flow velocity propagates along a vessel. The pulse wave velocity in the aorta for example can be a marker for the overall vascular health. Wave propagation and pulse wave velocity in the aorta will be discussed in chapter 4.

Stenoses can be treated with bypass surgery, angioplasty or stent placement. With bypass surgery the flow through the narrowed vessel is given a new pathway through a relocated vein of the patient which is placed around the stenosed area of the artery. In case of a coronary stenosed artery however this procedure requires a sternotomy, which is a very heavy procedure for the patient. The chances of renarrowing are limited, but 2.4% of the patients die during the procedure [17].

Angioplasty is a much less invasive technique where a balloon is inserted with a catheter through the femoral artery. The balloon is positioned in the narrowed vessel and is inflated, pushing the plaque together and expanding the vessel radially. Due to the limited invasive nature the patient recovers faster compared to bypass surgery. However two mechanisms limit the advantage of angioplasty over bypass surgery. On the short term recoil from the vessel is seen as soon as the bal-

loon is removed due to the energy released by the elastic fibers in the vessel wall after balloon deflation. On long term restenosis of the vessel wall is responsible for renarrowing of the lumen. Studies showed that about 30% of the patients show renarrowing of the vessel wall 12 months after intervention [18].

From the mid-nineties stents were added to the angioplasty procedure in order to limit the renarrowing. Stents are tube-like supporting prostheses which stay in the narrowed vessel after the catheter is removed to push the vessel open. This way recoil of the vessel wall is prevented. However, much as is seen in angioplasty, restenosis is also seen after stent placement. Studies as BenestentI an BenestentII in the Benelux [18, 19] and the STRESS-trial in the USA [20] compared the effect of stenting and angioplasty. These studies showed that the vessel wall reaction on stenting is much stronger, however, due to the initial gain in lumen increase after stent placement the overall renarrowing is higher after angioplasty intervention.

4.1.2 Aneurysms

An aneurysm is a local bulging from the vessel wall, as shown in Fig. 1.8, which mainly develops at a weak spot in the vessel wall. One can catalog aneurysms by their shape, saccular (Fig. 1.8, left panel) and fusiform (Fig. 1.8, right panel) aneurysms, and by their location. Most aneurysms are located in the cerebral vessels, called cerebral aneurysms, or in the abdominal aorta, called abdominal aorta aneurisms (AAA), which will be studied in chapter 5. The main cause of aneurysms is atherosclerosis, but aneurysms can also develop due to infections or after a car-crash trauma. Patients with a congenital weakness of the vessel wall also show higher risk to develop aneurysms.

Figure 1.8: Left panel : saccular aneurysm. Right panel : fusiform aneurysm.

Aneurysms are often accidentally discovered during an MRI- or CT-scan for example, as the patient is symptom free until the aneurysm puts too much pressure on the surrounding organs or until the aneurysm ruptures at which point a life threatening internal bleeding starts. The aneurysm is most commonly filled with intraluminal thrombus (ILT). This adds to the risk as pieces can break loose from the thrombus and be transported with the blood to clot smaller arteries. In a worst case scenario this can lead to a heart attack or a stroke.

The parameter which predicts rupture risk is the peak stress in the vessel wall;

if the wall stress exceeds the yield stress the aneurysm will break. However this parameter is not measurable in vivo, hence other criteria are used. If the aneurysm has a diameter higher than $5.5cm$ or if the aneurysm grows faster than $1cm$ in diameter a year, an intervention is considered. In chapter 5 the influence of a thrombus on the peak wall stresses in the aneurysmal wall will be studied in order to gain insight in the actual risk criteria of aneurysms.

Aneurysms can be treated by an endovascular intervention ($EVAR$) or using open surgery. In open repair surgery the weakened part of the aorta containing the aneurysm is replaced by a graft. As the intervention requires opening of the abdomen, it increases the risk of complication. Bonneux et al. [21] mention a morbidity of 7%. As the patient loses a lot of blood during the intervention a long hospitalization is required.

An endovascular intervention does not require surgical abdominal access. In this procedure a graft-covered stent is inserted, similar to the procedure described in the previous section. The graft around the stent prevents blood flow in the aneurysmal sac, so the blood in the aneurysmal sac clots and the rupture risk is diminished. The main advantages of this technique are the minimal invasive nature and the low morbidity during the intervention. However, some problems occur when the stent-graft starts migrating or when the stent does not stop the inflow of blood into the aneurysmal sac completely.

4.2 Congestive heart failure

Congestive heart failure (CHF) is a general term to group the pathologies that result in the incapability of the heart to generate a sufficient cardiac output to match the metabolic needs of the body, or that the heart only succeeds in generating a sufficient cardiac output under high filling pressures. As explained in section 3 cardiac output is influenced by many parameters, such as heart rate, afterload, preload and inotropy, so the inability of generating a sufficiently elevated cardiac output can have many causes. Stenosis of the coronary arteries, valve deficiency, arrhythmias or high blood pressure will, amongst others, reduce the efficiency of the heart.

One specific case of heart failure is caused by narrowing (stenosis) or obstruction of a coronary artery, limiting or stopping the blood supply to the myocytes downstream the constriction. As the affected myocytes will receive insufficient oxygen and nutrients, their function will be jeopardized. It is clear that the restoration of blood flow to the ischemic tissue is mandatory. However, the situation is not that simple as reperfusion is shown to induce further worsening of the situation. This specific kind of congestive heart failure will be discussed in chapter 7.

Cardiologists often make a distinction between systolic and diastolic heart fail-
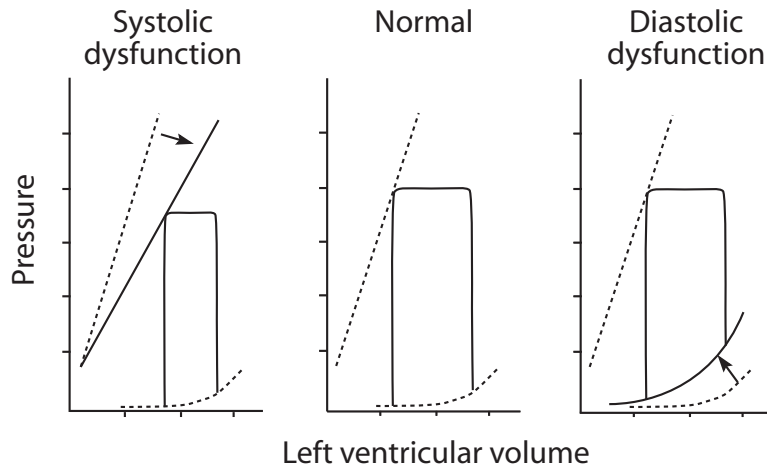
Figure 1.9: Pressure-volume loops with systolic (left) and diastolic (right) heart failure, compared to the healthy situation (middle). Adapted from [22].

ure. Systolic heart failure shows a reduced stroke volume due to a limited cardiac contraction, shown in the left panel of Fig. 1.9. The heart has difficulties to eject against the aortic pressure. Diastolic heart failure on the other hand is characterized by a decrease of ventricular compliance. The ventricle has difficulties to fill at low atrial pressure. Other ways to classify heart failure is by the limitations it causes in every day life of a patient. The New York Heart Association ($NYHA$) distinguishes four classes, from no limitations and symptom free in rest and exercise (class I) to severe limitations and symptoms, even at rest (class IV).

Congestive heart failure is a widespread condition in the western world. Population studies in the US indicated that the prevalence of heart failure is 3-20 cases per 1000 people [23], increasing to 100 cases per 1000 people aged 65 years or older [24]. According to the European Society of Cardiology, 3 million people of the 1000 million people living in Europe may have heart failure, however, only a minority sees a cardiologist about it [25]. Not only is the prevalence very high, the 5-year mortality of heart failure, 75%, is worse than for most forms of cancer [26].

The high prevalence makes that about 2% of the health care budget in industrialised countries is accounted for by CHF [25]. Annual costs of CHF to health care resources increase with increasing $NYHA$-class. In Belgium, the annual cost of a class IV patient is about 25.000 euro [27]. The greatest burden of congestive heart failure however falls on the patients themselves, severly limiting their quality of life. Heart failure depresses the self-reported quality of life more than diabetes,

arthritis or chronic lung disease [28].

5   Aim of this research

When the blood flow is alternated in some way (prosthesis, stent, anastomosis,...) in order to treat a pathology, it is important that no large velocity flow disturbances are induced in the cardiovascular system [29]. Hence, it is important to study the flow field prior and post to surgical alternation in order to quantify the differences so that the surgical procedure or the prosthesis can be designed to cause minimal disturbances. Especially when a prosthesis is being designed, numerical computations offer the advantage that a design can be evaluated and improved before it is physically made. This highly accelerates the design process.

Computational models can also be coupled with patient-specific imaging and empirical data. In this setting numerical models have a predictive value, they can help the physician to decide which treatment is best [30]. For example, in case of an aneurysm, they can help to decide whether or not to perform surgery. These ideas are further developed later in this work.

Numerical models offer the benefit of being able to study the influence of each individual flow parameter separately. Moreover, good spatial and temporal resolution can be reached. Hence they can help to understand the physiology and pathology of the cardiovascular system. Using numerical flow simulations for example, wall shear stress can be quantified, which can help to understand endothelial mechanical response mechanisms and its role in atherosclerosis [31].

The application field of biomechanical numerical simulations will only increase [32]. However, it is crucial that when building the numerical model, the reality is resembled as closely as possible. In vascular simulations the compliance of the wall is of great importance, so that a lot of research is going on on how to model the interaction between the blood and the vessel wall correctly. The aim of this research was to develop a multipurpose fluid-structure interaction code for vascular applications using the partitioned solver approach in order to use commercially available software packages: for the computational fluid dynamics problem Fluent software (ANSYS, Inc.) and for the computational solid mechanics Abaqus software (Simulia, Inc.).

Given this aim, the next chapter will first give a background on computational fluid dynamics and computational solid mechanics. The main approaches of fluid-structure interaction (FSI) problem solution will be highlighted as well. In chapter 3 the approach followed in the development of the FSI code during this research will be explained. The validation of the code's results is also given. In the next two chapters applications of the code are given. In chapter 4 the wave reflection pattern due to tapering of the aorta is studied, in chapter 5 the stress distributions in the aneurysmal wall are studied, where special attention is put into the

influence of the presence of an interluminal thrombus. Chapter 6 focuses on wave intensity analysis for cardiac applications, which is illustrated with results from an FSI-model of the left ventricle. It illustrates the strengths and pitfalls of this analyzing technique. In chapter 7 the limitations of pure mechanical models are highlighted with in situ measurements of ischaemia and reperfusion. Finally some conclusions will be drawn and possible future developments will be highlighted.

2

Modeling cardiovascular mechanics with computational methods

When studying fluid-structure interaction, it is vital to first have profound notions of fluid flow characteristics and continuum mechanics characteristics. The basics of modeling blood flow will be given in the first section of this chapter. The overview on continuum mechanics, both small and large deformation theory, will be elaborated in the second section. As the fluid-structure interaction (FSI) algorithm used in this work employs partitioned solvers, this chapter also treats the discretization procedures in computational fluid mechanics (CFD) (section 1.3) and in computational solid mechanics (CSM) (section 2.4). Finally, in the last section, an overview is given of FSI-approaches.

First however it is useful to highlight an important difference between CFD and CSM: the Lagrangian and the Eulerian way of describing motion. In an *Eulerian formulation*, shown in the upper panel of Fig. 2.1, the motion is described from a fixed observer's point of view. At each point in space the flow variables change with time and mass flows from cell to cell in the grid. This is the description used in pure CFD methods, where the fluid is described using a fixed numerical grid. The *Lagrangian formulation*, lower panel of Fig. 2.1, is the formulation used in CSM methods. The numerical grid is fixed to the material and the deformation of the material is described by the deformation of the grid in time.
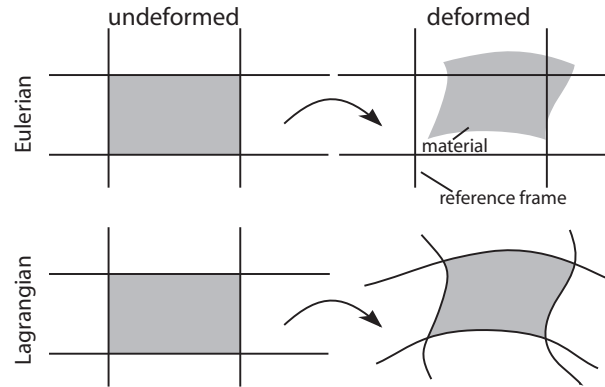
Figure 2.1: Upper panel illustrates the Eulerian way to look at motion and deformation, lower panel illustrates the Lagrangian approach.

1   Modeling blood flow

1.1   One-dimensional flow

Let us first consider a one-dimensional inviscid, incompressible flow in a straight, compliant tube, as shown in figure 2.2. Writing down the conservation laws in this idealized case will help to gain insight in the meaning of the different terms in the continuum equations in the next section. It will also lay some groundwork for equations that will be used in later chapters. Only the conservation of mass and momentum is studied, as the biomechanical processes are considered isothermal, a well accepted approximation.
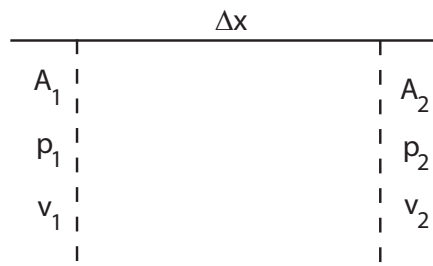
Figure 2.2: One-dimensional inviscid incompressible flow, characterized by pressure p and flow velocity v, in a segment of a straight, compliant tube, with length Δx and cross-section S.

Conservation of mass   Mass conservation in a flow means that in a fixed control volume the generated mass is zero. The total generated mass is the sum of the temporal change of mass stored in the control volume and the net mass leaving the control volume. Written down mathematically for the case given in Fig. 2.2 one obtains

$$\frac{\partial}{\partial t}(\rho A \Delta x) + \rho v_2 A_2 - \rho v_1 A_1 = 0 \tag{2.1}$$

or, as the fluid is incompressible and thus fluid density ρ is a constant

$$\frac{\partial A}{\partial t} + \frac{\partial v A}{\partial x} = 0 \tag{2.2}$$

$$\frac{\partial A}{\partial t} + A\frac{\partial v}{\partial x} + v\frac{\partial A}{\partial x} = 0 \tag{2.3}$$

Now consider the cross-section A a function of the pressure p alone, $A(p)$. Taking this relation into account the mass conservation equation can be rewritten

$$\frac{\partial p}{\partial t} + \frac{A}{\frac{dA}{dp}}\frac{\partial v}{\partial x} + v\frac{\partial p}{\partial x} = 0 \tag{2.4}$$

Conservation of momentum   In a similar way, one can establish the conservation of momentum in the tube as

$$\frac{\partial}{\partial t}(\rho A v \Delta x) + \rho v_2^2 A_2 - \rho v_1^2 A_1 = A_1 p_1 - A_2 p_2 + p(A_1 - A_2) \tag{2.5}$$

or

$$\frac{\partial A v}{\partial t} + \frac{\partial A v^2}{\partial x} = -\frac{A}{\rho}\frac{\partial p}{\partial x} \tag{2.6}$$

$$\frac{\partial v}{\partial t} + v\frac{\partial v}{\partial x} + \frac{1}{\rho}\frac{\partial p}{\partial x} = 0 \tag{2.7}$$

taking into account equation (2.3) and dividing by A.

Wave propagation   Both conservation equations are now written as combinations of derivatives of v and p with respect to t and x. In system notation these equations can be written as

$$\frac{\partial}{\partial t}\begin{bmatrix} p \\ v \end{bmatrix} + \begin{bmatrix} v & \frac{A}{\frac{dA}{dp}} \\ \frac{1}{\rho} & v \end{bmatrix}\frac{\partial}{\partial x}\begin{bmatrix} p \\ v \end{bmatrix} = 0 \tag{2.8}$$

The matrix has eigenvalues $v \pm c$ and eigenvectors $[\pm\rho c \quad 1]$ with c the wave speed.

$$c = \sqrt{\frac{A}{\rho}\frac{dp}{dA}} \qquad (2.9)$$

Eq. (2.9) is called the Bramwell-Hill equation. It is the more general form of the Moens-Korteweg equation to calculate the wave speed. The combination $dp + \rho cdv$ is transported invariantly with speed $v + c$ along characteristic C_+ and $dp - \rho cdv$ is transported with speed $v - c$ along characteristic C_-. Characteristics are curves in the p-v-plane along which the partial differential equations degenerate into ordinary differential equations in which form the equations can be solved. A more elaborate explanation can be found in Parker and Jones [33]. $dp + \rho cdv$ and $dp - \rho cdv$ are called Riemann invariants.

Physically this means that, considering a steady flow in a tube, a change in pressure $2dp$ in the middle of the tube will induce an according change in flow. A flow change $dv = dp/\rho c$ will propagate forward along half the pressure change dp with speed $v + c$ and a flow change $dv = -dp/\rho c$ will propagate backward accompanying dp with speed $v - c$ along the considered tube until equilibrium is reestablished. This is the basis of the wave intensity analysis as further elaborated in chapter 6.

1.2   Three-dimensional flow

1.2.1   The Navier-Stokes equations

Integral formulation   Let us now generalize the conservation laws for a three-dimensional, isothermic, incompressible, viscous flow. In integral formulation over a fixed volume, the Eulerian formulation, these conservation laws write

$$\rho \int_S \vec{v} \cdot \vec{n} dS = 0 \qquad (2.10)$$

$$\rho \frac{\partial}{\partial t} \int_V \vec{v} dV + \rho \int_S \vec{v}\vec{v} \cdot \vec{n} dS = \rho \int_V \vec{f} dV + \int_S \vec{t} dS \qquad (2.11)$$

These equations are the Navier-Stokes equations. $\vec{f}$ denotes the body force per unit mass working on the volume and $\vec{t}$ denotes the surface tension working on the surface of the considered volume. In a viscous fluid, the surface tension $\vec{t}$ is the sum of the pressure force $-p\vec{n}$ and a contribution of the shear stress tensor $\bar{\bar{\tau}}$ due to the viscosity of the fluid. When gravity or any other body force is not taken into account, one can write the equations as

$$\int_S \vec{v} \cdot \vec{n} dS = 0 \qquad (2.12)$$

$$\rho\frac{\partial}{\partial t}\int_V \vec{v}dV + \rho\int_S \vec{v}\vec{v}\cdot\vec{n}dS = -\int_S p\vec{n}dS + \int_S \bar{\bar{\tau}}\cdot\vec{n}dS \qquad (2.13)$$

Differential formulation As an alternative for the integral formulation of the Navier-Stokes equations one can also write the equations down in differential form. Indeed, applying the divergence theorem to Eq. (2.10)-(2.11), on obtains

$$\int_V \nabla\cdot(\vec{v})dV = 0 \qquad (2.14)$$

$$\rho\frac{\partial}{\partial t}\int_V \vec{v}dV + \rho\int_V \nabla\cdot(\vec{v}\vec{v})dV = -\int_V \nabla p dV + \int_V \nabla\cdot\bar{\bar{\tau}}dV \qquad (2.15)$$

Now, as these equations need to hold for any fixed control volume, the integrands need to be zero

$$\nabla\cdot(\vec{v}) = 0 \qquad (2.16)$$

$$\rho\frac{\partial\vec{v}}{\partial t} + \rho\nabla\cdot(\vec{v}\vec{v}) = -\nabla p + \nabla\cdot\bar{\bar{\tau}} \qquad (2.17)$$

The divergence of the dyad $\vec{v}\vec{v}$ can be further elaborated into $\vec{v}\cdot\nabla\vec{v} + (\nabla\cdot\vec{v})\vec{v}$, where the second term is zero due to the conservation of mass, thus yielding the Navier-Stokes equations in differential form for a laminar, incompressible, viscous flow in the absence of body forces

$$\nabla\cdot(\vec{v}) = 0 \qquad (2.18)$$

$$\rho\frac{\partial\vec{v}}{\partial t} + \rho\vec{v}\cdot\nabla\vec{v} = -\nabla p + \nabla\cdot\bar{\bar{\tau}} \qquad (2.19)$$

1.2.2 Kinematic decomposition of the flow field

The velocity gradient tensor $\nabla\vec{v}$ in Eq. (2.19) can be decomposed in two tensors. Tensor $\bar{\bar{R}}$ denotes the solid body rotation, while tensor $\bar{\bar{D}}$ denotes the deformation tensor. One can show that the rotation tensor holds the asymmetrical part of the velocity gradient tensor

$$\bar{\bar{R}} = \frac{1}{2}\left(\nabla\vec{v} - (\nabla\vec{v})^T\right) \qquad (2.20)$$

while the deformation tensor holds the symmetrical part

$$\bar{\bar{D}} = \frac{1}{2} \left(\nabla \vec{v} + (\nabla \vec{v})^T \right) \tag{2.21}$$

This deformation tensor can be further decomposed into tensor $\bar{\bar{\delta}}$ associated with volume change or dilatation

$$\bar{\bar{\delta}} = \frac{1}{3} \left(\nabla \cdot \vec{v} \bar{\bar{I}} \right) \tag{2.22}$$

and tensor $\bar{\bar{\gamma}}$, the strain rate tensor, associated with shape change

$$\bar{\bar{\gamma}} = \frac{1}{2} \left(\nabla \vec{v} + (\nabla \vec{v})^T \right) - \frac{1}{3} \left(\nabla \cdot \vec{v} \bar{\bar{I}} \right) \tag{2.23}$$

1.2.3   Blood viscosity

As already denoted in the previous paragraph, the tension forces on a surface with normal vector $\vec{n}$ in a viscous, laminar flow can be written as

$$\vec{t} = -p\vec{n} + \bar{\bar{\tau}} \cdot \vec{n} \tag{2.24}$$

Tensor $\bar{\bar{\tau}}$ is called the viscous or deviatoric stress tensor, which we postulate as a function of the velocity gradient tensor $\nabla \vec{v}$

$$\bar{\bar{\tau}} = 2\mu \bar{\bar{\gamma}} + \lambda \bar{\bar{\delta}} \tag{2.25}$$

where μ and λ are scalars. Eq. (2.25) is called Lamé's theorem. As already mentioned in the previous paragraph, $\bar{\bar{\delta}}$ is the dilatation tensor and $\bar{\bar{\gamma}}$ is the strain rate tensor. Now, as blood is modeled as an incompressible fluid, the continuity equation yields that the divergence of the velocity vector is zero everywhere in the fluid domain and from Eq. (2.22) that the dilatation tensor $\bar{\bar{\delta}}$ is zero.

$$\bar{\bar{\tau}} = 2\mu \bar{\bar{\gamma}} \tag{2.26}$$

With the expression for the strain rate tensor $\bar{\bar{\gamma}}$ from the previous paragraph, Eq. (2.24) yields

$$\vec{t}_{face} = -p\vec{n} + \mu \left(\nabla \vec{v} + (\nabla \vec{v})^T \right) \cdot \vec{n} \tag{2.27}$$

This equation will be used in the next chapter when the face force coupling between the fluid solver and the structural solver is discussed. Parameter μ is called the dynamic viscosity, which is constant for a Newtonian fluid.

1.2.4 Moving grid formulation

In the previous paragraph, the control volume was considered fixed in time. However, when using computational fluid dynamics for fluid-structure interaction, a moving mesh formulation is needed. So, the Navier-Stokes equations need to be written in a moving control volume formulation, which in case of an inviscid flow in the absence of external forces yields

$$\frac{\partial}{\partial t} \int_V \rho dV + \int_S \rho(\vec{v} - \vec{v}_b) \cdot \vec{n} dS = 0 \tag{2.28}$$

$$\frac{\partial}{\partial t} \int_V \rho\vec{v} dV + \int_S \rho\vec{v}(\vec{v} - \vec{v}_b) \cdot \vec{n} dS = -\int_S p\vec{n} dS \tag{2.29}$$

where $\vec{v}_b$ denotes the velocity of the boundary of the control volume, which can be arbitrarily chosen. When choosing $\vec{v}_b = 0$, the equations are the Eulerian equations for a fixed volume. However with choice $\vec{v}_b = \vec{v}$, the control volume follows the flow and the equations yield the Lagrangian formulation. Therefore this formulation is called the arbitrary Lagrangian-Eulerian formulation.

1.3 Computational fluid mechanics

1.3.1 Solving partial differential equations

The Navier-Stokes equations form a set of coupled non-linear partial differential equations (PDE). Solving the equations analytically is not possible in most cases. Therefore other techniques, numerical techniques, are needed in order to find the solution. The differential equations are discretized into a set of algebraic equations and these algebraic equations are solved with a computer so that an approximation of the solution of the differential equations is obtained. For this, different approaches exist.

Finite Difference Method (FDM)   The finite difference method is the most simple method to solve a partial differential equation. Central idea is to approximate the differential operator based on the Taylor series of the one-dimensional flow velocity $v(x + \Delta x)$

$$v(x) = v(x - \Delta x) - \Delta x \left(\frac{dv}{dx}\right)_{v(x)} + O(\Delta x^2) \tag{2.30}$$

From Eq. (2.30) the differential dv/dx in $v(x)$ can be approximated by a difference of $v(x)$ or v_i and $v(x - \Delta x)$ or v_{i-1}.

The Navier-Stokes equations contain both derivatives with respect to time and space present, so both differentials need to be approximated. One can hereby make a distinction between explicit and implicit schemes. *Explicit schemes* use

the solution from the previous known time step n to approximate the differential with respect to space. For example, in case of the wave equation

$$\frac{\partial v}{\partial t} + c\frac{\partial v}{\partial x} = 0 \qquad (2.31)$$

an explicit discretization using Eq. (2.30) then states

$$\frac{v_i^{n+1} - v_i^n}{\Delta t} + c\frac{v_i^n - v_{i-1}^n}{\Delta x} = 0 \qquad (2.32)$$

where the superscript ^{n} refers to the time step and the subscript $_i$ refers to the position. *Implicit schemes* use the unknown solution at time step $n+1$ to approximate the spatial derivative.

$$\frac{v_i^{n+1} - v_i^n}{\Delta t} + c\frac{v_i^{n+1} - v_{i-1}^{n+1}}{\Delta x} = 0 \qquad (2.33)$$

The explicit scheme does not require matrix inversion, however one can show with a stability analysis that, in case of the wave equation, the stability is limited to a Courant-number smaller or equal to one. The Courant number is defined by

$$C = \frac{c\Delta t}{\Delta x} \qquad (2.34)$$

where Δt denotes the time step Δx is the spatial step and c denotes the wave speed. The implicit scheme requires matrix inversion, but is, in this case, always stable.

Finite Volume Method (FVM)   The finite volume method starts from the integral form of the conservation equations (2.12)-(2.13). The volume considered is divided into smaller volumes, 'cells', and the integral conservation equations are applied to each cell individually. Thus the mass and momentum are conserved over the cell. For example, take the mass conservation equation for incompressible flow, Eq. 2.12,

$$\int_S \vec{v} \cdot \vec{n} dS = 0 \qquad (2.35)$$

where $\vec{n}$ is the normal of the surface S of the control volume.

Consider a rectangular control volume in a two-dimensional flow calculation, as given in Fig 2.3, where the control volume is aligned with the coordinate axes. As the conservation of mass needs to hold for any volume in the flow, it also has to hold for the cell we consider. Integration over the cell yields

$$-u_1\Delta y - v_2\Delta x + u_3\Delta y + v_4\Delta x = 0 \qquad (2.36)$$
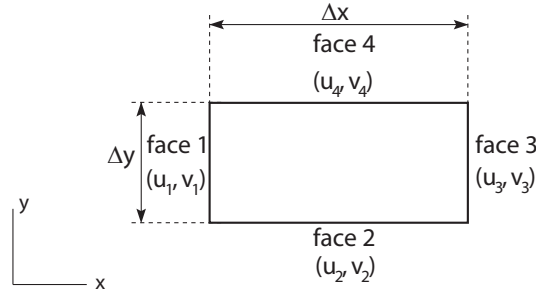
Figure 2.3: A rectangular cell in a two-dimensional flow.

Equation (2.36) states that no fluid will enter or leave the cell. It gives the discretized form of the conservation of mass equation for the cell. Similarly one can discretize the conservation of momentum equation. The finite volume method finds thus a pressure and flow field where the conservation laws are fulfilled for each cell. The values of the pressure p and flow velocity v are typically stored in the cell center. An interpolation scheme is needed to find the values at the interface between two adjacent cells from their cell center values. An example is given in the next paragraph.

Finite Element Method (FEM) The finite element method on the other hand uses shape functions to discretize an integral equation. The integral needs to be written in variational or weak formulation. More details will be given in the next section 2.

Note that the finite element method, as the finite volume method from the pervious paragraph, considers the spatial derivatives. They do not include temporal discretization, which is to be discretized using the finite difference method. A space-time formulation of the finite element method does exist, where the equations are discretized with one single finite element discretization method using space-time finite elements. However detailed description falls beyond the scope of this work, examples are found in [34] and [35].

Very often numerical continuum mechanics are referred to as finite element method (FEM). It is clear from this section that this name is not well-chosen. The name "finite element method" refers to the way the continuum equations are discretized, however it does not state which equations are discretized. Indeed, one could also discretize the Navier-Stokes equations using the finite element method. Therefore in this work numerical continuum mechanics are referred to as computational solid mechanics (CSM).

1.3.2   Fluent software as finite volume solver

Spatial discretization   Fluent (ANSYS, Inc.) uses the finite volume method to solve the Navier-Stokes equations where the discrete values are stored at the cell centers. As stated in the previous paragraph, the values at the faces between cells need to be interpolated. Fluent uses upwind schemes to do so, meaning that the value of a scalar ϕ at a face is retrieved from the cell that lies upstream to the considered face. One possibility is the second order upwind scheme, where the value at the face is calculated as

$$\phi_f = \phi_{cc} + (\nabla\phi)_{cc} \cdot \vec{r} \tag{2.37}$$

$\vec{r}$ denotes the displacement vector from the upstream cell center to the face center. ϕ_f denotes the value of the scalar at the considered face, ϕ_{cc} is the scalar stored in the upstream cell center, where also the gradient of the scalar, $(\nabla\phi)_{cc}$ is stored.

Temporal discretization   In Fluent a first and a second order accurate scheme is used to perform temporal discretization. However, when calculating with moving meshes, only the first order backward Euler scheme can be used. Consider an equation of a scalar ϕ

$$\frac{\partial\phi}{\partial t} = F(\phi) \tag{2.38}$$

where the function $F(\phi)$ incorporates the terms due to spatial discretization. The first order backward Euler scheme discretizes the temporal derivative of ϕ as

$$F(\phi^{n+1}) = \dot{\phi}^{n+1} = \frac{\phi^{n+1} - \phi^n}{\Delta t} \tag{2.39}$$

or

$$\phi^{n+1} = \phi^n + \Delta t \dot{\phi}^{n+1} \tag{2.40}$$

where $\dot{\phi}^{n+1}$ can be replaced by $F(\phi^{n+1})$. The superscript $n+1$ denotes the value at time step $n+1$, $\dot{\phi}$ is the first derivative with respect to time.
As the equation

$$\frac{\partial\phi}{\partial t} = F(\phi) \tag{2.41}$$

with $F(\phi)$ any given function of ϕ is discretized as

$$\frac{\phi^{n+1} - \phi^n}{\Delta t} = F(\phi^{n+1}) \tag{2.42}$$

the first order backward Euler temporal discretization scheme is implicit.

2   Modeling vessel wall deformation

Vessel wall behavior can be modeled with continuum mechanics. Continuum mechanics study the deformation and motion of solids induced by external loads, where the solid's motion is restricted due to imposed boundary conditions. A distinction is made between small deformation and large deformation theory. When the maximal strain is more elevated than 5% small deformation theory can no longer yield accurate results and a large deformation formulation is needed. Biological tissues normally undergo large deformation and displacement, however before getting to large deformation theory a notion of small deformation theory is essential.

This chapter starts with some deformation theory basics. The second part will treat small deformation theory. Fluid-structure interaction is taken into account, when the movement and/or deformation of the solid involved is too elevated, so in the third part large deformation theory is explained. Finally, in the fourth part of this section some basics of computational solid mechanics will be treated.

2.1   General concepts in continuum mechanics

2.1.1   Deformation gradient tensor

In general continuum mechanics a time dependent external force is studied, but in this section the case will be limited to a two-state quasi-static treatment. An initial state, referred to as reference state or undeformed state, is deformed into a second state, the deformed state, as shown in Fig. 2.4.
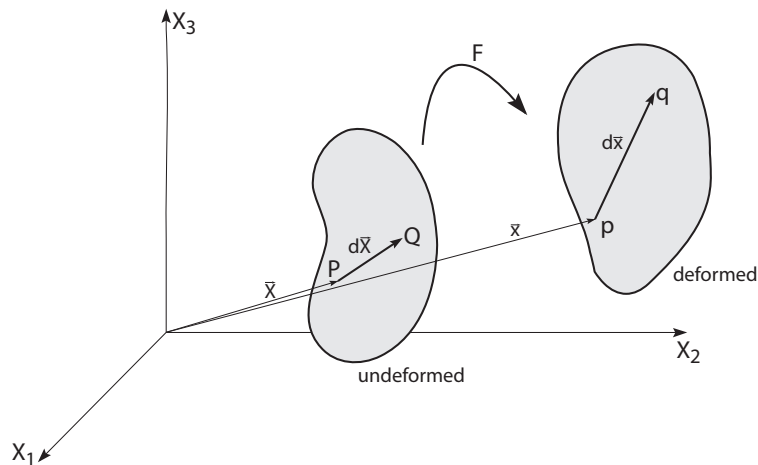
Figure 2.4: General motion of a deformable body.

When considering two states of the solid, the undeformed state and the deformed state, it is clear a relation F is needed between the two states. Consider a line segment $d\vec{X}$ in the undeformed state, consisting of the components (dX_1, dX_2, dX_3) in the rectangular coordinate system $\vec{X}_1, \vec{X}_2, \vec{X}_3$. Due to external loads this line segment will be transformed into a line segment $d\vec{x}$ with components (dx_1, dx_2, dx_3) in the same coordinate system.

The deformation gradient tensor $\bar{\bar{F}}$ describes this deformation from $d\vec{X}$ to $d\vec{x} = \bar{\bar{F}} d\vec{X}$ and is in $\vec{X}_1, \vec{X}_2, \vec{X}_3$ defined by

$$F_{ij} = \frac{\partial x_i}{\partial X_j} \tag{2.43}$$

Evidently, now we can also describe the deformation from the deformed state $d\vec{x}$ to the undeformed state $d\vec{X} = \bar{\bar{F}}^{-1} d\vec{x}$, as the transformation $\bar{\bar{F}}$ is a one on one mapping, so the inverse $\bar{\bar{F}}^{-1}$ exists.

When considering the deformed position $\vec{x}$ of point P as the sum of the undeformed position $\vec{X}$ and a displacement $\vec{u}$, the deformation gradient tensor can also be written as

$$F_{ij} = \frac{\partial X_i + u_i}{\partial X_j} = \frac{\partial X_i}{\partial X_j} + \frac{\partial u_i}{\partial X_j} = \delta_{ij} + \frac{\partial u_i}{\partial X_j} \tag{2.44}$$

with δ_{ij} Kronecker delta. In matrix representation Eq. (2.44) writes $\bar{\bar{F}} = \bar{\bar{I}} + \nabla \vec{u}$.

At this point also a rigid body motion will result in a non-unity deformation gradient tensor. Therefore it is useful to split the tensor in two parts, rigid body motion and stretch. The rigid body motion is described by an orthonormal rotation tensor $\bar{\bar{R}}$ and the stretch is described by a symmetric and positive definite stretch tensor $\bar{\bar{U}}$ in such a way that $\bar{\bar{F}} = \bar{\bar{R}} \bar{\bar{U}}$. Note that the stretch tensor $\bar{\bar{U}}$ contains the material strain information.

With the deformation gradient tensor we can now calculate the change in length of the line segment $d\vec{X}$. Indeed the squared length after deformation is given by

$$dl^2 = \vec{dx}^T \vec{dx} = (\bar{\bar{F}} d\vec{X})^T \bar{\bar{F}} d\vec{X} = d\vec{X}^T \bar{\bar{F}}^T \bar{\bar{F}} d\vec{X} = d\vec{X}^T \bar{\bar{C}} d\vec{X} \tag{2.45}$$

with the Cauchy-Green deformation tensor

$$\bar{\bar{C}} = \bar{\bar{F}}^T \bar{\bar{F}} \tag{2.46}$$

In the chosen coordinate system the Cauchy-Green deformation tensor $\bar{\bar{C}}$ gives the contribution of each component of the undeformed line segment to the squared length after deformation. Tensor $\bar{\bar{C}}$ can thus be written as a sole function of the stretch tensor $\bar{\bar{U}}$, as the rotation tensor is orthonormal. Indeed, $\bar{\bar{C}} = \bar{\bar{U}}^2$ taking the symmetry of $\bar{\bar{U}}$ into account.

Apart from the Cauchy-Green deformation tensor, one can also write down the Green-Lagrange strain tensor $\bar{\bar{E}}$ as

$$\bar{\bar{E}} = \frac{1}{2}(\bar{\bar{C}} - \bar{\bar{I}}) = \frac{1}{2}(\bar{\bar{F}}^T \bar{\bar{F}} - \bar{\bar{I}}) \tag{2.47}$$

Note that a pure rigid body deformation will result in a Green-Lagrange tensor equal to the zero tensor, where the Cauchy-Green tensor will be equal to the unity tensor.

When considering Eq. 2.44 the Green-Lagrange tensor can now be rewritten as a function of the displacement gradient $\nabla \vec{u}$

$$\bar{\bar{E}} = \frac{1}{2}((\bar{\bar{I}} + \nabla \vec{u})^T(\bar{\bar{I}} + \nabla \vec{u}) - \bar{\bar{I}}) = \frac{1}{2}(\nabla \vec{u} + \nabla \vec{u}^T + \nabla \vec{u}^T \nabla \vec{u}) \tag{2.48}$$

One can define three combinations I_1, I_2 and I_3 of components of $\bar{\bar{C}}$, which remain invariant under coordinate transformations[1]

$$I_1 \qquad = tr\bar{\bar{C}} \tag{2.49}$$

$$I_2 \quad = \frac{1}{2det\bar{\bar{C}}}\left[(tr\bar{\bar{C}})^2 - tr\bar{\bar{C}}^2\right] \tag{2.50}$$

$$I_3 \qquad = det\bar{\bar{C}} \tag{2.51}$$

where det denotes the determinant of the matrix and tr denotes the trace. Finally, consider a specific coordinate transformation from the given coordinate system to a coordinate system along the eigenvectors of $\bar{\bar{C}}$, as, since $\bar{\bar{C}}$ is symmetric, the eigenvectors are orthogonal. If λ_1^2, λ_2^2 and λ_3^2 are the eigenvalues of $\bar{\bar{C}}$, the equations 2.52 can be rewritten in functions of these eigenvalues

$$I_1 \quad = \lambda_1^2 + \lambda_2^2 + \lambda_3^2 \tag{2.52}$$

$$I_2 \quad = \frac{1}{\lambda_1^2} + \frac{1}{\lambda_2^2} + \frac{1}{\lambda_3^2} \tag{2.53}$$

$$I_3 \qquad = \lambda_1^2 \lambda_2^2 \lambda_3^2 \tag{2.54}$$

The eigenvectors of $\bar{\bar{C}}$ are called the principle axes of stretch and λ_1, λ_2 and λ_3 are the principal stretches. The root of the third invariant $\sqrt{I_3}$, the product of the stretches in the three principal directions, gives the relative volume change due to the transformation. Incompressible materials require thus an additional constraint $I_3 = 1$.

---

[1] In some books the second invariant is defined as $I_2 = 1/2[(tr\bar{\bar{C}})^2 - tr\bar{\bar{C}}^2]$. Of course any combination of the three invariants will remain invariant as well.

2.1.2   Governing equations

In the previous part the basics of kinematics were described. In order to be able to write down Newton's laws for the solid volume under deformation some additional definitions are necessary. In the first paragraph different possible stress definitions will be given. While in the second paragraph the conservation laws will be derived.

Stress tensors

In its most basic form, stress is a force acting on a small plane surface. If the force acts perpendicular to the plane it causes normal stress, if the force acts tangentially to the plane it causes a shear stress. However one can write down the stress with the force vector from the deformed or undeformed configuration. The same goes for the area of the small plane surface, which can be the deformed area or the undeformed area. Combining the choices, three possible useful stress tensors arise.

The Cauchy stress tensor σ_{ij} denotes the force measured per unit deformed area acting on a surface in the deformed configuration. Index i gives the direction of the normal to the surface, index j gives the component of the direction of the force. As will be clear in the next paragraph this stress tensor is used in small deformation continuum mechanics.

The first Piola-Kirchoff stress tensor s_{ij} gives the force measured per unit deformed area but acting on a surface in the undeformed configuration. This approach is often used in experiments, where the force is measured during deformation, but the surface is measured in the undeformed configuration.

The second Piola-Kirchoff stress tensor T_{ij} gives the force measured per unit undeformed area acting on a surface in the undeformed configuration. This stress tensor is used in large deformation theory.

The link between the force per undeformed area $\vec{p}$ and the force per deformed area $\vec{P}$ is prescribed by the deformation gradient tensor, $\vec{P} = \bar{\bar{F}}^{-1}\vec{p}$. At this point the relations between the different stress tensors can be written down.

$$\bar{\bar{s}} = J\bar{\bar{F}}^{-1}\bar{\bar{\sigma}} \qquad \bar{\bar{s}} = \bar{\bar{T}}\bar{\bar{F}}^{T} \tag{2.55}$$

$$\bar{\bar{T}} = \bar{\bar{s}}(\bar{\bar{F}}^{T})^{-1} \qquad \bar{\bar{\sigma}} = \frac{1}{J}\bar{\bar{F}}\bar{\bar{s}} \tag{2.56}$$

$$\bar{\bar{T}} = J\bar{\bar{F}}^{-1}\bar{\bar{\sigma}}(\bar{\bar{F}}^{T})^{-1} \quad \bar{\bar{\sigma}} = \frac{1}{J}\bar{\bar{F}}\bar{\bar{T}}\bar{\bar{F}}^{T} \tag{2.57}$$

J denotes the Jacobian of transformation $\bar{\bar{F}}$ from undeformed to deformed status, $J = det\bar{\bar{F}} = \sqrt{I_3}$.

Conservation Laws

The conservation of mass When considering a volume V with density ρ_o in the undeformed state which is deformed to a volume v with density ρ, conservation of material is needed :

$$\int_V \rho_o dV = \int_v \rho dv = \int_V \rho J dV \qquad (2.58)$$

with J again the Jacobian of the transformation represented by $\bar{\bar{F}}$. As the integral equation needs to hold for any arbitrary volume, the densities of the undeformed and deformed solid are related by

$$\rho_o = \rho J = \rho \sqrt{I_3} \qquad (2.59)$$

Evidently this relation is unaffected by any coordination transformation.

The conservation of linear momentum Consider the same volume v as before, with a surface s and consider the external forces working on the volume, surface force $\vec{t}$ per unit area and volume force $\vec{b}$ per unit mass. According to Newton's second law of motion, the total linear momentum is equal to the sum of the external forces working on the volume

$$\int_s \vec{t} ds + \int_v \rho \vec{f} dv = \frac{d}{dt} \int_v \rho \vec{v} dv \qquad (2.60)$$

with d/dt the material derivative[2] and $\vec{v}$ the velocity vector. As the Cauchy stress tensor relates the normal $\vec{n}$ of ds to $\vec{t}$ [36], one can write

$$\int_s \bar{\bar{\sigma}} \cdot \vec{n} ds + \int_v \rho \vec{f} dv = \frac{d}{dt} \int_v \rho \vec{v} dv \qquad (2.61)$$

By applying the divergence theorem

$$\int_v \nabla \cdot \bar{\bar{\sigma}} dv + \int_v \rho \vec{f} dv = \int_v \frac{d}{dt}(\rho \vec{v}) dv \qquad (2.62)$$

one can rearrange the integrands into one integral

$$\int_v \left(\nabla \cdot \bar{\bar{\sigma}} + \rho \vec{f} - \frac{d}{dt}(\rho \vec{v}) \right) dv = 0 \qquad (2.63)$$

which has to hold for any arbitrary chosen volume v. This can only be fulfilled if

$$\nabla \cdot \bar{\bar{\sigma}} + \rho \vec{f} - \frac{d}{dt}(\rho \vec{v}) = 0 \qquad (2.64)$$

Note that in case of static equilibrium and in the absence of external forces the conservation of momentum reduces to $\nabla \cdot \bar{\bar{\sigma}} = 0$.

---

[2]The material derivative or convective derivative is a derivative taken with respect to a coordinate system moving with velocity $\vec{u}$. The material derivative of a scalar ϕ writes $d\phi/dt = \partial\phi/\partial t + (\vec{u} \cdot \nabla)\phi$.

The conservation of angular momentum The description of the conservation of angular momentum goes beyond the scope of this work. From this conservation law, one can derive that the Cauchy stress tensor and thus the second Piola-Kirchoff stress tensor needs to be symmetrical. This limits the number of independent stress components to six : three normal components and three shear components.

2.1.3 Constitutive equations

Now that we wrote down the conservation laws and the relation between the deformed and the undeformed state, some attention needs to go to the constitutive equations, experimental equations that describe the reaction of a specific material to mechanical load[3]. Constitutive equations are established experimentally, so it is clear that for a specific load case constitutive equations need to be used which were obtained by experiments which result in a similar load cases. Finite element modeling of shear behavior of a rubber block with a material model obtained from an uniaxial tensile test only will yield inaccurate results.

A second requirement is that the constitutive equations need to be independent from the chosen coordinate system. Thirdly, any rigid body motion should not have an influence on the constitutive equations. This is fulfilled when taking a *strain energy function* (SEF) W, a scalar function giving the work per unit volume done by the stresses to get from the undeformed position to the current position. This strain energy function W is a function of the components of the strain tensors, either $\bar{\bar{C}}$ or $\bar{\bar{E}}$. One can show that for example the components of the 2nd Piola-Kirchoff stress tensor T_{ij} can be given as

$$T_{ij} = \frac{1}{2} \left(\frac{\partial W}{\partial E_{ij}} + \frac{\partial W}{\partial E_{ji}} \right) \tag{2.65}$$

where W is written as function of the Green-Lagrange strain components E_{ij}.

If the material is isotropic, it does not have any preferred direction and thus the strain energy function W, function of $\bar{\bar{C}}$, needs to be a function with rotational symmetry around all directions and reflectional symmetry around any plane. This can only be fulfilled if the strain energy function is a function of the invariants I_1, I_2 and I_3. This function can be polynomial, but that is not a requirement, it needs to have a form that matches the experimental observations. The major weakness here however is that the parameters of a strain energy function do not have a physical meaning.

---

[3]Other loads such as electromagnetic loads or thermal loads are possible too, however in the scope of this work the description of constitutive equations will be limited to responses to mechanical loads.

2.2 Small deformations

2.2.1 Linear versus nonlinear continuum mechanics

Two types of nonlinearity can be distinguished when dealing with continuum mechanics, material and geometrical nonlinearity. *Material nonlinearity* occurs when the constitutive relation is nonlinear, for example when using a hyperelastic material. *Geometric nonlinearity* occurs when the changes in geometry, which can be big or small, have a substantial influence on the load deformation behavior. These two types of nonlinear effects result in three classes of analysis, depending on which nonlinearity is taken into account.

Fully linear analysis When only small displacements and deformations occur and the constitutive relation is linear, the analysis can be both geometrically and materially linear. In this case the governing equations are given as functions of the Cauchy stress $\bar{\bar{\sigma}}$ and the linearized Green-Lagrange strain $\bar{\bar{\epsilon}}$.

Materially nonlinear analysis When the same problem is studied as in the previous analysis, but the material behavior is nonlinear, a different formulation will be needed. The governing equations will still be written as functions of the Cauchy stress $\bar{\bar{\sigma}}$ and linearized Green-Lagrange strain $\bar{\bar{\epsilon}}$, but an iterative scheme will be needed to obtain the solution.

Geometrically nonlinear analysis with or without material non-linearity Contact problems, for example, are typically geometrically non-linear problems. Also, when the maximal strain exceeds the 5%-limit, a geometrically non-linear formulation is needed, in most cases also requiring a non-linear material model. The governing equations are no longer written as function of Cauchy stress and linearized Green-Lagrange strains, but as function of the second Piola-Kirchoff stress $\bar{\bar{T}}$ and the non-linearized Green-Lagrange strain $\bar{\bar{E}}$. This large deformation approach will be discussed in section 2.3, it is the most common situation for biological tissue mechanics.

2.2.2 Geometrically linear equations

Consider a general structural problem of reference volume V, as shown in Fig. 2.5, subjected to loads and boundary conditions. Let us now put all the information from the previous parts together, starting with the conservation of linear momentum Eq. (2.64)

$$\nabla \cdot \bar{\bar{\sigma}} + \rho \vec{f} = \rho \ddot{\vec{u}} \qquad (2.66)$$

where $\bar{\bar{\sigma}}$ denotes the Cauchy stress tensor, ρ denotes the density of the geometry, $\vec{f}$ denotes the external body forces per unit mass and $\ddot{\vec{u}}$ denotes the second derivative of the displacement vector $\vec{u}$ with respect to time. From the conservation of
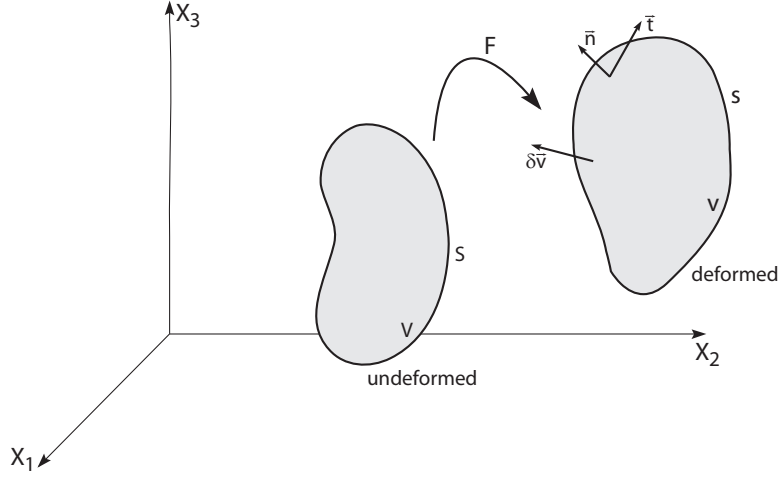
Figure 2.5: General motion of a deformable body.

angular momentum, we know that only six components of the stress tensor are independent.

When the displacements are small, the linearized Green-Lagrange strain $\bar{\bar{\epsilon}}$ as function of the displacements $\vec{u}$ (Eq. (2.48)) can be written as

$$\bar{\bar{\epsilon}} = \frac{1}{2} \left[\nabla \vec{u} + (\nabla \vec{u})^T \right] \tag{2.67}$$

At this point the problem has nine unknown quantities: the six independent stress quantities and the three displacement components in each point P. The conservation of momentum only results in three scalar equations, therefore an independent set of six more scalar equations are needed, the constitutive equations. The constitutive equations give the relation between the stress tensor components and the strain components. For a linear material, this constitutive law is given in eq. 2.68.

$$\bar{\bar{\sigma}} = \lambda (tr\bar{\bar{\epsilon}})\bar{\bar{I}} + 2\mu\bar{\bar{\epsilon}} \tag{2.68}$$

Where λ and μ are the Lamé coefficients, which, for compressible materials, can be written as a function of the more common Young's modulus and Poisson coefficient.

$$\lambda = -\frac{\nu E}{(1+\nu)(2\nu-1)} \tag{2.69}$$

$$\mu = \frac{E}{2(1+\nu)} \tag{2.70}$$

The equations (2.66)-(2.68) define the unsteady continuum mechanics problem, together with the initial conditions

$$\vec{u}(x, t = 0) = \vec{u}_0(x) \tag{2.71}$$

$$\dot{\vec{u}}(x, t = 0) = \dot{\vec{u}}_0(x) \tag{2.72}$$

and the boundary conditions. Boundary conditions can be Dirichlet conditions as in Eq. (2.73), also called essential conditions, or Neumann conditions as in Eq. (2.74), also called natural conditions.

$$\vec{u}(x, t) = \vec{u}(x, t)_{BC} \tag{2.73}$$

$$\vec{t}(x, t) = \bar{\bar{\sigma}}(x, t) \cdot \vec{n} = \vec{t}(x, t)_{BC} \tag{2.74}$$

2.2.3 Principle of virtual work

Let us now consider an equilibrium situation, so that the acceleration term is absent in the conservation equation of linear momentum

$$\nabla \cdot \bar{\bar{\sigma}} + \rho \vec{f} = 0 \tag{2.75}$$

During an iterative process, where equilibrium is not reached yet, one can use this equation to quantify a residual $\vec{r}$, the residual force per unit volume, as

$$\vec{r} = \nabla \cdot \bar{\bar{\sigma}} + \rho \vec{f} \tag{2.76}$$

In finite element calculations the conservation equation is solved in a weak form through a virtual work equation. Let us consider an arbitrary virtual velocity $\delta \vec{v}$. Now the out-of-balance residual force $\vec{r}$ performs virtual work δw per unit volume and time

$$\delta w = \vec{r} \delta \vec{v} \tag{2.77}$$

which needs to be zero as an equilibrium requirement. Equation (2.77) is completely equivalent with the equilibrium requirement $\vec{r} = 0$, as $\delta \vec{v}$ is arbitrarily chosen[4]. Integrating the virtual work over the considered volume, one gets a weak representation of the equilibrium equation

$$\delta W = \int_v (\nabla \cdot \bar{\bar{\sigma}}) \cdot (\delta \vec{v}) dv + \int_v \rho \vec{f} \cdot \delta \vec{v} dv = 0 \tag{2.78}$$

---

[4]For example one can chose $\delta \vec{v}$ equal to $[100]^T$, $[010]^T$ and $[001]^T$.

Or, as $\nabla \cdot (\bar{\bar{\sigma}} \delta \vec{v}) = (\nabla \cdot \bar{\bar{\sigma}}) \cdot (\delta \vec{v}) + \bar{\bar{\sigma}} : \nabla \delta \vec{v}$,[5] the equation can be rewritten, taking the Gauss theorem into account

$$\int_s (\vec{n} \cdot \bar{\bar{\sigma}}) \cdot \delta \vec{v} ds - \int_v \bar{\bar{\sigma}} : \nabla \delta \vec{v} dv + \int_v \rho \vec{f} \cdot \delta \vec{v} dv = 0 \qquad (2.79)$$

As previously stated the surface force vector $\vec{t}$ equals $\vec{n} \cdot \bar{\bar{\sigma}}$ on the surface s of the volume.

$$\int_s \vec{t} \cdot \delta \vec{v} ds - \int_v \bar{\bar{\sigma}} : \nabla \delta \vec{v} dv + \int_v \rho \vec{f} \cdot \delta \vec{v} dv = 0 \qquad (2.80)$$

Now the virtual velocity $\delta \vec{v}$ can be written as a derivative $\delta \dot{\vec{u}}$ of the virtual displacement $\delta \vec{u}$. Finally, as $\bar{\bar{\sigma}}$ is a symmetric vector, only the symmetric part of $\nabla \delta \dot{\vec{u}}$ will contribute to the double product. The symmetric part $1/2(\nabla \delta \dot{\vec{u}} + (\nabla \delta \dot{\vec{u}})^T)$ is the time derivative of the linearized Green-Lagrange strain $\dot{\bar{\bar{\epsilon}}}(\delta \vec{u})$ related with the virtual displacement $\delta \vec{u}$, or thus the virtual strain rate $\delta \dot{\bar{\bar{\epsilon}}}$. So the the scalar equation describing the equilibrium of a deforming body writes

$$\int_v \bar{\bar{\sigma}} : \delta \dot{\bar{\bar{\epsilon}}} dv = \int_s \vec{t} \cdot \delta \vec{v} ds + \int_v \rho \vec{f} \cdot \delta \vec{v} dv \qquad (2.81)$$

The terms are rearranged so that the rate of internal virtual work is isolated in the left hand side and the rate of external virtual work is grouped in the right hand side of the equation.

This scalar equation is the basis for finite element formulations. As no material model was used at this point, the weak virtual work equation is valid for fully linear and materially nonlinear cases, as long as the deformations are small. Note that, as the deformations are supposed small, the unknown volume and surface integration over deformed volume v and surface s can be replaced by an integration over the known undeformed volume V and surface S.

2.3   Large deformations

Equation (2.80) is still valid for large deformation. However, as the linearization of the Green-Lagrange strain tensor is no longer valid in the large deformation case, a different approach is needed.

Now, the gradient of the virtual velocity $\nabla \delta \vec{v}$ defines the virtual velocity gradient $\delta \bar{\bar{l}}$. Again, as $\bar{\bar{\sigma}}$ is a symmetric vector, only the symmetric part of $\delta \bar{\bar{l}}$ will contribute to the double product, hence the virtual velocity gradient $\delta \bar{\bar{l}}$ can be replaced by the symmetric virtual rate of deformation $\delta \bar{\bar{d}}$ [36].

---

[5]The operator ":" denotes the double product or double contraction of two tensors $\bar{\bar{A}}$ and $\bar{\bar{B}}$ as $(\bar{\bar{A}} : \bar{\bar{B}})_{ij} = A_{ij} B_{ij}$. So, one can also write $\bar{\bar{A}} : \bar{\bar{B}} = \bar{\bar{A}}^T \bar{\bar{B}} = \bar{\bar{B}}^T \bar{\bar{A}} = \bar{\bar{A}} \bar{\bar{B}}^T = \bar{\bar{B}} \bar{\bar{A}}^T$.

$$\int_v \bar{\bar{\sigma}} : \delta\dot{\bar{\bar{d}}}dv = \int_s \vec{t} \cdot \delta\vec{v}ds + \int_v \rho\vec{f} \cdot \delta\vec{v}dv \qquad (2.82)$$

At this point the second simplification from the small deformation case plays up, as now the integration over the deformed volume v and surface s can not be approximated by integration over the undeformed volume V and surface S. Instead a transformation is needed to write the integrals in the equation with respect to the undeformed volume V and surface S.

$$\int_V J\bar{\bar{\sigma}} : \delta\dot{\bar{\bar{d}}}dV = \int_S \vec{t_o} \cdot \delta\vec{v}dS + \int_V \rho_o\vec{f_o} \cdot \delta\vec{v}dV \qquad (2.83)$$

The one term in this equation which is not straight forward to calculate is the rate of virtual internal work. One can show however that the rate of deformation tensor $\bar{\bar{d}}$ equals $\bar{\bar{F}}^{-T}\dot{\bar{\bar{E}}}\bar{\bar{F}}^{-1}$ [36]. The rate of internal work can then be rewritten as

$$\int_V J\bar{\bar{\sigma}} : \delta\dot{\bar{\bar{d}}}dV \quad = \int_V J\bar{\bar{\sigma}} : \delta\bar{\bar{F}}^{-T}\dot{\bar{\bar{E}}}\bar{\bar{F}}^{-1}dV \qquad (2.84)$$

$$= \int_V J\bar{\bar{\sigma}} : (\bar{\bar{F}}^{-T}\delta\dot{\bar{\bar{E}}}\bar{\bar{F}}^{-1})dV \qquad (2.85)$$

$$= \int_V tr\left[\bar{\bar{F}}^{-1}J\bar{\bar{\sigma}}\bar{\bar{F}}^{-T}\delta\dot{\bar{\bar{E}}}\right] dV \qquad (2.86)$$

$$= \int_V \bar{\bar{T}} : \delta\dot{\bar{\bar{E}}}dV \qquad (2.87)$$

where $\bar{\bar{T}}$ is the second Piola-Kirchoff stress tensor (cf. Eq. (2.57)) so that Eq. (2.83) yields

$$\int_V \bar{\bar{T}} : \delta\dot{\bar{\bar{E}}}dV = \int_S \vec{t_o} \cdot \delta\vec{v}dS + \int_V \rho_o\vec{f_o} \cdot \delta\vec{v}dV \qquad (2.88)$$

At this point all parameters in the virtual energy equilibrium equation are written with respect to the undeformed reference frame. That way all parameters are known and the integration is possible.

The actual physical meaning of the second Piola-Kirchoff stress is not so easy to interpret, it is merely a mathematical aid to solve the integral equation (2.88). After a problem is solved however the Cauchy stress is calculated from the second Piola-Kirchoff stress for interpretation.

2.4 Computational solid mechanics

2.4.1 Discretization of the equations with the finite element method

The finte element method will be illustrated discretizing the equations governing the small deformation theory. The approach for large deformation theory is similar. The variational formulation of the small deformation conservation equation yields

$$\int_v \bar{\bar{\sigma}} : \delta\dot{\bar{\bar{\epsilon}}}dv = \int_s \vec{t} \cdot \delta\dot{\vec{u}}ds + \int_v \rho\vec{f} \cdot \delta\dot{\vec{u}}dv \qquad (2.89)$$

Due to the symmetry of the stress and strain tensor, the tensors are sometimes written in a vector notation. Consider a chosen coordinate system, then the stress and strain tensors can also be written as vectors[6]

$$\vec{\sigma} = \{\sigma_{11}\sigma_{22}\ \sigma_{33}\ \sigma_{12}\ \sigma_{23}\ \sigma_{31}\}^T \qquad (2.90)$$

$$\delta\vec{\epsilon} = \{\delta\epsilon_{11}\ \delta\epsilon_{22}\ \delta\epsilon_{33}\ 2\delta\epsilon_{12}\ 2\delta\epsilon_{23}\ 2\delta\epsilon_{31}\}^T \qquad (2.91)$$

Consistently,

$$\delta\vec{u} = \{\delta u_1\ \delta u_2\ \delta u_3\}^T \qquad (2.92)$$

$$\vec{t} = \{t_1\ t_2\ t_3\}^T \qquad (2.93)$$

Note that in the strain tensor the added "2" makes it possible to leave behind the symmetric parts $\delta\epsilon_{21}$, $\delta\epsilon_{32}$ and $\delta\epsilon_{31}$ in the notation.

The virtual work equation in variational form Eq. (2.89) can now be written as

$$\int_v \delta\dot{\vec{\epsilon}}^T \vec{\sigma}dv = \int_s \delta\dot{\vec{u}}^T \vec{t}ds + \int_v \rho\delta\dot{\vec{u}}^T \vec{f}dv \qquad (2.94)$$

At this point the discretization can start. In finite element methods shape functions are used in order to interpolate the solution. The shape functions are stored in a shape function matrix $\bar{\bar{N}}$ and the nodal values of $\delta\dot{\vec{u}}$ are written as

$$\delta\dot{\vec{u}} = \bar{\bar{N}}\delta\dot{\vec{u}}_d \qquad (2.95)$$

with $\delta\dot{\vec{u}}_d$ the discretized vector of $\delta\dot{\vec{u}}$

An example of choice of shape function N_a in a structured square mesh can be a pyramid-shaped function with value 1 at the node a and value 0 at the closest nodes and elsewhere. In three dimensions each node has three degrees of freedom u_1, u_2, u_3 and Eq. (2.94) can be written

$$\left\{\begin{array}{c} \delta\dot{u}_1 \\ \delta\dot{u}_2 \\ \delta\dot{u}_3 \end{array}\right\} = \left[\begin{array}{cccccc} N_1 & 0 & 0 & N_2 & 0 & \cdots \\ 0 & N_1 & 0 & 0 & N_2 & \cdots \\ 0 & 0 & N_1 & 0 & 0 & \cdots \end{array}\right] \left\{\begin{array}{c} \delta(\dot{u}_1)_{d,node1} \\ \delta(\dot{u}_2)_{d,node1} \\ \delta(\dot{u}_3)_{d,node1} \\ \delta(\dot{u}_1)_{d,node2} \\ \delta(\dot{u}_2)_{d,node2} \\ \delta(\dot{u}_3)_{d,node2} \\ \vdots \end{array}\right\} \qquad (2.96)$$

---

[6]Sometimes the elements $2\epsilon_{ij}\ i \neq j$ are written as $\gamma_{ij}\ i \neq j$.

Note that the dependency of the coordinates is stored in the shape functions and not in $\delta \dot{\vec{u}}_d$. The virtually small strain vector can be written as function of the shape functions

$$\delta \dot{\vec{\epsilon}} = \epsilon(\delta \dot{\vec{u}}) = \bar{\bar{B}} \delta \dot{\vec{u}}_d \tag{2.97}$$

where $\bar{\bar{B}}$ is the spatial derivative of the shape function tensor $\bar{\bar{N}}$. Now the discretized virtual work equation can be written as

$$\int_v \delta \dot{\vec{u}}_d^T \bar{\bar{B}}^T \vec{\sigma} dv = \int_s \delta \dot{\vec{u}}_d^T \bar{\bar{N}}^T \vec{t} ds + \int_v \rho \delta \dot{\vec{u}}_d^T \bar{\bar{N}}^T \vec{f} dv \tag{2.98}$$

As this equation has to hold for all choices of $\delta \dot{\vec{u}}_d$ it yields the finite element matrix equation

$$\int_v \bar{\bar{B}}^T \bar{\bar{\sigma}} dv = \int_s \bar{\bar{N}}^T \vec{t} ds + \int_v \rho \bar{\bar{N}}^T \vec{f} dv \tag{2.99}$$

Consider a linear elastic constitutive equation $\vec{\sigma} = \bar{\bar{C}} \vec{\epsilon}$, with $\vec{\epsilon} = \bar{\bar{B}} \vec{u}_d$. Note that $\bar{\bar{C}}$ is a tensor, as the engineering stress and strain are written down in vector notation. Now the finite element matrix equation writes, as $\vec{u}_d$ does not contain geometrical information,

$$\left[\int_v \bar{\bar{B}}^T \bar{\bar{C}} \bar{\bar{B}} dv \right] \vec{u}_d = \int_s \bar{\bar{N}}^T \vec{t} ds + \int_v \rho \bar{\bar{N}}^T \vec{f} dv \tag{2.100}$$

or

$$\bar{\bar{K}} \vec{u}_d = \vec{F} \tag{2.101}$$

with $\bar{\bar{K}}$ the stiffness matrix and $\vec{f}$ the force vector. The discretization in this paragraph holds for a fully linear case. Discretization in the materially and/or geometrically nonlinear case is beyond the scope of this work. The interested reader can find the details in Bonet and Wood [36].

2.4.2 Abaqus as a computational solid mechanics solver

Spatial discretization As denoted in this section, the spatial discretization in the finite element method is done using shape functions. The rectangular, bi-quadratic, two-dimensional elements in Abaqus are 'Serendipity' elements, they have eight nodes, as shown in Fig. 2.6. The shape functions are expressed in the local coordinates (r, s) with r and s ranging from -1 to 1. The shape functions h_i for the eight nodes $i = 1..8$ are given in Eq. 2.102.
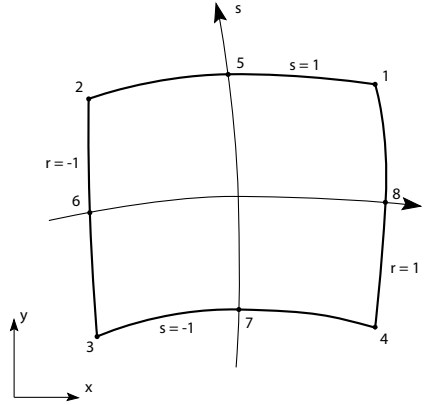
Figure 2.6: A rectangular, bi-quadratic, two-dimensional element with eight nodes, with local coordinates (r, s) indicated.

$$h_1(r, s) = -\tfrac{1}{4}(1 + r)(1 + s)(1 - r - s) \qquad h_5(r, s) = \tfrac{1}{2}(1 - r^2)(1 + s)$$

$$h_2(r, s) = -\tfrac{1}{4}(1 - r)(1 + s)(1 + r - s) \qquad h_6(r, s) = \tfrac{1}{2}(1 - r)(1 - s^2)$$

$$h_3(r, s) = -\tfrac{1}{4}(1 - r)(1 - s)(1 + r + s) \qquad h_7(r, s) = \tfrac{1}{2}(1 - r^2)(1 - s)$$

$$h_4(r, s) = -\tfrac{1}{4}(1 + r)(1 - s)(1 - r + s) \qquad h_8(r, s) = \tfrac{1}{2}(1 + r)(1 - s^2)$$

$$(2.102)$$
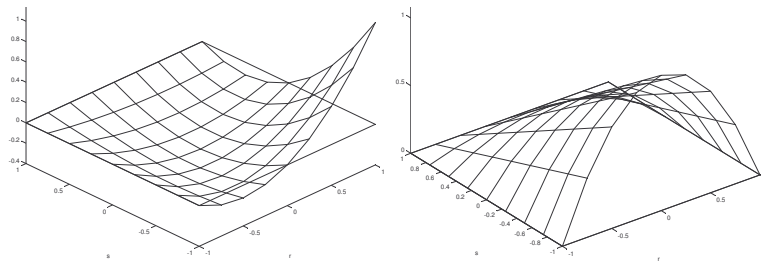
Figure 2.7: Two shape functions of a rectangular, bi-quadratic, two-dimensional element with eight nodes, in local coordinates (r, s). Left panel: shape function for node 4 (1,-1); Right panel: shape function for node 7 (0,-1).

Note that, as stated previously, the shape functions have value '1' in their corresponding node and '0' in the other nodes of the element. Two characteristic shape

functions are given in Fig. 2.7.

Temporal discretization The previous paragraph only dealt with spatial discretization, however in unsteady analysis a temporal discretization is also needed. The implicit calculations in Abaqus 6.5 use a Hilber-Hughes-Taylor temporal discretization scheme, given in Eq. (3.13).

$$
\begin{aligned}
\phi_{n+1} &= \phi_n + \tfrac{\Delta t}{1+\alpha}\dot{\phi}_n + \tfrac{1}{2}\left(\tfrac{\Delta t}{1+\alpha}\right)^2 [(1-2\beta)\ddot{\phi}_n + 2\beta\ddot{\phi}_{n+1}] \\
\dot{\phi}_{n+1} &= \dot{\phi}_n + \tfrac{\Delta t}{1+\alpha}[(1-\gamma)\ddot{\phi}_n + \gamma\ddot{\phi}_{n+1}]
\end{aligned}
\tag{2.103}
$$

An extra restriction is put on parameters α, β and γ

$$
\beta = \frac{(1-\alpha)^2}{4} \tag{2.104}
$$

$$
\gamma = \frac{1-2\alpha}{2} \tag{2.105}
$$

The temporal discretization and its consequences for a fluid-structure interaction code will be discussed in paragraph 3.5.2 and the next chapter, in section 1.7.2.

3 Modeling fluid-structure interaction

When performing biomedical fluid calculations with moving geometries, two approaches can be followed. One can consider the movement of the structure, for example the ventricle wall, known, which is then prescribed in the calculation. In this case only the influence of the structure, e.g. the ventricle wall, on the fluid, e.g. the blood, is incorporated in the model.

A second, more elaborated approach also considers the influence the fluid exerts on the structure, hence taking the full fluid-structure interaction into account. The movement of the structure depends on the movement of the fluid and vice versa. Different methods to arrive at a full fluid-structure interaction approach are discussed in this section.

Consider a general fluid-structure interaction problem with a fluid domain Ω^f and a structural domain Ω^s, where both domains share an interface Γ, as shown in Fig. 2.8. Generally, the undiscretized fluid-structure interaction equations to be solved can be written as
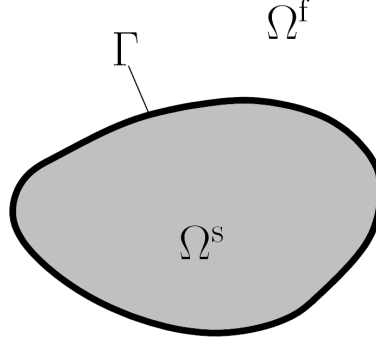
Figure 2.8: General fluid-structure interaction geometry. Adapted from [37]

$$F(\vec{v}^f, \vec{p}^f) \quad = 0 \quad in \ \Omega^f, \tag{2.106}$$

$$S(\vec{u}^s, \bar{\bar{\sigma}}^s) \quad = 0 \quad in \ \Omega^s, \tag{2.107}$$

$$\vec{t}^f \quad = \vec{t}^s \quad on \ \Gamma, \tag{2.108}$$

$$\vec{X}^f \quad = \vec{X}^s \quad on \ \Gamma \tag{2.109}$$

where $\vec{v}^f$ and $\vec{p}^f$ denote the flow velocity and the pressure distribution in the fluid domain Ω^f. The flow domain is described by the Navier-Stokes equations $F(\vec{v}^f, \vec{p}^f) = 0$, which were explained in detail in the first section in this chapter. Similarly, $\vec{u}^s$ and $\bar{\bar{\sigma}}^s$ are the displacement and the stress tensor in the structural domain Ω^s, described by equations $S(\vec{u}^s, \bar{\bar{\sigma}}^s) = 0$, described in the second section. $\vec{t}^f$ and $\vec{t}^s$ denote the forces on the interface Γ per unit area, on the fluid side and the structural side, respectively. They define the Neumann boundary condition, Eq. (2.108), while Eq. (2.109) defines the Dirichlet boundary condition with position $\vec{X}^f$ and $\vec{X}^s$ of the interface on fluid and solid side, respectively. In this section the implementation of this generic FSI problem will be discussed.

3.1   Moving grid formulations

As stated at the beginning of the previous chapter, there are two major ways to look at motion. In the Eulerian way one looks at the motion from a fixed point, in the Lagrangian formulation one looks at the motion from a point moving along with the material. The Eulerian way is the preferred way to look at fluid flow, whereas the Lagrangian way is the intuitive way to look at solid deformation. When solving a fluid-structure interaction problem there are different ways of matching these two distinct ways of describing the problem. One possibility is the fixed grid approach, discussed in the next paragraph, where the whole domain is meshed with

a fixed grid and an overlaying structural mesh is imposed. Another possibility is the arbitrary Lagrangian-Eulerian (ALE) approach, discussed in paragraph 3.1.2, where the fluid grid is deformable, using the ALE-formulation of the Navier-Stokes equations (Eqs. (2.28)-(2.29)).

3.1.1 Fixed grid methods

In this group of methods, the extended fluid domain $\Omega^f + \Omega^s$ is meshed with a (structured) fixed grid and the Navier-Stokes equations are written in Eulerian form. The solid domain Ω^s is meshed with a mesh that does not necessarily follow the mesh of the fluid domain and that is overlaying over the extended fluid domain. This mesh follows the materials' deformation and the continuum equation is written in Lagrangian form. The state of the system at any time is the combination of the pressure and flow distribution in the fixed grid, and the location of the material points of the overlaying solid volume.

The no-slip boundary condition at the interface Γ, derived from Eq. (2.109), can be imposed in different ways. Here two ways will be highlighted, the immersed boundary method and the fictitious domain method. Since the fixed grid formulation allows large displacements, it is often used for fluid-structure interaction of heart valves [38–42].

Immersed boundary method   The immersed boundary method was developed by Peskin who used the method to develop a full FSI-model for the mitral valve [43]. Originally, the solid structure consisted of a spring-like fiber structure, which was then extended to a woven net of fibers to represent a three-dimensional structure. Recently the method is furter elaborated into a three-dimensional finite element formulation [44, 45].

The solid is deformed by interpolating the fluid velocities from the surrounding (Eulerian) fluid nodes onto the (Lagrangian) nodes of the solid. The elastic forces of the solid onto the fluid are interpollated to the fluid nodes and inserted into the Navier-Stokes equations as body forces $\vec{f}_f$

$$\rho \left(\frac{\partial \vec{u}}{\partial t} + \vec{u} \cdot \nabla \vec{u} \right) + \nabla p = \mu \nabla^2 \vec{u} + \vec{f}_f \tag{2.110}$$

$$\nabla \cdot u = 0 \tag{2.111}$$

where ρ denotes the density of the fluid and μ the dynamic viscosity. The Lagrangian force density $\vec{f}_s(s,t)$ of the structural interface needs to be translated to an Eulerian force density $\vec{f}_f(s,t)$, which is done by the convolution over the structure

$$\vec{f}_f(x,t) = \int \vec{f}_s(s,t)\delta(x - X(s,t))ds \tag{2.112}$$
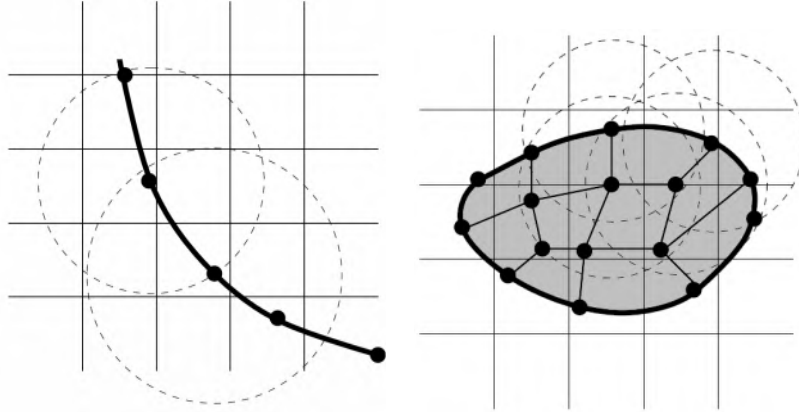
Figure 2.9: Illustrations of immersed boundary-type methods: The interpolation functions (dashed circles) centered at the structural Lagrangian nodes (•) map the elastic forces onto the background fluid mesh. Adapted from [37]

where X denotes the position of the structural nodes and δ the three-dimensional Dirac function. The no-slip condition on the interface is fulfilled as the solid follows the motion of the fluid.

The main advantage of this approach is that the structured fluid grid allows efficient implementation of the fluid solver. An other advantage is the fact that it allows large deformation and displacement of the solid volume without the need of remeshing the fluid volume. The method does have some disadvantages. The way the force $\vec{f}$ is discretized over the fluid determines the accuracy of the method, together with the mesh size ratio between the fluid and the solid solver [46].

Moreover the method is quite straightforward for structures which are submerged in the fluid, such as heart valves. However, when one wants to establish a fluid-structure interaction model of the left ventricle, the applicability of the method is less obvious. In that case one also needs to assume that the structural domain (the ventricle wall) is submerged in blood. Due to this unnaturally chosen fluid domain, a non-physical boundary condition has to be imposed at the non-FSI edges of the fluid domain. Peskin applied the immersed boundary method to a FSI-model of the heart [47]. He used a periodic boundary condition at the fluid domain edges, which could be an adequate assumption if the distances from the heart to the edges of the flow domain are quite big. However assuming that the heart is surrounded by blood induces a large error, as this blood outside the heart needs to be accelerated as well.

Quantification of flow velocities close to the solid boundary is difficult, so wall shear stress (WSS) cannot be adequately assessed. This can be tackled using

a Chimera-like formulation [37, 48]. The technique uses two fluid domains, a smaller, ALE-deformable fluid domain (cf. paragraph 3.1.2) close to the solid volume and a big fixed grid volume in such a way that the two fluid volumes have an overlap at all times. Now the immersed boundary approach is used between the solid-attached moving ALE fluid grid and the fixed fluid grid. The ALE-grid assures a good WSS resolution while the fixed grid limits the errors induced by ALE approaches.

Fictitious domain method   The fictitious domain method is quite similar to the immersed boundary method, it also uses a fixed fluid grid and an overlaying solid volume. The no slip boundary condition on the solid-interface is fulfilled trough momentum sources or Lagrange multipliers $\vec{\lambda}$, which are inserted in both the fluid and the solid conservation equations, in order to match the velocity of the fluid and the solid [49, 50]. Thus, in this method, the fluid filling the space where the solid domain is overlaying, is forced to the same velocity field as the solid.
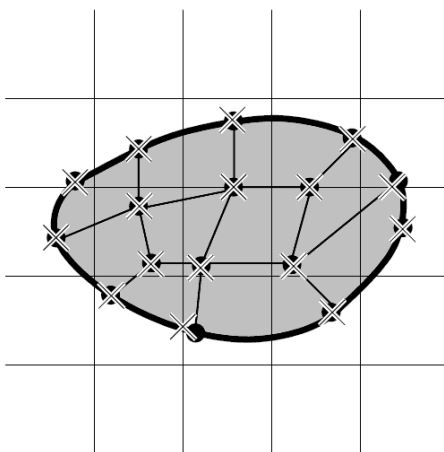
Figure 2.10: Illustration of fictitious domain-type methods: Several discretization types exist for the Lagrange multiplier field (Lagrange multiplier nodes marked with ($\times$), Lagrangian structure nodes with ($\bullet$)). Several proposals exist on the proper discretization of the Lagrange multiplier field. Adapted from [37]

Due to the grid topology it is not easy to achieve good resolution for wall shear stress and pressure close to the solid here as well. This was tackled [40, 51] in a adapted fictitious domain method, where the nodes of the fluid grid were shifted so that, each time step, they matched with the position of the solid mesh. This method describes a method in between the fictitious domain method and the

arbitrary Lagrangian-Eulerian approach.

However even in this more elaborate version of the fictitious domain method the problem remains to accurately represent the stress jump over the fluid-structure interface. An other direct disadvantage of the formulation is that the solid needs to have the same compressibility behavior as the fluid that is considered. For biomechanical problems this does not imply a big problem, as the solid is incompressible as the fluid, however it is an issue for other applications. Problem in biomechanical cases is that the viscosity of the blood "inside" the solid domain creates a non-physical damping.

A solution proposed by Wall et al. [37], describes a FEM-discretization of the fluid solver with a jump function $H(\vec{x}, t)$ that can be added to the shape functions. The jump function has a value "1" in the real fluid domain and value "-1" in the fictitious fluid domain. With this jump function they arrive at a decoupling of the solution of the real fluid domain and the fictitious fluid domain, so that jumps in variables can be represented. This also means that the viscosity of the fluid in the fictitious domain thus not interferes with the solution in the real fluid domain and that the compressibility of both the fluid and the solid does not need to be matched. The resolution of the wall shear stress is however still an issue.

3.1.2 Arbitrary Lagrangian Eulerian method

In the arbitrary Lagrangian Eulerian method [52–54], the grid of the fluid domain is allowed to deform in an arbitrary way, so that its boundaries follow the structural domains' deformation. The structural problem is then formulated in the Lagrangian manner. In that way the two approaches, Eulerian and Lagrangian, which could seem incompatible at first, are combined. It is generally used in vascular FSI-applications [55–61].
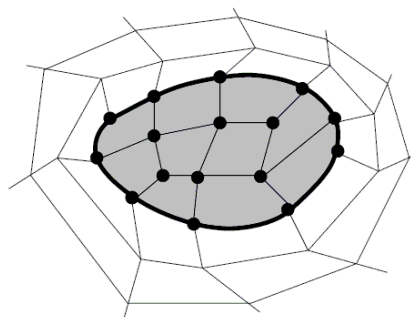
Figure 2.11: Illustration of the arbitrary Lagrangian-Eulerian methods. The fluid domain and the structural domain share an interface, there is no overlap. Adapted from [37]

As shown in Fig. 2.11 there is no overlap between the fluid domain and the structural domain as in the previous fixed grid approach. The fluid domain and the structural domain share an interface at which the loads and displacements are consistent. The movement of the grid is accounted for by inserting the velocities of the nodes into the conservation equations as mentioned in paragraph 1.2.4.

This technique requires algorithms that redistribute the cells over the fluid domain when the fluid-structure interface has moved. On the interface the velocity of the mesh faces $\vec{v}_b$ is defined by the velocity of the structural mesh faces on the structural side of the interface. In the interior of the fluid domain the mesh face velocity $\vec{v}_b$ needs to be established. Different mesh smoothing algorithms exist in order to generate a mesh movement of the nodes and faces so that a sufficient mesh quality is obtained.

These methods to redistribute the nodes over the fluid domain are mostly based on a pseudo-structural approach. One intuitive approach is the spring method, where edges are replaced by springs with a spring constant inverse to the length of the edge [62]. When the interface nodes are moved, the interior nodes will distribute evenly over the fluid domain. Other more elaborate methods are the pseudo-pressure penalty method [63] and the pseudo-elasticity method [64], however a detailed description of these methods goes beyond the scope of this work.

These smoothing algorithms have limitations too and when large deformations occur or the topology of the fluid domain changes, for example in case of a closing heart valve, partial or complete remeshing of the domain is unavoidable. Due to the remeshing an interpolation is needed from the pressure and velocity field attached to the old mesh to the new mesh. This inevitably induces inaccuracies and errors in the calculation. Hence, when frequent remeshing is unavoidable, fixed grid approaches might be a good choice.

This arbitrary Lagrangian-Eulerian approach is widely used to solve fluid-structure interaction problems, for it is a more reliable way to quantify wall shear stress close to the fluid-solid-interface. Moreover, it provides a more physical way to model vascular and ventricular fluid-structure interaction problems. As in these cases the structural domain is the boundary of the fluid domain, the previous methods with a fixed fluid mesh are not adequate, requiring an unphysical symmetry boundary conditions at the limits of the fluid mesh. With the arbitrary Lagrangian-Eulerian approach this artificial boundary condition is elegantly avoided. As no topology change is present in the flows in the arteries, it will be the approach followed in this research.

3.2 Monolithic solvers versus partitioned solvers

When the discretization method of both sets of equations (2.106) and (2.107) are the same, both groups of equations can be treated as one big set of equations

which is solved simultaneously. This is called the monolithic approach [34, 65–67]. Alternatively, in the partitioned solver approach [55–57, 59–61], the fluid and structural problem are solved separately and data is exchanged every time step or every iteration. In this approach a coupling scheme is needed to take care of the communication of the solution of the one problem to the other.

The monolithic approach is straightforward, especially for simple FSI-problems, resulting in a strongly coupled fluid approach, which is easily parallelized. However the method is not very suitable for large, complex, real world problems, as in these problems the size and condition of the associated system matrix becomes an issue. Moreover as the equations need to be written in one big set, specific solution strategies for complex behavior in fluid or solid mechanics are no longer applicable. So existing expertise in solving the two separate problems can not be reused and modularity is lost. Therefore the use of monolithic schemes is in many cases sub-optimal.

In complex problems the partitioned solver approach has many benefits. Here, the specific solution strategies for the two parts of the problem can be used. For biomedical problems this is a big advantage as for example biological tissues behave in a materially nonlinear way and they undergo large deformations. However a coupling scheme is needed, so an overview of possible coupling schemes is given in paragraph 3.4.

3.3 Black-box solvers versus own written code

When looking at commercially available FSI-codes, codes using monolithic approaches and iterative partitioned approaches exist. ADINA (ADINA R&D, Inc.) offers the choice between a monolithic approach and an iterative, partitioned approach for larger solutions [68, 69]. ANSYS 11.0 multiphysics solver (ANSYS, Inc.) uses a partitioned approach [70].

Other commercial coupling solvers such as the MpCCI software (Fraunhofer SCAI) are available which couple commercially available solvers amongst which fluid solver Fluent (ANSYS, Inc.) and solid solver Abaqus (Simulia, Inc.), obviously using a partitioned solver approach [71]. Disadvantage of this software is that until now only staggered approaches are allowed [72].

Both solutions work as a black box, no intervention in the code itself is possible. An alternative is to write the entire FSI-code, perhaps using available packages to perform matrix operations, such as matrix inversion, in an efficient way. In this option both the partitioned solver approach or the monolithic approach can be followed. Intervention is possible anywhere during the solution process, however in biomechanical cases for example, where large deformations and nonlinear solid material behavior are combined with possible non-Newtonian fluid behavior, developing an own written code is not straight-forward.

A third approach, in between the two previous ones, is to use a partitioned approach where the solid solver and/or the structural solver are commercially available packages and where an own coupling algorithm is written, if needed with an own written solid or fluid solver. This choice limits the possibility of coupling stabilization which will be treated in the next paragraph 3.4. But the programming work is limited and intervention is possible, either only in the FSI-coupling, or in the FSI-coupling and in the other solver if only one commercial solver was chosen.

Fluid solvers such as Fluent (ANSYS, Inc.) support the ALE-formulation for moving grids. The flow field can be calculated with an imposed movement of the boundary, making it possible to use the solver in a partitioned FSI-approach. Solvers such as Abaqus (Simulia, Inc.) allow a Neumann boundary condition with any given surface tension $\vec{t}$, making the solver a valuable possibility in a black box partitioned solver approach.

3.4   Coupling algorithms for the partitioned approach

When choosing a partitioned approach, a coupling scheme is needed to transfer the data from the fluid solver to the structural solver and vice-versa. Two main possibilities can provide this coupling, the staggered scheme (Fig. 2.12, left panel) and the iterative scheme (Fig. 2.12, right panel). Both approaches will be highlighted here.
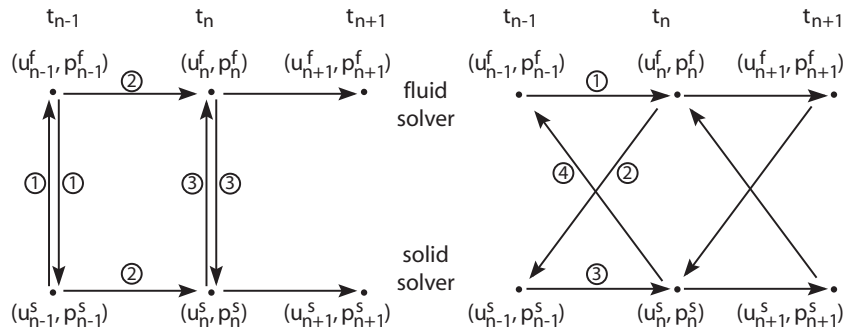
Figure 2.12: Two main possibilities to couple partitioned solvers. Left panel : parallel staggered approach. Data exchange between the fluid and solid solver (1), both solvers march in time (2); Right panel : iterative approach. The fluid solver marches in time (1), data transfer to the solid solver (2), the solid solver marches in time (3), data transfer to the fluid solver (4).

3.4.1   Staggered formulation

The staggered algorithm does not use iterations within one time step, the coupling information is exchanged only once each time step (step (1), Fig. 2.12, left). One can distinguish between a serial staggered approach, where the fluid and structural solver are called the one after the other, or a parallel scheme, as shown in the left panel of Fig. 2.12, where the fluid and structural problem are solved simultaneously (step (2)). More elaborate versions of the parallel and serial staggered scheme exist [73].

As no iterations are performed, the approach promises to be very computationally efficient. While the approach is very useful in aeroelastic fluid-structure interaction problems, it has its limits in biomechanical problems. Indeed, one can show that stability is limited due to an artificial added mass effect. The stability limit is dependent of the ratio ρ^f/ρ^s and the time step, where ρ_f denotes the density of the fluid and ρ_s the density of the solid. The higher the density ratio and the smaller the time step, the more instable this approach is [74]. In aeroelastic applications the mass ratio is sufficiently small, so that stability is not an issue. In vascular applications however the mass ratio is about 1, so that this approach is not an option. Causin et al. also showed that for FSI-problems in tubes the length of the tube plays a role, once the length of the tube is greater than a certain threshold the algorithm becomes instable [75].

3.4.2   Iterative formulation

An iterative formulation is suitable for biomechanical application, although more computationally expensive. In this approach iterations between the fluid and the solid solver (steps (1) - (4) in Fig. 2.12, right panel) are performed in each time step until convergence is reached. Only then is proceeded to the next time step.

During these iterations, several approaches are possible providing a stabilization of the FSI-approach. First, the approach without stabilization is discussed. Secondly the use of underrelaxation is described to accelerate the solution construction. When both the fluid-solver and the structural solver are open source codes, a Newton method can be used. When only the structural solver is open source, the quasi-Newton method can be used, which is discussed next. Finally the domain decomposition method and the reduced order method will be highlighted.

No stabilization   When the solution from the structural solver is directly inserted in the fluid solver, aside from possible spatial interpolation, the algorithm will tend toward instabilities. This approach works for problems with a high wall density or a high wall stiffness. However one can show that the added mass effect does also add to instability in an iterative scheme without stabilization [75]. So, when the density of the wall is about the same as the density of the fluid, as in biomechan-

ical applications, this approach has a limited use due to possible instability with compliant solid materials.

Fixed point formulation with acceleration methods using underrelaxation Instead of the general FSI-problem defined in Eq. 2.106-2.109 here we look at the fluid and structural solver trough their action on the discretized interface tension $\vec{t}_d^{\,n}$ and position $\vec{X}_d^{\,n}$

$$\vec{t}_d^{\,n} = F^\Gamma(\vec{X}_d^{\,n}) \tag{2.113}$$

$$\vec{X}_d^{\,n} = S^\Gamma(\vec{t}_d^{\,n}) \tag{2.114}$$

The discretized tension distribution at the interface $\vec{t}_d$ is a vector of $\mathbb{R}^m$ and the function $R^\Gamma(\vec{t}_d^{\,n}) = F^\Gamma \circ S^\Gamma(\vec{t}_d^{\,n}) - \vec{t}_d^{\,n}$ is a vector map from $\mathbb{R}^m$ to $\mathbb{R}^m$. The subscript $_d$ denoting the discretized vector and the superscript ^{n} denoting the time step will be omitted here for clarity of the equations.

Now the fluid-structure interaction solution for time step n $\vec{t}_{n,sol}$ is the root of the vector function $R(\vec{t})$. Indeed, the requirement $R^\Gamma(\vec{t}^{\,n}) = 0$ equals the equation $F^\Gamma \circ S^\Gamma(\vec{t}^{\,n}) = \vec{t}^{\,n}$ which denotes the solution of the FSI-problem[7].

This group of stabilization schemes uses an underrelaxation parameter ω to accelerate the convergence of the FSI-problem. For example, instead of coupling the pressure at the interface directly to the solid solver, it is first tempered using

$$\vec{t}_{k+1} = \vec{t}_k - \omega R^\Gamma(\vec{t}_k) \tag{2.115}$$

where $R^\Gamma(\vec{t}_k)$ is the residual from the previous iteration $R^\Gamma(\vec{t}_k) = F^\Gamma \circ S^\Gamma(\vec{t}_k) - \vec{t}_k$, where F^Γ denotes the interface focusing fluid solver and S^Γ denotes the interface focusing solid solver. It is the difference between the pressure at a given time step and subiteration $\vec{t}_k$ and the pressure that was obtained when taking $\vec{t}_k$ to the solid solver and then taking this solution from the solid solver S^Γ back to the fluid solver F^Γ, $F^\Gamma \circ S^\Gamma(\vec{t}_k)$. The parameter ω can be a constant that is required as an input, in which case an optimal ω need to be found by trial and error. Luckily some methods, such as the Aitken method, exist to establish an optimal underrelaxation factor.

The Aitkin method bases the estimation of ω on the two previous solutions $\vec{t}_k$ and $\vec{t}_{k-1}$. The Aitken method to establish ω was first developed for scalar problems and later extended for vectorial problems by Irons and Tuck [76] which was then applied to fluid-structure interaction problems by Mok et al. [77]. The method defines an optimal underrelaxation factor as

---

[7]Similarly one could define the operator $Q^\Gamma(\vec{X}^n) = S^\Gamma \circ F^\Gamma(\vec{X}^n) - \vec{X}^n$ and find a root for this operator in order to find the solution of the FSI-problem.

$$\omega_k = \frac{(\vec{t}_k - \vec{t}_{k-1}) \cdot (R^\Gamma(\vec{t}_k) - R^\Gamma(\vec{t}_{k-1}))}{R^\Gamma(\vec{t}_k) - R^\Gamma(\vec{t}_{k-1})) \cdot (R^\Gamma(\vec{t}_k) - R^\Gamma(\vec{t}_{k-1})} \tag{2.116}$$

A more elaborated description of the Aitken formulation is given in the next chapter in paragraph 3.3.2. Although the vectorial formulation of the Aitken acceleration does not have a solid base which guarantees success as in the scalar case, experience showed the usefulness of the approach [77]. Moreover, compared to the following methods, an underrelaxation method such as the Aitken method is easily implemented.

Root-finding Newton methods   In this approach the fluid and solid solvers are written in a root-finding form as

$$f(x, y) = x - F(x, y) = 0 \tag{2.117}$$

$$s(x, y) = y - S(x, y) = 0 \tag{2.118}$$

following the notation of Matthies et al. [56, 61], where $x = (\vec{v}, \vec{p})$ characterizing the fluid domain field and $y = (\vec{u}, \bar{\bar{\sigma}})$ characterizing the solid domain field. Note that here the fluid solver F and the solid solver S are working on the entire fluid domain and solid domain, respectively, whereas in the previous paragraph the solvers F_Γ and S_Γ were evaluated through their action on the interface Γ.

Now an iterative approach is used, requiring an updated set $x_{k+1} = x_k + \Delta x$ and $y_{k+1} = y_k + \Delta y$, where an optimal Δx and Δy needs to be found, in order for x_{k+1} and y_{k+1} to approach to the solutions x_{sol} and y_{sol} of Eq. (2.117) and (2.118).

Using the Newton method, the step Δx and Δy can be found by solving

$$\begin{bmatrix} D_x f(x_k, y_k) & D_y f(x_k, y_k) \\ D_x s(x_k, y_k) & D_y s(x_k, y_k) \end{bmatrix} \begin{bmatrix} \Delta x \\ \Delta y \end{bmatrix} = - \begin{bmatrix} f(x_k, y_k) \\ s(x_k, y_k) \end{bmatrix} \tag{2.119}$$

So the Jacobian $\bar{\bar{J}}$

$$\bar{\bar{J}} = \begin{bmatrix} D_x f(x_k, y_k) & D_y f(x_k, y_k) \\ D_x s(x_k, y_k) & D_y s(x_k, y_k) \end{bmatrix} \tag{2.120}$$

needs to be known in order to solve the matrix Eq. (2.120) for Δx and Δy, which is not the case. D_x denotes the Jacobian with respect to x and D_y with respect to y.

However instead of trying to find an exact or approximated formulation for the Jacobian, the method tries to find an approximation of the product of the Jacobian with a vector for each coupling iteration k to find the optimal value of step Δx

and Δy to the next iteration. As now one iteration k of the coupling solver is considered, the subscript $_k$ is omitted.

One can solve the upper-part of Eq. (2.119) to find Δx as a function of Δy

$$\Delta x = -[D_x f]^{-1}[D_y f]\Delta y - [D_x f]^{-1}f \qquad (2.121)$$

which can now be substituted into the lower part of Eq. (2.119) to find an expression for Δy

$$([D_y s] - [D_x s][D_x f]^{-1}[D_y f])\Delta y = -s + [D_x s][D_x f]^{-1}f \qquad (2.122)$$

or, with $\bar{\bar{S}}\Delta y = -r$,

$$\bar{\bar{S}} = [D_y s] - [D_x s][D_x f]^{-1}[D_y f] \qquad (2.123)$$

$$r = s - [D_x s]q \qquad (2.124)$$

$$q = [D_x f]^{-1}f \qquad (2.125)$$

Now one needs to find an expression for the Jacobians of the partitioned solver operators in order to find the optimal step Δy.

Fernandez and Moubachir derived the exact Jacobian in a finite element approach for both the fluid and the solid equations, where only a linear solid is considered [58]. Most of the Jacobian calculations however were established with finite differences approaches.

When a black box solver is used, the Jacobian is impossible to obtain in its exact form, and even if the exact Jacobian is assessed, the inverse of the Jacobian is very expensive to calculate. Therefore a wide variety of techniques exist to avoid the use of the exact Jacobian. Methods as the quasi-Newtonian method try to approximate the inverse Jacobian, where underrelaxation schemes consider an inverse Jacobian as a scalar ω times the unity matrix $\bar{\bar{I}}$. Loose coupling is obtained when the inverse of the Jacobian is omitted.

Note that the Newton method is just a general method to solve a system of (non-linear) equations. Hence the method can also be used to solve the fluid equations or the solid equations or the both equations at the same time in case of a monolithic solver.

Root-finding quasi-Newton methods   Although the Newton method is more robust, it is not possible to implement the approach when one or two black box solvers are used [58]. However, when only a fluid black box solver is used, with

an open source solid solver, one can use a quasi-Newton method using finite differences [56,61,65].

In the quasi-Newton difference method [56,61], the general idea is that in order to approximate the equation (2.125), the operator $D_x f$ does not need to be known. Indeed, one can look at the equation $[D_x f]^{-1} f - q = 0$ as the first iteration of a Newton-Raphson method to solve the fluid solver $f(x_k + q, y_k) = 0$

$$f(x_k + q, y_k) = f(x_k, y_k) + [D_x f]q \qquad (2.126)$$

hence the name finite differences method. So the converged solution $x_{sol,k}$ of $f(x_{sol,k}, y_k) = 0$ can now be used to approximate $q = x_{sol,f} - x_k$. Next, with the found q, r can be established in a similar way from eq. (2.124). Note here that we need the residual of the first iteration in the Newton-Raphson method for the solid solver, which requires an open source solid solver to access r.

Now that q and r are established, one can start solving $\bar{\bar{S}} \Delta y = -r$. $\bar{\bar{S}}$ is the Schur complement matrix of the Jacobian $\bar{\bar{J}}$, which can be solved using, for example, the generalized minimal residual method ($GMRES$) [78]. In the $GMRES$ method a matrix equation $\bar{\bar{A}} \vec{x} = \vec{b}$ is solved by finding a vector $\vec{w}$ from a prescribed subspace of vectors for which the residual $Aw - b$ is minimal. Hence the product of $\bar{\bar{S}}$ with another vector $\vec{w}$ needs to be evaluated, where h denotes the step size

$$
\begin{aligned}
\frac{1}{h}[S][hw] &= \frac{1}{h}([D_y s][hw] - [D_x s][D_x f]^{-1}[D_y f][hw]) \\
&= \frac{1}{h}\left(s(x_k - [D_x f]^{-1}[D_y f][hw], y_k + hw) - s(x_k, y_k)\right)
\end{aligned}
$$
$$(2.127)$$

the unknown in this relation is $[D_x f]^{-1}[D_y f][hw]$. The solution toward the expression of $[D_x f]^{-1}[D_y f][hw]$ is split in two parts. First $[D_y f][hw]$ is evaluated as using the fluid solver

$$[D_y f][hw] \approx f(x_k, y_k + hw) - f(x_k, y_k) \qquad (2.128)$$

after which one can solve $[D_x f]^{-1}[D_y f][hw] = s$ as

$$[D_x f]s = [D_y f][hw] \qquad (2.129)$$

again, using the fluid solver. At this point Eq. (2.127) can be evaluated, giving the steps Δx and Δy for the next iteration.

One can also use the iterative $GMRES$-method used in the previous method to solve Eq. (2.119) directly, called the *the Newton-Krylow method* [79]. In this method a vector $\vec{w}$ is selected from a subspace of vectors, for which the residual

$$[J][w] + \begin{bmatrix} f(x_k, y_k) \\ s(x_k, y_k) \end{bmatrix} \qquad (2.130)$$

is minimal. The product $\bar{\bar{J}}\vec{w}$ can be approximated using the fixed point operator $R = \bar{\bar{I}} - F \circ S$ as

$$[J] [w] = D_d R(\vec{d_k})[w] \tag{2.131}$$

$\vec{d_k}$ is a short writing version of $[x_k \ y_k]^T$. Now using finite differences the Jacobian of R can be approximated as

$$[J] [w] \approx \frac{1}{h} \left(R(\vec{d_k} + h\vec{w}) - R(\vec{d_k}) \right) \tag{2.132}$$

where the minimal residual vector $\vec{w}$ can be used as a new step vector $[x_{k+1} \ y_{k+1}]^T$ $= [x_k \ y_k]^T + \vec{w}$. Iterations are done until convergence is reached.

A *reduced model approach*, proposed by Gerbeau et al. [55, 59], not to be confused with a reduced order model approach explained in a next paragraph, also considers the operator $R = \bar{\bar{I}} - F \circ S$ to approximate $\bar{\bar{J}}$ as in the Newton-Kyrlow method. However now the Jacobian of R is not approximated as Eq. 2.132 but as

$$\begin{aligned} D_d R(\vec{d_k}) &= D_d \bar{\bar{I}}\vec{d_k} - D_d F \circ S(\vec{d_k}) \\ &= I - D_d S(F(\vec{d_k})) \cdot D_d F(\vec{d_k}) \end{aligned} \tag{2.133}$$

so that the matrix product $\bar{\bar{J}}\vec{w}$ can be approximated as

$$[J] [w] \approx \left(I - D_d S(F(\vec{d_k})) \cdot D_d F(\vec{d_k}) \right) [w] \tag{2.134}$$

Now if the solid solver is an open source solver using the Newton-Raphson method, the Jacobian from the solid solver is readily available. The Jacobian of the fluid solver is replaced by a Jacobian calculated using simplified fluid equations. The simplified fluid problem considers a linear inviscid model for the flow in a fixed fluid domain. With the approximating expression of the Jacobian, a $GMRES$-method is used to quantify an optimal step for the next iteration.

Stress-equilibrium domain decomposition approach   Newton methods and quasi-Newton methods look at the FSI-problem from a root-finding point of view, while methods such as the Aitken acceleration method look at the problem from a fixed-point problem point of view. The domain decomposition approach looks at the problem as a stress-equilibrium problem at the interface [57, 60, 80]. The fluid solver operator and the structural solver operators' function here is limited to what they do at the interface Γ.

Consider a position vector $\vec{X}$ of the discretized nodal positions at the interface. Now the fluid solver can be considered as a Dirichlet-to-Neumann operator F^Γ, meaning that the position of the interface $\vec{X}$ is the input of the operator and the operator gives the associated normal stress $\vec{t^f}$ on the interface

$$F^\Gamma(\vec{X}) = \vec{t}^{f,\Gamma} \equiv \bar{\bar{\sigma}}^{f,\Gamma}(\vec{u}, \vec{p}) \cdot \vec{n}^{f,\Gamma} \tag{2.135}$$

Similarly, the structural solver is seen as a Dirichlet-to-Neumann operator $(S^\Gamma)^{-1}$, associating a normal stress $\vec{t}^s$ at the wet side of the interface with a given interface position $\vec{X}$.

$$(S^\Gamma)^{-1}(\vec{X}) = \vec{t}^{s,\Gamma} \equiv \bar{\bar{\sigma}}^s(\vec{d^s}) \cdot \vec{n}^{s,\Gamma} \tag{2.136}$$

Note that the formulation of the structural solver operator in this approach is the inverse of the formulation in other approaches. In other approaches the structural solver operator is considered a Neumann-to-Dirichlet operator, starting with a tension vector at the interface and associating a position at the interface with it.

The central equation in this approach is the force equilibrium equation at the interface

$$(S^\Gamma)^{-1}(\vec{X}) + F^\Gamma(\vec{X}) = 0 \tag{2.137}$$

This equation is also called the Steklov-Poincaré equation, while this method is also referred to as the Steklov-Poincaré formulation.

Now an FSI-problem is solved iteratively by starting with a guess of interface position X_k, either from the previous time step or from the previous iteration $k - 1$. With this X_k the fluid solver associates an interface stress distribution $\vec{t}^f$ at the dry interface, while the structural solver, possibly in parallel with the fluid solver, associates to X_k a surface tension $\vec{t}^s$ at the wet interface. With these surface tensions the net out-of-balance surface tension is quantified $\vec{t}_k = -(\vec{t}^s + \vec{t}^f)$.

With this out-of-balance tension $\vec{t}_k$ an optimal step direction δX_k is established, using a preconditioning operator or scaling operator $(P_k)^{-1}$ as

$$\delta \vec{X}_k = (P_k)^{-1} \vec{t}_k \tag{2.138}$$

with which a new guess of the interface position is quantified using an underrelaxation factor ω_k to define the optimal step size.

$$\vec{X}^{k+1} = \vec{X}_k + \omega_k (P_k)^{-1} \vec{t}_k \tag{2.139}$$

$$\omega^k = \frac{(\delta \vec{X}_k - \delta \vec{X}_{k-1}) \cdot (\vec{X}_k - \vec{X}_{k-1})}{\left\| \delta \vec{X}_k - \delta \vec{X}_{k-1} \right\|^2} \tag{2.140}$$

Several preconditioners can be defined, an overview is given in [57, 60].

Reduced order models One can also construct a reduced order model of the fluid solver or the structural solver. A reduced order model method approaches the Jacobian of the fluid solver or the structural solver instead of the Jacobian of the whole FSI-model. The approach is elaborated in more detail in the next chapter, however the general idea is to approximate for example the fluid solver operator on the interface $F^\Gamma(\vec{X}^f, \vec{t}^f)$ from Eq. (2.106) by an optimal replacing operator in a given subiteration $k + 1$ and time step n

$$\vec{t}^f_{k+1} = \vec{t}^f_k + \hat{F}_X(\vec{X}^f_{k+1} - \vec{X}^f_k) \tag{2.141}$$

This estimation can now be used as a dynamic Neumann boundary condition for the solid solver.

If the accessibility of the solid solver is limited, implementation of such a dynamic boundary condition is not impossible. However in such cases a variation of the approach is possible. Indeed, one can also construct a reduced order model for the solid solver operator $S^\Gamma(\vec{X}^f, \vec{t}^f)$ from Eq. (2.107)

$$\vec{X}^s_{k+1} = \vec{X}^s_k + \hat{S}_p(\vec{t}^s_{k+1} - \vec{t}^s_k) \tag{2.142}$$

Given the Dirichlet and Neumann boundary conditions one can now find a solution $\vec{t}, \vec{X}$ from both sets of equations (2.141) and (2.142). One could look at this approach as a monolithic approach, not of the actual equations (2.106)-(2.109) but of reduced order model equations (2.141) and (2.142). An approach in this category is followed in this work.

3.5 Transfer of quantities

3.5.1 Spatial interpolation

When choosing a partitioned approach, either with a staggered or an iterative scheme, a correct transfer of parameters at the boundary is essential [81, 82]. Dynamic and kinematic continuity (Eq. (2.108)-(2.109)) is required on the interface Γ. In order to make a distinction between the fluid side or wet side of the interface and the solid or dry side, the wet side is denoted with Γ^f and the dry side with Γ^s. Again the subscript '$_d$' will denote discretized quantities.

Conforming and matching interfaces When studying interfaces, distinction has to be made between conforming and non-conforming interfaces and between matching and non-matching interfaces. On a conforming interface the nodes at the interface match and the same discretization and interpolation is used on Γ^f and Γ^s. A non-conforming interface has a different discretization and/or interpolation order at both sides of the interface or the nodes at the interface do not match. Matching interfaces show no gaps at the interface, where at a non-matching interface gaps and/or overlaps are present.

Conservation of energy   Important in this coupling is the conservation of energy
at the interface. Consider, in a partitioned iterative approach, the displacement of
the structural interface side $\vec{u}^s$ is known and needs to be imposed on the wet side
of the interface by prescribing $\vec{u}^f$. Since the fluid solver and the solid solver can be
discretized in different ways the discretized kinematic boundary condition reads

$$\vec{u}_d^f = \bar{\bar{H}}_{\vec{u}} \vec{u}_d^s \tag{2.143}$$

with a transformation matrix $\bar{\bar{H}}_{\vec{u}}$. The discretization of $\vec{u}^f$ to $\vec{u}_d^f$ can be written
down using a shape function vector, a vector similar to the shape function matrix
used in the finite element approach

$$\vec{u}^f(x) = \bar{\bar{N}} \vec{u}_d^f = \sum_j N_{ij}^f(x) u_{j,d}^f \tag{2.144}$$

Essential in the coupling between differently discretized solid an fluid solvers
is the conservation of virtual work over the interface so that energy is preserved.
For the fluid solver this virtual work is given

$$
\begin{aligned}
\delta W^f &= \int_{\Gamma^f} (\vec{t}^f(x))^T \vec{u}^f(x) ds \\
&= \sum_i \sum_j \int_{\Gamma^f} t_i^f(x) N_{ij}^f(x) ds\, u_{j,d}^f \\
&= \sum_j F_j^f u_{j,d}^f \\
&= (\vec{F}^f)^T \vec{u}_d^f
\end{aligned}
\tag{2.145}
$$

with F_j^f the pressure force induced by the fluid in point j.

$$F_j^f = \sum_i \int_{\Gamma^f} t_i^f(x) N_{ij}^f(x) ds \tag{2.146}$$

Now $p^f(x)$ can also be written as a product of a shape function vector $\bar{\bar{D}}$ and the
discretized form $\vec{p}^f$.

$$t_i^f(x) = [\bar{\bar{D}} \vec{t}_d^f]_i = \sum_k t_{k,d}^f D_{ki}^f(x) \tag{2.147}$$

so that the force vector can be written

$$F_j^f = \sum_i \sum_k \int_{\Gamma^f} t_{k,d}^f D_{ki}^f(x) N_{ij}^f(x) ds \tag{2.148}$$

or defining $\bar{\bar{M}}^f = \int_{\Gamma^f} \bar{\bar{D}}^f \bar{\bar{N}}^f ds$ so that the force vector writes

$$\vec{F}^f = \bar{\bar{M}}^f \vec{t}_d^f \tag{2.149}$$

Hence the virtual energy on the wet interface is given $\delta W^f = (\vec{F}^f)^T \vec{u}^f$. Similarly one can write down the virtual energy delivered on the dry side of the interface as $\delta W^s = (\vec{F}^s)^T \vec{u}^s$ with a similar definition of the force vector $\vec{F}^s$

$$\bar{\bar{F}}^s = \bar{M}^s \vec{t}_d^s = [\int_{\Gamma^s} \bar{\bar{D}}^s \bar{\bar{N}}^s ds] \vec{t}_d^s \qquad (2.150)$$

Now the preservation of virtual energy $\delta W^f = \delta W^s$ or thus $(\vec{F}^f)^T \vec{u}^f = (\vec{F}^s)^T \vec{u}^s$ so that, taking Eq. (2.143) into account, yields

$$\vec{F}^s = \bar{\bar{H}}_{\vec{u}}^T \vec{F}^f \qquad (2.151)$$

So, $\bar{\bar{H}}_{\vec{t}} = \bar{\bar{H}}_{\vec{u}}^T$, meaning that for the transfer of pressure forces from Γ^f to Γ^s the same transformation matrix can be used, thus avoiding an expensive inverse.

Conservation of force Now one can show that as long as the column sum of $\bar{\bar{H}}_{\vec{u}}^T$ is 1, the sum of forces over Γ^f is equal to the sum of forces over Γ^s, thus preserving the total force over the interface

$$\sum_i F_{s,i} = \sum_i \sum_j H_{\vec{u},ij}^T F_{f,j} = \sum_j F_{f,j} \sum_i H_{\vec{u},ij}^T = \sum_j F_{f,j} \qquad (2.152)$$

Note that a column sum of $\bar{\bar{H}}_{\vec{t}}$ is equal to a row sum of $\bar{\bar{H}}_{\vec{u}}$.

Algorithms for $\bar{\bar{H}}$ The most simple formulation of $\bar{\bar{H}}_{\vec{u}}$ is obtained by using the nearest neighbor interpolation. For each fluid node x^f of Γ^f the closest structural node x^s on Γ^s is located. The value of the displacement at x^f is then taken the same as the displacement at x^s. As with this method the row sum of $\bar{\bar{H}}_{\vec{u}}$ is one, the global force is conserved. This approach is used in MpCCI for example.

Interpolations using Lagrange multipliers or residual weighted methods are also an option. Or methods using the area of intersection of the cells or elements of both meshes. Many different possibilities exist to find the transformation matrix $\bar{\bar{H}}$, an overview is given in [82].

3.5.2 Temporal interpolation

At least as much effort that went to the spatial interpolation of quantities at the interface needs to go to the temporal preservation of quantities. Indeed, Vierendeels et al. [83] showed that a different temporal discretization between the fluid solver and the solid solver causes instabilities in a simplified model of mechanic valve FSI-problems.

Consider a matching and conforming interface, so that no spatial interpolation is required, but with a fluid solver using a different temporal discretization scheme

than the structural solver. The fluid solver calculates the temporal derivative of a scalar ϕ as $\dot{\phi}_{f,n} = f(\phi_{f,n}, \phi_{f,n+1})$, where the solid solver uses the function $\dot{\phi}_{s,n} = s(\phi_{s,n}, \phi_{s,n+1})$.

Consider an equilibrium position $X_{n-1} = X_{f,n-1} = X_{s,n-1}$ of the interface as time t_{n-1} when the interface position at time t_n is calculated in the structural solver, denoted $X_{s,n}$. When this position is passed on to the fluid solver as position $X_{f,n} = X_{s,n}$, this does not necessarily mean that the displacement velocity at the interface is the same in the fluid solver as the structural solver.

Indeed the displacement velocity is calculated from the given positions and the previous positions of the interface. In the fluid solver the velocity will be calculated as $\dot{X}_{f,n} = f(X_{f,n}, X_{f,n-1}, X_{f,n-2})$, whereas in the solid solver the velocity is quantified as $\dot{X}_{s,n} = s(X_{s,n}, X_{s,n-1}, X_{s,n-2}) \neq \dot{X}_{f,n}$. Hence the velocities at the wet and dry side of the interface differ.

Unfortunately not much can be done to avoid instabilities related to this discrepant temporal discretization schemes. This issue will be further addressed in the next chapter.

3

Implementation and validation of fluid-structure interaction

In this chapter an overview is given of the implementation and validation of the fluid-structure interaction code developed during the research presented in this dissertation. The first section highlights the general fluid-structure interaction issues as geometry construction and data transfer. A next section describes the reduced order model approach more in detail, for both an accessible structural solver and a black box structural solver. Two validation computations were performed. In section 3 the wave propagation computation in a reflectionless straight compliant tube is given, while the last section gives the details of a benchmark FSI-case, proposed by Turek and Hron [84] [1].

1 Implementation of a generic fluid-structure interaction problem

1.1 Summary of choices

In the previous chapter a wide variety of possible fluid-structure interaction approaches was given. In this work the iterative, partitioned solver approach was chosen, with a black box fluid solver and a black box structural solver. Fluent software (ANSYS, Inc.) was used as a fluid solver and Abaqus software (Simulia, Inc.) was used to solve the structural problem. The arbitrary Lagrangian-Eulerian approach was used to deal with the moving structural grid for the fluid solver. In this chapter the used coupling algorithm that will be explained in more detail.

The general geometry for such problems is given in Fig. 3.1, dividing the computational domain in a fluid part Ω^f, solved by the fluid solver, and a structural part Ω^s, solved by the structural solver. As we choose to use the ALE-formulation, the only common part between Ω^f and Ω^s is the interface Γ.
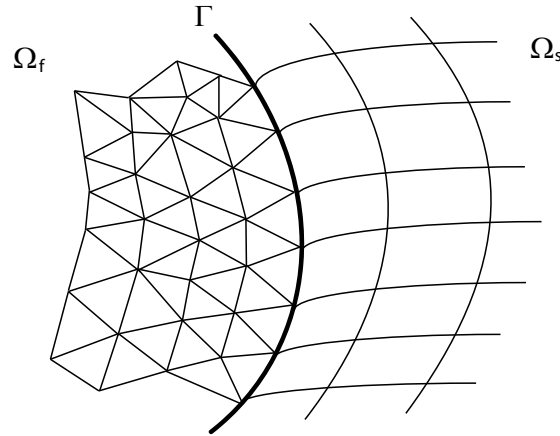
Figure 3.1: General geometry of the computational domain for an FSI problem using an ALE approach with partitioned solvers.

Generally, the fluid-structure interaction equations to be solved can be written as

$$
\begin{aligned}
F(X^f, p^f) &= 0 \quad in\ \Omega^f, & (3.1) \\
S(X^s, p^s) &= 0 \quad in\ \Omega^s, & (3.2) \\
p^f &= p^s \quad on\ \Gamma, & (3.3) \\
X^f &= X^s \quad on\ \Gamma & (3.4)
\end{aligned}
$$

where X^f and p^f denote the flow velocity and the surface tension distribution vectors in the discretized fluid domain Ω^f. The flow domain is described by equations $F(X^f, p^f) = 0$. Similarly, X^s and p^s are the position and the pressure vectors in the discretized structural domain Ω^s, described by equations $S(X^s, p^s) = 0$. p^f and p^s denote the tension forces on the interface Γ per unit area, on the fluid side and the structural side, respectively. These forces are functions of X^f, p^f and X^s, p^s, respectively. Note that X^f, p^f, X^s and p^s are vectors, carrying the information in discretized points in the domain, however in this chapter the $\bar{}$and $_d$-signs are omitted. Secondly, note that the fluid solver and the structural solver are written through their function on the interface variables, however the superscript 'Γ' was also omitted. In this section the implementation of this generic FSI problem will be discussed.

1.2   Construction of the computational domain

The computational domain is the union of Ω^f and Ω^s, while the interface is the common face Γ. As we choose to use a matching grid at the interface Γ, the geometry of the fluid part and the structural part was constructed in one grid generating package, to make sure that the nodes at the interface have the exact same position on the fluid as on the structural side and that the connectivity between the nodes are identical. For the applications in this thesis Gambit 2.2 (ANSYS, Inc.) was used as a mesh generator package. The geometry was generated with a fluid volume Ω^f and a structural volume Ω^s, where both volumes were exported separately in a mesh file to be used as an input to Fluent software.

From this point the mesh-file containing the *fluid grid* Ω^f can be directly imported in Fluent 6.3 (ANSYS, Inc.) to start the fluid problem definition. In Fluent the solver-information, boundary and initial conditions, fluid properties, ... are defined, if necessary using a user defined function (UDF). At this point the dynamic meshes are defined too. Two files are generated, one which will be used in the fluid-structure interaction calculations and one used for the FSI-initialization, as will be discussed in the next paragraph.

In order to do the same for the structural problem definition the mesh-file containing the *structural grid* Ω^s needs to be imported in Fluent first, where it can be directly exported to an input-file for Abaqus containing the grid and the connectivity. From the geometry info imported in Abaqus the boundary and initial conditions are applied, as well as the material laws. If necessary a user subroutine is used to obtain the desired material properties if these material properties are not directly available in the Abaqus material library. Three files are generated. First an input file is generated used during the initialization procedure, an other file is generated used for the first time step's calculation and the third file is a restart file,

which is used to continue the calculation where the previous time step's calculation stopped. More details about these restart files can be found in the Abaqus manual [85].

1.3 Initialization procedure

At this point an initialization procedure is needed to establish the correspondence between the node numbering and face numbering in Abaqus and Fluent at the interface Γ. The assessment starts with calling Fluent and writing a file containing the nodes and node-coordinates of the interface Γ as shown below. Another file containing the face numbers and the center point coordinates of the faces is also generated. Secondly Abaqus is called and similar files are generated for the structural side of the interface Γ.

> nokn=1, x=0.600000, y=0.210000
> nokn=2, x=0.600000, y=0.205000
> nokn=3, x=0.594986, y=0.210000
> nokn=4, x=0.600000, y=0.200000
> nokn=5, x=0.600000, y=0.195000
> nokn=6, x=0.600000, y=0.190000
> nokn=7, x=0.589971, y=0.210000
> nokn=8, x=0.594986, y=0.190000
> nokn=9, x=0.584957, y=0.210000
> ...

Next the node correspondence is assessed. Starting with a fluid node number, a loop over the node numbers of the structural interface side is performed, to establish which undeformed Abaqus node number's position is closest to the initial Fluent node number's position. As the two grids are conform, the Fluent node numbers position and the Abaqus node numbers position will be the same, apart from errors due to rounding off. This is done for all interface nodes and the result is written to a file, giving the list of Abaqus node numbers "a" and the corresponding Fluent node number "f", as shown below.

> a 1 f 6
> a 2 f 41
> a 3 f 7
> a 4 f 2
> a 5 f 10
> a 6 f 8
> a 7 f 5
> a 8 f 3

a 9 f 9

...

A similar routine is called to assess the correspondence for the faces numbers. As these routines will be called only once at the start of the calculation, optimization of the routines is not very relevant. The assessment of the corresponding nodes and faces at the wet and the dry side of the interface means that a nearest neighbor algorithm, as described in section 3.5, is used to transfer data at the interface.

1.4 Face force transfer

Next the coupling of the forces $p^f = \bar{\bar{H}}_p p^s$ per surface area on the interface Γ is needed. The forces p_n on a surface with normal vector $\vec{n}$ in a viscid, incompressible, laminar flow of a Newtonian fluid were described in the previous chapter

$$p_n = -p\vec{n} + \mu \left(\nabla \vec{v} + (\nabla \vec{v})^T \right) \cdot \vec{n} \tag{3.5}$$

Eq. (3.5) is used to quantify the forces on the interface induced by the fluid.

However when coupling the force vector p to the structural side of the interface, the force vector needs to be decomposed in a component p_n normal to the interface and a component p_t tangential to the interface. Indeed, the traction force user subroutine $UTRACLOAD$ does only allow forces that are parallel to the surface, while the pressure user subroutine $DLOAD$ results in forces perpendicular to the interface [85].

The normal component of the interface force vector

$$p_n = -p\vec{n} + \left\{ \left[\mu \left(\nabla \vec{v} + (\nabla \vec{v})^T \right) \cdot \vec{n} \right] \cdot \vec{n} \right\} \vec{n} \tag{3.6}$$

is transferred to Abaqus as a corrected pressure p_{p_n}

$$p_{p_n} = -p + \left[\mu \left(\nabla \vec{v} + (\nabla \vec{v})^T \right) \cdot \vec{n} \right] \cdot \vec{n} \tag{3.7}$$

and applied through the pressure module $DLOAD$.

The tangential component of the interface force vector

$$p_t = \mu \left(\nabla \vec{v} + (\nabla \vec{v})^T \right) \cdot \vec{n} - \left\{ \left[\mu \left(\nabla \vec{v} + (\nabla \vec{v})^T \right) \cdot \vec{n} \right] \cdot \vec{n} \right\} \vec{n} \tag{3.8}$$

on the other hand is applied through the $UTRACLOAD$ module. As interpolation from Γ^f to Γ^s a nearest neighbor algorithm is used to construct $\bar{\bar{H}}_p$.

1.5 Displacement transfer

At this point the positions $X^f = \bar{\bar{H}}_X X^s$ on the interface Γ need to be matched. We imposed a kinematic constrained, meaning that the nodes on the interface on the

fluid-side and the structural side are kept on the same position, using the Dynamic Mesh possibilities in Fluent, combined with a user defined function to impose the position of the nodes from Abaqus on the Fluent mesh. A nearest neighbor algorithm is used to establish $\bar{\bar{H}}_X$. This approach might seem fulfilling and straightforward, however some limitations are related to it. These limitations are sensitivities for all partitioned solver approaches. They will be addressed in section 1.7

1.6   Convergence and output

The residual is quantified as the L_1-norm of the pressure changes on the interface and the L_1-norm of the relative position changes over the last subiteration. The residuals are calculated after each subiteration k from the third subiteration on.

$$\epsilon_p \quad = \quad \frac{1}{N_{f,i}} \sum_{i=1}^{N_{f,i}} \left\| p_k^i - p_{k-1}^i \right\| \tag{3.9}$$

$$\epsilon_X \quad = \quad \frac{1}{N_{n,i}} \sum_{i=1}^{N_{n,i}} \left\| \vec{X}_k^i - \vec{X}_{k-1}^i \right\| \tag{3.10}$$

$N_{n,i}$ denoting the number of nodes of the interface, $N_{f,i}$ denoting the number of faces of the interface. When both norms are lower than the limit set before, convergence is said to be reached and the output is generated.

As output, the flow and pressure field in the fluid domain Ω^f are written with Fluent, as well as the strains and stresses in the structural domain Ω^s with Abaqus. Any other required output is possible as well, such as e.g. lift and drag forces on the structural domain, as long as it is supported by Fluent or Abaqus.

1.7   Limitations

1.7.1   Interface interpolation

However the coupling is not as simple as all that. Indeed, Fluent uses only linear elements, where as Abaqus needs quadratic elements, as first order elements have a higher stiffness than the imposed Young modulus [85]. This means a non-matching interface is inevitable when coupling both programs in an FSI code, as shown in Fig. 3.2.

A non-matching, non-conforming interface due to a use of quadratic elements in Abaqus and linear elements in Fluent and the difference in discretization between the two solvers can lead to a creation or annihilation of virtual energy when transferring positions and face forces between Abaqus and Fluent. This could be tackled by using an extra routine when transferring the position vector from Abaqus to Fluent and the surface tension from Fluent to Abaqus. In this routine,
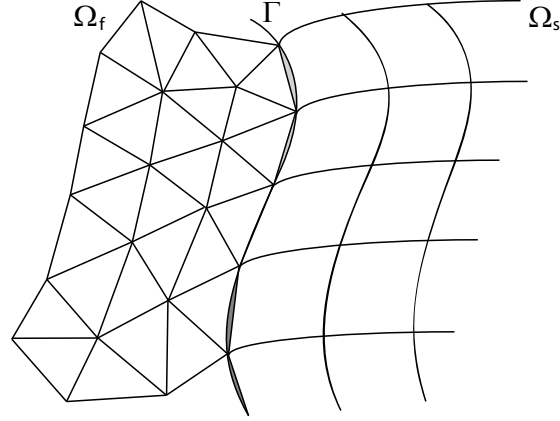
Figure 3.2: Non-matching mesh due to linear elements in the fluid solver and quadratic elements in the structural solver. Light gray: gap; dark gray: overlap.

the virtual energy on the fluid side and the structural side of the interface could be calculated

$$\delta W^f = \delta W^s \tag{3.11}$$

$$\int_{\Gamma^f} (p^f)^T \Delta X^f ds = \int_{\Gamma^s} (p^s)^T \Delta X^s ds \tag{3.12}$$

so that an alteration in position and face force could be performed in order to keep both sides of the equation in balance. Implementation of such a routine is not straight-forward, as is shown by De Boer [82]. Since physical and accurate solutions were found (see section 3 and 4), no such a subroutine was implemented and the nearest neighbor transformation matrix $\bar{\bar{H}}$ was considered to be sufficient.

1.7.2 Temporal discretization

Related to the issues discussed in the previous paragraph, besides the spatial fit at the interface, also the temporal fit needs to be considered. The implicit calculations in Abaqus 6.5 use a Hilber-Hughes-Taylor temporal discretization scheme, given in Eq. (3.13).

$$\phi_{n+1} = \phi_n + \frac{\Delta t}{1+\alpha}\dot{\phi}_n + \frac{1}{2}\left(\frac{\Delta t}{1+\alpha}\right)^2 [(1-2\beta)\ddot{\phi}_n + 2\beta\ddot{\phi}_{n+1}] \tag{3.13}$$

$$\dot{\phi}_{n+1} = \dot{\phi}_n + \frac{\Delta t}{1+\alpha}[(1-\gamma)\ddot{\phi}_n + \gamma\ddot{\phi}_{n+1}] \tag{3.14}$$

An extra restriction is put on parameters α, β and γ

$$\beta \;\; = \;\; \frac{(1-\alpha)^2}{4} \tag{3.15}$$

$$\gamma \;\; = \;\; \frac{1-2\alpha}{2} \tag{3.16}$$

with $\alpha \in [-\frac{1}{3}, 0]$. The smaller α, the more numerical damping that is imposed [86].

However, Fluent 6.2 with moving mesh enabled uses a first order backward Euler scheme, given by

$$\phi_{n+1} = \phi_n + \Delta t \dot{\phi}_{n+1} \tag{3.17}$$

As previously stated by Vierendeels et al. [83] an inconsistency in time discretization scheme between the fluid solver and the structural solver used in a strongly coupled FSI-system might induce wiggles in the solution. We did observe these wiggles in some cases we studied. As the wiggles are a consequence of the choice of software package used, not much could be done to prevent them but to use a steady formulation for the structural part. This means that we neglect the inertia with respect to the pressure-induced forces in the structural domain.

1.7.3   Computational cost

A final limitation of the code is the rather high computational cost needed to solve a fluid-structure interaction with partitioned solvers. Each FSI-time step the fluid problem and the structural problem are solved several times separately. This means that each FSI time step will be several times more time consuming than solving just the fluid problem with rigid walls. Extra computational time will also be used by a stabilizing algorithm if it is implemented, often needing the inverse of a Jacobian. It is essential to first decide that this extra cost is justified. For biomedical problems however the wall positions are too big and the fluid structure interaction needs to be taken into account.

2   Reduced order model for the coupling

Vascular FSI problems are often very strongly coupled problems. As the vessels studied are usually rather long, compared to the diameter, with relatively high compliant walls, where the density of the blood and the vessel wall are about the same, instabilities are inevitable when a weak coupling is used. The coupling method used in the fluid-structure interaction algorithm implemented in the research presented in this dissertation uses reduced order models of the fluid and structural

solver, which will be explained in this chapter. As already highlighted in the previous chapter, a reduced order model is an operator replacing the complex fluid or solid solver operator on the interface. A reduced order model is constructed using computed input and output pairs of the original solver, as will be elaborated in the next section.

2.1 Building a reduced order model

The reduced order models are built up during the coupling iterations. After k subiterations, where the fluid solver is called k times, k interface positions $X_i, i = 1, .., k$ are known to correspond with k stress distributions $p_i, i = 1, .., k$ on the interface, calculated by the fluid solver.

When at least two couples (X_i, p_i) are calculated from the interface positions $X_{i=1,...,k}$, $k - 1$ displacement modes for the fluid solver $\Delta X_j^f = X_j^f - X_k^f, j = 1, .., k-1$ can be calculated. With these displacement modes a displacement modes matrix V can be constructed as given in Eq. (3.18).

$$V = \begin{bmatrix} \Delta X_1^f \\ \vdots \\ \Delta X_j^f \\ \vdots \\ \Delta X_{k-1}^f \end{bmatrix} \tag{3.18}$$

Similarly from the k known stress distributions on the fluid-structure interface $k-1$ corresponding stress distribution modes $\Delta p_j^f = p_j^f - p_k^f, j = 1, .., k - 1$ are calculated, with which a stress distribution modes matrix W can be constructed.

$$W = [\Delta p_1^f \cdots \Delta p_j^f \cdots \Delta p_{k-1}^f] \tag{3.19}$$

At this point any given arbitrary displacement ΔX^f can be approximated by a linear combination of the displacement modes $\Delta X_j^f, j = 1, .., k - 1$

$$\Delta X = \sum_{m=1}^{k-1} \alpha_m \Delta X_m^f + \Delta X_{corr} \tag{3.20}$$

where α_m are actually the coordinates of ΔX in set V_m. As the number of displacement modes is much smaller than the dimension of ΔX, a correction term ΔX_{corr} is to be added. If the displacement modes are well chosen, ΔX_{corr} is small, so that ΔX can be approximated by $\Delta \tilde{X}$.

$$\Delta X \approx \Delta \tilde{X} = \sum_{m=1}^{k-1} \alpha_m \Delta X_m^f \tag{3.21}$$

Again as the dimension of ΔX is much larger than the number of displacement modes, this problem is overdetermined for the coordinates α_m, so that they can be found using a least square approach, yielding α^T

$$
\begin{bmatrix} \alpha_1 \\ \vdots \\ \alpha_{k-1} \end{bmatrix} = \begin{bmatrix} & \vdots & \\ \cdots & \langle \Delta X_i, \Delta X_j \rangle & \cdots \\ & \vdots & \end{bmatrix}^{-1} \begin{bmatrix} \Delta X_1^T \\ \vdots \\ \Delta X_{k-1}^T \end{bmatrix} \Delta X \qquad (3.22)
$$

This least square approach, minimizing the correction term ΔX_{corr}, is actually nothing else than finding the optimal projection of the $\mathbb{R}^n$-dimensional vector ΔX on the set of $k-1$ $\mathbb{R}^n$-dimensional vectors ΔX_m^f.

The coordinates α_m denote the contribution of the mth displacement mode ΔX_m^f to the displacement ΔX. The corresponding pressure change, induced by the displacement ΔX of the interface, can thus be approximated as the same linear combination of the pressure modes Δp_m^f

$$
\Delta p \approx \sum_{m=1}^{k-1} \alpha_m \Delta p_m^f = W \alpha^T \qquad (3.23)
$$

After substitution of Eq. (3.22) in Eq. (3.23)

$$
\Delta p = \begin{bmatrix} \Delta p_1^f \cdots \Delta p_{k-1}^f \end{bmatrix} \begin{bmatrix} & \vdots & \\ \cdots & \langle \Delta X_i, \Delta X_j \rangle & \cdots \\ & \vdots & \end{bmatrix}^{-1} \begin{bmatrix} \Delta X_1^T \\ \vdots \\ \Delta X_{k-1}^T \end{bmatrix} \Delta X
$$
$$
(3.24)
$$

the Jacobian $\hat{F}_X$ of the reduced order model of the fluid solver is found

$$
\hat{F}_X = \begin{bmatrix} \Delta p_1^f \cdots \Delta p_{k-1}^f \end{bmatrix} \begin{bmatrix} & \vdots & \\ \cdots & \langle \Delta X_i, \Delta X_j \rangle & \cdots \\ & \vdots & \end{bmatrix}^{-1} \begin{bmatrix} \Delta X_1^T \\ \vdots \\ \Delta X_{k-1}^T \end{bmatrix} \qquad (3.25)
$$

The reduced order model of the fluid solver, after k subiterations, can be written as

$$
\hat{p}_{k+1}^{n+1} = p_k^{n+1} + \hat{F}_X (X_{k+1}^{n+1} - X_k^{n+1}) \qquad (3.26)
$$

2.2 High accessibility of the structural solver

As we used Fluent as a black box fluid solver, we can not retrieve nor construct the Jacobian F_X needed for the implicit solving of the structural problem

$$G(X_{k+1}^{n+1}, p_{k+1}^{n+1}) = 0 \qquad (3.27)$$

However one can use the reduced order model of the fluid solver

$$\hat{p}_{k+1}^{n+1} = \hat{F}\left(X_{k+1}^{n+1}\right) \qquad (3.28)$$

in order to solve the structural solver in an implicit way.

$$G(X_{k+1}^{n+1}, \hat{p}_{k+1}^{n+1}) = G\left[X_{k+1}^{n+1}, \hat{F}\left(X_{k+1}^{n+1}\right)\right] = 0 \qquad (3.29)$$

From Eq. (3.29) one can assess X_{k+1}^{n+1} iteratively, for example using a newtonian method

$$\begin{aligned} &G(X_{k+1,l+1}^{n+1}, \hat{p}_{k+1,l+1}^{n+1}) \\ &\approx G(X_{k+1,l}^{n+1}, \hat{p}_{k+1,l}^{n+1}) + \left[\frac{\partial G}{\partial X} + \frac{\partial G}{\partial \hat{p}}\frac{\partial \hat{p}}{\partial X}\right]\left(X_{k+1,l+1}^{n+1} - X_{k+1,l}^{n+1}\right) = 0 \end{aligned} \qquad (3.30)$$

for the lth iteration of the structural solver to $X_{k+1,l+1}^{n+1}$, with $\hat{P}^l = P_k^f + \hat{F}_X^k(X^l - X_k^f)$, where k denotes the iteration on the partitioned level. Or written as Eq. (3.31) since we can approximate the Jacobian $\frac{\partial \hat{p}}{\partial X}$ of the fluid solver by the Jacobian $\hat{F}_X$ of the reduced order model for the fluid solver.

$$\begin{aligned} &G(X_{k+1,l+1}^{n+1}, \hat{p}_{k+1,l+1}^{n+1}) \\ &\approx G(X_{k+1,l}^{n+1}, \hat{p}_{k+1,l}^{n+1}) + \left[\frac{\partial G}{\partial X} + \frac{\partial G}{\partial \hat{p}}\hat{F}_X^k\right]\left(X_{k+1,l+1}^{n+1} - X_{k+1,l}^{n+1}\right) = 0 \end{aligned} \qquad (3.31)$$

This equation actually means that the structural solver iteratively calculates the position of the interface, initially given the stress distribution from Fluent, but each consecutive iteration of the structural solver the imposed pressure at the boundary is updated using the reduced order model of the fluid solver. The imposed stress distribution at the interface in structural iteration l is altered in such a way that, through the reduced order model of the fluid solver, the change in pressure induced by the displacement calculated in the structural iteration $l-1$ is taken into account.

In order to be able to start constructing the modes, two iterations are needed to create two sets (X_1, p_1) and (X_2, p_2). This can be done using a chosen underrelaxation factor ω for the fist two iterations. This is shown in figure 3.3. Each time step the algorithm is build up by the following steps :

1. Each time step starts with the initial guess of the position of the interface X_1 based on the results of the two previous time steps.
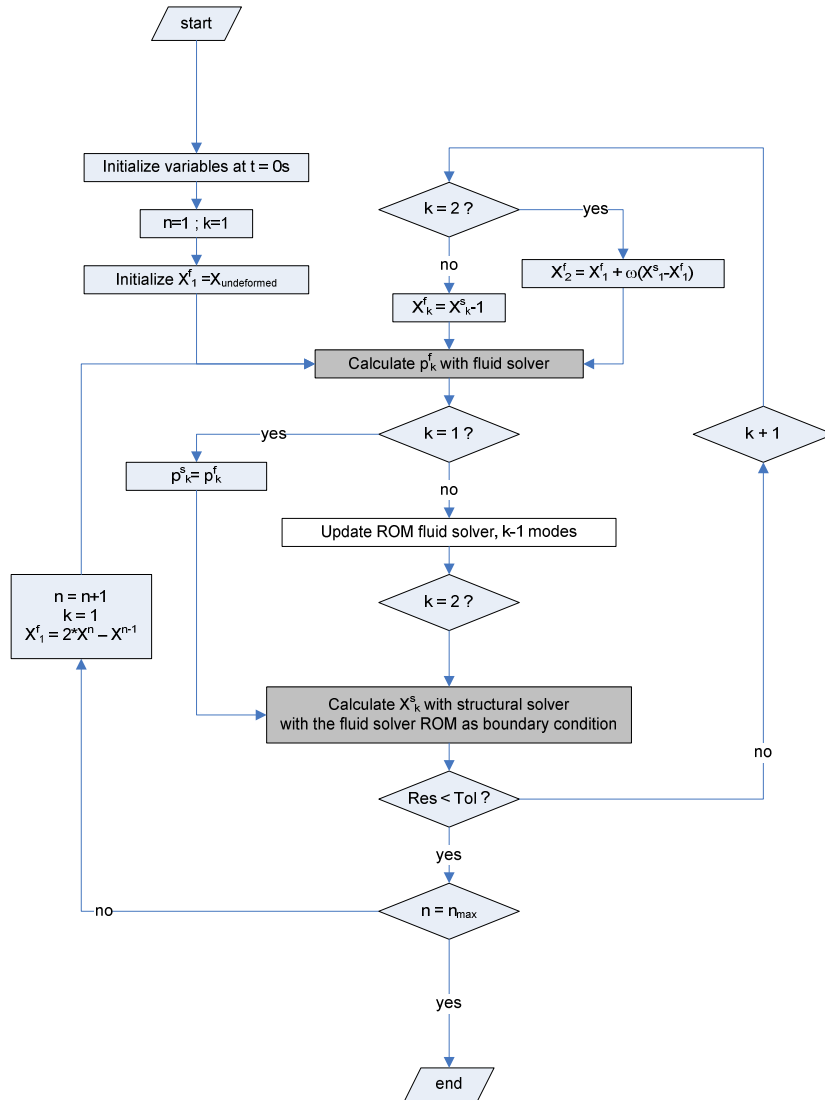
Figure 3.3: Flow chart of the reduced order model approach where the structural solver is highly accessible, so that only a reduced order model of the fluid solver is needed (white box) in order to realize a strong coupling between a fluid solver and structural solver (dark boxes).

2. The according stress distribution p_1 is calculated with the fluid solver.

3. With this stress distribution the new interface position X_1^s is calculated with the structural solver.

4. The interface position X_2 of the new subiteration is calculated using a chosen underrelaxation factor, eg. 0.05.

5. The FSI-loop is started with $k = 2$.

6. The fluid solver is used to calculate the corresponding stress distribution p_k

7. The reduced order model is build with $k - 1$ modes.

8. Using equation (3.31) the structural solver iterates to the new interface position X_{k+1}^f.

9. The residual is calculated.

10. If convergence is not achieved, k is updated to $k + 1$ and everything is repeated from step 6.

2.3 Limited accessibility of the structural solver

It is clear that in the method proposed in the previous paragraph a structural solver is needed with high accessibility. One has to be able to apply the reduced order model dynamically as a boundary condition on the interface. This requires for example that during the structural solvers iterations, the immediate unknown position change of the interface X^l has to be accessible in the boundary condition calculation. In this research we used Abaqus as a commercially available structural solver. Since the accesibility of the solver is limited a slightly different approach was used for the FSI calculation in this work.

A reduced order model for the fluid solver is constructed, as in the previously described case using a high accessible solid solver. After k calls of the fluid solver k interface positions X_k^f are known to correspond with k stress distributions p_k^f, resulting in the reduced order model

$$\hat{p}_{k+1}^f = p_k^f + \hat{F}_X(X_{k+1}^f - X_k^f) \tag{3.32}$$

In order to distinguish between the couples (X_k^f, p_k^f) of the fluid solver and the couples $(p_{k'}^s, X_{k'}^s)$ related to the structural solver, the superscript $'^{n+1}'$ is omitted and superscripts $'^f'$ and $'^s'$ are introduced for the fluid solver and the structural solver respectively.

Similarly, after k' calls of the structural solvers, k' stress distributions $p_{k'}^s$ are known to correspond with k' interface positions $X_{k'}^s$. A reduced order model for

the structural solver (3.33) can be constructed in the same way as it was described for the fluid solver in the first paragraph of this chapter.

$$\hat{X}^s_{k'+1} = X^s_{k'} + \hat{S}_p(p^s_{k'+1} - p^s_{k'}) \tag{3.33}$$

Solving an FSI problem in this case means finding a set of $\hat{p}$ and $\hat{X}$ fulfilling both equations

$$\hat{p} \quad = p^f_{k+1} \quad = p^s_{k'+1} \tag{3.34}$$

$$\hat{X} \quad = X^f_{k+1} \quad = X^s_{k'+1} \tag{3.35}$$

Solving equations (3.32) and (3.33) to $\hat{X}$ results in

$$\hat{X} = \left(I - \hat{S}_p\hat{F}_X\right)^{-1} \left[X^s_{k'} + \hat{S}_p\left(p^f_k - p^s_{k'} - \hat{F}_X X^f_k\right)\right] \tag{3.36}$$

Solving to $\hat{p}$ yields

$$\hat{p} = \left(I - \hat{F}_X\hat{S}_p\right)^{-1} \left[p^f_k + \hat{F}_X\left(X^s_{k'} - X^f_k - \hat{S}_p p^s_{k'}\right)\right] \tag{3.37}$$

The equations (3.36) and (3.37) result in a positions of the interface $\hat{X}$ and a stress distribution $\hat{p}$ in equilibrium with both reduced order models of both the fluid solver and the structural solver. They can be used to update the interface stress distribution from the fluid solver going to the structural solver and the interface position from the structural solver going to the fluid solver.

This can be done for structural solvers and fluid solvers with low accessibility, such as black box commercially available solvers. The only requirement for the fluid solver is that it has to be able to impose a prescribed motion on the interface boundary and that the stresses on the interface have to be able to be written to a file. Both conditions are fulfilled by Fluent. The requirements for the structural solver are similar. It has to be possible to impose a stress distribution on the interface. It also has to be possible to write the computed positions of the nodes to a file. Both of these conditions are met by Abaqus.

In order to be able to start constructing the modes, also here two iterations are needed to create twice two sets (X^f_1, p^f_1), (X^f_2, p^f_2) and (X^s_1, p^s_1), (X^s_2, p^s_2). This can be done using a chosen underrelaxation factor ω for the first two iterations. This is shown in figure 3.4. Each time step the algorithm is built up by the following steps :

1. Each time step starts with the initial guess of the position of the interface X^f_1 based on the results of the two previous time steps.

2. The according stress distribution p^f_1 is calculated with the fluid solver.
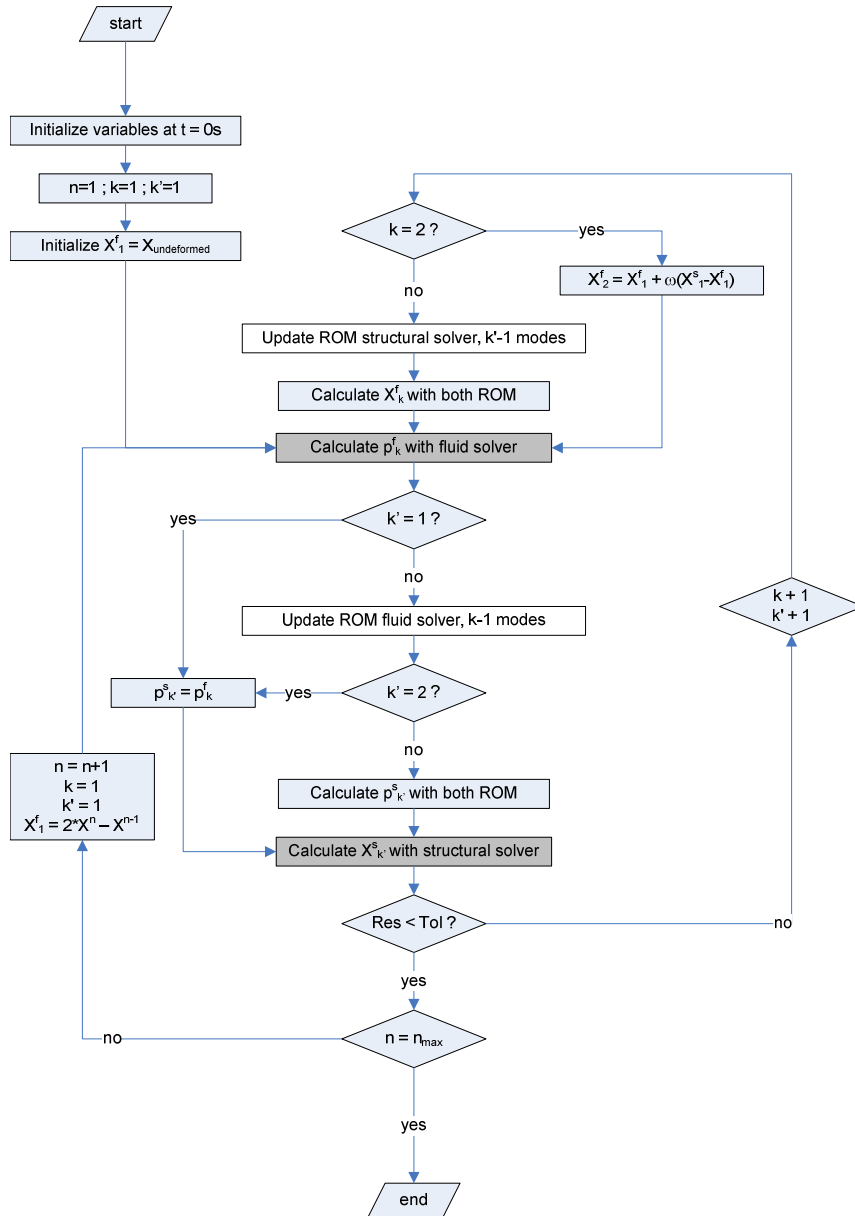
Figure 3.4: Flow chart of fluid-structure interaction approach using two reduced order models (white boxes) in order to realize a strong coupling between a fluid solver and structural solver (dark boxes).

3. As an estimation of the stress distribution to be used as input for the structural solver $p_1^s = p_1^f$ is taken.

4. With this stress distribution the new interface position X_1^s is calculated with the structural solver.

5. The interface position X_2^f of the new subiteration is calculated using a chosen underrelaxation factor ω, eg. 0.05, yielding $X_2^f = X_1^f + \omega(X_1^s - X_1^f)$.

6. The reduced order model of the fluid problem is build with 1 mode.

7. The fluid solver is used to calculate the stress distribution p_2^f corresponding to X_2^f.

8. As an estimation of the stress distribution to be used as input for the structural solver $p_2^s = p_2^f$ is taken.

9. The structural solver is used to calculate the interface position X_2^s corresponding to p_2^s.

10. The FSI-loop is started with $k = 3$ and $k' = 3$.

11. The reduced order model of the structural solver is build with $k' - 1$ modes.

12. An updated X_k^f is calculated in equilibrium with both reduced order models.

13. The fluid solver is used to calculate the stress distribution p_k^f corresponding to X_k^f.

14. The reduced order model of the fluid solver is build with $k - 1$ modes.

15. An updated $p_{k'}^s$ is calculated in equilibrium with both reduced order models.

16. The structural solver is used to calculate the interface position $X_{k'}^s$ corresponding to $p_{k'}^s$.

17. The residual is calculated.

18. If convergence is not achieved, k is updated to $k + 1$, k' is updated to $k' + 1$ and everything is repeated from step 6.

Here, the reduced order model is used to stabilize a coupling with positions and pressures on the interface, as will be treated in the next section. the reduced order model is not limited to these applications however. One can also enter the temperature distribution on the wall in the interface when temperature plays a role in the coupling.

3 Wave propagation in a straight compliant vessel - comparison of two FSI approaches

3.1 Aim

In the previous sections the implementation of the FSI code was discussed. It is essential to validate the code first, in order to check the reliability of the obtained results. In this first benchmark problem, the reduced order model is compared with the results obtained with an Aitken acceleration approach. Both FSI methods were used to simulate the wave propagation in a straight compliant vessel in order to compare the reliability and the efficiency of the methods.

3.2 Geometry and boundary conditions
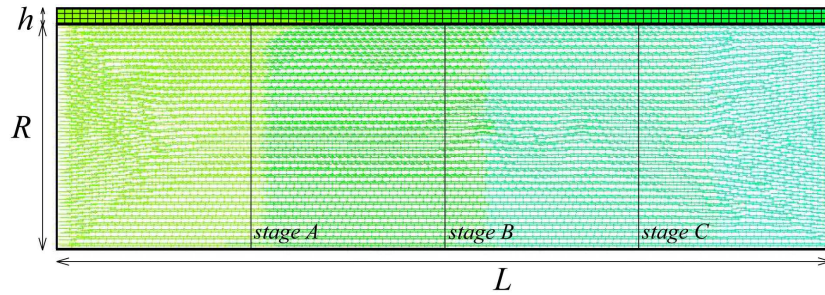
Figure 3.5: The computational domain. Stages A, B and C are used for analysis of the results.

The geometry is a two-dimensional axi-symmetrical straight tube shown in figure 3.5. The tube has length L $50mm$, radius R $14.5mm$ and wall thickness h $0.85mm$, a geometry that matches the ascending human aorta.

The fluid domain is meshed using 3468 nodes and 6674 triangular cells. The structural domain was meshed using 1107 nodes and 300 quadratic, hybrid, reduced, rectangular elements ($CAX8RH$).

Blood, is modeled as a Newtonian fluid [87] with density $\rho^f = 1050 kg/m^3$ and dynamic viscosity $\mu^f = 2.678 \cdot 10^{-3} kg/m.s$. The wall is modeled as a linear-elastic material with Young modulus $E^s = 4.0 \cdot 10^5 Pa$ and Poisson modulus $\nu^s = 0.49$. Large deformation theory is used in the finite element analysis to calculate the deformation of the wall.

A uniform, pulsatile inlet velocity profile with period $0.2s$ is prescribed at the inlet

$$v^f(t, 0, y) = 0.01 \cdot cos^2(\pi\ t/0.2) \tag{3.38}$$

At the downstream end of the computational domain a non-reflecting boundary condition is imposed,

$$p^f(t, 0.05, y) = p_0^f + \rho c(v^f(t, 0.05, y) - v_0^f)) \qquad (3.39)$$

so that no backward traveling waves are present in the tube. p_0^f and v_0^f denote the equilibrium pressure and flow velocity respectively, which are denoted zero in this simulation. At the other boundaries a non-slip condition is imposed.

A time step $5ms$ is used for the calculations and 300 time steps were calculated. Abaqus 6.5 (Simulia, Inc.) was used to solve the structural problem, while Fluent 6.2 (ANSYS, Inc.) was used as fluid-solver, both commercially available state-of-the-art simulation packages.

3.3 Two FSI approaches

3.3.1 Reduced order models

The first FSI approach which is used in this study is the reduced order model approach, where both the fluid solver and the solid solver are inaccessible. Hence, the coupling described in section 2.3 will be used, combined with the approaches elaborated in the previous section 1. An other FSI approach using Aitken acceleration was implemented. As such the efficiency of the reduced order model approach could be compared with the Aitken approach. The basics of the Aitken acceleration approach will be highlighted more elaborately in the next paragraph.

3.3.2 Aitken-acceleration

The Aitken-acceleration looks at the fluid-structure interaction problem as a fixed point problem that has to be solved each time step n. We are using partitioned solvers, we can represent the black box fluid solver F and structural solver S as

$$\begin{array}{rcl} p^n & = & F(X^n) \\ X^n & = & S(p^n) \end{array} \qquad (3.40)$$

where X^n denotes the position of the interface at time step n and p^n the pressure distribution at the interface at the same time step. For each time step a solution has to be found, in equilibrium with these two equations. After rewriting of the two equations (3.40), one can see that the FSI-problem at time step n can also be rewritten as

$$\begin{array}{rcl} F[S(p^n)] & = & F \circ S(p^n) = p^n \\ S[F(X^n)] & = & S \circ F(X^n) = X^n \end{array} \qquad (3.41)$$

which are two fixed point problems, or rewritten in a root's problem form as

$$\begin{array}{rcl} F \circ S(p^n) - p^n & = & 0 \\ S \circ F(X^n) - X^n & = & 0 \end{array} \qquad (3.42)$$

The Aitken acceleration method is a more elaborate version of an underrelaxation method, as the underrelaxation parameter ω is optimally chosen. It was first developed for one-dimensional problems and later extended for multi-dimensional problems [76, 77]. After discretisation the pressure distribution at the interface is a vector of $\mathbb{R}^m$ and the function $R(p^n) = F \circ S(p^n) - p^n$ is a vector map from $\mathbb{R}^m$ to $\mathbb{R}^m$, with m the degrees of freedom of faces on the interface Γ.

As stated previously, following the newton method, one would solve

$$p_{k+1}^n = p_k^n - \bar{\bar{J}}_R^{-1}(p_k^n) R(p_k^n) \qquad (3.43)$$

iteratively, where $\bar{\bar{J}}_R(p_k^n)$ is the Jacobian of R, calculated in p_k^n. The inverse of the Jacobian is very expensive to calculate, let alone impossible in our case of black box solvers for both the fluid an the structural problem. A different approach is applied where $\bar{\bar{J}}^{-1}$ is approximated by $\omega \bar{\bar{I}}$.

The scalar Aitken method. When $m = 1$, p_n is a scalar, and the inverse of the Jacobian is a constant, which we call ω. Under the extra condition that function R is linear, the newtonian method will converge in one iteration, whatever the initial guess p_0^n was. Let's call this solution of the now scalar equation (3.40) p_{sol}^n. If we take two not necessarily related pressure distributions p_k^n and p_{k-1}^n, one can write

$$\begin{array}{rcl} p_{sol}^n & = & p_{k-1}^n - \omega^n R(p_{k-1}^n) \\ p_{sol}^n & = & p_k^n - \omega^n R(p_k^n) \end{array} \qquad (3.44)$$

this can be interpreted as a set of two equations with two unknowns p_{sol}^n and ω. For the linear one-dimensional root-problem $R(p) = 0$, the solution is now known

$$\begin{array}{rcl} \omega_k^n & = & \frac{p_k^n - p_{k-1}^n}{R(p_k^n) - R(p_{k-1}^n)} \\ p_{sol}^n & = & p_k^n - \omega_k^n R(p_k^n) \end{array} \qquad (3.45)$$

For a non-linear one-dimensional root-problem the answer is not known yet, but the equations (3.45) can be used to iterate toward the solution, when p_{sol}^n is used as a new estimate p_k^n.

The vector Aitken method. As in the scalar case, we suppose again that the vector function R is linear. The Jacobian matrix in equation (3.43) is now approximated as a scalar ω^n time the identity matrix $\bar{\bar{I}}$.

$$\begin{array}{rcl} p_{sol,k-1}^n & = & p_{k-1}^n - \omega^n R(p_{k-1}^n) \\ p_{sol,k}^n & = & p_k^n - \omega^n R(p_k^n) \end{array} \qquad (3.46)$$

Unlike the scalar problem, this system of equations is not well defined, so we need another method to retrieve ω^n, for example using the least square approach.

$$
\begin{aligned}
\omega_k^n &= \omega \left(min \left\| p_{sol,k}^n - p_{sol,k-1}^n \right\| \right) \\
&= \omega \left(min \left\| p_k^n - p_{k-1}^n - \omega^n (R(p_k^n) - R(p_{k-1}^n)) \right\| \right) \\
&= \omega \left(min \left\| \Delta p^n - \omega^n (\Delta R^n) \right\| \right)
\end{aligned}
\tag{3.47}
$$

where $\Delta p^n = p_k^n - p_{k-1}^n$ and $\Delta R^n = R_k^n - R_{k-1}^n$. The notation $\omega(min \|..\|)$ denotes the value ω for which the expression $\|..\|$ is minimal. Solving this minimum problem is the equivalent to solving

$$
\Delta p^n \cdot \Delta R^n = \omega_k^n \Delta R^n \cdot \Delta R^n
\tag{3.48}
$$

Hence, the same flow chart as the scalar model can be used with

$$
\begin{aligned}
\omega_k^n &= \frac{(p_k^n - p_{k-1}^n) \cdot (R(p_k^n) - R(p_{k-1}^n))}{(R(p_k^n) - R(p_{k-1}^n)) \cdot (R(p_k^n) - R(p_{k-1}^n))} \\
p_{sol,k+1}^n &= p_k^n - \omega_k^n R(p_k^n)
\end{aligned}
\tag{3.49}
$$

leading iteratively to the desired solution.

A flow chart of the algorithm used for this calculation using the Aitken is given in figure 3.6. The algorithm uses the following steps :

1. Each time step starts with the initial guess of the position of the interface X_1 based on the results of the two previous time steps.

2. The according stress distribution p_1 is calculated with the fluid solver.

3. With this stress distribution the new interface position X_2 is calculated with the structural solver.

4. The FSI-loop is started with $k = 2$.

5. The fluid solver calculates the according stress distribution p_k.

6. At this point ω_k is calculated from the previous calculated p_{k-1} and p_{k-2} and an updated $\hat{p}_k$ is assessed.

7. With $\hat{p}_k$ the new interface position X_{k+1} is calculated using the black box structural solver.

8. Everything from step 5 is repeated with $k = k + 1$.
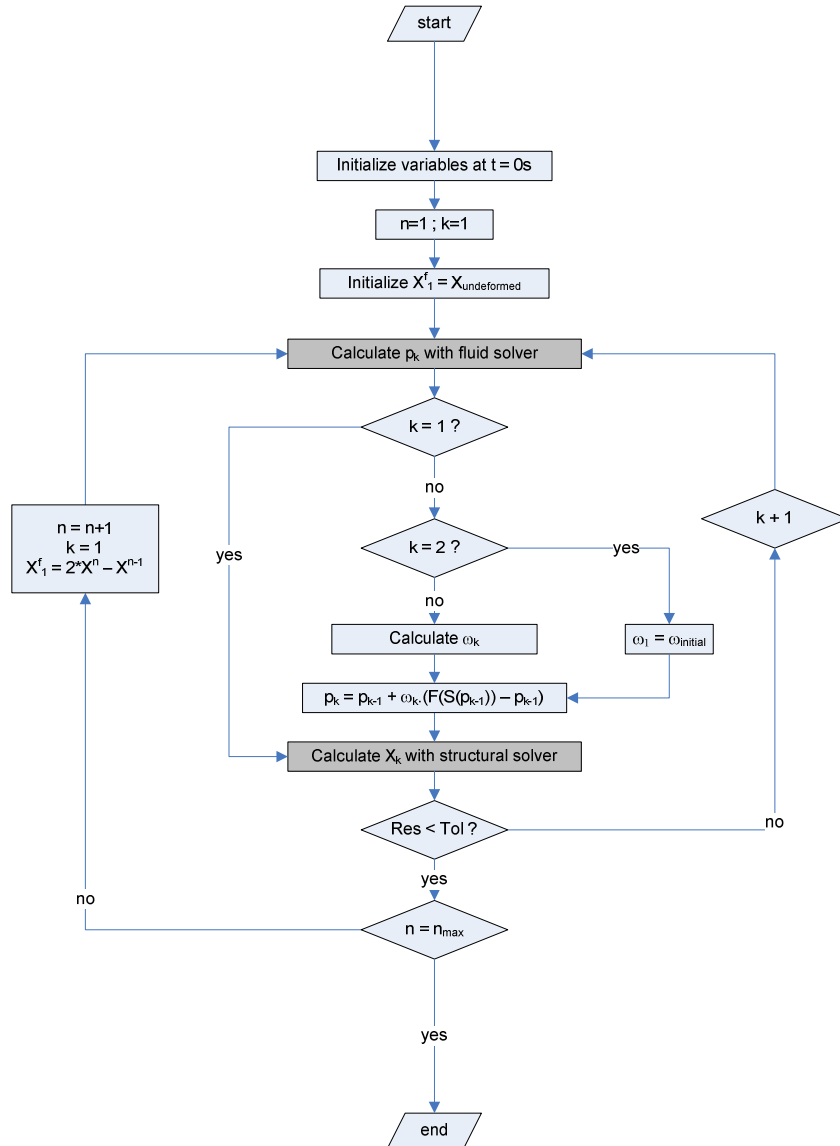
Figure 3.6: Flow chart of the Aitken FSI algorithm used in this calculation.
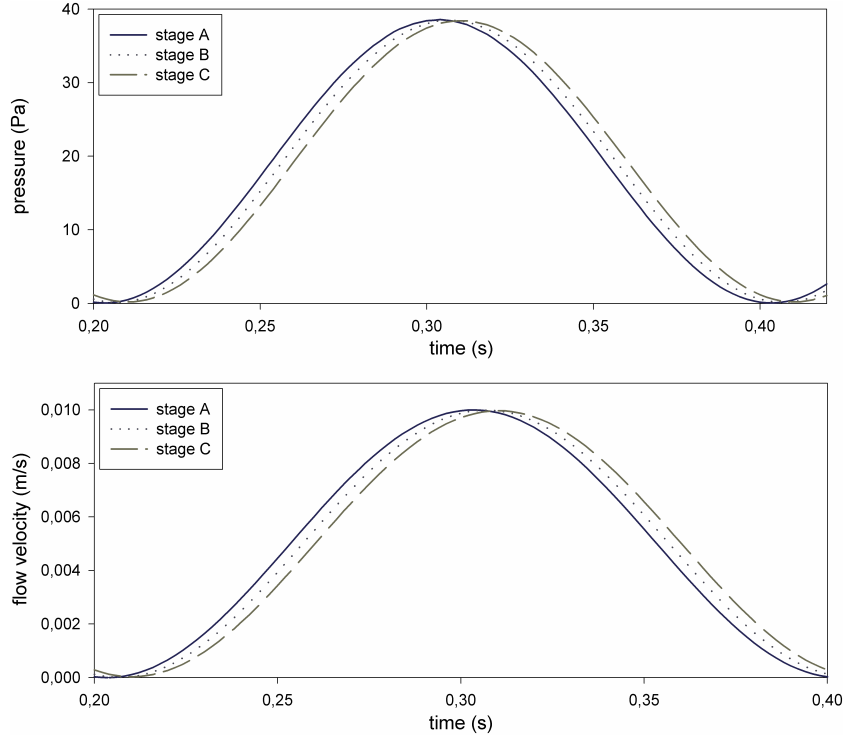
Figure 3.7: The pressure (upper panel) and flow velocity (lower panel) at three stages, one at $12.5mm$ (stage A), one at $25.0mm$ (stage B) and one at $37.5mm$ form the inlet (stage C) during the second simulated period. The reduced order model approach was used to solve the FSI-problem.

3.4 Results

In order to test the simulation results the wave speed was calculated. The reference value of the wave speed was assessed using the Bramwell-Hill-equation[2] which was derived in the previous chapter.

$$c^2 = \frac{A}{\rho}\frac{dp}{dA} \qquad\qquad (3.50)$$

with p the internal pressure, A the cross-section area and c the wave speed. Using only Abaqus, the static $A(P)$-relation was established, where, after substitution in equation (3.50) $3.671m/s$ was found.

---

[2]The more common Moens-Korteweg equation to quantify the wave speed is based on more assumptions, such as a thin wall compared to the vessels diameter and a small deformation formulation for the structural solver. We therefore choose to use the less common Bramwell-Hill equation.

Using both approaches, the wave propagation in the vessel is calculated. In three equidistant stages in the fluid domain (Fig. 3.5) the pressure and flow velocity was written. An example, using the results of the reduced order model approach is given in Fig. 3.7. Due to the finite wave speed, a delay is seen between the increase of the pressure in the three stages.

From the FSI-simulations it was seen that, for both approaches, the delay of the increase in pressure at stage B shows a delay of $3.40ms$ compared to the raise of stage A. As the distance between the stages is $12.5mm$, one can derive that a perturbation in the pressure field travels trough the tube with a wave speed of $3.68m/s$, which is differing less than 0.5% from the Bramwell-Hill wave speed.

3.5   Discussion and conclusion
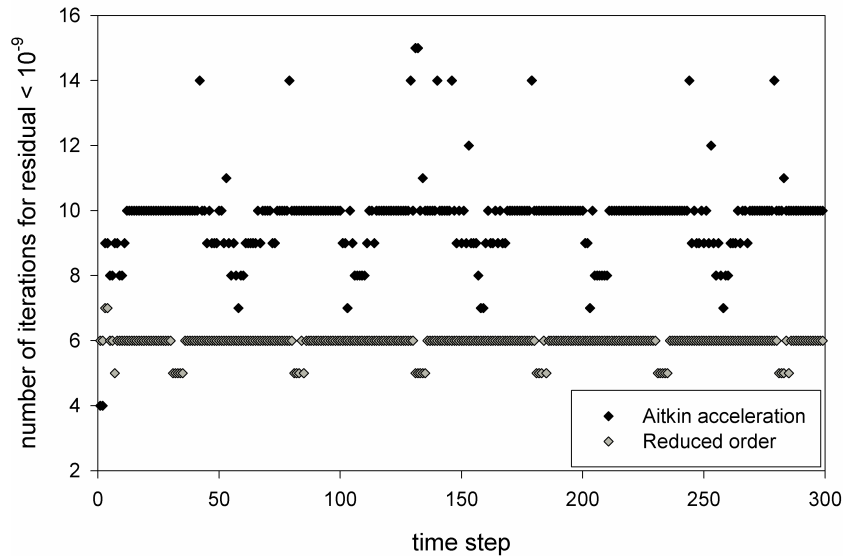
Figure 3.8: Number of modes used to reduce the residual below 10^{-9}.

Both schemes result in a stable FSI coupling, resulting in a correct wave propagation simulation. However, as seen in figure 3.8, the reduced order model approach requires about 4 modes each time step, whereas the Aitken acceleration method requires the double to reduce the residual below 10^{-9}. The residual was computed as $1/N$ times the L1-norm of $X_{k+1} - X_k$ with X_{k+1} the last calculated interface position with the structural solver and N the number of interface nodes.

Using a 2.4GHz Xeon processor one time step using the reduced order approach required about $2.1min$, whereas the Aitken acceleration required $3.5min$.

This verification shows that for both approaches the coupling scheme leads to a correct and stable wave propagation simulation with a finite wave speed. However the reduced order model approach is about 70% faster in this particular case.

4 A flexible slab downstream a fixed cylinder

4.1 Geometry and boundary conditions

This benchmark, proposed by Turek and Hron [84], is the FSI-version of the CFD-benchmark problem 'flow around a cylinder' [88]. It consists of a flexible slab downstream a fixed cylinder, immersed in an incompressible laminar flow, as shown in Fig. 3.9.
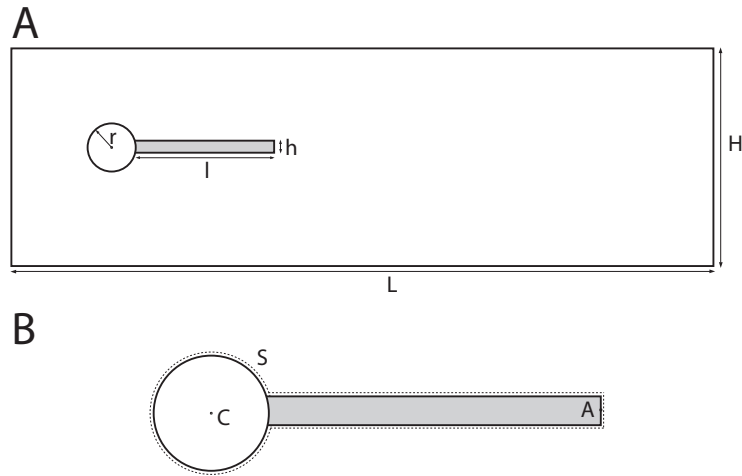
Figure 3.9: The computational domain.

The geometry parameters are listed in table 3.1. The benchmark problem is splitted in a CFD-, a CSM- and a FSI-part. It allows to compare the performance of different FSI-approaches.

geometry parameters		value $[m]$
Channel length	L	2.5
Channel width	H	0.41
Cylinder center	C	$(0.2, 0.2)$
Cylinder radius	r	0.05
Elastic bar length	l	0.351
Elastic bar width	h	0.02
Reference point $(t = 0)$	A	$(0.2, 0.6)$

Table 3.1: The geometry parameters used for the benchmark problem. Values are given in meter.

The fluid is modeled as a newtonian fluid with density $\rho^f = 1000 kg/m^3$ and

static viscosity $\nu^f = 1 \cdot 10^{-3} m^2/s$. The elastic bar is modeled as a linear-elastic material with density $\rho^s = 1000 kg/m^3$, Poisson modulus $\nu^s = 0.4$ and varying Young modulus. Large deformation theory is used in the finite element analysis to calculate the deformation of the bar.

At the upstream end of the duct, a parabolic inlet velocity profile is imposed with mean flow velocity U,

$$v^f(0, y) = 1.5U \frac{y(H - y)}{\left(\frac{H}{2}\right)^2} \tag{3.51}$$

while at the downstream end of the computational domain zero pressure is imposed. At the other boundaries a non-slip condition is imposed. A time step $5ms$ is used for the calculations.

4.2 Results

4.2.1 CFD-benchmark

For the first part of the benchmark problem, the computational fluid dynamics solver in the partitioned solver approach is tested. The slab is taken as a rigid object and the drag force F_D and lift force F_L on the cylinder and slab are calculated as given in Eq. 3.52. The integration path S is the closed path around cylinder and slab, as shown in Fig. 3.9.

$$(F_D, F_L) = \int_S \bar{\bar{\sigma}} \cdot \vec{n} dS \tag{3.52}$$

CFD1 In the $CFD1$-calculation, the mean inlet velocity is set to $U = 0.2m/s$, resulting in a steady state solution. Three meshes build up of triangular cells were considered with increasing mesh refinement, as shown in Fig. 3.10. Results are given in Table 3.2, where the ∞-solution denotes the solution of Turek and Hron [84] with a highly refined mesh.

$\#n$	drag $F_D[N]$	lift $F_L[N]$
6803	14.26	1.108
17513	14.29	1.099
37176	14.30	1.127
∞	14.29	1.119

Table 3.2: Results of the first CFD-test. $\#n$ denotes the number of nodes in the mesh.
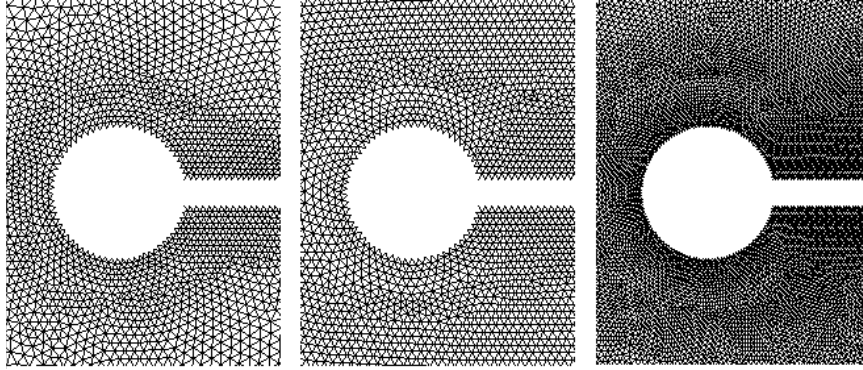
Figure 3.10: Close-up around the cilinder of the three meshes used for the CFD-computations, with 6803 nodes (left panel), 17513 nodes (middle panel) and 37176 nodes (right panel).

CFD2   Secondly the inlet velocity was increased to $U = 1.0m/s$, still resulting in a steady state solution of the flow. The obtained lift and drag forces for the same three meshes used in the previous test are given in Table 3.3

$\#n$	drag $F_D[N]$	lift $F_L[N]$
6803	138.8	10.97
17513	139.6	9.11
37176	137.3	10.84
∞	136.7	10.53

Table 3.3: Results of the second CFD-test. $\#n$ denotes the number of nodes in the mesh.

CFD3   Thirdly the inlet velocity is increased further, resulting in an unsteady solution. A transient, parabolic velocity profile is prescribed at the inlet. The velocity profile is initialized at $v^f(0,0,y) = 0m/s$ and varies over time as given in Eq.3.53.

$$v^f(t,0,y) = \begin{cases} v^f(0,y)\frac{1-cos(\pi/2\,t)}{2} & if\ t < 2.0s \\ v^f(0,y) & otherwise \end{cases} \tag{3.53}$$

The amplitude and average of the oscillations in lift and drag force in fully developed flow are given in Table 3.4. Calculations are performed with a time step

$\Delta t = 0.25 ms$. All of the force curves have the same characteristic pattern shown in Fig. 3.11, which are in correspondence to the results found by Turek and Hron.

$\#n$	drag $F_D[N]$	lift $F_L[N]$	frequency $f[Hz]$
6803	457.93 ± 5.9481	-47.782 ± 353.51	4.4346
17513	462.54 ± 4.9659	-28.607 ± 447.47	4.4385
37176	444.85 ± 5.4018	-17.630 ± 416.15	4.4444
∞	439.45 ± 5.6183	-11.893 ± 437.81	4.3956

Table 3.4: Results of the third CFD-test. Values are reported mean $\pm$ amplitude. $\#n$ denotes the number of nodes in the mesh.
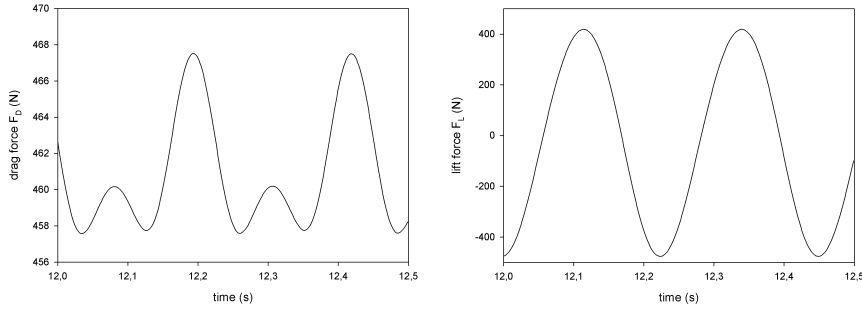
Figure 3.11: The lift and drag force curves in fully developed unsteady flow for the calculation using the medium grid.

4.2.2 CSM-benchmark

In order to test the performance of the structural solver and chosen mesh, the displacement of reference point A is studied due to a gravitational force with gravitational acceleration $\vec{g} = (0, -2)m/s^2$ for different Young moduli for the compliant slab. The influence of the surrounding fluid was not taken into account as we just wanted to check the CSM-partitioned solver.

CSM1 In a first calculation the slab is considered to have a Poisson modulus $\nu^s = 0.4$ and a Young modulus $E^s = 1.4e^6 kg/m.s^2$. The steady state condition for the displacement of point A is calculated for four meshes with increasing mesh density, all using quadratic, quadrilateral elements with plane strain approach ($CPE8RH$), and given in Table 3.5.

$\#n$	$u_x[e^{-3}m]$	$u_{y,A}[e^{-3}m]$
285	-7.139	-66.00
989	-7.152	-66.07
4821	-7.159	-66.11
12392	-7.160	-66.11
∞	-7.187	-66.10

Table 3.5: Results of the first CSM-test. $\#n$ denotes the number of nodes in the mesh.

CSM2 The second CSM-test consists of a slab with Poisson modulus $\nu^s = 0.4$ and Young modulus $E^s = 5.6e^6 Pa$ which bends due to gravity. The displacement of reference point A is given in Table 3.6. The same meshes used in the $CSM1$-problem are considered.

$\#n$	$u_{x,A}[e^{-3}m]$	$u_{y,A}[e^{-3}m]$
285	-0.4958	-16.94
989	-0.4665	-16.96
4821	-0.4670	-16.97
12392	-0.4671	-16.97
∞	-0.4690	-16.97

Table 3.6: Results of the second CSM-test. $\#n$ denotes the number of nodes in the mesh.

CSM3 Thirdly the Young modulus E^s is set to $1.4e^6 Pa$ and the Poisson modulus ν^s is set to 0.4 as in $CSM1$, however here the time dependent response to a sudden onset of gravitational acceleration $\vec{g} = (0, -2)m/s^2$ is calculated. The amplitude and average value of the oscillations of reference point A are given in Table 3.7, calculated with time step $\Delta t = 5ms$. All of the displacement curves have the same characteristic pattern shown in Fig. 3.12, which are, again, in correspondence to the results found by Turek and Hron.

4.2.3 FSI-benchmark

Finally the two partitioned solvers are combined into the FSI-benchmark problem.

FSI1 In the FSI-benchmark problem the mean inlet velocity is set to $U = 0.2m/s$, with the fluid having density $\rho^f = 1000kg/m^3$ and dynamic viscosity $\mu^f = 1kg/s.m$. The slab is set to Young modulus $E^s = 1.4e^6 Pa$ and Poisson

$\#n$	$u_{x,A}[e^{-3}m]$	$u_{y,A}[e^{-3}m]$	frequency $f[Hz]$
285	-14.175 ± 14.149	-63.443 ± 64.992	1.0929
989	-14.184 ± 14.154	-63.478 ± 65.056	1.0944
4821	-14.194 ± 14.168	-63.503 ± 65.087	1.0938
21807	-14.195 ± 14.168	-63.504 ± 65.509	1.0929
∞	-14.305 ± 14.305	-63.607 ± 65.160	1.0995

Table 3.7: Results of the third CSM-test. Values are reported mean $\pm$ amplitude. $\#n$ denotes the number of nodes in the mesh.
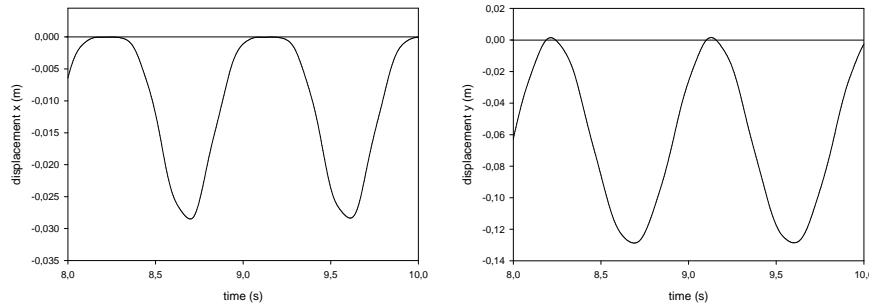
Figure 3.12: The displacement u_x and u_y curves of reference point A using the finest grid with $\Delta t = 5ms$.

modulus $\nu^s = 0.4$. This parameter combination results in a steady state solution. The fluid domain is meshed with triangular cells; the structural domain is meshed using quadrilateral, quadratic, reduced integration, hybrid, plane strain elements ($CPE8RH$). Results are given in Table 3.8.

As a test the coupling between the two solvers was first limited to a pressure-coupling only, instead of taking the forces due to fluid viscosity also into account as explained in section 1.4. The results for the coarse mesh show an important deviation of the expected values given in table 3.8 under 'ns'.

4.3   Discussion and conclusion

The calculations show good correspondence to the results by Turek and Hron. The steady state $FSI1$-problem gives results, even for the coarse mesh, differing less than 3%. This is very good, given the deviation on the $CFD1$ and $CFD2$ benchmark calculations. This difference has to do with the fact that Fluent uses the finite volume method, whereas Turek and Hron implemented higher order elements in their own written finite element monolithic FSI-solver. The difference

$\#n$	$u_{x,A}[e^{-3}m]$	$u_{y,A}[e^{-3}m]$	drag $F_D[N]$	lift $F_L[N]$
17513 'ns'	$0.442e^{-3}$	0.8068	14.309	0.7496
17513	0.0223	0.8207	14.310	0.7437
35146	0.0225	0.8224	14.314	0.7666
∞	0.0227	0.8209	14.295	0.7638

Table 3.8: Results of the first FSI-test. $\#n$ denotes the number of nodes in the mesh. 'ns' denotes a calculation where only the pressure distribution was transfered as a surface load to the structural solver.

between the reference value and the value obtained for the unsteady calculations $CFD3$ also follows from the fact that when the Dynamic Mesh module is used in Fluent only a first order accuracy in time is achievable. While Hron and Turek used a time step of $5ms$ in the $CFD3$-calculation, in Fluent no oscillations were observed when using such a time step. The time step needed to be decreased to $0.25ms$ in order to observe the oscillations sufficiently reliable. Both limitations are restricted to the choice of fluid solver.

Another part of the calculations causing inaccuracies is the calculation of the face forces on the interface. Therefore, as explained in section 1.4, derivatives of the velocity with respect to the coordinates are needed on the interface. In Fluent, however, such derivatives were only known in the cell center and were, in this algorithm, interpolated with 0th order to the interface. Obtaining acceptable estimations of the derivatives thus requires a very fine and regular grid close to the interface. When shear is of minor importance, because the dynamic viscosity of the fluid μ^f is relatively low, better results are obtained because the contribution of the viscosity forces are negligible compared to the pressure contribution in the face force on Γ.

For the wave propagation simulation this influence of shear was negligible, compared to the influences of pressure, so not much accuracy is lost there. In such cases it is advisable to use only a pressure coupling on the interface, as the algorithm will be faster. Indeed, when the shear-component of the face force does not need to be taken into account, the pressure mode matrix $[\Delta p_1^f \cdots \Delta p_{k-1}^f]$ will be half of the matrix's size compared to when the viscosity forces are taken into account. Hence the matrices used in the reduced order model algorithm are smaller and the inversion of the matrices is much faster.

5 Conclusion

Overall, the FSI results that were obtained are accurate. When studying the wave propagation in the vessel, it is also seen that the FSI-coupling produced a wave speed very close to the value assessed with the Bramwell-Hill equation. These

findings enforce the conviction that the virtual energy at the interface is as good as preserved and does not influence the solution of the FSI problem outside the obtainable accuracy.

The benchmark by Turek en Hron [84] showed that the accuracy of the FSI-problem is as good as can be expected given the limitations of the partitioned solvers. When the contribution of the interface forces due to the viscosity of the flow are negligible compared to the influence of the force, as in the wave propagation case, the accuracy is even higher.

In this chapter the FSI-tools are described which are developed during the research presented in this dissertation. Now that the approach is proved to be reliable and accurate, some applications are studied in the next chapters.

4

Wave reflection and pulse wave velocity in the human thoracic aorta

Abstract

The aorta is a tapered blood vessel and due to this gradual narrowing a forward wave is continuously reflected, even if, in a theoretical model, no side branches are present. Wave reflections can be studied using one-dimensional models of the vascular tree or using more-dimensional fluid-structure interaction models. In this study the findings of both models are compared. The material model used was obtained from pressure-area relations found in literature [89]. A hyperelastic, isotropic material law with a polynomial strain energy function was used to fit to the pressure-area data using a least square method in order to establish the material parameters. The geometry, with a length of $20cm$, was designed in such a way that at diastolic pressure the aorta had the geometry of an in vitro model of arterial tree present in our research facility.

A two-dimensional axisymmetrical fluid-structure interaction model was constructed, as well as a one-dimensional compliant-tube model in order to allow comparison of the results obtained with the two approaches. The one-dimensional model uses the solver developed by Stergiopulos et al. [1]. Wave separation was performed in the frequency domain with impedance theory and in the time domain using wave intensity analysis. The obtained pressure and flow waves showed good resemblance. Both approaches yield a physiological wave intensity analysis pattern with two forward and one backward wave peak throughout the aorta.

Impedance analysis showed similar patterns for the modulus and the phase of the impedance for both approaches. Due to the simplified pressure-area-relation used in the one-dimensional model, the timing of the forward and backward waves differs from the two-dimensional case.

One-dimensional models are useful when studying wave propagation in the vascular tree, as they do not require huge numerical resources. However, when flow velocity and pressure fields are required, for example when one wants to assess wall shear stress distributions, a two-dimensional axisymmetrical approach is vital. Hence both approaches are complementary. However, the pressure-area-relationship used in the one-dimensional case needs to be chosen with care, as overdone simplification of the relation can yield a wrong wave speed, which will result in incorrect wave propagation simulations. The study highlighted that, when strong reflections are present, the foot-to-foot method and the dU-dp-curve method to assess the pulse wave velocity yield deviating values, due to the fact that the no-reflections requirement is not fulfilled anywhere during the cardiac cycle.

1   Background

In the previous chapter, arterial wave propagation was used to validate the FSI-approach. However, as a comparison with the theoretical, one-dimensional wave speed was required, the boundary conditions in the validation study were non-physiological. The imposed inlet velocity was very small, slip at the fluid-structure interface was allowed and a non-reflecting outlet boundary condition was used. In this chapter a physiological numerical model of the thoracic aorta was constructed to study wave reflections.

As already highlighted when describing vascular pathologies in chapter 1 atherosclerosis affects the entire vascular system. Atherosclerosis stiffens the vessels, resulting in a lower compliance and thus higher stiffness of the aorta. The compliance of a vessel determines the velocity at which pressure and flow disturbances propagate and hence the timing of the forward and backward running waves in the cardiovascular system, thus determining the shape of the pressure and flow curves in the vessels. The study of the wave reflections and determination of the wave speed in the aorta can give insights in the overall vascular condition.

Different one-dimensional models of the arterial tree have been developed to allow the study of wave behavior in the vascular system [1, 90–94]. In a model of a normal healthy arterial tree one can study the different determinants of reflections of the pressure and flow waves [90], for example using transfer functions [93, 94]. One can also evaluate different approaches to assess the same parameter, for example total arterial compliance [91]. Alternatively, the influence of pathologies such as stenoses [1] or aneurysms [95] on the arterial waves can be quantified in order to try and facilitate detection of the pathology.

While the one-dimensional modeling of wave propagation is widely used, improvements still remain. Detailed three-dimensional studies of the flow at bifurcations for example, may lead to an enhanced formulation of the flow separation [96, 97]. Also, the attenuation of the waves due to fluid viscosity and viscoelastic wall behavior remains an issue [92, 97]. This study compares the results of a two-dimensional axisymmetrical fluid-structure interaction approach and a one-dimensional model approach for wave propagation behavior in the thoracic aorta.

2 Methods

2.1 Two-dimensional model

2.1.1 Geometry

The thoracic aorta segment was considered as an axisymmetrical tapered tube without side branches. The stressless geometry was constructed as such that for transmural pressure $56mmHg$ and longitudinal stretch $\lambda_z = 1.075$ [89] the aorta has the geometry given in table 4.1. This reconstruction of the stressless geometry was done following the approach by Raghavan et al. [98].

loaded diameter at aortic valve D_{av}	$31.0mm$
loaded wall thickness at aortic valve h_{av}	$1.71mm$
loaded diameter at $20cm$ D_{di}	$23.0mm$
loaded wall thickness at $20cm$ h_{di}	$1.35mm$
stretched length L	$200.0mm$

Table 4.1: The geometry of the aorta at transmural pressure $56mmHg$.

This loaded geometry is taken from Segers et al. [99], the ratio local wall thickness to local diameter was taken from [100].

Gambit (ANSYS, Inc.) was used to generate the geometry and the mesh for both the fluid and the solid domain. The fluid domain was meshed using triangular cells, while the wall was meshed using rectangular, bi-quadratic, reduced, hybrid elements ($CAX8RH$). A mesh independence study was performed, consisting of several stages.

First a mesh was found which yielded a mesh-independent static flow velocity and pressure distribution in Fluent (ANSYS, Inc.) and a mesh-independent static deformation and stress field in Abaqus (Simulia, Inc.) using the load obtained from the Fluent computation. Next the time step Δt was determined using an unsteady CFD-computation in Fluent. Finally, four FSI-cases were constructed (i) a case with the mesh density and time step obtained from the previous mesh-independency stages (ii) a case with the same mesh density and time step half of

Δt (iii) a case with a higher mesh density and the same time step and (iv) a case with higher mesh density and a time step half of Δt. The results obtained from the first 10% of the cardiac cycle were compared to ensure a mesh-independent and time step-independent solution. The aorta was meshed using 38528 fluid cells and 2500 elements in the wall.

2.1.2   Constitutive laws

The blood was modeled as a Newtonian fluid, a good approximation in the macro-circulation [87], with density $\rho_f = 1050 kg/m^3$ and dynamic viscosity $\mu_f = 4 mPas$, representing blood at 37^oC.

   The wall was modeled as a hyperelastic, incompressible [101] material. A reduced third order polynomial strain energy function (SEF) for an isotropic material was used, as given in Eq. (4.1) [102, 103]. W gives the strain energy per unit of reference volume.

$$
\begin{aligned}
W = \quad & C_{10}(I_1 - 3) + C_{01}(I_2 - 3) + C_{20}(I_1 - 3)^2 + C_{02}(I_2 - 3)^2 \\
& + C_{11}(I_1 - 3)(I_2 - 3) + C_{30}(I_1 - 3)^3
\end{aligned} \tag{4.1}
$$

where I_1 and I_2 are the first and second deviatoric strain invariants.

$$
\begin{aligned}
I_1 &= \lambda_1^2 + \lambda_2^2 + \lambda_3^2 \\
I_2 &= \lambda_1^{-2} + \lambda_2^{-2} + \lambda_3^{-2}
\end{aligned} \tag{4.2}
$$

   The parameters were estimated from the pressure-area relationships measured by Langewouters et al. [89], using an approach similar to the one proposed by Schulze-Bauer et al. [104].

   From Langewouters' pressure-area measurements for the thoracic aorta of the group aged between 50 and 59 years, mean circumferential nominal stress-strain data points $(\epsilon_{c,i}^{meas}, \sigma_{c,i}^{meas})$ were obtained. A two-dimensional shell approach was used for this conversion, omitting the radial nominal stress variation. The documented longitudinal stretch and the incompressibility of the vessel wall material were taken into account.

   From the strain energy function, one can quantify the according nominal circumferential stress $\sigma_{c,i}^{SEF}$ to a given circumferential stretch $\lambda_{c,i} = 1 + \epsilon_{c,i}^{SEF} = 1 + \epsilon_{c,i}^{meas}$ as

$$
\sigma_{c,i}^{SEF} = \left(\frac{\partial W}{\partial \lambda_c} \right)_{\lambda_{c,i}} \tag{4.3}
$$

Again the wall's incompressibility and the documented longitudinal stretch were taken into account in order to transform the strain energy function to a function of the circumferential stretch λ_c and the given longitudinal stretch λ_z.

$$I_1 = \lambda_c^2 + \lambda_c^{-2}\lambda_z^{-2} + \lambda_z^2$$
$$I_2 = \lambda_c^{-2} + \lambda_c^2\lambda_z^2 + \lambda_z^{-2} \tag{4.4}$$

A least-square method was used, minimizing the sum of the squared errors χ^2

$$\chi^2 = \sum_{i=1}^{n}(\sigma_{c,i}^{meas} - \sigma_{c,i}^{SEF})^2 \tag{4.5}$$

for the n data points. Following this approach, the parameters of the third order reduced polynomial function are identified, given in Table 4.2.

C_{10}	C_{01}	C_{20}	C_{02}	C_{11}	C_{30}
$6.875e^3$	$-1.875e^3$	$-23.0e^3$	$0.0e^3$	$23.0e^3$	$14.5e^3$

Table 4.2: The coefficients from the reduced third order material model (Eq. (4.1)) used to model the material properties of the entire aortic wall. Coefficients are given in $[Pa]$.
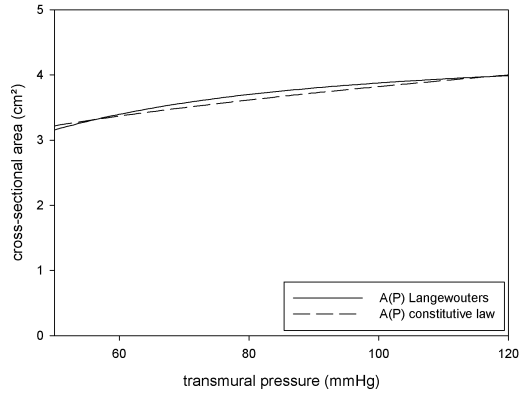
Figure 4.1: The difference between the pressure-area relationship measured by Langewouters in the human thoracic aorta and the pressure-area relationship obtained with the matched constitutive law

Finally, as a test, an axisymmetrical vessel wall model was constructed using the geometry information given by Langewouters et al. [89] for the 50-59 years age group with the described material model. The pressure-area relationship, shown in Fig. 4.1, was calculated with Abaqus 6.6 (Simulia, Inc.), giving a maximum difference of 2% with the pressure-area-relationship that was measured by Langewouters et al. in the pressure interval of interest in this study.

2.1.3   Boundary conditions

As an upstream boundary condition for the wall, the aortic wall is attached to the aortic valve plane, hence an encastre boundary condition is used. At the downstream side of the wall, a longitudinal stretch $\lambda_z = 1.075$ is imposed, as measured by Langewouters et al., while the radial deformation is not restricted.

The boundary conditions for the fluid problem were taken from previous one-dimensional numerical simulations [99], with a heart rate of $60 beats/min$. At the inlet flow was imposed, while at the outlet static pressure was imposed. Both profiles are given in figure 4.2.
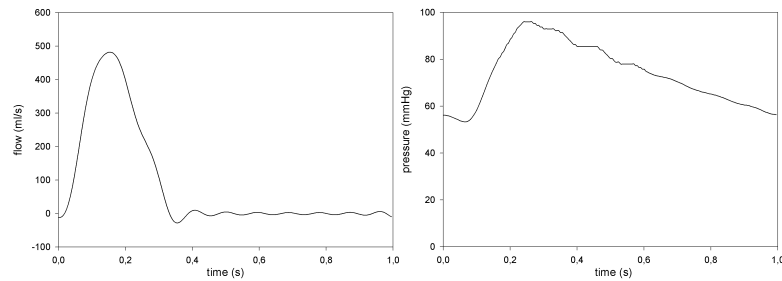
Figure 4.2: Boundary conditions, upstream flow (left panel) and downstream static pressure (right panel), taken from Segers et al. [99]

A time step $\Delta t = 5ms$ proved to yield time step independent flow velocity and pressure field results. Two cycles were calculated in order to eliminate the influence of the initial conditions on the results.

2.1.4   Fluid-structure interaction approach

Fluent (ANSYS, Inc.) and Abaqus (Simulia, Inc.) were used as commercially available black box solvers in an iterative, partitioned solver fluid-structure interaction approach. As fluid-structure interaction method, the validated approach, elaborated in the previous chapter, was used. Two reduced order models were constructed each time step, one for the fluid solver and one for the structural solver. Each iteration, an extra mode is added to the two reduced order models. As a new estimate for the interface position and the interface pressure distribution, an interface position and interface pressure distribution were assessed in equilibrium with both reduced order models. Wall shear stress was not taken into account in the FSI-coupling, as its influence was negligible compared to the influence of the interface pressure on the vessel wall deformation.

2.2   One-dimensional model

To compare the results of a one-dimensional approach and a two-dimensional axisymmetrical approach, a one-dimensional model was implemented, based on the solver developed by Stergiopulos et al. to study wave propagation in the arterial tree [1].

2.2.1   Geometry and constitutive laws

The one-dimensional geometry is built up out of different consecutive segments of at least two nodes, with a given length and input and output cross-sectional area at reference pressure $100mmHg$. The cross-sectional area is considered to change linearly from input to output of the segment. Given these restrictions, the geometry described in paragraph 2.1.1 was implemented in the one-dimensional model.

   The constitutive laws of the aorta wall are implemented by defining the distensibility β_o at reference pressure $100mmHg$ for each segment.

$$\beta_o = \frac{1}{A_o} \left(\frac{\partial A}{\partial p} \right)_{100mmHg} \tag{4.6}$$

The encastre boundary condition and the longitudinal stretch which are imposed in the axisymmetrical model are implemented by using the diameter at reference pressure and distensibility at reference pressure obtained from computational solid mechanics computations done for the axisymmetrical case (section 2.1). Independence of the spatial discretization was studied, resulting in the use of 9 segments, with 37 nodes, where the length of the segments increased from upstream to downstream. The geometry and distensibility of the nine segments is given in Table 4.3.

ID	L [cm]	A_{in} [cm^2]	A_{out} [cm^2]	β [$1/MPa$]
1	1.0	7.71	8.12	1.58
2	1.0	8.12	8.07	2.41
3	2.0	8.07	7.70	2.66
4	2.0	7.70	7.29	2.74
5	3.0	7.29	6.69	2.79
6	3.0	6.69	6.12	2.86
7	3.0	6.12	5.57	2.94
8	3.0	5.57	5.06	3.03
9	2.0	5.06	4.82	3.09

Table 4.3: The geometry and distensibility of the one-dimensional aorta segments. Segment number ID, segment length L, surface area at inlet A_{in} and outlet A_{out} of the segment and segment distensibility $\beta = (1/A) \, dA/dp$.

2.2.2 Boundary conditions

The used one-dimensional solver allows to impose upstream flow, for which the upstream flow boundary condition of the axisymmetrical model was taken, shown in Fig. 4.2. The downstream boundary condition, however, is a three-element windkessel model, with a resistance R_1 in series with a parallel combination of a resistance R_2 and a capacitor C [1]. The parameters of the windkessel model, given in Table 4.4, were identified from the output impedance found in the axisymmetrical FSI-computation. A time step $1ms$ gave results independent of temporal discretization.

R_1	$4.456 \cdot 10^{-3} mmHgs/ml$
R_2	$0.8572 mmHgs/ml$
C	$1.128 ml/mmHg$

Table 4.4: The coefficients from the three-element windkessel model used as output boundary condition in the one-dimensional computation.

2.2.3 Fluid-structure interaction approach

Stergiopulos et al. use the following one-dimensional flow equations in a compliant vessel

$$
\begin{aligned}
\frac{\partial A}{\partial t} + \frac{\partial Q}{\partial x} &= 0 \\
\frac{\partial Q}{\partial t} + \frac{\partial}{\partial x}\frac{Q^2}{A} &= \frac{-A}{\rho}\frac{\partial p}{\partial x} + \frac{\pi D \tau}{\rho}
\end{aligned}
\tag{4.7}
$$

where A denotes the cross-section area, D the diameter, Q the flow, p the pressure, ρ denotes the fluid density and τ denotes the wall shear stress, which is taken [105]

$$
\tau = \frac{-\rho}{\pi D}\left[\frac{8 c_v \pi \mu Q}{\rho A} + (c_u - 1)\frac{\partial Q}{\partial t}\right]
\tag{4.8}
$$

with μ the dynamic viscosity of the flow. Parameters c_u and c_v are function of the Womersley number $Wo = (D/2)\sqrt{2\pi f_{HR}\rho/\mu}$ with f_{HR} the frequency related to the heart rate. A non-linear pressure-area relation $A(p,x)$ is used, through a pressure-dependent $\partial A/\partial p$-relation (4.9).

$$
\frac{\partial A}{\partial p} = \frac{\partial A}{\partial p}_{100mmHg}\left(a + \frac{b}{1 + (p - p_a)^2/p_b^2}\right)
\tag{4.9}
$$

where parameters a, b, p_a and p_b are 0.4, 5, $20mmHg$ and $30mmHg$ respectively [92]. $(\partial A/\partial p)_{100mmHg}$ is computed from the given distensibility β and the reference cross-sectional area A_o.

The set of equations (4.7)-(4.9) is solved in the time-domain using a second-order Lax-Wendorff finite difference scheme for the spatial and temporal discretization and solution. Stability is obtained for Courant number $C_o = c\Delta t/\Delta x$ less than 1, where c denotes the wave speed, Δx the distance between nodes and Δt the time discretization.

2.3 Wave analysis theory

Pressure and flow waves in the cardiovascular system are the result of complex wave reflection patterns [106]. However, one can consider the pressure p the sum of one forward p_+ and one backward p_- component, which are the sums of all forward and backward traveling waves respectively [107]. Similarly the flow Q can be considered to be the sum of a forward component Q_+ and a backward component Q_- and the flow velocity U the sum of U_+ and U_-.

When looking at the pressure and flow waves in the cardiovascular system, two possible wave separation theories are frequently used. The impedance analysis treats pressure and flow as voltage and current and uses the frequency domain to separate the waves following electrical circuit theory, as first done by Westerhof et al. [108]. The wave intensity analysis, proposed by Parker and Jones [33], uses the waterhammer equations to separate forward and backward waves in the time domain. As both approaches give different information, the obtained pressure and flow waves were analyzed using both techniques.

2.3.1 Impedance analysis

In impedance analysis the pressure and flow waves are separated using Fourier decomposition. The superposition principle used in the decomposition requires that (1) the cardiovascular system is in a steady state condition and that (2) the mechanical properties of the system are sufficiently linear. In such cases the pressure p and flow Q can be decomposed into a sum of sine waves with harmonic frequencies nf

$$p = \sum_{n=0}^{\infty} p_n = \sum |p_n|\, e^{i(2\pi nft + \varphi_{p_n})} \tag{4.10}$$

$$Q = \sum_{n=0}^{\infty} Q_n = \sum |Q_n|\, e^{i(2\pi nft + \varphi_{Q_n})} \tag{4.11}$$

with time t and p_n and Q_n the nth harmonic of the pressure and flow, respectively. $|p_n|$ and $|Q_n|$ denote the moduli of the nth harmonic and φ_{p_n} and φ_{Q_n} its phase, respectively of the pressure and the flow. In general, when the decomposition of hemodynamic parameters such as pressure or flow are considered, the summation can be limited to 10 to 15 harmonics [109, 110].

For each harmonic the impedance Z_n can be derived

$$Z_n = \frac{p_n}{Q_n} = \frac{|p_n|}{|Q_n|} e^{\varphi_{p_n} - \varphi_{Q_n}} \tag{4.12}$$

with modulus $|Z_n| = |p_n| / |Q_n|$ and phase $\varphi_{Z_n} = \varphi_{p_n} - \varphi_{Q_n}$. The phase of the impedance typically oscillates around 0° for high frequencies, while the modulus is about constant. The averaging of the impedance of the higher harmonics results in the characteristic impedance Z_c [111].

2.3.2   Wave intensity analysis

Wave intensity analysis (WIA) separates the waves in the time domain, by studying the sign of the wave intensity dI, the energy carried by a single wave. As shown in chapter 2, along the characteristics, incremental differences in pressure $dp_\pm$ and flow velocity $du_\pm$ are related

$$dp_\pm = \pm \rho c dU_\pm \tag{4.13}$$

for both the forward (denoted with '+') and the backward wave, denoted with '−'. When the contributions of both waves are assumed additive, $dp = dp_+ + dp_-$ and $dU = dU_+ + dU_-$, one can separate the increments

$$dp_\pm = \frac{1}{2} (dp \pm \rho c dU) \tag{4.14}$$

$$dU_\pm = \pm \frac{1}{2} (\frac{dp}{\rho c} \pm dU) \tag{4.15}$$

The wave intensity dI, defined as $dU\,dp$, can now be separated into a forward and a backward component, dI_+ and dI_-, respectively, where $dI = dI_+ + dI_-$.

$$\begin{aligned} dI_+ &= dU_+ dp_+ = \frac{1}{4\rho c}(dp + \rho c dU)^2 \\ dI_- &= dU_- dp_- = -\frac{1}{4\rho c}(dp - \rho c dU)^2 \end{aligned} \tag{4.16}$$

Thus, the wave intensity associated with a forward wave is positive, while the wave intensity associated with a backward wave is negative. Four different wave types are distinguished, given in Table 4.5.
From Eq. (4.14) and (6.5) one can compute the forward and backward traveling contribution to the pressure and the flow velocity as

$$\begin{aligned} p_+(t) &= p_d + \textstyle\sum_{t=0}^{t} dp_+ & p_-(t) &= \textstyle\sum_{t=0}^{t} dp_- \\ U_+(t) &= \textstyle\sum_{t=0}^{t} dU_+ & U_-(t) &= \textstyle\sum_{t=0}^{t} dU_- \end{aligned} \tag{4.17}$$

where p_d denotes the diastolic pressure.

dp	dU	dI	wave type	
$+$	$+$	$+$	FCW	forward compression wave
$+$	$-$	$-$	BCW	backward compression wave
$-$	$+$	$-$	BEW	backward expansion wave
$-$	$-$	$+$	FEW	forward expansion wave

Table 4.5: Definition of the four different wave types.

2.4 Pulse wave velocity assessment

Finally, pulse wave velocity was assessed, using three frequently used approaches. From wave intensity theory, one can estimate the pulse wave velocity in a dU-dp-graph from the cardiac cycle. In the idealized case, if only forward waves or if only backward waves are present, Eq. (4.13) shows that the dU-dp-graph is a straight line through the origin with slope ρc. Now, at the onset of systole one expects only forward waves to be present in the arterial system and hence the dU-dp-graph shows a linear part, where the slope is related to the pulse wave velocity.

A second approach, used in clinical practice, is the foot-to-foot method. Here the pulse wave velocity is assessed by measuring the time difference between the foot of the pressure or flow curve at two different locations. This approach was used in the previous chapter to establish the pulse wave velocity from the FSI-computation in section 3. As the foot of the pressure or flow curve is sometimes not clearly visible, the time delay between points at 10% of the height of the curves is taken to calculate the pulse wave velocity. Foot-to-foot pulse wave velocity measurement can be affected by wave reflections [112].

The last approach uses the distensibility β. From the Bramwell-Hill relation for the wave speed, one can write

$$c^2 = \frac{A}{\rho} \frac{dp}{dA} = \frac{1}{\rho\beta} \qquad (4.18)$$

So, when the pressure-area relation is known, one can compute the pulse wave velocity. This pulse wave velocity assessment does not suppose only forward wave to be present, it follows directly from the one-dimensional conservation equations in a compliant tube, as denoted at the start of chapter 2.

3   Results

The pressure, flow and flow velocity are given in Fig. 4.3, for three stages, the inlet, the outlet and a stage in the middle. One can see a qualitative resemblance, however the pulse pressure in the one-dimensional case is overall about 72% of the the pulse pressure seen in the results from the two-dimensional computation.

The one-dimensional flow computation also shows more elevated oscillations in the flow during diastole, while more damping is seen in the two-dimensional calculations.
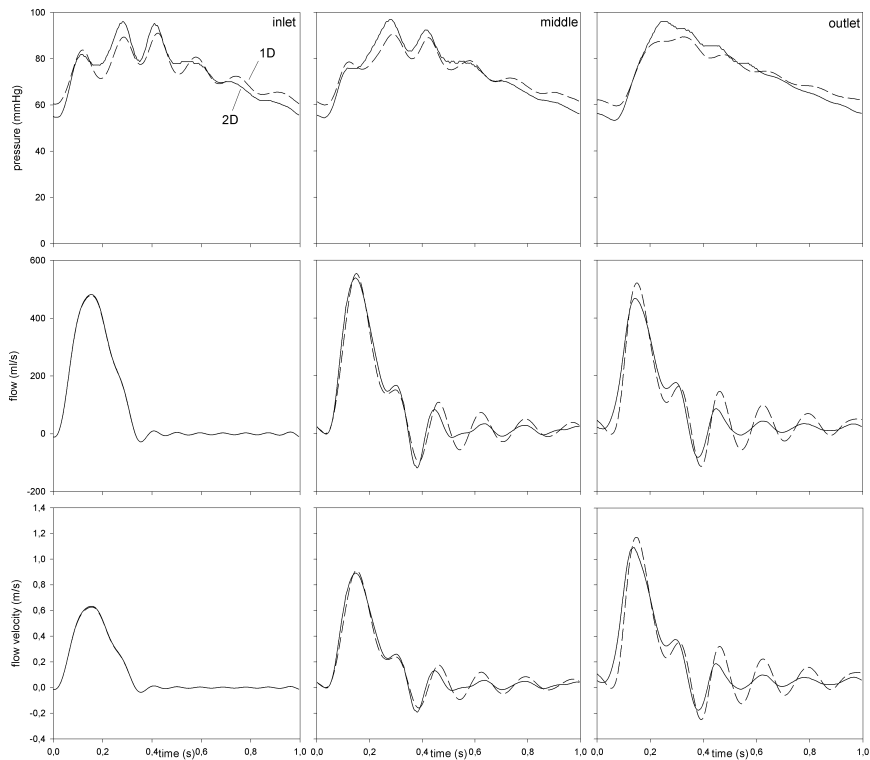
Figure 4.3: The pressure p (top), flow Q (middle) and flow velocity u (bottom) over one cycle at the inlet (left), at $10cm$ from the inlet (middle) and at the outlet (right), for both the one-dimensional computation (dashed line) and the axisymmetrical computation (solid line).

The results from the impedance analysis performed on the pressure and flow data at the three stages is shown in Fig. 4.4. Complex impedance patterns are observed in both cases, with a qualitative resemblance for both the modulus and the phase. At the outlet the limits of a three-element windkessel model as outlet boundary are observed, as the windkessel model can not account for the oscillation in phase signal (bottom right panel Fig. 4.4) seen in the two-dimensional computation.

Fig. 4.5 gives the results from the wave intensity analysis at the three loca-
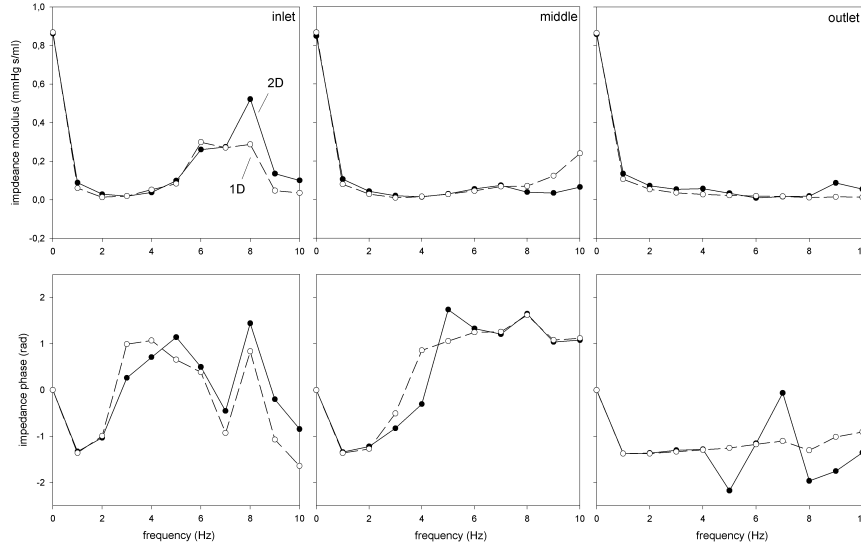
Figure 4.4: The impedance's modulus $|Z_n|$ (top) and the phase φ_{Z_n} (bottom) at the inlet (left), at $10cm$ from the inlet (middle) and at the outlet (right), for both the one-dimensional computation (dashed line) and the axisymmetrical computation (solid line).

tions. The wave intensity pattern dI consists of three peaks, a forward compression wave FCW, followed by a backward compression wave BCW after which a small forward expansion wave FEW is observed. As the pulse pressure in the two-dimensional case is more elevated, the observed wave intensity peaks are more elevated in this case. The difference in attenuation of the waves between the one-dimensional and the two-dimensional computation are also observed in the separated wave intensity graphs. One can also observe a slight difference in wave propagation behavior, as the waves in the two-dimensional case appear to be traveling faster than the waves observed in the one-dimensional geometry.

Finally pulse wave velocity was assessed using three different approaches. The results of the pulse wave velocity using the dU-dp-graph are given in the top section of Table 4.6, while the results of the foot-to-foot technique on the pressure waves are given in the middle section and the results for the flow waves on the bottom section. The Bramwell-Hill approach, using the distensibility, yields a pulse wave velocity pattern over the length of the aorta segment shown in Fig. 4.6. In the two-dimensional case the pulse wave velocity tends to infinity at ($x = 0$) due to the imposed boundary conditions at the aortic valve.
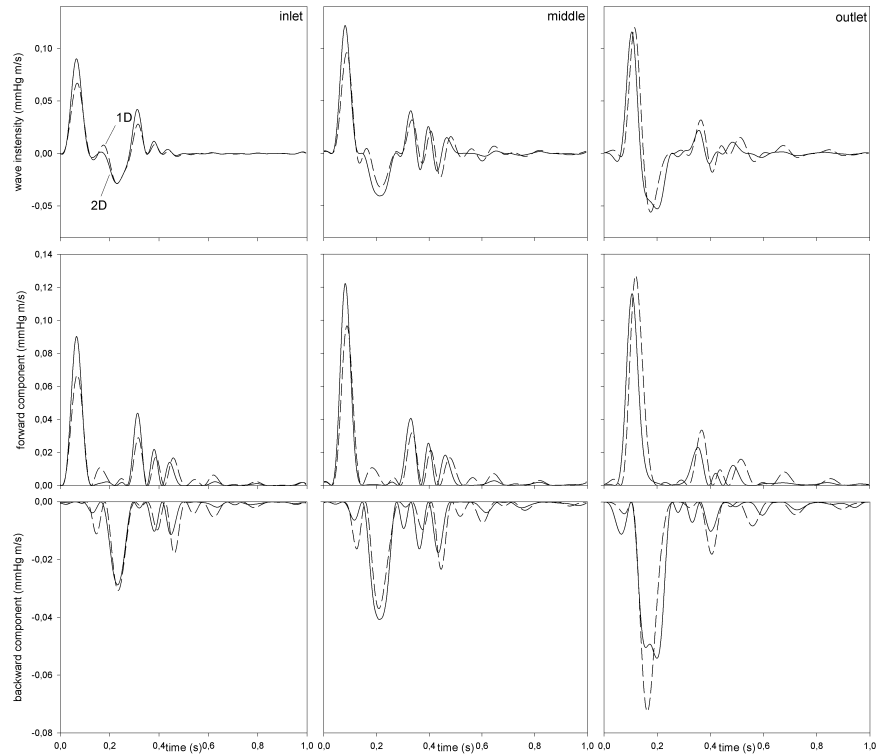
Figure 4.5: The total wave intensity dI (top), its forward component dI_+ (middle) and its backward component dI_- (bottom) over one cycle at the inlet (left), at $10cm$ from the inlet (middle) and at the outlet (right), for both the one-dimensional computation (dashed line) and the axisymmetrical computation (solid line).

4   Discussion

One-dimensional compliant models and more-dimensional fluid-structure interaction models are complementary. As one-dimensional models do not require large numerical resources, they offer the best approach when one wants to study wave propagation and reflection in a vast vascular network. They are also the best option when one wants to study flow redistribution due to occlusion in a periferal artery [94]. However no detailed information of the cross-sectional distribution of the flow velocity profile is provided. Two-dimensional models give the cross-sectional distribution of the flow velocity, an example of the radial distribution of the axial flow velocity when the blood is decelerating is given in Fig. 4.7. So, when one wants to study wall shear stress, one-dimensional models are not

on dU-dp-graph:		
position [m]	c_{1D} [m/s]	c_{2D} [m/s]
0.00	6.72	5.20
0.10	3.93	4.23
0.20	2.38	1.37
foot-to-foot on p:		
distance [m]	c_{1D} [m/s]	c_{2D} [m/s]
$0.00 \rightarrow 0.05$	4.98	7.59
$0.05 \rightarrow 0.10$	4.85	5.85
$0.10 \rightarrow 0.15$	3.80	3.12
$0.15 \rightarrow 0.20$	1.60	2.21
foot-to-foot on Q:		
distance [m]	c_{1D} [m/s]	c_{2D} [m/s]
$0.00 \rightarrow 0.05$	3.61	3.09
$0.05 \rightarrow 0.10$	3.04	4.03
$0.10 \rightarrow 0.15$	4.49	12.3*
$0.15 \rightarrow 0.20$	9.82	-6.21*

Table 4.6: Pulse wave velocity estimations using the dU-dp-curve (top panel) and the foot-to-foot technique on the pressure wave (middle panel) and on the flow wave (bottom panel). c_{1D}: pulse wave velocity with one-dimensional approach; c_{2D}: pulse wave velocity with two-dimensional approach; distance: two points on the axis in between which the foot-to-foot method was applied; *: deviating values due to the limitations of the foot-to-foot method.

adequate. More-dimensional numerical fluid dynamics models provide more insight in the local hemodynamics, but they require far more computer power, especially when one wants a geometrically realistic model where fluid-structure interaction is taken into account. These models are more fit for smaller geometries, such as a vessel segment with an aneurysm or a stenosis. Combining both approaches, Formaggia et al. and Vignon-Clementel et al. showed the benefit of one-dimensional models providing alternate boundary conditions for more-dimensional CFD-computations, whether computed a priori or iteratively during the CFD-simulation [113–115].

Essential in obtaining realistic wave behavior results with one-dimensional models is the translation of the vessel behavior to a one-dimensional approach. More-dimensional FSI models can aid to enhance the performance of one-dimensional models. They provide a test environment where adaptations in one-dimensional model parameters can be evaluated, for example by studying flow separation behavior at bifurcations with different geometries. The wave behavior at bifurcations can be implemented in a more realistic way for both forward and backward waves [96]. This study is situated in this application field. We wanted
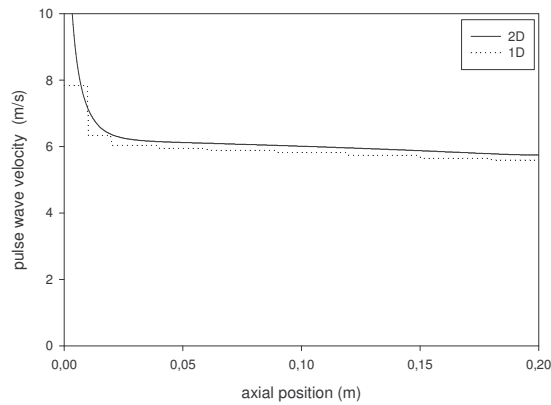
Figure 4.6: The pulse wave velocity assessed using the Bramwell-Hill equation (Eq. (4.18)) at $p = 75mmHg$ for the two-dimensional case (solid line) and the one-dimensional case (dashed line).
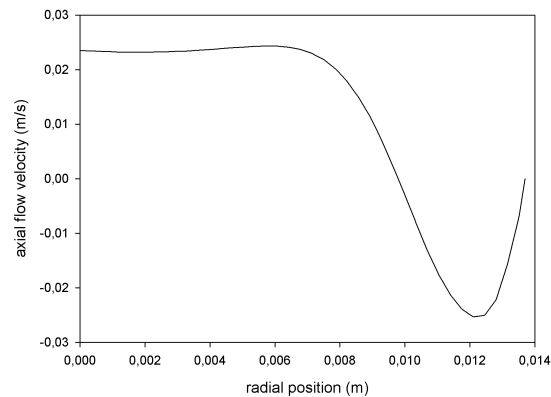
Figure 4.7: Axisymmetrical, two-dimensional, radial distribution of the axial flow velocity profile at $t = 0.875s$ in a cross-section in the middle between inlet and outlet. The deceleration of the blood induces recirculation zones close to the interface.

to compare the results from previously used one-dimensional models with the results for the same geometry obtained with the developed fluid-structure interaction approach.

Both approaches show good qualitative results. The matched impedance of the output boundary from the results of the two-dimensional approach to the one-

dimensional computation shows good correspondence for low frequencies, as can be seen in the right panel of Fig 4.4. However, for frequencies above $4Hz$ the matching is not adequate, as can be seen in the phase-graph. This could explain the difference in behavior of the flow during diastole between the one- and two-dimensional model. As the flow oscillations observed during diastole at the outlet stage have frequencies in this range, the observed difference of the flow behavior could be induced by the mismatch in impedance for these frequencies.

When looking at the assessed pulse wave velocity, Fig. 4.6 shows that the one-dimensional approach, using Eq. 4.9, results in an underestimation of the pulse wave velocity c due to an overestimation of β for pressures under $100mmHg$. The two-dimensional model is thus slightly stiffer than the one-dimensional model, which could explain why the pulse pressure is more elevated in the two-dimensional model. Other than this a good resemblance is seen between both curves. Though, the pulse wave velocity assessed using the foot-to-foot method and the dU-dp-curve method yield deviating results. Both methods are based on the assumption that no backward waves are present in the vascular system at onset of systole. Still, in the thoracic aorta simulated here strong reflections are observed. The reflection coefficient Γ

$$\Gamma = \frac{max(p_-) - min(p_-)}{max(p_+) - min(p_+)} \tag{4.19}$$

computed at the outlet yields 0.92 for the two-dimensional computation and 0.93 for the one-dimensional case, indicating that the assumption of a reflection-free time interval is not straightforward for locations close to the outlet. The discrepancy between the pulse wave velocities assessed with the foot-to-foot method for the pressure waves and the flow waves demonstrate this assumption. Indeed, if at the onset of systole the aorta would be reflection-free, the pressure and flow waves would be in phase and the foot-to-foot method applied to the pressure and flow waves would yield the same results.

Moreover, the delay between 10% points on two curves depends on the absolute height of the curve. Here, for example, the peak value of the flow at the outlet is lower than the peak value of the flow at $15cm$ of the aortic valve. This shifts the 10% point of the flow curve at the outlet relatively to the left, whereas for the flow curves at $15cm$ the 10% point is shifted to the right, explaining the deviating results of pulse wave velocity assessed with the foot-to-foot method on the flow signal (Table 4.6).

Some limitations of the approach are present. Firstly, the translation of the encastre boundary condition at the aortic valve plane from the axisymmetrical model to the one-dimensional model was not straightforward. The modification of the pressure-area relationship in the zone close to the valve was taken into account through the distensibility. The boundary condition reduces the distensibility close

to the valve, as a pressure increase will yield a smaller diameter increase of the lumen than if the valve plane would not be restricted to move radially. This spatial variation of the distensibility requires segments with small length Δx close to the aortic valve plane in order to catch these changes sufficiently. However, an diminished distensibility equals an elevated pulse wave velocity c, which will tend to infinite in the valve plane. Due to stability reasons however, the segments can not be chosen too small, as the Courant-criterion needs to be met. Indeed, numerical stability requires $Co = c\Delta t/\Delta x$ to be smaller than unity.

Secondly, the mesh convergence study was performed based on the pressure and flow velocity patterns and the displacement of the vessel wall. While such a mesh independence study ensures the lower frequency behavior to be independent of the grid density, it does not necessarily ensures the grid to be independent from the higher frequency behavior of the flow. This discrepancy can partially account for the differences in higher-frequency behavior observed in the impedance spectrum.

Thirdly, for the used one-dimensional computation only a lumped parameter boundary condition using a three-element windkessel model was possible, while in the two-dimensional FSI-computation a prescribed transient static pressure outlet boundary condition was implemented. This difference in outlet boundary condition might induce reflections which differ between both approaches. The use of lumped parameter models as outlet boundary condition, however, requires an iterative computation over several cycles until the outlet boundary condition does not change with an additional cycle. As the two-dimensional FSI-computation was already numerically time consuming, implementation of a lumped parameter outlet boundary condition was not done. The parameters of the one-dimensional lumped parameter outlet boundary condition were fit to the impedance spectrum from the FSI-resulting pressure p and flow Q in order to try and minimize the differences induced by this discrepancy in boundary conditions. However, the three element windkessel model could not entirely capture the behavior of the impedance phase at the outlet of the FSI-model, observed in Fig. 4.4, especially at high frequencies. For future studies it is thus important that, when comparing the behavior of waves with the two techniques, the same output impedance is used. A pure resistive lumped parameter model as outlet boundary condition could be helpful here. Even though a resistive outlet boundary condition might not be the best option to generate physiological wave behavior [92], no phase difference is induced at the outlet and implementation of the outlet boundary condition in the time domain does not require knowledge of the pressure and flow in the whole cycle.

5 Conclusion

One-dimensional models are useful when studying wave propagation in the vascular tree, as they do not require huge numerical resources. However, when flow velocity and pressure fields are required, for example when one wants to assess wall shear stress distributions, a two-dimensional axisymmetrical approach is vital. Hence both approaches are complementary. However, the pressure-area-relationship used in the one-dimensional case needs to be chosen with care, as overdone simplification of the relation can yield a wrong wave speed, which will result in incorrect wave propagation simulations. The study highlighted that, when strong reflections are present, the foot-to-foot method and the dU-dp-curve method to assess the pulse wave velocity yield deviating values, due to the fact that the no-reflections requirement is not fulfilled anywhere during the cardiac cycle.

5

Fluid-structure interaction model of an abdominal aortic aneurysm (AAA), decoupled versus fully coupled approach

Abstract

The application described in this chapter, considers an abdominal aortic aneurysm (AAA), a pathological dilatation of the abdominal aorta. When the local wall stress in the aneurysm exceeds the local failure strength, the aneurysm ruptures inducing a heavy and in 90% of the cases fatal internal bleeding. Aneurysms can be treated but the treatment holds some risk itself. Therefore a good criterion is needed to establish the potential rupture risk. The currently used diameter criterion, however, is insufficient.

In literature several approaches to establish a patient-specific wall stress distribution are mentioned. In this study the results of four different approaches are compared: a fully coupled transient fluid-structure interaction approach, a fully coupled static FSI-approach, a decoupled approach, where the pressure distribution from a static flow computation is used as a non-uniform pressure load for the solid computation, and a pure solid mechanics approach with uniform pressure load.

A simplified, axisymmetrical geometry was used, once computed without throm-

bus and once computed with an intraluminal thrombus (ILT) filling the aneurysmal sac. The wall of the aneurysm was modeled as a hyperelastic, isotropic material model, while the thrombus was modeled as a linear elastic material. Both material models were obtained from population studies in literature. Boundary conditions were assessed using a non-linear one-dimensional model of the systemic circulation.

Results showed that a decoupled or a static FSI-approach do not necessarily provide results closer to the transient FSI results as compared to the computational solid mechanics approach, even though they are computationally more expensive. Finally we showed that when comparing the stress distribution with and without ILT, the change of blood flow through the aneurysm needs to be taken into account in the imposed boundary conditions. This redistribution of blood is caused by the thrombus-related change in resistance and compliance in the abdominal region.

1   Introduction

An aneurysm is a pathological dilatation of an artery. When the aneurysm is situated on the abdominal aorta, it is called an abdominal aortic aneurysm. As an aneurysm has a real rupture risk, it is essential that the aneurysm is treated before rupture occurs, as rupture of an abdominal aortic aneurysm is linked to a mortality rate of 90% [116]. The treatment of an aneurysm is not without risk [117], hence, treatment is advised when the rupture risk is bigger than the risk brought along with intervention.

As a current intervention criterion both the diameter of the aneurysm and the growth of the aneurysm is used. If the diameter is more elevated than $5.5cm$ or if the aneurysm's diameter increases more than $10mm/year$ intervention is advised [118, 119]. Several studies, however, showed that the diameter criterion, based on Laplace's law, is insufficient and that aneurysms with a diameter less than $5.5cm$ rupture, while some aneurysms with a diameter higher than $5.5cm$ show to be stable [120, 121]. A more specific criterion is therefore needed. Several studies tried to answer this need using more elaborate risk-rupture criteria [122–124].

An aneurysm ruptures if the local wall stress exceeds the local failure strength. Several research groups have studied the failure strength of abdominal aortic aneurysms [98, 125–128]. Raghavan et al. [98] showed that the failure tension shows regional variation. Recently, Vande Geest et al. [128] derived a patient-specific, region dependent failure strength distribution which can be quantified non-invasively using four parameters: gender, normalized AAA diameter, local intraluminal thrombus thickness and family history.

In many large aneurysms the intraluminal sac is filled with thrombus, the intraluminal thrombus (ILT). The influence of the presence of a thrombus on the

rupture criterion is still debated. While computational studies denote that the presence of an ILT diminishes the peak wall stress [129, 130], other studies showed that the ILT does not reduce the pressure on the aneurysmal wall. This indicates that the actual load on the aneurysmal wall is not reduced when an ILT is present and, hence, that the ILT does not reduce rupture risk of an aneurysm [131, 132]. Moreover Vorp et al. [127, 133] showed that the presence of an aneurysm induces anoxia in the aneurysmal wall which is covered, thereby inducing wall weakening.

In order to assess a patient-specific rupture criterion, the patient-specific wall stress distribution is needed. Since wall stress cannot be measured, it can only be calculated. The first wall stress estimates used a numerical continuum solid mechanics (CSM) approach with a uniform pressure load distribution, either using a simplified geometry [134, 135] or patient-specific data [120, 121, 136, 137]. The most accurate way of quantifying the wall stress is by using transient fluid-structure calculations (FSI). Several studies applied this approach, again using either simplified geometries [138–140] or patient-specific data [141, 142]. However these calculations are very time consuming and are, to date, not suitable for in clinical practice.

Recently, static decoupled fluid-structure interactions were proposed by Papaharilaou et al. [143] as a means of more accurately assessing the peak wall stress in the aneurysm. In these computations the static pressure distribution is first computed using a fixed geometry static flow calculation after which the pressure distribution on the vessel wall is exported to the solid finite element calculation as boundary condition. Such approaches are still very time efficient. While in previous studies the results of a pure solid mechanics approach to compute wall stress are compared to the results of fully coupled transient FSI-calculations [138, 142], to the best knowledge of the authors the accuracy of the static FSI approach and the decoupled approach, compared to a fully coupled transient FSI approach, still needs to be assessed.

In this study two axisymmetrical abdominal aortic aneurysm geometries are considered, one without and one with an ILT. The wall stress is quantified using four different approaches. First a transient, fully coupled iterative FSI approach is used to assess the real wall stress distribution. Next the results of three computationally more efficient approaches are compared to the fully coupled results: a static solid finite element approach using a uniform pressure distribution, a static decoupled approach and thirdly a fully coupled static FSI approach.

2 Methods

2.1 Geometry

A simplified, axisymmetrical AAA geometry was used in order to allow a fully coupled approach. The stress-free geometry is given in Fig. 5.1. The geometry without ILT is shown in the upper panel, the geometry with ILT is shown on the lower panel. The ILT-free geometry has a maximum lumen diameter of $6.32cm$; the geometry with ILT supposes the aneurysmal cavity to be completely filled with thrombus. A uniform wall thickness of $2.14mm$ was used, adapted from Thubrikar et al. [144].
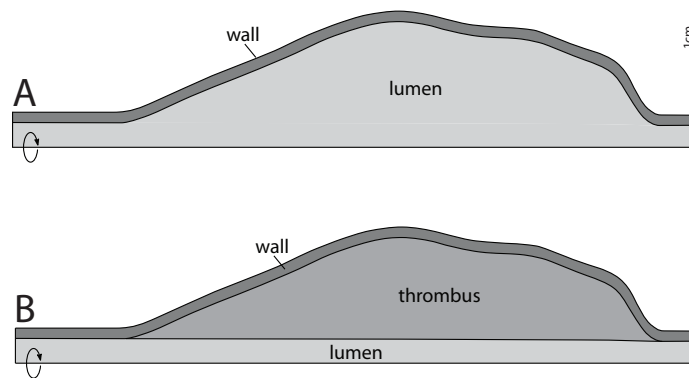
Figure 5.1: The simplified, axisymmetric abdominal aortic aneurysm geometry used in this study. Panel A: geometry without thrombus. Panel B: geometry with thrombus filling the aneurysmal sac.

The geometry was created and meshed using Gambit (ANSYS, Inc.). The fluid domain was meshed using triangular cells. For the structural domain the thrombus was meshed with triangular, quadratic elements ($CAX6$), while the wall was meshed using quadratic, hybrid, reduced, rectangular elements ($CAX8RH$). The geometry without thrombus was meshed with 50496 cells in the fluid domain and 4000 elements in the wall. The geometry with ILT consisted of 16244 fluid cells, 32510 elements in the thrombus and 4000 elements in the wall. Following the approach elaborated in section 2.1.1 of the previous chapter, both meshes yielded mesh-independent wall deformation and Von Mises stress distribution results.

2.2 Solid mechanics computation

The finite element software Abaqus (Simulia, Inc.) was used to compute the wall deformation and stress distribution in the aneurysmal wall and in the thrombus. A

large displacement formulation was used. On both ends of the aneurysm symmetric boundary conditions were imposed, allowing radial movement but preventing axial movement of the nodes in both planes.

The aneurysmal wall was modeled as an incompressible, isotropic, hyperelastic material as proposed by Raghavan et al. [145], using a strain energy function W

$$W = \alpha(I_C - 3) + \beta(I_C - 3)^2 \tag{5.1}$$

with material parameters $\alpha = 0.174 MPa$ and $\beta = 1.881 MPa$. These values are obtained from uniaxial testing of 69 excised human AAA's. I_C denotes the first invariant, the trace, of the left Cauchy-Green tensor. The intraluminal thrombus was modeled as an isotropic, elastic material with Young's modulus $0.11 MPa$ and Poisson ratio 0.45, population-mean values obtained from uniaxial testing of harvested human AAA's by Di Martino et al. [146].

2.3   Flow computation

Fluent (ANSYS, Inc.) was used as a computational dynamics fluid solver to solve the Navier-Stokes equations. Using an arbitrary Lagrangian-Eulerian approach the solver allows for moving mesh flow computations. Blood is modeled as a Newtonian fluid, a good assumption in the macrocirculation [87], with a density $1050 kg/m^3$ and a viscosity $4 mPa \cdot s$, representative for human blood at 37^oC.

The transient boundary conditions for both geometries were assessed using the non-linear one-dimensional model of the human systemic circulation of Stergiopulos et al. [1]. The parameters of the model were somewhat tuned so that the flow and pressure results from the one-dimensional model match the flow and pressure results measured in an anatomically correct 1:1 scale hydraulic elastic tube model of the arterial tree present in our research group [95, 99]. More details on the tuning of the parameters can be found in Swillens et al. [95]. This match will allow multi-field studies in the future.

The 55 segments of the model, shown in Fig. 5.3, were extended with extra segments in the abdominal region to allow implementation of an abdominal aortic aneurysm geometry. In the ILT-free case 6 segments were added, in the ILT-filled case 5 segments were added. The compliance of the abdominal aorta segments, given in Table 5.1, were changed to match a pressure-area relationship which was computed using a finite element model of both geometries.

Flow was used as an input for the one-dimensional model and a heart rate of $60 beats/min$ was used throughout the calculations. The flow upstream the aneurysm and the pressure downstream the aneurysm which were obtained for both geometries are given in Fig. 5.2. The upper panel denotes the transient boundary conditions for the thrombus-free geometry, while the lower panel gives
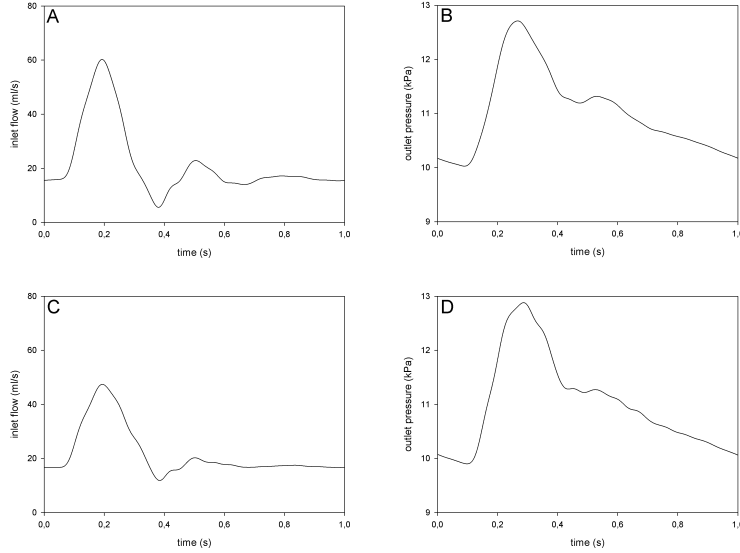
Figure 5.2: The boundary conditions imposed in the transient fluid-structure inter-action coupled calculation. Upper panels: Boundary conditions for the ILT-free geometry; Inlet flow (panel A) and outlet static pressure (panel B). Lower panels: Transient FSI-boundary conditions for the geometry with ILT; Inlet flow (panel C) and outlet static pressure (panel D).

the transient boundary conditions for the ILT-geometry. A time step of $5ms$ proved to be a good choice with regard to stress distribution and deformation of the aneurysmal wall and thrombus. If one was interested in the precise flow veloc-ity distribution in the aneurysmal sac a smaller time step is imperative, however in this application independence of the wall stress distribution is sufficient. Two cycles are computed and the results from the second cycle were analyzed in order to avoid dependency of the results from initialization choices.

For the thrombus-free geometry the flow peak $Q_{max} = 60.21ml/s$ occurred at $0.193s$, while the pressure peak $P_{max} = 12.71kPa$ occurred at $0.267s$. The ILT-geometry had a peak flow $Q_{max} = 47.42ml/s$ at $0.194s$ and a peak pressure $P_{max} = 12.88kPa$ at $0.287s$. For the static computations, the peak inlet flow was used as a steady inlet boundary condition and the peak outlet pressure was used as a steady outlet boundary condition. The pure solid mechanics computation used a uniform pressure distribution with P_{max}.
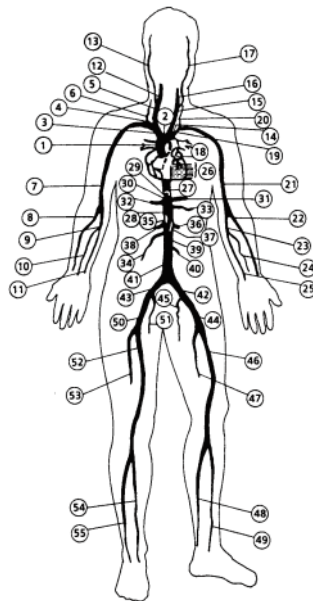
Figure 5.3: The segments of the original Stergiopulos model. Taken from [1].

2.4 Fluid-structure interaction

As stated in the introduction, the problem was tackled using four approaches. The fluid-structure interaction approach, used for the transient and the static FSI-calculation, will be briefly explained in the next paragraphs. The third approach used a decoupled method, where the static fluid problem was solved first. The computed pressure distribution at the fluid-solid interface was then used as a non-uniform pressure distribution for a static continuum solid mechanics computation of the aneurysmal wall (and thrombus). The fourth approach used a pure computational solid mechanics approach with uniform pressure distribution.

The used FSI method for the transient calculations was based on an iterative partitioned solver approach. One can show that in transient, biomechanical fluid-structure interaction problems an iterative loose coupling between the fluid and the solid solver will tend toward instability [75]. A stabilization scheme is thus required. Here, reduced order models [147] of the fluid and structural solver were used to obtain a strong coupling between Fluent 6.3 (ANSYS, Inc.) and Abaqus 6.6 (Simulia, Inc.).

Generally, the FSI equations to be solved can be written as

ID	L [cm]	A_{in} [cm²]	A_{out} [cm²]	β [1/MPa]
35	0.5	1.12	1.26	5.46
37	1.3	1.26	4.22	5.95
39	1.3	4.22	9.79	6.67
40	1.1	9.79	16.6	7.16
41	1.6	16.6	28.3	7.18
42	1.8	28.3	31.9	6.11
43	1.7	31.9	26.4	6.29
45	1.4	26.4	20.3	7.11
46	1.0	20.3	13.2	6.31
47	2.0	13.2	1.32	5.22
35	1.5	1.15	1.38	6.0
37	1.4	1.38	1.53	17.8
39	1.6	1.53	1.58	25.8
40	1.8	1.58	1.57	29.8
41	1.9	1.57	1.53	30.9
42	1.6	1.53	1.47	31.3
43	1.6	1.47	1.36	30.4
45	1.4	1.36	1.09	27.2
46	0.9	1.09	0.5	14.2

Table 5.1: The specifications of the relevant abdominal aorta segments to mimic the presence of an aneurysm, without ILT (top table) and with ILT (bottom table). Segment number ID, segment length L, surface area at inlet A_{in} and outlet A_{out} of the segment and segment distensibility $\beta = (1/A) \, dA/dP$.

$$F(u^f, p^f) \quad = 0 \quad in \; \Omega_f, \tag{5.2}$$

$$S(\epsilon^s, \sigma^s) \quad = 0 \quad in \; \Omega_s, \tag{5.3}$$

$$X^f \quad = X^s \quad on \; \Gamma \tag{5.4}$$

$$p^f \quad = p^s \quad on \; \Gamma, \tag{5.5}$$

where u^f and p^f denote the flow velocity and the pressure distribution in the fluid domain Ω^f. The fluid domain is described by equations $F(u^f, p^f) = 0$. Similarly, ϵ^s and σ^s are the strain and the stress distributions in the structural domain Ω^s, described by equations $S(\epsilon^s, \sigma^s) = 0$. X^f and X^s denote the positions of the interface nodes on the fluid side and the structural side of the interface Γ respectively. p^f and p^s denote the pressure distribution on the interface Γ, on the fluid side and the structural side, respectively. Only pressure was coupled between the two solvers, as the deformation of the vessel wall due to shear was negligible.

Each iteration, the fluid solver is called, resulting, after k iterations, in k couples (X_i^f, p_i^f) $i = 1, .., k$. X_i^f denotes the vector keeping the position information of the fluid side of the interface nodes of iteration i; p_i^f denotes the vector holding the pressure distribution information for the faces on the fluid-side of the interface of iteration i. From these couples $k - 1$ couples are constructed, holding the displacement $\Delta X_i^f = X_i^f - X_k^f$ $i = 1, .., k - 1$ of the interface and the induced pressure changes $\Delta p_i^f = p_i^f - p_k^f$ $i = 1, .., k - 1$.

At this point an unknown displacement $\Delta X^f = X^f - X_k^f$ can be approximated as an optimal linear combination of the displacement modes ΔX_i $i = 1, .., k - 1$

$$\Delta X^f \approx \sum_{i=1}^{k-1} \alpha_i \Delta X_i^f \qquad (5.6)$$

Now, the unknown induced pressure change $\Delta p^f = p^f - p_k^f$ can be approximated as the same linear combination of the pressure modes.

$$\Delta p^f \approx \sum_{i=1}^{k-1} \alpha_i \Delta p_i^f \qquad (5.7)$$

After assessing the optimal linear combination, one arrives at matrix Eq. (5.8), where $\hat{F}_X$ is the approximating Jacobian for the fluid solver.

$$p^f = p_k^f + \hat{F}_X(X^f - X_k^f) + p_{corr} \qquad (5.8)$$

The same can be done with the pressure distribution on the structural side of interface and the induced displacement of the structural interface nodes (p_i^s, X_i^s) $i = 1, .., k$. An unknown pressure distribution p^s can then be written as a linear combination of the known pressure changes, so that the induced position of the structural nodes can be approximately quantified by the matrix equation (5.9).

$$X^s = X_k^s + \hat{S}_p(p^s - p_k^s) + X_{corr} \qquad (5.9)$$

With each additional iteration, an additional mode is added to the approximations of the respective Jacobians $\hat{F}_X$ and $\hat{S}_p$, resulting in a decrease of the residual terms p_{corr} and X_{corr}. Neglecting the correction terms, one obtains

$$\begin{aligned} p^f &= p_k^f + \hat{F}_X(X^f - X_k^f) \\ X^s &= X_k^s + \hat{S}_p(p^s - p_k^s) \end{aligned} \qquad (5.10)$$

Now the solution of the FSI problem can be calculated as the solution (X, p) for which both equations 5.10 are fulfilled.

$$X = \left(I - \hat{S}_p\hat{F}_X\right)^{-1} \left[X_k^s + \hat{S}_p\left(p_k^f - p_k^s - \hat{F}_X X_k^f\right)\right] \qquad (5.11)$$

$$p = \left(I - \hat{F}_X \hat{S}_p\right)^{-1} \left[p_k^f + \hat{F}_X \left(X_k^s - X_k^f - \hat{S}_p p_k^s\right)\right] \qquad (5.12)$$

These solutions X, p can serve as a new estimate for an other iteration of the solver until convergence is reached. More details about the approach can be found in [147] and chapter 3. The approach showed to be considerably faster than the Aitken acceleration method [148].

3   Results

The main interest is the comparison of the wall stress distributions in the different cases. Wall stress is given as Von Mises stress σ_{VM} (Eq. (5.13)). The Von Mises stress is a scalar, computed from the stress tensor, and proportional to the strain energy density at each point.

$$\sigma_{VM} = \frac{1}{\sqrt{2}} \sqrt{(\sigma_1 - \sigma_2)^2 + (\sigma_1 - \sigma_3)^2 + (\sigma_2 - \sigma_3)^2} \qquad (5.13)$$

where σ_1, σ_2 and σ_3 denote the principal stresses.

The stress distribution of the thrombus-free geometry is given in Fig. 5.4, one quarter of the circumference is taken out to allow the stress distribution in the wall to be visible. The different approaches show very good resemblance, both qualitatively and quantitatively.

method	$\sigma_{peak}(Pa); ILT - free$	$\sigma_{peak}(Pa); ILT$
transient FSI	$1.713\ 10^5$	$6.331\ 10^4$
static FSI	$1.703\ 10^5$	$6.375\ 10^4$
decoupled	$1.717\ 10^5$	$6.363\ 10^4$
solid mechanics	$1.692\ 10^5$	$6.347\ 10^4$

Table 5.2: The peak Von Mises stresses.

Fig. 5.5 shows the results for the aneurysm with intraluminal thrombus. Again, both qualitative and quantitative resemblance is seen. Additionally, the peak Von Mises stress observed in all eight cases is given in Table 5.2.

The CPU-time for the eight calculations is given in Table 5.3. The computations for the thrombus-free geometry were performed on a 64-bit, $2.4GHz$ Intel Cor 2Duo E6600-processor, while the computations for the ILT-geometry were performed on a 32-bit, $2.4GHz$ Intel XEON processor.
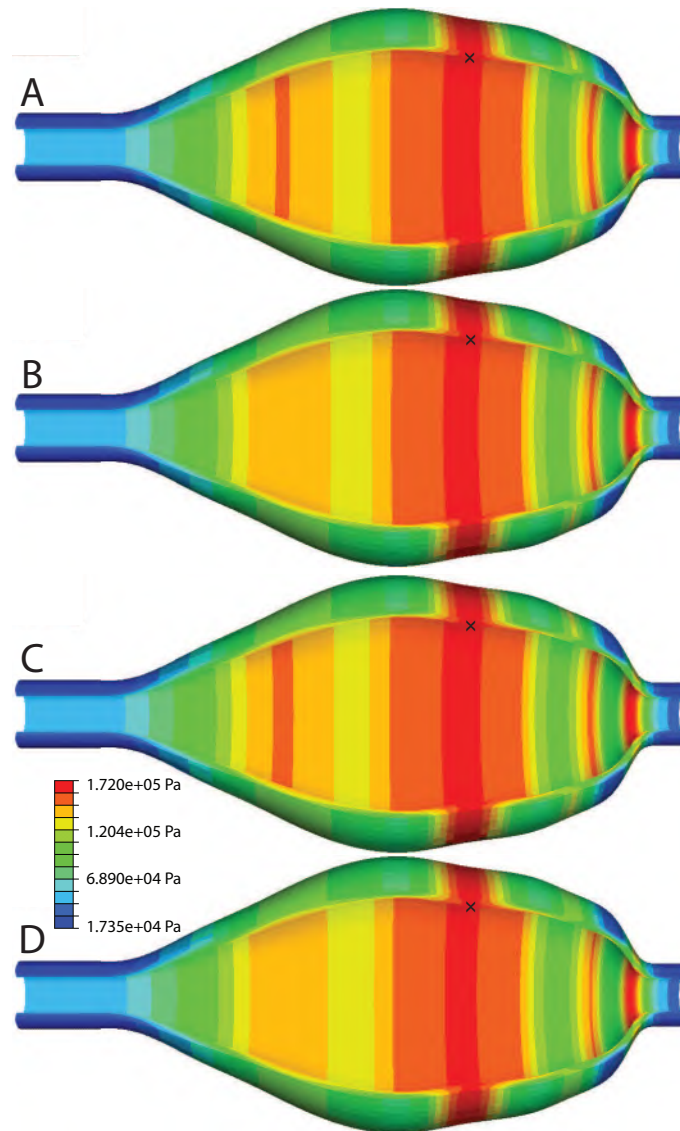
Figure 5.4: The Von Mises stress distribution of the ILT-free aneurysm, where one quarter of the circumference is taken out. The maximum is marked with an "x". Panel A: result from a transient, fully coupled FSI calculation at $t = 1.265s$ where the peak stress occurs. Panel B: result from a static, fully coupled FSI calculation. Panel C: result from a static, decoupled calculation. Panel D: result from a pure solid mechanics computation.
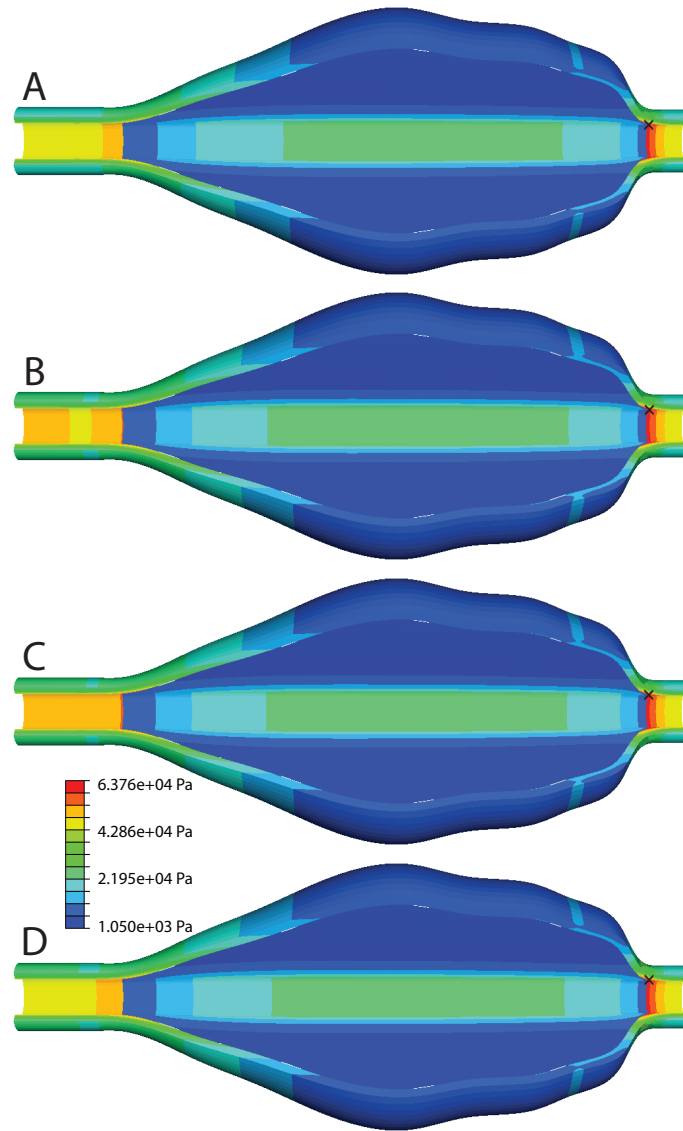
Figure 5.5: The Von Mises stress distribution of the aneurysm with thrombus-filled aneurysmal sac, where one quarter of the circumference is taken out. The maximum is marked with an "x". Panel A: result from a transient, fully coupled FSI calculation at $t = 1.285s$ where the peak stress occurs. Panel B: result from a static, fully coupled FSI calculation. Panel C: result from a static, decoupled calculation. Panel D: result from a pure solid mechanics computation.

method	$ILT - free$	ILT
transient FSI (one cycle)	$6\ days$	$8\ days$
static FSI	$3\ hours$	$4\ hours$
decoupled	$35\ minutes$	$1\ hour$
solid mechanics	$2\ minutes$	$25\ minutes$

Table 5.3: Computational time for the different approaches.

4   Discussion

As found by Leung et al. [142] the finite element approach yields results which do not differ much from the fully coupled transient approach. In this study we showed that a static fully coupled and a decoupled approach do not add extra accuracy compared to the CSM-computation, while they are more CPU-time consuming. Moreover, as seen from the results presented here, it is not predictable if, in a patient-specific peak wall stress calculations, the computationally cheaper approaches will yield an overestimation, as in the ILT-filled aneurysm, or underestimation, as in the ILT-free aneurysm, of the stress peak compared to the fully coupled transient FSI-approach.

In the simplified ILT-calculation the overestimation of peak stress is quite easily explained, as, from the blood flow point of view, this case can be considered as an aneurysm-free vessel with locally varying elastance. In the transient FSI computation, the pressure in the aneurysm is lower than the pressure imposed as a boundary condition at the outlet. Indeed, the maximum flow at the inlet occurs before the maximum in pressure at the outlet is seen. Hence, when the pressure in the aneurysmal cavity reaches its maximum, this maximum will be a little lower than the maximum at the outlet due to the deceleration of the blood flow. In the other three approaches static computations are performed so this effect is not seen in the results. On the contrary, the decoupled and static FSI approach yield a cavital pressure higher than the pressure at the outlet. Obviously, if the outflow duct after the aneurysm would have been taken longer, this effect would be more pronounced, but still the solid mechanics computation would yield the more accurate results. The analysis of the results from the ILT-free computations however is not this easily analyzed.

Based on the stress distribution results, one could also conclude on the beneficial wall stress-reduction of a thrombus. However, since neither the porosity of the thrombus, nor the possible weakening of the aneurysmal wall due to anoxia was taken into account, we believe such a statement can not be made for all intraluminal thrombi. Moreover, rupture risk of the ILT needs to be taken into account. While partial rupture of the thrombus might be less life threatening than rupture of

the aneurysm, the ruptured piece can induce an embolism, a blockage of a down-stream artery and lead to important morbidity. This additional risk, which can add to the decision for intervention, does need to be taken into account when studying the relative advantages of an ILT.

What this study does take into account is the change in boundary conditions occuring when an aneurysm is filled with thrombus or not. To our best knowledge, this effect has not been taken into account before when studying the influence of the ILT. However, due to the difference in compliance and resistance of the abdominal aorta between the thrombus-free aneurysm and the aneurysm with ILT, an overall redistribution of blood flow occurs. As seen on Fig. 5.2, especially the influence on the inlet flow in the aneurysm is more pronounced.

In this study a simplified geometry was used as opposed to a patient-specific geometry. The followed approach, however, is generally applicable to a patient-specific case. As denoted by Raghavan et al. [145], the material law used for the aneurysmal wall is applicable to patient-specific studies as the population variation did show a peak wall stress variation of only 4% when the material parameters were varied within the 95% confidence interval of the population. The material model used for the intraluminal thrombus can also be used for patient-specific studies, as peak stress was seen to be very insensitive to variations in the material parameters. However, as denoted by the authors, the material laws for intraluminal thrombus do only apply to well organized thrombi [146, 149].

In order to calculate the wall stress, the stress-free geometry is needed. Marra et al. [150]and Raghavan et al. [98] developed a technique to establish the stress-free geometry for patient-specific AAA-geometries, where the stress-free geometry is not known a priori. This adds to the accuracy of the stress distributions which are obtained. Next, a good resolution of the images is important, so that the actual, patient-specific, wall thickness distribution can be reconstructed from the images. It is shown that wall thickness does influence the obtained stress distribution [137], hence the use of averaged wall thickness values are only an option if no sufficient imaging resolution is obtained. The resolution is obviously determined by the medical imaging technique which is used.

In the geometry used here the pressure is known at the outlet of the aneurysm, as the boundary conditions are assessed with a non-linear, one-dimensional model of the systemic circulation [1]. However, as opposed to non-invasive flow velocity measurements, the assessment of pressure at the outlet of the aneurysm is not easy in a patient-specific study. One can use the systemic systolic blood pressure as a static load, as done in finite element studies [120, 121, 136]. When transient boundary conditions are needed, one could use flow and pressure curves found in literature, e.g., the curves from Olufsen et al. [151] are used in several studies [141, 142]. The one-dimensional model could also prove useful. By tuning the general properties of the model to match the patient more closely partially patient-specific

boundary conditions can be obtained. However, tuning of the overall compliance parameters of the model is quite time consuming, the geometry on the other hand is easily adapted. Obviously the non-invasive estimation of the patient-specific pressure in the aneurysm is the biggest challenge for future research, whether it is used as a boundary condition for a steady or transient FSI computation or a decoupled approach or for a uniform load in a computational solid mechanics calculation.

The used approach has some limitations. Firstly, while Abaqus (Simulia, Inc.) and Fluent (ANSYS, Inc.) are state of the art solvers, their coupling did not prove to be straightforward. As both packages use a different temporal discretization scheme, instabilities occur. This was solved by eliminating the inertia from the aneurysmal wall and thrombus. Tests comparing the static and dynamic behavior of the wall showed that the inertia forces in the wall are very small compared to the dynamic hydraulic loading induced by the blood, even when the pressure curve as function of time is steepest. Moreover the peak wall stress will occur at or near the maximum of the outlet pressure curve, where evidently the temporal changes in pressure are minimal, adding to the fact that the assumption of the wall being in static equilibrium with the fluid holds.

Secondly, a simplified axisymmetrical geometry was used. For the geometry, two extreme cases were studied, a case where no thrombus was present at all and a case where the aneurysmal sac was completely filled with thrombus. In reality the aneurysmal sac is rarely entirely filled with thrombus, hence, will be found in between the two extreme cases studied here. However, as the findings do not rely on the axisymmetrical assumption, we believe that the findings still hold in a three-dimensional patient-specific case. The fact that static approaches to quantify AAA wall stress do not take the inertia of the blood into account, limits the applicability of the static decoupled and static FSI approaches.

A decoupled approach where this inertia is taken into account could therefore be a useful approach. In such an approach one could first perform a transient flow calculation with fixed boundaries. Once the non-uniform pressure distributions for the different time steps are assessed, they could be used as a transient, non-uniform load to a time dependent finite element computation. This approach will be more time consuming than the static approaches, but less time consuming than a transient FSI computation. One could also limit the computed time period to the end-diastole-peak-systole time interval to further optimize the approach, starting with a static step at end-diastole.

5   Conclusion

We used four common ways to assess peak wall stress in abdominal aortic aneurysms, for both a thrombus-free geometry and a geometry where the aneurysmal

sac is filled with thrombus. Results from a static computational solid mechanics approach, a static decoupled approach, a static and a transient FSI-computation were compared and showed very little difference in obtained peak stress value and location. The added value of a static FSI-computation or a decoupled approach is limited compared to the pure computational solid mechanics calculation. Finally we showed that when comparing the stress distribution with and without ILT, the redistribution of blood flow needs to be taken into account in the imposed boundary conditions.

6

Wave Intensity Analysis of the left ventricle using FSI

In previous chapters wave reflection and propagation behavior was studied, which helped to gain insight in the physiology of the vascular system. In these wave reflection and propagation studies one considers blood flow to be a one-dimensional flow, where the vessel wall interaction is inserted directly into the Navier-Stokes equations, as was done at the beginning of chapter 2. Wave propagation and reflection can be studied with wave intensity analysis. However when studying the propagation of waves in the heart, the wave intensity analysis theory needs adjusting. In this chapter a new method is presented to obtain the wave intensities in the left ventricle during diastole. This may help to unravel the processes leading to diastolic heart failure.

The proposed additions to the classic wave intensity analysis are illustrated using an existing FSI model of left ventricular relaxation. This validated, thin-walled, quasi-three dimensional, axisymmetrical fluid-structure interaction model differs from the fluid-structure approach elaborated in the previous chapters. The fluid-structure interaction model, developed by Vierendeels et al., uses an iterative partitioned solver approach with pseudo-compressibility [152–154]. The illustration shows that the modified method has an influence on the results which can not be neglected[1].

---

[1]The contents of this chapter is published in Transactions of ASME - Journal of Biomechanical Engineering 2005;127:862-867.
Wave Intensity Analysis of Left Ventricular Filling.

Abstract

Wave intensity analysis (WIA) is a powerful technique to study pressure and flow velocity waves in the time domain in vascular networks. The method is based on the analysis of energy transported by the wave through computation of the wave intensity $dI = dpdU$, where dp and dU denote pressure and flow velocity changes per time interval respectively. In this study we propose an analytical modification to the WIA so that it can be used to study waves in conditions of time varying elastic properties, such as the left ventricle (LV) during diastole. The approach is first analytically elaborated for a one-dimensional elastic tube-model of the left ventricle with a time-dependent pressure-area relationship. Data obtained with a validated quasi-three dimensional axisymmetrical model of the left ventricle are employed to demonstrate this new approach. Along the base-apex axis close to the base wave intensity curves are obtained, both using the standard method and the newly proposed modified method. The main difference between the standard and modified wave intensity pattern occurs immediately after the opening of the mitral valve. Where the standard WIA shows a backward expansion wave, the modified analysis shows a forward compression wave. The proposed modification needs to be taken into account when studying left ventricular relaxation, as it affects the wave type.

1   Introduction

It is well established that the propagation and reflection of pressure and flow waves in the cardiovascular system, through the interaction of forward and backward running components, determine the final shape of these waves as they are measured in vivo [107, 155]. In the arterial system, early return of reflected waves in the arterial system present an increased load on the heart and increase cardiovascular risk [156, 157]. In the clinical literature, indices like the augmentation index are being used, with the purpose of quantifying the intensity of wave reflection [158].

Despite this increased interest in wave reflection, many questions still remain unsolved. In the arterial system, the continuous branching of the vessels, their geometric and elastic tapering and their 'termination' in the arteriolar and capillary beds all contribute to the complexity of the pattern of wave reflection. When analyzing pressure and flow waves, the origin and magnitude of reflected components is not easily dissociated from the forward component. In the ventricle, a three-dimensional closed-end system in diastole with actively time-varying elastic properties, the analysis of pressure waves is even more complex.

Lieve Lanoye[1], Jan Vierendeels[2], Patrick Segers[1], Pascal Verdonck[1].
[1]Cardiovascular Mechanics and Biofluid Dynamics, Institute of Biomedical Technology, Ghent University, Belgium.
[2]Department of Flow, Heat and Combustion, Ghent University, Belgium.

Wave intensity analysis (WIA) is a mathematical tool that helps to understand the fluctuations in pressure and flow velocity in a one-dimensional tube system like the arterial system. With an origin in electric network theory, arterial pressure and flow wave analysis is often done in the frequency domain, using the Fourier theorem to decompose the waves in series of sinusoidal harmonics and to assess information on wave reflection via analysis of the impedance spectrum. Although this approach is not mathematically complex, results are not intuitively interpretable.

Wave intensity analysis however sticks to the time domain and the results are more intuitively interpretable than when the analysis is done in the frequency domain. Since the introduction of the theory by Parker and Jones [33], its application has become well established and has been applied to many different vascular flow problems [94, 159–161], an overview is found in Bleasdale et al. [162].

However, tools and theories are sometimes applied beyond their limitations and intended field of application. In our opinion, this is the case with the 'classical' wave intensity analysis when it is being applied in the left ventricle to analyze diastolic function. MacRae et al. [163] were the first to use wave intensity analysis to analyze the wave intensity pattern in the left ventricle during diastole. They measured the apical pressure and the transmitral flow velocity and calculated wave intensity in the way that it is commonly done in one-dimensional tubes. The obtained pattern was explained using the theory of wave-reflections at the base and the apex.

Wave intensity analysis, however, is based on a one-dimensional 'passive' theory, by which is meant that it is applicable to one-dimensional elastic tubes with time invariant wall properties. As the left ventricle (LV) is a three-dimensional relaxing structure, the theoretical basis of wave intensity analysis no longer applies, and modifications should be considered. In this study we introduce a methodology that takes into account the time-varying elastic properties of the left ventricular wall during diastole, which may expand the applicability of this technique to estimate wave intensities in the left ventricle during diastole.

2 Methods

2.1 Wave intensity analysis in a one-dimensional vessel

Standard wave intensity analysis, as it is used in arterial mechanics, is based on the equations of flow in a one-dimensional elastic tube. These hyperbolic equations describe the pressure and flow velocity variations that occur when a one-dimensional flow pattern in a tube is changed. These perturbations induce pressure and flow velocity waves which travel with speed $U \pm c$, where c is the wave speed and U the flow velocity. The wave traveling at $U + c$ is a forward wave, labeled with a '$_+$' in the calculations. As the wave speed in the cardiovascular system is

generally larger than the flow velocity (subcritical flow), the wave which travels with speed $U - c$ is a backward wave and the variables linked to this wave are labeled with a '$_-$'.

From the equations, using the method of characteristics [33], one derives that the incremental differences in pressure $dp_\pm$ and in flow velocity $dU_\pm$ of both forward and backward waves are related through the equation:

$$dp_\pm = \pm \rho c dU_\pm \tag{6.1}$$

where ρ is the density of blood and c the wave speed. If the contributions of the forward and the backward waves are assumed additive, i.e.,

$$dp = dp_+ + dp_- \tag{6.2}$$
$$dU = dU_+ + dU_- \tag{6.3}$$

the measured changes in pressure dp Eq. (6.2) and flow velocity dU Eq. (6.3) can be separated into the two contributions:

$$dp_\pm = \frac{1}{2}\left(dp \pm \rho c dU\right) \tag{6.4}$$
$$dU_\pm = \pm \frac{1}{2}\left(\frac{dp}{\rho c} \pm dU\right) \tag{6.5}$$

These equations are only valid if the system can be linearized [33]. In order to separate these waves, the density of the fluid has to be known, which is easy to measure. The wave speed c has to be determined too. This can be estimated, using the Moens-Korteweg equation, or by measurement. To measure the wave speed one assumes that right after the aorta valve opens only forward waves are present in the vascular arteries. At that time the a pU-diagram is a straight line, which slope is ρc. An overview of both techniques is given by Khir et al. [164].

The wave intensity dI $[\frac{W}{m^2}]$, defined as follows

$$dI = dp dU \tag{6.6}$$

represents the energy carried by a single wave. The wave intensity of a forward wave dI_+ and of a backward wave dI_- is given in Eq 6.7 [161].

$$
\begin{aligned}
dI_+ &= dU_+ dp_+ = \frac{1}{4\rho c}(dp + \rho c dU)^2 \\
dI_- &= dU_- dp_- = -\frac{1}{4\rho c}(dp - \rho c dU)^2
\end{aligned}
\tag{6.7}
$$

Based on the sign of dp and dU four different types of waves are distinguished. When the pressure rises in time ($dp > 0$) the wave is called a compression wave, when it decreases in time ($dp < 0$) the wave is called an expansion wave. Once an

orientation of the axis in the one-dimensional system is chosen to be the forward direction, the change in flow velocity is called positive ($dU > 0$) if the flow velocity rises in this direction. If the flow velocity decreases in this direction or rises in the opposite direction, the change in flow velocity is called negative ($dU < 0$).

dp	dU	dI	wave type	
$+$	$+$	$+$	FCW	forward compression wave
$+$	$-$	$-$	BCW	backward compression wave
$-$	$+$	$-$	BEW	backward expansion wave
$-$	$-$	$+$	FEW	forward expansion wave

Table 6.1: Definition of the four different wave types.

By taking a look at Table 6.1, it can be seen that a forward wave has a positive wave intensity, whereas a backward wave has a negative intensity. Equation (6.1) states that for a forward expansion wave (FEW) the flow velocity decreases in time and that for a forward compression wave (FCW) the flow velocity increases in time. Furthermore for a backward expansion wave (BEW) the flow velocity will rise as a function of time, but for a backward compression wave (BCW) the flow velocity will decrease in time. These relations are given in Table 6.1.

Using Eq. (6.1) one can show that, if intersecting wave components are additive, the wave intensity of a wave is the sum of the intensities of the forward and the backward components of that wave, so that the wave intensity becomes

$$
\begin{aligned}
dI &= dpdU \\
&= (dp_+ + dp_-)(dU_+ + dU_-) \\
&= dp_+dU_+ + dp_-dU_- \\
&= dI_+ + dI_-
\end{aligned}
\tag{6.8}
$$

When the total wave intensity dI is calculated, its sign tells whether it is the forward wave which dominates the backward wave or whether it is the other way around.

Equations (6.2) and (6.3) are based on a linearization of the system. If this is not possible, the above mentioned equations are no longer valid. However, the most important property of the wave intensity here, namely that it is positive for forward waves and negative for backward waves, is not based on this assumption [33]. It is thus possible to use wave intensity analysis to study the waves in a highly non-linear system.

2.2 Wave intensity analysis in the relaxing left ventricle

Some modifications are necessary to adapt wave intensity analysis to relaxing structures, such as the ventricle during diastole. The ventricular wall is a relaxing

structure whereas the standard wave intensity analysis assumes elastic wall properties which do not change in time. It is well accepted that the ventricular wall has time-varying mechanical properties over the cardiac cycle [165]. The analysis as explained before is thus no longer valid.

2.2.1 Analytical derivation

The one-dimensional flow equations in an impermeable and uniform elastic tube reduce to Eq. (6.9) along the characteristic directions [33].

$$\frac{dU}{dt} \pm \frac{1}{\rho c}\frac{dp}{dt} = \mp\frac{c}{A}\left(\frac{\partial A}{\partial t} + U\frac{\partial A}{\partial z}\right) \tag{6.9}$$

U is the flow velocity, p is the pressure, c is the wave speed and A is a function that gives the cross-sectional area S as a function of p, z and t given in Eq. (6.10).

$$S = A(p; z, t) \tag{6.10}$$

Partial derivatives with respect to time t or place z are written as $\partial/\partial t$ and $\partial/\partial z$, respectively. The derivatives d/dt here denote the derivatives along the characteristics.

$$\frac{d}{dt} = \frac{\partial}{\partial t} + (U \pm c)\frac{\partial}{\partial z} \tag{6.11}$$

To avoid confusion the notation $\delta/\delta t$ will be used when a total derivative is meant.

In a straight tube where the material properties do not change in time or space, the term in the right hand side of Eq. (6.9) is zero leading to Eq. (6.1) as applied in arterial mechanics.

During relaxation in the ventricle however this term has to be taken into account. Eq. (6.9) can be rewritten as

$$\frac{dU}{dt} \pm \frac{1}{\rho c}\frac{d}{dt}\left(p + \int_t \frac{\rho c^2}{A}\left(\frac{\partial A}{\partial t} + U\frac{\partial A}{\partial z}\right) dt\right) = 0 \tag{6.12}$$

Instead of calculating with the measured pressure p, the analysis can be done using a modified pressure p'

$$p' = p + \int_t \frac{\rho c^2}{A}\left(\frac{\partial A}{\partial t} + U\frac{\partial A}{\partial z}\right) dt \tag{6.13}$$

Equation (6.12) can then be written in the new form, which has the same form as the equation in the water hammer theory [33], but with a modified pressure p'.

$$\frac{dU}{dt} \pm \frac{1}{\rho c}\frac{dp'}{dt} = 0 \tag{6.14}$$

This leads to a modified wave intensity dI' $[W/m^2]$, defined in Eq. (6.15).

$$dI' = dU \, dp' \tag{6.15}$$

To calculate dI' the wave speed c and the function $A(p; z, t)$ need to be known. Despite considerable efforts [166], it is not easy to determine the wave speed in the ventricle as a function of time at the points where wave intensity analysis is done. The correct expression for the function A is not well established. So this analytical modification can not be calculated easily.

2.2.2 One-dimensional approximation of the left ventricle

In order to calculate the integral on the right hand side of Eq. (6.13), the function $A(p; z, t)$ has to be known. In this study we want to demonstrate the proposed approach by looking at ventricular relaxation. In earlier papers [163] on left ventricular filling both terms in the integrand of Eq. (6.13) are neglected. Here we will focus on the influence $\partial A / \partial t$ has on the wave intensity pattern. Consider a one-dimensional approximation of the left ventricular relaxation where the ventricular wall relaxes in a synchronous manner, as done earlier by Owen [167]. The influence of this approximation will be discussed later.

Firstly, in order to find an expression for $\partial A / \partial t$, consider a complete diastole 'vc', 'valve closed', where the left ventricle relaxes, but without inflow through the mitral valve. The valve is blocked or forced to stay closed and the diastole becomes a *sustained isovolumetric relaxation*. To make a clear distinction between the normal diastole and the sustained isovolumetric relaxation a subscript '$_{vc}$' is added to all parameters of this latter case. In this case the unknown function $\partial A_{vc} / \partial t$ can be approximately calculated as explained next.

In the current model the relaxation is considered to be homogeneous, so, as there is no mitral inflow, no pressure gradients are present and the flow velocity is zero. The cross-section is a constant over time. On the other hand the change in cross-section can be written as a function of derivatives of $A_{vc}(p; z, t)$.

$$\frac{\delta S_{vc}}{\delta t} = \frac{\partial A_{vc}}{\partial p_{vc}} \frac{\partial p_{vc}}{\partial t} + \frac{\partial A_{vc}}{\partial t} = 0 \tag{6.16}$$

$\delta / \delta t$ denotes a total derivative, not to be confused with d/dt, the derivative along the characteristics. In Eq. (6.16) $\partial A_{vc} / \partial t$ can be isolated.

$$\frac{\partial A_{vc}}{\partial t} = -\frac{\partial A_{vc}}{\partial p_{vc}} \frac{\partial p_{vc}}{\partial t} = -\frac{A_{vc}}{\rho \, c_{vc}^2} \frac{\partial p_{vc}}{\partial t} \tag{6.17}$$

as the square of the wave speed is given by

$$c_{vc}^2 = \frac{A_{vc}}{\rho} \frac{\partial p_{vc}}{\partial A_{vc}} \tag{6.18}$$

p_{vc} denotes the pressure profile during this relaxation with a closed mitral valve. The pressure p_{vc} in the left ventricle during relaxation is independent of the coordinate along the base-apex axis, as the flow velocities are zero. The partial derivative $\partial p_{vc}/\partial t$ in Eq. (6.17) is identical to dp_{vc}/dt, the derivative along the characteristics, Eq. (6.11).

$$\frac{\partial A_{vc}}{\partial t} = -\frac{A_{vc}}{\rho\, c_{vc}^2}\frac{dp_{vc}}{dt} \tag{6.19}$$

Secondly, consider the same left ventricle, now *during regular diastole*. The function $A(p; z, t)$ here is the exact same function as $A_{vc}(p; z, t)$ in the previous situation, as this function only describes the wall properties, such as the wall's rate of relaxation. The wall properties do not change under different loading conditions, so this expression (6.19) for $\partial A_{vc}/\partial t$ is still valid for a regular diastole. Eq. (6.13) for the modified pressure p' can be rewritten as

$$p' = p - \int_t \frac{\rho c^2}{A}\left(\frac{A_{vc}}{\rho\, c_{vc}^2}\frac{dp_{vc}}{dt}\right)dt = p - \int_t \frac{c^2}{c_{vc}^2}\frac{dp_{vc}}{dt}dt \tag{6.20}$$

as $A_{vc}(p; z, t) = A(p; z, t)$. The fraction c^2/c_{vc}^2 is not equal to unity, as in the definition of the wave speed (Eq. (6.18)) the partial derivatives of the pressure with respect to the cross-sectional area are not the same. However from the calculations of the model described in the next section we saw that in normal filling circumstances this ratio will not exceed 1.11. Hereby the ratio is not taken into account.

$$p' = p - \int_t \frac{dp_{vc}}{dt}\, dt \tag{6.21}$$

In order to obtain a modified wave intensity dI' that changes only due to the pressure and flow velocity waves in the left ventricle and not because of the relaxation, the wave intensity analysis needs to be done based on the modified pressure p' defined as

$$p' = p - p_{vc} \tag{6.22}$$

2.2.3 Computational approximation

So far a one-dimensional approach is used. It is useful to apply the proposed approach to a more-dimensional model of the left ventricle in order to see whether the obtained pattern can help to understand the waves occurring in the left ventricle.

The pressures and velocities used to test the feasibility of the analysis are obtained from a validated computer model [152–154]. An axisymmetrical truncated prolate ellipsoid is used to represent the geometry of the left ventricle. The specifications given in Table 6.2 represent a canine ventricle.

Equilibrium volume	$12.00\,ml$
Diameter of the mitral valve	$1.50\,cm$
Distance base-apex	$4.00\,cm$
Short axis of the ellipsoid	$1.15\,cm$
Long axis of the ellipsoid	$2.28\,cm$

Table 6.2: The equilibrium geometry of the computational model.

We only consider the diastolic phase. The start of the isovolumetric relaxation corresponds to $t = 0$ where t denotes the time. Once the ventricular pressure reaches the atrial pressure (pressure cross over) a uniform velocity profile is imposed at the mitral valve. The atrial pressure at opening of the mitral valve ($0.89\,kPa$ or $6.7\,mmHg$), and the velocity profile (Fig. 6.11A) are calculated with the lumped parameter model of Meisner [168] using a heart rate of $80\,beats/min$ [154] to obtain a physiologically relevant parameter set.
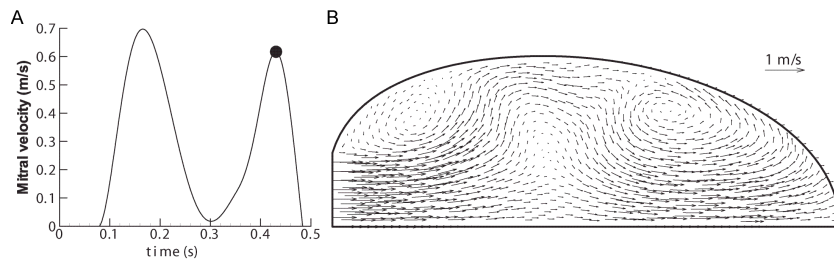
Figure 6.1: Panel A : The flow velocity profile imposed at the mitral valve in the computational model. At the start of the relaxation ($t = 0\,s$) the valves are closed and the imposed flow velocity is zero. Once the ventricular pressure drops below the left atrial pressure the velocity profile is no longer zero and the early filling phase starts (E-peak). After $t = 0.3\,s$ a second peak A occurs due to atrial contraction. The imposed profile is uniform. Panel B : Plot of the flow velocity pattern in the left ventricle at the top of the A-peak (atrial contraction).

In order to model the relaxation of the ventricle, an exponentially decreasing Young's modulus is used. The isovolumetric relaxation constant τ is $30\,ms$ [168], the initial value of the modulus is set so that an imposed pressure-volume loop is followed, matching the lumped parameter model of Meisner. This Young's modulus is then used in a non-linear stress-strain relationship, similar to the one used by Janz and Grimm [169, 170]. The calculation is performed starting from an end systolic pressure of $10\,kPa$ or $75\,mmHg$. Further details on the model can be found in [152–154].

3   Results and discussion

One-dimensional pressure and velocity waves are induced by dynamic changes in pressure or velocity. Wave intensity analysis studies these waves, but the theory as commonly applied is only analytically correct in an elastic tube of which the material properties do not change in time. We present an extension to this method that allows us to study wave intensities in the left ventricle during diastole.

The flow velocity and pressure curves at $0.5cm$ starting from the base along the base-apex axis are given in Fig. 6.2A and B as a function of time. In order to calculate p_{vc} and p' a numerical experiment with closed mitral valve is performed. The pressure in the left ventricle at $0.5\,cm$ starting from the base along the base-apex axis is given in Fig. 6.2B (dashed line). The time step Δt used in the calculations is $1.5ms$.

Wave intensity analysis is performed at $0.5cm$ from the base along the base-apex axis using the standard analysis, giving dI, and the modified analysis, giving dI' given in Fig. 6.2C. Before the opening of the mitral valve (isovolumetric relaxation) the flow velocities are very small and the wave intensity is negligible. Once the valve opens, waves occur and the intensity is no longer zero. The modified wave intensity dI' shows a forward compression wave with peak at $t = 0.116\,s$, followed by a backward compression wave starting at $t = 0.172\,s$. After $t = 0.284\,s$ a small forward expansion wave is seen, followed by a second forward compression wave at $t = 0.336\,s$. Finally from $t = 0.435\,s$ a backward compression wave ends the pattern.

The dI'-pattern can be explained with the basic rules of reflection physics, given in Bleasdale et al. [162]. A compression wave reaching a closed end, such as the apex, is reflected as a compression wave, where at an open end, such as the open mitral valve, the wave will be reflected as an expansion wave. The forward compression wave occurring right after the opening of the mitral valve is reflected at the apex (closed end) into a backward compression wave. This compression wave is then reflected at the open mitral valve (open end) into a forward expansion wave. This backward wave is soon dominated by a forward compression wave due to atrial contraction. Finally this forward compression wave reflects at the apex, inducing a backward compression wave.

There remain some pitfalls and practical limitations. Firstly, the parameter p_{vc} needs to be determined, representing the elastic status of the wall. As pointed out above it is easily calculated or simulated in a computational model. In an in vitro situation the parameter can be measured quite easily as well [171]. The main difficulty occurs when applying wave intensity analysis in vivo, in which case measuring the pressure during diastole with closed mitral valve is virtually impossible. Here one could use an exponential extrapolation for p_{vc}, where the relaxation constant τ is estimated from the measured pressure-curve during iso-
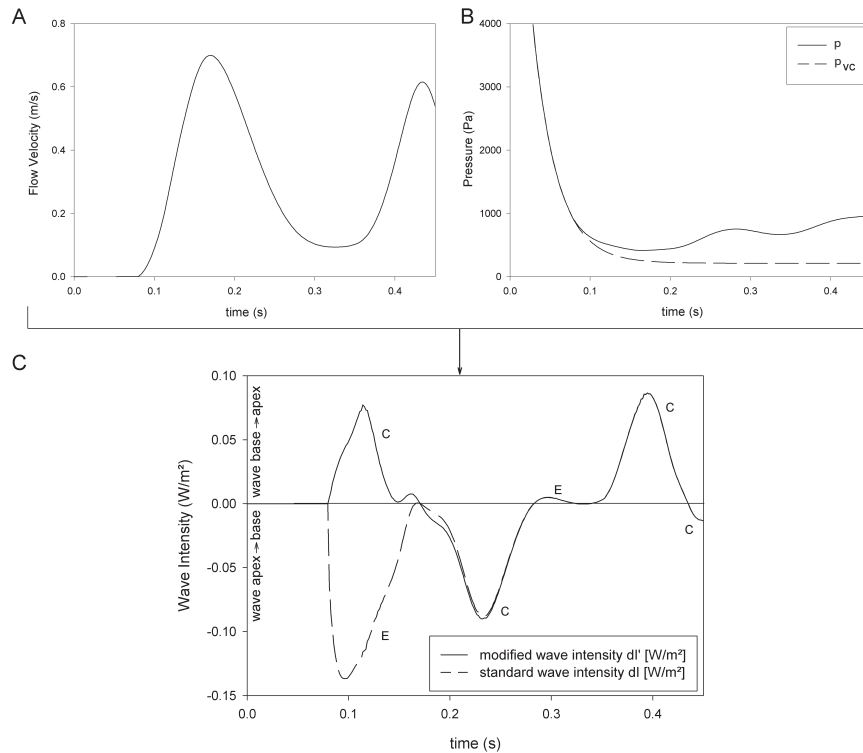
Figure 6.2: Panel A : The profile of flow velocity-component parallel to the base-apex axis at $0.5cm$ starting from the base along the base-apex axis. For all panels time $t = 0s$ corresponds to the closure of the aortic valve. After $0.08s$ the mitral valve opens and the filling phase starts. Panel B : The ventricular pressure as a function of time at $0.5\,cm$ starting from the base along the base-apex axis. Full line: Simulation where the mitral valve opens after $0.08s$ as described above. Dashed line: Simulation where the mitral valve remains closed during relaxation, this situation was simulated by imposing a mitral velocity zero during diastole. Panel C : The wave intensity at $0.5cm$ starting from the base along the base-apex axis. The curve dI' gives the modified wave intensity, the curve labelled dI gives the standard wave intensity. C : compression wave; E : expansion wave.

volumetric relaxation [172].

Secondly, as wave intensity analysis in the left ventricle is more complex than in a uniform tube, the dimensional aspect needs to be considered. The ventricle is a three-dimensional structure (an axisymmetrical quasi-three-dimensional approach is used in the model), but wave intensity analysis is a one-dimensional

theory. Figure 6.1B shows a vector plot of the flow field at the top of the A-peak in the left ventricle. It can be seen that a jet is formed. The velocity components perpendicular to the symmetry axis are significantly smaller than the components parallel to the axis. The velocity variations along the axis also dominate the variations perpendicular to the axis. Near the symmetry axis, compared to the radius of the mitral valve (here $0.75cm$), a one-dimensional approach is a good approximation. As the analysis is done along the axis, the waves are treated as if they were one-dimensional. This assumption is also supported by McRae et al. [163].

Moreover, the sequence of wave types obtained here can be entirely explained with the basic rules of wave reflection physics. It is very plausible that the one-dimensional approach might deform the shape of the curves slightly, but it will not affect the wave type. Therefore, even though wave intensity analysis is basically a one-dimensional theory, it is still very useful in the ventricle. The term $\partial A/\partial t$ however does need to be taken into account. This term affects the sign of the wave intensity, and thus the conclusion about the direction and type of wave is considered. This is clearly seen on figure 6.2, right after the opening of the mitral valve. The conventional wave intensity analysis shows a backward expansion wave, whereas, after taking into account the term $\partial A/\partial t$ through p_{vc}, a forward compression wave is seen. It is acknowledged that verification and further validation is necessary in anatomically and physiologically more complex numerical and/or experimental models.

4   Conclusion

Wave intensity analysis is a very promising technique to examine the general state of the cardiovascular system, as each part of the system influences the wave intensity profile. The conventional analysis however is a one-dimensional theory applicable on structures with passive wall properties. When applying the theory to a relaxing ventricle an adjustment is needed.

The proposed modification has important consequences on the sign of the wave intensity and hence on the interpretation of the observed wave pattern. When the conventional wave intensity analysis is applied to the pressures and flow velocities in the left ventricle, a backward expansion wave is initially seen at every point of the base-apex axis. The modified analysis shows a forward compression wave right after the mitral valve opens. The modified wave pattern can be explained from the reflections at the apex and the base from two forward compression waves associated at early filling (E) and atrial contraction (A) phases in the velocity profile.

The modification here presented is of importance to study left ventricular filling, but it might be useful for any other situation where Young's modulus changes, for example during ventricular contraction.

Acknowledgments

Nomenclature

$A(p; z, t)$	=	function giving cross-section, $[m^2]$
c	=	wave speed, $[m/s]$
$\partial/\partial t$	=	partial derivative with respect to time, $[s^{-1}]$
$\delta/\delta t$	=	total derivative with respect to time, $[s^{-1}]$
d/dt	=	$\partial/\partial t + (U \pm c)\partial/\partial z$
		derivative with respect to time taken along the characteristics, $[s^{-1}]$
I	=	wave intensity, $[W/m^2]$
p	=	pressure, $[Pa]$
p_d	=	end-diastolic pressure, $[Pa]$
p_{vc}	=	pressure with closed mitral valve, $[Pa]$
S	=	cross-section, $[m^2]$
t	=	time, $[s]$
Δt	=	time step, $[s]$
U	=	flow velocity, $[m/s]$
z	=	the coordinate along the symmetry axis, $[m]$
ρ	=	density of the fluid, $[kg/m^3]$
τ	=	relaxation constant of the myocardial wall, $[s]$

Subscripts

$+$	=	referring to the forward traveling wave
$-$	=	referring to the backward traveling wave
t	=	partial derivative with respect to time
z	=	partial derivative with respect to the z direction

Superscripts

$'$	=	referring to the applied modification

7

Cardiovascular haemodynamics and ventriculo-arterial coupling in an acute pig model of coronary ischaemia-reperfusion

In previous chapters the research was focused purely on the numerical simulation of blood flow and wall deformation in the cardiovascular system. However, when one is looking at the cardiovascular system, a wider look is imperative. It is important that one does not forget to look at the cell level and the metabolic changes blood flow alternations can induce. In this chapter such an interaction between blood flow and cell metabolism is illustrated, observed after blood flow is restored an hour after onset of clamping the left anterior descending coronary artery. From a purely mechanical point of view one would expect the cardiac function to recover partially, however after reperfusion a further worsening is observed. This example illustrates that when one is only looking at the heart from a mechanical point of view, as done in the previous chapters, the findings of computer models can be far from the actual cardiovascular response[1].

Lieve Lanoye[1], Patrick Segers[1], Vincent Tchana-Sato[2], Stephanie Rolin[3], Jean-Michel Dogne[3], Alexandre Ghuysen[2], Bernard Lambermont[2], Julien Hanson[4], Thomas Desaive[5], Pascal Verdonck[1], Vincent D'Orio[2] and Philippe Kolh[2].
[1]Cardiovascular Mechanics and Biofluid Dynamics, Institute of Biomedical Technology, Ghent Uni-

Abstract

Although reperfusion after coronary occlusion is mandatory for myocardial salvage, reperfusion may trigger a cascade of harmful events (reperfusion injury) adding to myocardial injury. We investigated effects of reperfusion on left ventricular (LV) haemodynamics and ventriculo-arterial (VA) coupling in pigs following acute myocardial ischaemia induced by coronary artery occlusion. Experiments were performed in six animals,with measurements of cardiac and arterial function at baseline, after 60 min of ischaemia ($T60$) and after 2 ($T180$) and 4 h of reperfusion ($T300$). Ventriculo-arterial coupling was assessed using the ventriculo-arterial elastance ratio (E_{es}/E_a; E_a : effective arterial elastance; E_{es} : ventricular end-systolic stiffness) , as well as using a 'stiffness coupling' and 'temporal coupling' index. Reperfusion following ischaemia ($T180$ versus $T60$) induced a progressive decline in cardiovascular function, evidenced by a decrease in mean arterial blood pressure, cardiac output and ejection fraction which was not restored at $T300$. Although reperfusion also induced an increase in slope of the end-systolic pressure-volume relationship ($ESPVR$), the $ESPVR$ curve shifted to the right, associated with a depression of contractile function. Histology demonstrated irreversible myocardial damage at $T300$. The ventriculo-arterial elastance ratio and the 'stiffness coupling' index were unaffected throughout the protocol, but the 'temporal coupling' parameter indicated a relative shift between heart period and the time constant of the arterial system. It is unlikely that these alterations are attributable to ischaemic injury alone. The combination of both the stiffness and temporal coupling index may provide more information when studying ventriculo-arterial coupling than the more commonly used E_{es}/E_a ratio.

1   Introduction

Myocardial ischaemia in the clinical setting is often a consequence of a thrombotic occlusion of a coronary artery at the site of a ruptured atherosclerotic plaque or downstream from it. It appears obvious that prompt re-establishment of coronary flow following coronary occlusion is mandatory for the preservation of myocardial tissue and to decrease postmyocardial infarction mortality [173, 174]. It has, however, been demonstrated that even after early initiation of successful reperfusion, myocardial damage may still occur [175, 176]. This prevalence of damage even after reperfusion, along with other observations, revealed that, although reperfusion is needed for myocardial salvage, it may also trigger a cascade of harmful events which add to myocardial injury. The part of the myocardial injury and the clinical manifestations specifically triggered by reperfusion have been labelled as

versity, Belgium.

[2] Haemodynamic Research Center (HemoLiège), University of Liège, Belgium.

[3] Department of Pharmacy, University of Namur, Belgium.

[4] Department of Medicinal Chemistry, University of Liège, Belgium.

[5] Thermodynamics of Irreversible Processes, University of Liège, Belgium.

'reperfusion injury' [175, 176]. The issue of reperfusion injury is still not fully understood. On the one hand, it has been suggested that the impact of reperfusion only accelerates the expression of irreversible myocardial damage caused by ischaemia, but does not cause any damage in itself. On the other hand, however, there is evidence that the ischaemic myocardium remains still viable at the end of reasonably long ischaemic periods [177]. The latter evidence suggests that irreversible injury caused by the reperfusion itself (and not the prolonged ischaemia) is indeed a true phenomenon. This concept, where reperfusion induces further injury, also has support from infarct-limiting effects of pharmacological interventions initiated immediately before or at the onset of reperfusion [178, 179]; if the damage were solely the result of ischaemia, these pharmacological agents would have no effect at all.

Reperfusion injuries have mostly been assessed at the cellular level, and the direct causes of necrosis and apoptosis have been studied at the molecular level. Many different mechanisms of reperfusion-induced cell damage and cell death have been identified. For example, oxidants and free radicals play an important role in reperfusion injury [180]. In addition, cell damage caused by Ca^{2+} overload-induced contracture and reoxygenation-induced rigor contracture is observed [181].

Nonetheless, it is equally important to study the overall cardiovascular changes that result from the ischaemia. reperfusion-induced mechanisms. Some more recent studies have focused on the influence of ischaemia and reperfusion on circulatory parameters in pigs [182–184]. In all these studies, however, only a limited haemodynamic analysis was performed, and the studies did not incorporate pressure-volume analysis or ventriculo-arterial coupling, which enable assessment of the 'matching' between cardiac and arterial parameters that results in a working point of the cardiovascular system (producing a certain cardiac output and blood pressure) and its associated energetic cost.

The primary aim of this study was to gain insight into and document the wide range of alterations in haemodynamics induced by prolonged ischaemia and subsequent reperfusion. We chose to perform the experiment in a large animal model with coronary structure and function closely resembling those of humans. Focusing on ventriculo-arterial function and coupling, we analysed our data in terms of the 'classical' ventriculo-arterial elastance, as well as in terms of a recently proposed coupling concept using both a stiffness and a temporal coupling index.

2 Methods

2.1 Animal preparation

All experimental procedures and protocols used in this investigation were reviewed and approved by the Ethics Committee of the Medical Faculty of the University of Liège. All procedures conformed to the Guiding Principles in the Care and Use of Animals of the American Physiological Society and were performed according

to the Guide for the Care and Use of Laboratory Animals (NIH publication no. 85-23, revised 1996).

Experiments were performed on six healthy pure pietran pigs of either sex (20-28kg). The animals were premedicated with intramuscular administration of ketamine (20$mgkg^{-1}$) and diazepam (1$mgkg^{-1}$). Anaesthesia was then induced and maintained by a continuous infusion of sufentanil (0.5$\mu gkg^{-1}h^{-1}$) and sodium pentobarbitone (3$mgkg^{-1}h^{-1}$). Spontaneous movements were prevented by pancuronium bromide (0.1$mgkg^{-1}$). After endotracheal intubation through a cervical tracheostomy, the pigs were connected to a volume-cycled ventilator (Evita 2, Dräger, Lübeck, Germany) set to deliver a tidal volume of 10$mlkg^{-1}$ at a respiratory rate of 20min^{-1}. Measurements of end-tidal partial pressure of CO_2 (Capnomac, Datex, Helsinki, Finland) were used to monitor the adequacy of ventilation. Respiratory settings were adjusted to maintain end-tidal CO_2 in the range of 35-40$mmHg$ (4.67 - 5.33kPa). Arterial oxygen saturation was closely monitored and maintained above 95% by adjusting the fractional inspired O_2 if necessary. Core temperature was measured with a rectal probe and maintained at 37^oC by means of a heating blanket. A standard lead electrocardiogram was used for the monitoring of heart rate (HR).

The chest was entered through median sternotomy, the pericardium was incised and sutured to the chest wall to form a cradle for the heart, and the root of the aorta was dissected clear of adherent fat and connective tissue. A combined conductance-micromanometer catheter (CD Leycom, Zoetermeer, The Netherlands) was inserted through the right carotid artery and advanced into the left ventricle. A micromanometer-tipped catheter (Sentron pressure measuring catheter, Cordis, Miami, FL, USA) was inserted through the right femoral artery and advanced into the ascending aorta. A 14mm diameter perivascular flow probe (Transonic Systems Inc., Ithaca, NY, USA) was closely adjusted around the aorta 2cm downstream to the aortic valve. The micromanometer-tipped catheter was manipulated so that the pressure sensor was positioned just distal to the flowprobe. Right atrial pressure was measured with a micromanometer-tipped catheter inserted into the cavity through the superior vena cava. A 2.0mm Fogarty balloon catheter (Baxter Healthcare Corp., Oakland, CA, USA) was advanced into the inferior vena cava through a right femoral venotomy. Inflation of this balloon produced a leftward shift in pressure-volume (P-V) loops by reducing venous return. Thrombus formation along the catheters was prevented by administration of 100$i.u.kg^{-1}$ of heparin sodium intravenously just before the catheter insertion.

A segment of the left anterior descending (LAD) coronary artery was isolated distal to the first diagonal branch for later application of a surgical clamp. An electromagnetic flow probe (Transonic Systems Inc.) was placed around the LAD coronary artery 3cm distal to the site of occlusion, to verify the occlusion (complete loss of coronary artery blood flow). In case of occurrence of ventricular fibrillation, animals were defibrillated at 1Jkg^{-1} using internal paddles.

2.2 Experimental protocol

The animals were continuously infused intravenously with Ringer lactate solution ($5 ml kg^{-1} h^{-1}$), and, when necessary,with hydroxyethyl starch (6%) to maintain central venous pressure up to 6-7$mmHg$ over 30min. After placement of all instrumentation and verification of their proper functioning, animals were allowed to equilibrate for an additional 30min, after which baseline (BL) recordings were made. Thereafter, the LAD coronary artery was occluded at the site of previous dissection for 1 h, and measurements were repeated before coronary perfusion was restored (T60). Subsequent measurements were repeated after 2 (T180) and 4 h of reperfusion (T300; Fig. 7.1A).

2.3 Haemodynamic data collection

The conductance catheter was connected to a Sigma-5 signal-conditioner processor (CD Leycom). Each ultrasonic flow probe was connected to a flowmeter (HT 207, Transonic Systems Inc.), and each micromanometer-tipped catheter to the appropriate monitor (Sentron pressure monitoring). All analog signals and the ventricular pressure-volume loops were displayed on screen for continuous monitoring. The analog signals were continuously converted to digital form with appropriate software (Codas, DataQ Instruments Inc., Akron, OH, USA) at a sampling frequency of 200Hz.

2.3.1 Ventricular systolic function and energetics

Ventricular systolic function was assessed through different parameters. Left ventricular volumes were inferred using the dual field conductance catheter technique [185, 186]. Calibration of the conductance signal to obtain absolute volume was performed by the hypertonic saline method [185]. Therefore, a small volume ($1 - 2 ml$) of 10% $NaCl$-solution was injected into the pulmonary artery during continuous data acquisition. Stroke volume (SV) was calculated from steady-state recordings as the difference between end-diastolic (EDV) and end-systolic volume (ESV). Cardiac output (CO) was calculated as the product of heart rate (HR) and SV. Ejection fraction (EF) was calculated as SV/EDV. Left ventricular contractile function was assessed by the end-systolic pressure-volume relation ($ESPVR$) [187], and the preload recruitable stroke work ($PRSW$) relation [188]. Both indices require pressure-volume loops (PV loops) measured under gradual preload decline obtained through inhibition of venous return (Fig. 7.1D).

All measurements were taken immediately after the animal was disconnected from the ventilator to sustain end expiration. The caval occlusion was limited to a few seconds to avoid reflex responses. The instantaneous pressure-volume relationship was considered in terms of a time-varying elastance $E(t)$, defined by:

$$E(t) = \frac{P(t)}{V(t) - Vd} \tag{7.1}$$
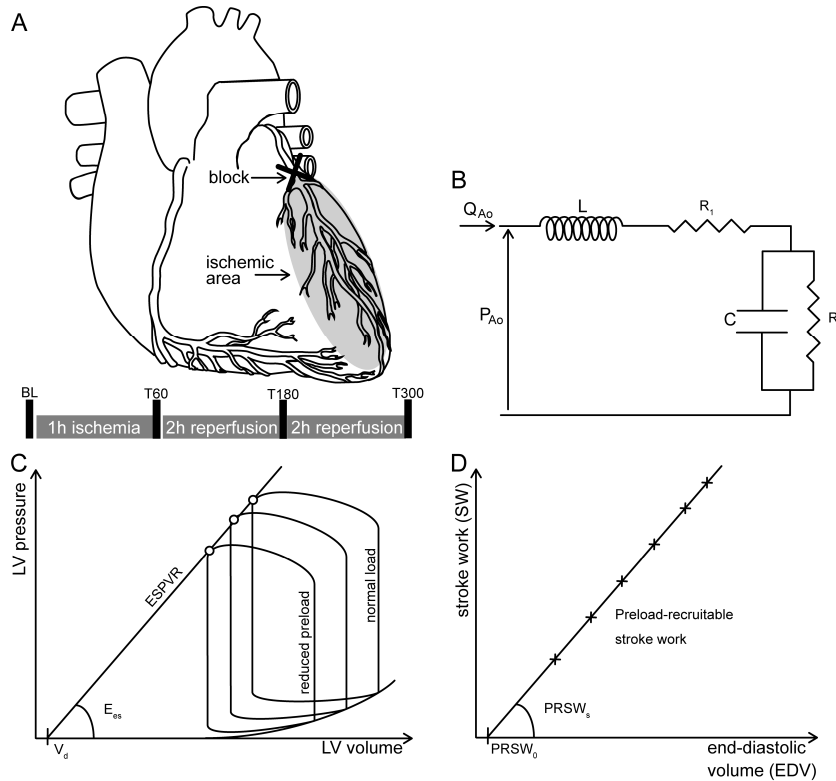
Figure 7.1: Protocal and assessment of arterial and ventricular function parameters. Panel A: protocol used in this study. Panel B: the four-element windkessel model used to assess the vascular properties (Q_{Ao} : aortic flow; P_{Ao} : aortic pressure). Panel C: how end-systolic elastance (E_{es}) and dead volume (V_d) were assessed from caval occlusion. Panel D: how the preload-recruitable stroke work curve was assessed from the PV loops in panel C.

where $P(t)$ and $V(t)$ are, respectively, the instantaneous ventricular pressure and volume; dead volume, V_d, is a correction term. End systole was defined as the instant of time in the ejection phase at which $E(t)$ reaches its maximum, E_{max}. It has been demonstrated that $E(t)$ and V_d are insensitive to preload, at least within physiological ranges [187]. Stroke work (SW) was calculated as the area enclosed within each pressure-volume loop and was plotted against EDV to generate the SW-EDV relation (preload recruitable stroke work, $PRSW$).

Myocardial energetics were assessed by computation of pressure-volume area (PVA) using steady-state measurements. In the time-varying elastance model of the ventricle, the total energy generated by each contraction is represented by the total area under the end-systolic pressure-volume relation line and the systolic seg-

ment of the pressure-volume loop, and above the end-diastolic pressure-volume relation curve, and denoted by PVA [187]. Pressure-volume area is the sum of SW, or the energy that the ventricle delivers to the blood at ejection, and potential energy (PE), necessary to overcome the viscoelastic properties of the myocardium itself. It has been demonstrated that PVA is highly correlated with myocardial oxygen consumption [10]. Mechanical efficiency is defined as the SW/PVA ratio.

2.3.2 Arterial function

Arterial properties were assessed from ascending aortic pressure and flow measurements during steady-state conditions and represented with a four-element windkessel model ($WK4$; see Fig. 1B) [189]. In this $WK4$ model, the resistor R_2 represents the resistive properties of the systemic bed, which reside primarily in the arteriolar system. The capacitor, C, placed in parallel with R_2, represents the compliant properties of the systemic vessels. The resistor R_1 represents the characteristic impedance, the level of which depends predominently on the elastic properties of the proximal aorta. Finally, an inductance, L, is introduced to take blood inertia into account. Furthermore, L restores positive phase angles at high frequencies of the impedance spectrum [190]. The values of R_1, R_2, C and L were estimated by a previously described method [189]. Effective arterial elastance (E_a) was calculated according to the equation [191]:

$$E_a = \frac{R_1 + R_2}{T_s + R_2C(1 - e^{T_d/R_2C})} \tag{7.2}$$

where T_s and T_d are the systolic and diastolic time intervals, respectively. In the aortic pressure wave, T_s was calculated as the time interval between the point just before the abrupt rise and the dicrotic notch.

2.3.3 Ventriculo-arterial coupling

Ventriculo-arterial (VA) coupling was first studied through the ratio E_{es}/E_a, where E_{es} is the ventricular end-systolic stiffness. It has, however, been demonstrated by Stergiopulos et al. [192] and Segers et al. [193] that VA coupling can be described in more detail using two dimensionless parameters, i.e. a 'stiffness coupling index', calculated as the ratio of E_{es} and arterial stiffness ($1/C$), yielding $E_{es}C$, and the 'temporal coupling index', calculated as the ratio of the time constant of the arterial system (R_2C) and the heart period (T), R_2C/T. We applied both the 'conventional' VA coupling approach, as well as this newer approach with the stiffness and temporal coupling indices.

2.4 Histopathological data collection

At the end of the protocol, the animal was killed with an intravenous injection of pentobarbitone ($100mgkg^{-1}$). The heart was then rapidly harvested, rinsed with

a cold isotonic saline solution and sectioned in five slices ($0.6cm$ thick) parallel to the atrioventricular groove from apex to base. Transverse tissue slices were rinsed with a cold isotonic saline solution and placed in 10% neutral-buffered formaldehyde. After 3 days of fixation, three or four tissue blocks were taken from each slice at standardized locations and routinely processed for paraffin histology. The tissue blocks from myocardium were cut at $6\mu m$, and each section was stained with Haematoxylin and Eosin (H&E) and Masson's trichrome. The stained sections were examined at magnifications of x25, x100, x200 and x400 to study the distribution of infarction. Photomicrographs were taken using a Zeiss photomicroscope (Axioscope 2 plus Sony 3CCD camera, 1024-768 pixels definition, Thornwood, NY, USA). In addition, tissue blocks of slice $S3$ were processed for immunohistochemical staining of desmin to investigate lesions of the cardiac muscle. Polyclonal antibodies to myoglobin (Dako, Glostrup, Denmark) were diluted 1:400. Monoclonal antibodies to desmin (clone D33, Biomeda, Foster City, CA, USA) were diluted 1:20. These methods to detect myocardial lesions were developed previously in other experimental protocols in pig [194–196].

2.5   Statistical analysis

Differences between the four measurements at baseline, after $1h$ of ischaemia and after 2 and $4h$ of reperfusion were tested with a general linear model for repeated measurements using SPSS software (SPSS Inc., Chicago, IL, USA). The model first revealed statistically significant differences in the evolution with time of the different parameters, with the level set at $P = 0.05$. If differences were present, post hoc tests were performed to detect at which instances in time the data were different. The Sidak confidential interval adjustment was used.

3   Results

Haemodynamic data (means±S.E.M.) at baseline (BL), after $1h$ of ischaemia ($T60$), after $2h$ of reperfusion ($T180$) and after $4h$ of reperfusion ($T300$) are shown in Table 7.1 and Figs 7.2-7.4.

3.1   Effects of acute regional ischaemia (comparing BL with $T60$)

Ligation of the LAD coronary artery induced an increase in HR from 97.9±15.6 $beatsmin^{-1}$ at BL to $106.4 \pm 12.8 beatsmin^{-1}$ at $T60$ (P <0.001). Cardiac output and mean aortic pressure (MAP) were not significantly affected by an hour of ischaemia, while EF decreased from 54.5 ± 11.3 (BL) to $45.4 \pm 9.0\%$ ($T60$; P = 0.033).

End-diastolic volume did not change significantly between BL and $T60$, but there was a trend towards elevated ESV ($35.8 \pm 16.2 ml$ at BL versus $42.9 \pm 13.1 ml$ at $T60$, $P = 0.074$). Over the same time interval, SV decreased from

	Baseline (BL)	1h ischaemia ($T60$)	1h ischaemia + 2h reperfusion ($T180$)	1h ischaemia + 4h reperfusion ($T300$)	Evolution with time
HR (beats min^{-1})	97.9 ± 15.6	$106.4 \pm 12.8^{*}$	$120.6 \pm 14.7^{*\dagger}$	$122.4 \pm 20.0^{*\dagger}$	P < 0.001
CO ($ml\ s^{-1}$)	62.0 ± 11.3	59.8 ± 6.4	$44.6 \pm 7.0^{*\dagger}$	$44.0 \pm 6.1^{*\dagger}$	P < 0.001
EF (%)	54.5 ± 11.3	$45.4 \pm 9.0^{*}$	$31.1 \pm 5.0^{*\dagger}$	$32.4 \pm 6.8^{*\dagger}$	P < 0.001
MAP ($mmHg$)	96.7 ± 22.1	102.7 ± 22.5	$88.1 \pm 19.6^{\dagger}$	$78.4 \pm 21.4^{*\dagger\ddagger}$	P < 0.001
EDV (ml)	75.0 ± 24.6	76.8 ± 13.3	73.1 ± 13.6	$68.9 \pm 11.1^{\dagger}$	P = 0.009
ESV (ml)	35.8 ± 16.2	42.9 ± 13.2	$50.9 \pm 12.3^{*\dagger}$	$46.9 \pm 10.4^{*\dagger}$	P < 0.001
SV (ml)	39.2 ± 11.6	34.0 ± 3.8	$22.2 \pm 2.5^{*\dagger}$	$22.0 \pm 4.1^{*\dagger}$	P < 0.001
SW ($mmHg\ ml$)	3600 ± 649	$3200 \pm 342.$	$1889 \pm 442^{*\dagger}$	$1767 \pm 567^{*\dagger}$	P < 0.001
PVA ($mmHg\ ml$)	6657 ± 1382	5941 ± 1080	$4586 \pm 872^{*}$	$3282 \pm 876^{*}$	P < 0.001
SW/PVA ($-$)	0.56 ± 0.06	0.55 ± 0.11	0.41 ± 0.09	0.46 ± 0.09	P = 0.335
Ea ($mmHg\ ml^{-1}$)	2.75 ± 1.45	$3.35 \pm 1.60.$	$4.76 \pm 2.11^{*\dagger}$	$4.57 \pm 2.68^{*\dagger}$	P < 0.001

Table 7.1: Overview of principal haemodynamic parameters. Values are means $\pm$ S.E.M. Significant differences: *P < 0.05 versus baseline; †P < 0.05 versus $T60$ measurement; ‡P < 0.05 versus $T180$ measurements. Indicated P values show the statistically significant differences in the evolution with time of the different parameters.
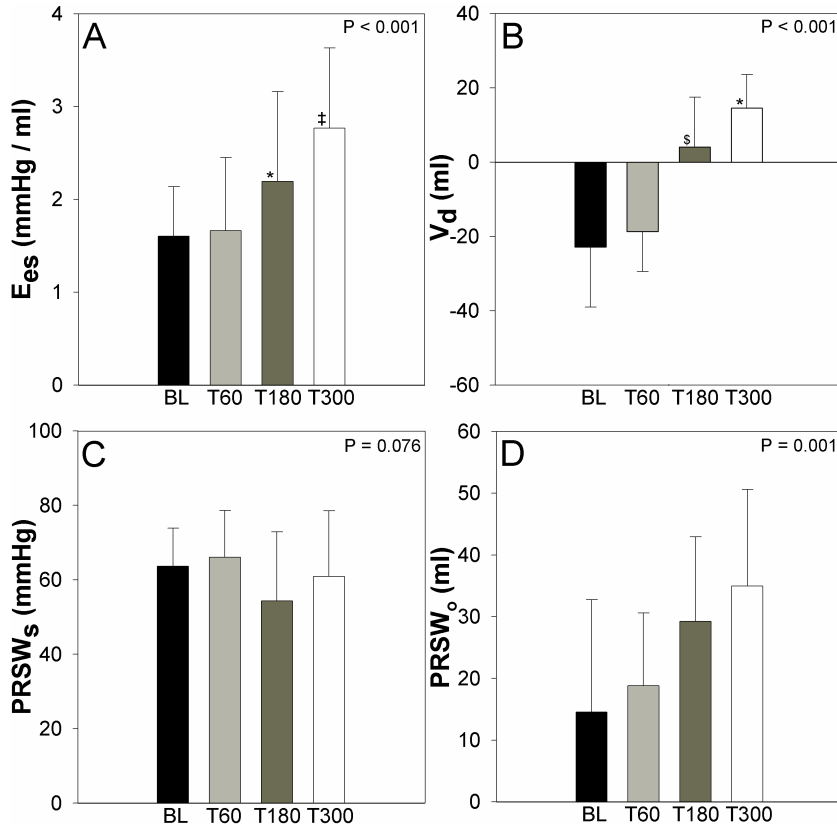
Figure 7.2: Left ventricular function parameters The figure shows the end-systolic elastance (E_{es}, panel A), dead volume (V_d, panel B), the slope of the preload-recruitable stroke work curve ($PRSW_s$, panel C) and the intercept of the preload-recruitable stroke work curve ($PRSW_0$, panel D). All parameters are shown at baseline (BL), after 1 h of ischaemia ($T60$), after 2 h of reperfusion ($T180$) and after 4 h of reperfusion ($T300$). Significant differences: *P < 0.05 versus baseline; $^\$$P < 0.05 versus T60 measurement. Near-significant differences: ‡P < 0.06 versus baseline. Indicated P values illustrate the statistically significant differences in the evolution with time of the different parameters.

$39.2 \pm 11.6ml$ to $34.0 \pm 3.8ml$ ($P = 0.001$). Neither end-systolic elastance nor V_d changed significantly between baseline and $T60$. The slope ($PRSW_s$) and the intercept ($PRSW_0$) of the preload recruitable stroke work curve were not significantly affected by the ischaemia either (Fig. 7.2).

Stroke work decreased from 3600 ± 649 to $3200 \pm 342mmHgml$ ($P = 0.002$), while pressure. volume area and mechanical efficiency (SW/PVA) did not significantly change between BL and $T60$. As for vascular function, we ob-

Figure 7.3: Arterial function parameters of the four-element windkessel model. The figure shows the characteristic impedance (R_1, panel A), peripheral resistance (R_2, panel B), blood inertia (L, panel C) and total compliance (C, panel D). All parameters are shown at BL, $T60$, $T180$ and $T300$. Significant differences: * $P < 0.05$ versus baseline; $^\$$ $P < 0.05$ versus $T60$ measurement. Indicated P values illustrate the statisti P ally significant differences in the evolution with time of the different parameters.
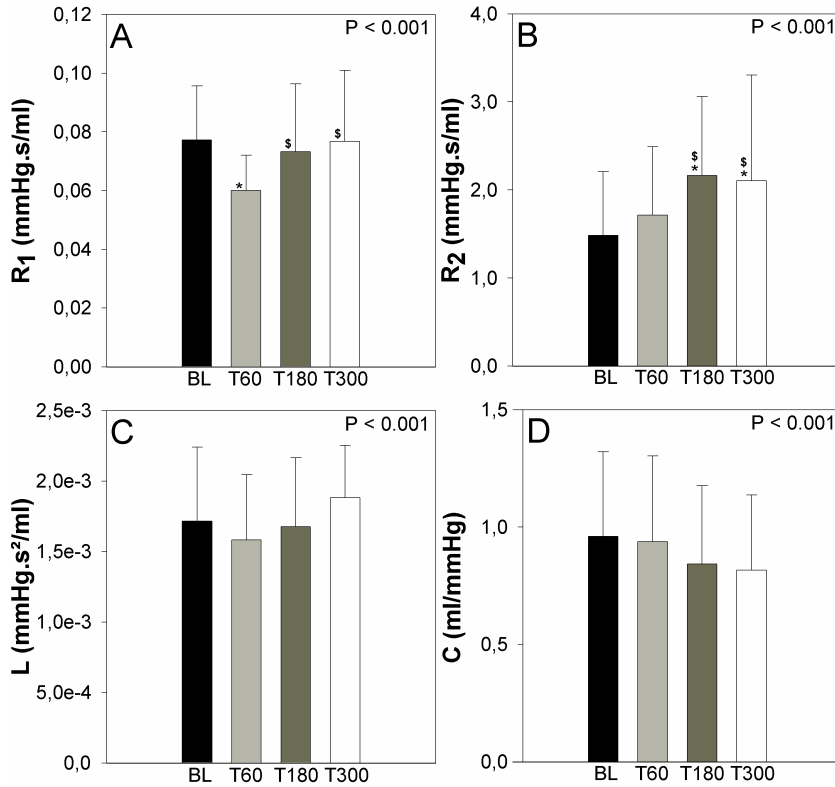
served that the only four-element windkessel parameter that demonstrated significant changes was characteristic impedance R_1, which decreased from 0.077 ± 0.018 to $0.060 \pm 0.012 mmHgsml^{-1}$ ($P = 0.001$) between BL and $T60$. Peripheral resistance R_2, C and L did not change significantly (Fig. 3). Effective arterial elastance (E_a) increased from 2.75 ± 1.45 to $3.35 \pm 1.60 mmHgml^{-1}$, between baseline and $T60$ ($P = 0.007$).

Ischaemia did not affect the ratio E_{es}/E_a significantly, nor did it affect $E_{es}C$. The ratio R_2C/T, however, showed a significant increase from 2.081 ± 0.298 at BL to 2.500 ± 0.417 at $T60$ ($P = 0.009$), as seen in Fig. 7.4.

3.2 Effects of sustained coronary reperfusion ($T180$ and $T300$ versus $T60$)

Heart rate increased further after reperfusion (from $106.4 \pm 12.8 beats min^{-1}$ at T60 to $120.6 \pm 14.7 beats min^{-1}$ at T180; $P = 0.001$), while sustained reperfusion ($T300$) did not lead to a further increase. Compared with ischaemia ($T60$), reperfusion induced a decrease in CO (from $59.8 \pm 6.4 mls^{-1}$ at $T60$ to $44.6 \pm 7.0 mls^{-1}$ at $T180$; $P < 0.001$), and CO remained at this level up to $T300$. Ejection fraction decreased (from $45.4 \pm 9.0\%$ at $T60$ to $31.1 \pm 5.0\%$ at $T180$; $P < 0.001$) and remained at this low level during sustained reperfusion. Mean arterial pressure decreased from $102.7 \pm 22.5 mmHg$ at T60 to $88.1 \pm 19.6 mmHg$ at T180 ($P = 0.024$) and to $78.4 \pm 21.4 mmHg$ at $T300$ ($P = 0.021$).

While end-diastolic volume remained unchanged, ESV increased from $42.9 \pm 13.2 ml$ at $T60$ to $50.9 \pm 12.3 ml$ at $T180$ ($P = 0.014$) and did not further increase at $T300$. Coronary reperfusion induced a decrease in SV from $34.0 \pm 3.8 ml$ at T60 to $22.2 \pm 2.5 ml$ at $T180$ ($P < 0.001$). Stroke volume did not change further between $T180$ and $T300$.

End-systolic elastance (E_{es}) showed an increasing trend from 1.66 ± 0.79 $mmHg ml^{-1}$ at $T60$ to $2.19 \pm 0.97 mmHg ml^{-1}$ at $T180$ ($P = 0.063$) and did not show a further increase with sustained reperfusion. The dead volume (Vd) increased significantly from $-18.70 \pm 10.77 ml$ at $T60$ to $4.08 \pm 13.46 ml$ at $T180$ ($P = 0.005$), but did not increase further with sustained reperfusion. The preload recruitable stroke work slope and intercept, in contrast, were not significantly influenced by coronary reperfusion.

Stroke work decreased as a result of early reperfusion, from 3200 ± 342 $mmHg ml$ at T60 to $1889 \pm 442 mmHg ml$ at $T180$ ($P < 0.001$), and did not change with sustained reperfusion. In the same interval, PVA and SW/PVA were not significantly affected by reperfusion.

Applying the four-element windkessel model, we observed that characteristic impedance R_1 increased significantly, from $0.060 \pm 0.012 mmHg s ml^{-1}$ at $T60$ to $0.073 \pm 0.023 mmHg s ml^{-1}$ at $T180$ ($P = 0.014$), after which R_1 remained constant (Fig. 7.3). Peripheral resistance R_2 showed a similar pattern, increasing from $1.71 \pm 0.78 mmHg s ml^{-1}$ at $T60$ to $2.16 \pm 0.89 mmHg s ml^{-1}$ at $T180$ ($P = 0.044$) and remaining at an elevated level with sustained reperfusion, while global vascular compliance C and inertance L remained unchanged. Effective arterial elastance (E_a) increased further to $4.76 \pm 2.11 mmHg ml^{-1}$ at $T180$ ($P = 0.020$), and remained constant at $T300$.

When looking at the left ventriculo-arterial coupling (Fig. 7.4), no statistical changes were observed for the ratio E_{es}/E_a from $T60$ to $T300$, whereas the ratio $R_2 C/T$ increased further from 2.500 ± 0.417 at $T60$ to 3.261 ± 0.678 at $T180$ ($P = 0.023$), after which this parameter remained constant. The product $E_{es}C$ remained unchanged during the whole period.
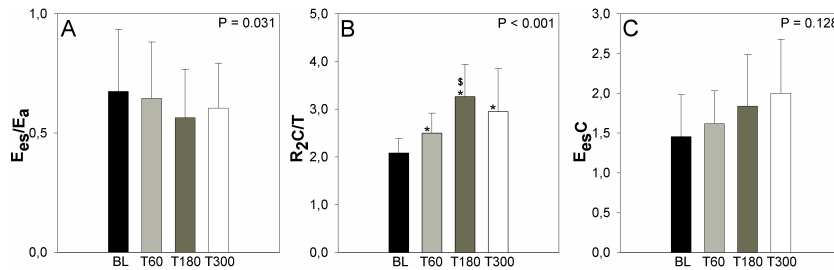
Figure 7.4: Ventriculo-arterial coupling. The figure shows the ratio E_{es}/E_a (panel A), the ratio of characteristic periods R_2C/T (panel B) and the ratio of total compliances $E_{es}C$ (panel C). All parameters are shown at BL, $T60$, $T180$ and $T300$. Significant differences: $^*P < 0.05$ versus baseline; $^\$P < 0.05$ versus $T60$ measurement; $^\dagger P < 0.05$ versus $T180$ measurement. Indicated P values illustrate the statistically significant differences in the evolution with time of the different parameters.
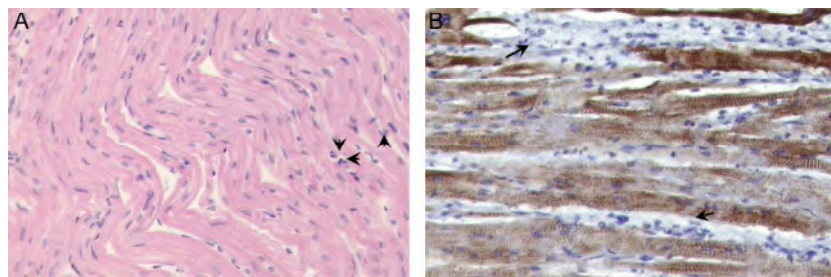
Figure 7.5: Panel A: Haematoxylin and Eosin staining of a histological section fromthe anteroseptal region froma heart suffering from 1 h ischaemia followed by 4 h of reperfusion (original magnification: x200). The wavy and stretched appearance of necrotic cells is seen. The nuclei of the muscle cells exhibit karyorrhexis and pycnosis. A few neutrophils are present (short arrows). Panel B: Immunohistochemical detection of desmin in the anterior region of heart suffering from 1 h ischaemia followed by 4 h of reperfusion (original magnification: x200). Several myofibrils have a preserved pattern of cross-striation. An intense leukocytic infiltrate is present (arrows).

3.3 Histopathological examination of infarcted myocardium

Histopathological examination revealed that main ischaemic changes were observed in the anterior left ventricle, corresponding to the area supplied by the LAD coronary artery. Reperfused myocardium displayed altered muscle cells, showing a waviness aspect which expresses prominent myofibrillar contraction bands, anisokaryosis and accumulation of interstitially infiltrated inflammatory

cells as neutrophils and lymphocytes (Fig. 7.5A). Immunohistochemical detection of desmin revealed, mainly in the anteroseptal region, blurred zones where it was difficult to clearly delineate a necrotic zone from healthy myocardium owing to a motley appearance (Fig. 7.5B). Clear zones of patchy necrosis were also observed. The area not supplied by the LAD artery (posterior region) showed myofibrils with normal morphology.

4   Discussion

The main objectives for the study were twofold. Firstly, we wanted to gain more insight into the haemodynamic impact of the ischaemia.reperfusion mechanism. While much has been published on reperfusion injuries at the cellular level [181, 197, 198], little is known about its influence on LV global function, arterial function and VA coupling. Secondly, we wanted to verify whether pigs with acute coronary ischaemia, which were reperfused after 1 h, provide a useful large animal model for further study of pharmacological treatments to minimize reperfusion injuries.

Pigs were used in this study because of the similarity between the hearts of pigs and humans concerning the anatomical distribution of coronary arteries, the lack of collateral circulation and the heart-to-body weight ratio [199, 200]. Open-chest preparation was used because it offers the advantage of a very strictly controlled induction of myocardial ischaemia and reperfusion using a clamp.

4.1   Ventricular systolic function and energetics

We assessed LV systolic function by the slope and intercept of the $ESPVR$ and the $PRSW$, both of which have been demonstrated to be relatively insensitive to changes in preload and afterload [187,188]. Our data illustrate some of the difficulties associated with the interpretation of these indices. An increase in contractility results in an $ESPVR$ that shifts to the left and upwards [187], i.e. a decrease of V_d combined with an increase of end-systolic elastance, E_{es}. We anticipated that contractility would be depressed following myocardial ischaemia, but this was not reflected by the slope of the $ESPVR$, which increased throughout the protocol. The dead volume, however, shifted to the right, indicating a loss of contractile function (Fig. 7.2).

To better elucidate the net effect of concomitant changes in slope and intercept of the $ESPVR$, we calculated the maximal realizable pressure, P_{max}, the pressure that would be generated by the LV in a sustained isovolumic contraction at EDV: $P_{max} = E_{es}(EDV - V_d)$. Figure 7.6A shows that an increase in E_{es} results in an increase in P_{max} (roughly equivalent to an increase in contractility), while an increase in V_d results in a decrease in P_{max} (roughly equivalent to a decrease in contractility). Clearly, increases in E_{es} as well as V_d, as seen in this study, have opposite effects on the maximal P_{max}. In Figure 7.6B, we used averaged $ESPVR$ values and calculated P_{max} using EDV data at BL, $T60$, $T180$
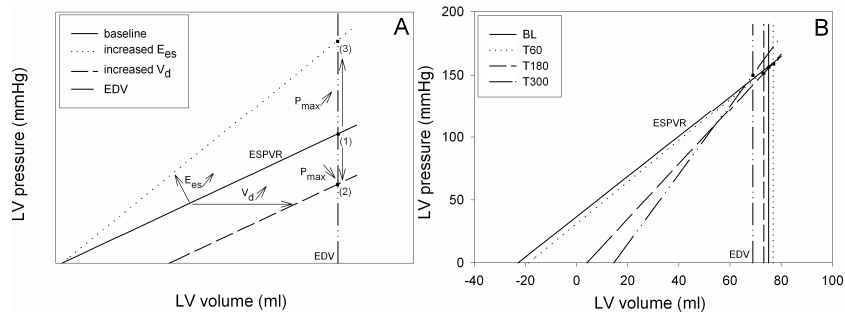
Figure 7.6: Panel A shows how an increase in dead volume (V_d) results in a drop of the maximum realizable pressure during isovolumic contraction, P_{max} (from point (1) to point (2)) and how the increase in end-systolic elastance (E_{es}) results in a rise of P_{max} (from point (1) to point (3)). Panel B shows the end-systolic pressure-volume relationships ($ESPVR$) and the enddiastolic volumes (EDV), at BL, $T60$, $T180$ and $T300$. It is seen that the maximal realizable pressure during isovolumic relaxation does not change, because the increase resulting from an increase of E_{es} and the decrease resulting from an increase of V_d cancel out.

and $T300$. The increase in V_d and increase in E_{es} counterbalance, and P_{max} remains unchanged. This finding is in line with the observation that the slope of the $PRSW$ was virtually unchanged throughout the experiment. Note, however, that this does not imply that LV systolic function was unchanged. The higher E_{es} may be the result of elevated sympathetic tone in response to the ischaemia, using the functional reserve of the LV to withstand the effects of ischaemia and making LV-function more sensitive to changes in volume and afterload. Also, there was a trend for an increase in the intercept of the $PRSW$. Since the end-diastolic volume did not change, this rightward shift of the $PRSW$ with ischaemia and reperfusion will result in a drop of stroke volume, which was observed, and thus a drop of inotropy. These findings illustrate that when studying LV function, both the slope and the intercept of the $ESPVR$ and $PRSW$ should be taken into account to reveal a complete picture of LV function.

When taking a closer look at the ventricular energetics, a drop in stroke work is seen owing to ischaemia. Reperfusion causes SW to drop further, while stabilization is seen after sustained reperfusion. The drop in PVA, a measure for the oxygen consumption, is less pronounced and is only significant at $T180$ and $T300$. Since stroke work decreases more than pressure-volume area, a drop in efficiency would be expected, showing that more energy is dissipated, while less energy is transmitted to the blood. The changes are, however, too small to reach the preset level of statistical significance.

4.2   Histopathological data collection

So far, we have only discussed 'macroscopic' findings and effects on global cardiovascular function, and we found that reperfusion following ischaemia does not restore function. The sustained haemodynamic decline that is observed is in agreement with the histological findings, in which we also observed features of irreversible damage despite the reperfusion. The question is whether the damage results from the ischaemia or from the ischaemia and subsequent reperfusion (true reperfusion injury). In two (additional) animals that we killed after 1 h of ischaemia, we found signs of necrosis within the area at risk, suggesting that 1 h of ischaemia induced by LAD ligation is already sufficient to induce severe lesions in pigs. This is in accordance with the findings of Taylor et al. [201], who also demonstrated that 1 h of ischaemia was sufficient to produce severe myocardial lesions in pigs. Like Taylor and co-workers, we believe that this probably results from the absence of a collateral circulation in the pig heart. We should nevertheless note that beyond the signs of necrosis observed, clear delineation between the reversible and the irreversible areas was not obvious even with immunohistochemical analyses, owing to the motley appearance of the staining in the myocardium from the anteroseptal region.

4.3   Arterial function

Besides LV function, we also addressed arterial function changes. Myocardial ischaemia ($T60$) does not affect systemic vascular resistance (R_2) which, together with a preserved cardiac output, results in an unaffected mean arterial blood pressure. However, an initial decrease of characteristic impedance R_1 is seen. Since R_1 depends merely on the elastic properties of the proximal aorta, this decrease, together with an unaffected mean aortic pressure, is suggestive of a (small) dilatation of the proximal aorta and/or decrease in aortic stiffness. With reperfusion ($T180$ and $T300$), R_2 increases, but because of the decrease in cardiac output, mean blood pressure decreases, resulting in higher R_1 (compared with $T60$) as the aorta will be less distended. Given the fact that sympathetic tone is likely to be elevated in these conditions, the higher R_1 may not be solely the effect of passive changes in aortic cross-section and function, but may also be modulated by changes in aortic vascular smooth muscle tone.

4.4   Ventriculo-arterial coupling

The coupling between the ventricle and the arterial system is commonly studied in terms of E_{es}/E_a. It has been argued, however, that E_{es}/E_a is not a very sensitive parameter [193]. Another problem involves the use of E_a as representing arterial function, since E_a cannot be considered as a 'pure' arterial function parameter [193]. In this study, ischaemia and reperfusion induced an alteration in ventricular and arterial function, yet the change in ventriculo-arterial coupling expressed using E_{es}/E_a was insignificant. This preservation of E_{es}/E_a may result

from the fact that coupling is preserved, but it may also be a demonstration of the relative insensitivity of the parameter.

In this respect, it may be relevant to address coupling using the approach first advocated by Stergiopulos et al. [192], who considered two independent coupling parameters, R_2C/T and $E_{es}C$, in order to assess the ventriculo-arterial coupling in a more elaborate model of the interaction between the LV and the arterial tree. The temporal coupling index R_2C/T relates the characteristic time periods of both the ventricle (T) and the arterial tree (R_2C). The product R_2C is the time constant of the arterial windkessel, and determines the time constant with which the pressure decays during diastole. In all mammals, R_2C/T is similar, which implies that the systolic-to-diastolic pressure difference (the pulse pressure) is constant. An increase in heart rate (smaller T) and R_2C/T allows less time for the arterial pressure to decay in diastole, with higher diastolic pressures (coronary perfusion pressure) as a consequence. In a setting of myocardial ischaemia, elevated coronary perfusion pressures may be beneficial. The stiffness coupling index, $E_{es}C$, is in fact the ratio of the ventricular stiffness E_{es} and the arterial stiffness, $1/C$. This ratio may be more meaningful than the usually used E_{es}/E_a because E_a is not a pure arterial parameter [193] and better describes the compliance mismatch between the arterial tree and the ventricle. In this study, the ratio is not significantly affected by ischaemia or by reperfusion, so there are no significant relative compliance changes of the arterial tree compared with the maximal compliance of the left ventricle. At this point, it is hard to tell which of the two coupling frameworks is more appropriate. It is certain that, although E_a has the dimensions of stiffness, it is not a measure of arterial stiffness [193]. It should also be pointed out that the E_{es}/E_a framework evolved from the analysis of cardiovascular function in the pressure-volume plane, where the dimension 'time' is not taken into account. Changes in heart rate are therefore not explicitly accounted for by E_{es}/E_a (although they are implicitly included in E_a). As such, the framework as proposed by Stergiopulos et al. [192] may be better suited to detect the effects of subtle changes in arterial stiffness and timing, and to place these changes in a context of ventriculo-arterial coupling.

4.5 Limitations

It is obvious that this study has some stringent limitations. Firstly, since this study mainly focused on the haemodynamic alternations observed during ischaemia and reperfusion, only limited histopathological data were collected. Nevertheless, it is important to underline that oxidants and free radicals generated in the ischaemic and reperfused heart are key mediators in the pathogenesis of the injury [180]. However, since accumulation of interstitially infiltrated inflammatory cells was observed at the histological level, no more complementary analyses were realized at the molecular level because biochemical dosages, histological analyses and electron microscopy data presented irreversible injury.

Secondly, our data indicate that in a pig model, 1 h of ischaemia may be too long when studying reperfusion injury. Confronting the histological findings with

the haemodynamic data, it is hard to attribute the decline in cardiac function solely to reperfusion injury. It is likely that we observed a dynamic process with a complex interaction between myocardial stunning,myocardial hibernation and progressive necrosis of myocardial areas where irreversible damage has occurred. Acute experiments in an open chest setting are probably too short to capture the time scale within which stabilization of events (and cardiac function) occurs. However, close monitoring of cardiovascular function, as we did in this experiment, is extremely demanding in a more 'chronic' experimental setting, and it is also not easy to differentiate the effect of the animal preparation and surgical interventions from the impact of ischaemia and subsequent reperfusion.

Also, further exploration of ischaemia-reperfusion injury would require the necessary control experiments to differentiate effects of ischaemia from effects of x reperfusion. In this context, we refer to previous work of Kolh et al. [202, 203] where, in a setting of sustained occlusion, it was shown that haemodynamic alterations took place primarily during the first half hour of ischaemia, followed by a plateau phase that was maintained for 3 h. These findings thus support the assumption that the changes observed in the present study are not solely due to ischaemia, and that reperfusion injuries may play a role in the haemodynamic decline.

5   Conclusion

In conclusion, we have demonstrated that 1 h of ischaemia in a pig model induces haemodynamic alterations which are not reversed by reperfusion, but rather sustained and worsened. It is unlikely that these alterations are attributable to ischaemic injury alone, indicating that acutely ischaemic pigs provide a valuable large animal model for further study of pharmacological treatments to minimize reperfusion injuries. We have further demonstrated that studying ventriculo-arterial coupling through both a stiffness and temporal coupling index may provide more detailed insights than the more commonly used E_{es}/E_a ratio.

8

Overall Conclusion and future work

Cardiovascular biomechanics provide a growing application field for numerical simulations [32]. Three main applications can be derived. Firstly, using numerical techniques the prosthesis design (e.g., a heart valve or a stent) can be tested and adapted before a prototype is made, strongly enhancing the design process. Secondly, numerical models provide a powerful research tool, allowing to study different parameters separately and with high spatial and temporal resolution. Thirdly, as emphasized by O'Rourke, once these research tools require less time and intervention, they can be implemented in clinical practice, to provide additional information to the physician [204].

As in cardiovascular applications the wall is very compliant, numerical flow computations using a fixed wall assumption will only yield limitedly useful results. A change in blood pressure and blood flow will alter the deformation of the wall and such a deformation of the lumen will determine the flow and pressure field. Indeed, in cardiovascular numerical models it is essential to take this fluid-structure interaction (FSI) in account when constructing a numerical model in order to obtain reliable results. Therefore, the aim of this research was to develop a multipurpose fluid-structure interaction code, applicable for vascular applications.

A method was proposed to perform multipurpose vascular flow calculations where the interaction between the blood flow and the vessel wall was taken into account. To achieve this a partitioned solver approach was chosen, a commercially available fluid and structural solver were embedded in an own-written coupling program. For the computational fluid dynamics problem Fluent software (ANSYS, Inc.) was chosen and for the computational solid mechanics Abaqus software (Simulia, Inc.) was used. Stabilizing the coupling was obtained by coupling reduced order models iteratively. Reduced order models, simplified matrix

representations of a complex problem, were constructed for the fluid solver and the solid solver separately. The reduced order models were built during the iterations within one time step and the more iterations were performed, the more the fluid and structural reduced order model mimicked the behavior of the actual fluid and solid solver, respectively. The approach was compared to the Aikten acceleration method and proved to be considerably faster. The approach was validated, first with a wave propagation model in a straight tube, where it showed to reproduce the theoretical wave speed within 0.5%. A second validation was done using the FSI-benchmark case proposed by Hron and Turek [84]. The static FSI-result differed less than 3% from the reference value. This difference is caused by the fact that in the benchmark problem shear is important as well, which requires spatial derivatives of the flow velocity.

Firstly, wave propagation phenomena in the thoracic aorta were studied. The thoracic aorta is a tapered vessel, which influences the reflection pattern of the present pressure and flow waves. The results of a two-dimensional FSI model of the thoracic aorta were compared to the results obtained with a one-dimensional model, frequently used to study arterial wave propagation. Both approaches are complementary. One-dimensional models are useful when studying wave behavior in a large geometry, such as the entire systemic circulation, as they are numerically cheap. Fluid-structure interaction models are useful when detailed information is needed in a small region. The results showed a qualitatively good resemblance. The pulse wave velocity was analyzed with three different techniques. The foot-to-foot method and the dU-dp-curve method suppose that no backward waves are present at the onset of systole. However, as the reflection coefficient of the simulated aorta was about 0.9, strong reflections are observed, explaining the deviating pulse wave velocity assessed with the three techniques, especially close to the outlet.

Secondly, the approach was applied to quantify the wall stress distribution in abdominal aortic aneurysms. Abdominal aortic aneurysms are pathological dilatations of the lumen in the abdominal aorta. The rupture of an abdominal aneurysm is shown to have a 90% mortality [116]. Patient-specific rupture risk prediction is a very important application field of biomechanics in clinical practice. However, fully coupled, transient fluid-structure interaction calculations are quite time consuming and are to date not fit for clinical practice. Numerically more time-efficient methods, such as static decoupled approaches or static fully coupled FSI-approaches, have been proposed, but so far no comparison was made to quantify the accuracy of the methods. It was shown in chapter 5 that these approaches do not yield more accurate results than a static computational solid mechanics model. In this chapter the complementary value of the models studied in chapter 4 was demonstrated, as a one-dimensional model of the systemic circulation provided boundary conditions for the two-dimensional FSI-model of the aneurysm itself.

The aneurysm study highlights a severe limitation of biomechanical fluid-structure interaction approaches: they are very time consuming, limiting their applicability in clinical practice. Moreover, as they are so time consuming the size of the problems studied needs to be limited. Therefor future work should be focus-

ing on *optimization of the FSI-approaches.* A first optimization can be done by improving the interpolation method to match the results from the wet and dry side of the interface. This adaptation will allow the use of meshes where the nodes on either side of the interface do not match, hence fluid and solid meshes of different density can be used and each subproblem can be meshed with an optimal mesh, thus reducing the computation time.

Secondly, the code can be optimized very severely if a way was found so that the fluid solver calculates the solution of a new iteration in a given time step starting from the solution of the previous iteration in the same time step. Indeed, each FSI-iteration $k+1$ of the new time step $n+1$ the solid solver needs to be restarted from the solution found in the previous time step n. Even if the wall movement compared to the solution found in the previous FSI-iteration k is minimal, the whole flow field for iteration $k+1$ needs to be recalculated from the solution at n. If one could move the nodes at the interface without the now necessary progress in time, one could move the nodes from the solution of FSI-iteration k slightly to match the interface needed at $k+1$ and with a few fluid-iterations i the new solution can be found. If this can be combined by letting the fluid solver wait for the solution of the structural solver without having to exit the fluid solver, it will also hugely enhance the profit that can be made by parallelizing the code, since a restart of the fluid solver, and a cost of parallelization it includes, will not be necessary each iteration k.

Next, the instabilities observed in some FSI-problems are, to date, not fully understood. When analyzing these instabilities, a simplified partitioned FSI-model is useful. In the more complex two- or three-dimensional FSI-models the results are influenced by a large number of parameters. Such a simplified model, however, can couple a one-dimensional own-written fluid solver to a thin-shelled one-dimensional own-written solid solver, thus allowing full access to the partitioned solvers. Like other simplified models of complex systems the model does not have a modeling value due to its simplified partitioned solvers, but it contains the same possible instabilities as a more complex FSI-model. That way it can help to identify instabilities [75, 83] and it provides a test environment for new, optimized FSI-approaches.

A pure mechanical FSI-approach has its limits, as was demonstrated in the last chapter. In this chapter the influence of reperfusion injuries on the cardiovascular hemodynamics are studied. Reperfusion injuries are injuries occurring after blockage and consecutive reperfusion of coronary arteries. Indeed, after reperfusion of the blocked coronary artery a further depression of cardiovascular function is observed, opposite to what one would expect from a pure mechanical point of view. This example illustrates that a *wide vision is needed* when performing FSI-calculations and a healthy portion of skepticism is required. Especially when strong feedback mechanisms are present on cellular level, as seen after reperfusion of a coronary artery, the purely mechanical cardiovascular models reach their limits. Implementing cellular processes, such as remodeling mechanisms or Ca^+-induced myocardial contraction, in a FSI-model is one of the greatest challenges for the future.

In conclusion, the proposed method delivers accurate results when performing FSI-calculations. The approach is stable and is applicable to biomechanical cases. It provides a research tool when studying wave propagation phenomena or when quantifying wall stresses. Different examples were given in this dissertation. Finally, the FSI-approach provides detailed flow field and deformation field data which can be used as part of a virtual test environment to validate medical imaging algorithms.

References

[1] N Stergiopulos, DF Young, and TR Rogge. *Computer simulation of arterial flow with applications to arterial and aortic stenoses*. J Biomech, 25(12):1477–1488, 1992.

[2] E Pierce. *http://commons.wikimedia.org/wiki/Image:Heart_labelled_large.png*, 9/7/2007 2005.

[3] N Sperelakis. *Cell physiology source book - A molecular approach*. Academic Press, San Diego, CA, 1996.

[4] S Price and L Wilson. *Pathophysiology, clinical concepts of disease processes*. Mosby-Year Book inc, Philadelphia, 4th edition, 1992.

[5] E Yellin. *The momentum of mass, the momentum of ideas, and diastolic function*. In N Ingels, G Daughters, J Baan, J Covell, R Reneman, and F Yin, editors, Systolic and diastolic function of the heart. IOS Press, 1995.

[6] J Levick. *An introduction cardiovascular physiology*. Butterworth-Heinemann, Ltd., Oxford, 2nd edition, 1995.

[7] R Esper, R Nordaby, J Vilarino, A Paragano, J Cacharron, and R Machado. *Endothelial dysfunction: a comprehensive appraisal*. Cardiovasc Diabetol, 5(1):4–21, 2006.

[8] SAI Ghesquiere. *http://commons.wikimedia.org/wiki/Image:Anatomy_artery.png*, 9/7/2007 2006.

[9] J Parker and R Case. *Normal left ventricular function*. Circulation, 60(1):4–12, 1979.

[10] S Denslow. *Relationship between PVA and myocardial oxygen consumption can be derived from thermodynamics*. Am J Physiol Heart Circ Physiol, 270:H730–H740, 1996.

[11] R Ross. *Atherosclerosis-an inflammatory disease*. N Engl J Med, 340(2):115–126, 1999.

[12] G Hansson. *Inflammation, atherosclerosis, and coronary artery disease*. N Engl J Med, 352(16):1685–1695, 2005.

[13] G Chisolm and D Steinberg. *The oxidative modification hypothesis of atherogenesis: an overview*. Free Radic Biol Med, 28(12):1815–1826, 2000.

[14] A Tedgui and Z Mallat. *Cytokines in atherosclerosis: pathogenic and regulatory pathways*. Physiol Rev, 86(2):515–581, 2006.

[15] S Glagov, E Weisenberg, C Zarins, R Stankunavicius, and G Kolettis. *Compensatory enlargement of human atherosclerotic coronary arteries*. N Engl J Med, 316(22):1371–1375, 1987.

[16] J Frohlich, M Dobiasova, S Lear, and K Lee. *The role of risk factors in the development of atherosclerosis*. Crit Rev Clin Lab Sci, 38(5):401–440, 2001.

[17] American Heart Association. *Update on heart disease and stroke statistics*. Lancet, 352:673–681, 1998.

[18] BenestentI Clinical Trial. *A comparison of balloon-expandable-stent implantation with balloon angioplasty in patients with coronary artery disease*. N Engl J Med, 331(8):489–495, 1994.

[19] BenestentII Clincal Trial. *Randomised comparison of implantation of heparin-coated stents with balloon angioplasty in selected patients with coronary artery disease*. Circ Res, 76(4):536–543, 1995.

[20] STRESS Clinical Trial. *A randomized comparison of coronary-stent placement and balloon angioplasty in the treatment of coronary artery disease*. N Engl J Med, 331(8):496–501, 1994.

[21] L Bonneux, I Cleemput, and F Vrijens. *De electieve endovasculaire behandeling van het abdominale aorta aneurisma (AAA)*. Technical report, Federaal Keniscentrum voor de Gezondheidszorg, 2005 2005.

[22] WH Gaasch, AS Blaustein, and MM LeWinter. *Heart failure and clinical disorders of left ventricular diastolic function*. In WH Gaash and MM LeWinters, editors, Left ventricular diastolic function and heart failure, pages 245–258. Lea&Febiger, 1994.

[23] JJV McMurray and S Stewart. *Epidemiology, aetiology, and prognosis of heart failure*. Heart, 83:596–602, 2000.

[24] DD Schocken, MI Arrieta, PE Leaverton, and EA Ross. *Prevalence and mortality rate of congestive heart failure in the United States*. J Am Coll Cardiol, 20:301–306, 1992.

[25] JJV McMurray and S Stewart. *The burden of heart failure*. Eur Heart J Supp, 4:D50–D58, 2002.

[26] S Stewart, K MacIntyre, DJ Hole, S Capewell, and JJV McMurray. *More 'malignant' than cancer? Five-year survival following a first admission for heart failure.* Eur J Heart Fail, 3:315–322, 2001.

[27] C Berry, DR Murdoch, and JJV McMurray. *Economics of chronic heart failure*. Eur J Heart Fail, 3(3):283–291, 2001.

[28] S Stewart, S Greenfield, and RD Hays. *Functional status and well-being of patients with chronic conditions. Results from the Medical Outcomes study.* JAMA, 262(907-913), 1989.

[29] D Liepsch. *An introduction to biofluid mechanics - basic models and applications*. J Biomech, 35:415–435, 2002.

[30] CA Taylor. *Predictive medicine: computational techniques in therapeutic decision-making*. Comp Aided Surg, 4:231–247, 1999.

[31] AM Malek, SL Alper, and S Izumo. *Hemodynamic shear stress and its role in atherosclerosis*. JAMA, 282:2035–2042, 1999.

[32] DA Steinman, DA Vorp, and CR Ethier. *Computational modeling of arterial biomechanics: insights into pathogenesis and treatment of vascular disease.* J Vasc Surg, 37:1118–1128, 2003.

[33] KH Parker and CJH Jones. *Forward and backward running waves in the arteries: analysis using the method of the characteristics.* ASME J Biomech Eng, 112:322–326, 1990.

[34] B Hübner, E Walhorn, and D Dinkler. *A monolithic approach to fluid-structure interaction using space-time finite elements.* Comp Meth Appl Mech Eng, 193:2087–2104, 2004.

[35] TE Tezduyar, S Sathe, S Stein, and L Aureli. *Modeling of fluid-structure interactions with space-time techniques*. In HJ Bungratz and M Schäfer, editors, Fluid-structure interaction - Modeling, simulation, optimization, Lecture notes in computational science and engineering. Springer, Berlin, Germany, 2006.

[36] J Bonet and RD Wood. *Nonlinear continuum mechanics for finite element analysis*. Cambridge University Press, Cambridge, UK, 1997.

[37] WA Wall, A Gerstenberger, P Gamnitzer, C Forster, and E Ramm. *Large deformation fluid-structure interaction - advances in ALE methods and new fixed grid approaches*. In HJ Bungratz and M Schäfer, editors, Fluid-structure interaction - Modeling, simulation, optimization, volume 53 of *Lecture notes in computational science and engineering*, pages 195–228. Springer, Berlin, 2006.

[38] PN Watton, XY Luo, X Wang, GM Bernacca, P Molloy, and DJ Wheatley. *Dynamic modelling of prosthetic chorded mitral valves using the immersed boundary method*. J Biomech, 40(3):613–626, 2007.

[39] J De Hart, GWM Peters, PJG Schreurs, and FPT Baaijens. *A two-dimensional fluid-structure interaction model of the aortic heart valve*. J Biomech, 33:1079–1088, 2000.

[40] J De Hart, FPT Baaijens, GWM Peters, and PJG Schreurs. *A computational fluid-structure interaction analysis of a fiber-reinforced stentless aortic valve*. J Biomech, 36:699–712, 2003.

[41] J De Hart, GWM Peters, PJG Schreurs, and FPT Baaijens. *A three-dimensional computational analysis of fluid-structure interaction in the aortic heart valve*. J Biomech, 36(1):103–112, 2003.

[42] J De Hart, GWM Peters, PJG Schreurs, and FPT Baaijens. *Collagen fibers reduce stresses and stabilize motion of aortic valve leaflets during systole*. J Biomech, 37:303–311, 2004.

[43] CS Peskin. *Flow patterns around heart valves: A numerical method*. J Comput Phys, 10:252–271, 1972.

[44] X Wang and WK Liu. *Extended immersed boundary method using FEM and RKMP*. Comp Meth Appl Mech Eng, 193(12-14):1305–1321, 2004.

[45] L Zhang, A Gerstenberger, X Wang, and WK Liu. *Immersed finite element method*. Comp Meth Appl Mech Eng, 193(21-22):2051–2067, 2004.

[46] EA Fadlun, R Verzicco, P Orlandi, and J Mohd-Yusof. *Combined immersed-boundary finite-difference methods for three-dimensional complex flow simulations*. J Comp Phys, 161:35–60, 2000.

[47] CS Peskin. *Numerical analysis of blood flow in the heart*. J Comput Phys, 25:220–252, 1977.

[48] JL Steger, FC Dougherty, and JA Benek. *A Chimera grid scheme*. In KN Ghia and U Ghia, editors, Advances in grid generation, volume 5, pages 59–69. ASME - FED, Houston, USA, 1983.

[49] M Fortin and R Glowinski. *Augmented Lagrangian methods*, volume 15 of *Studies in mathematics and its applications*. Elsevier, Amsterdam, The Netherlands, 1983.

[50] KJ Bathe. *Finite element procedures in engineering analysis*. Prentice-Hall, Inc., New Jersey, USA, 1982.

[51] FN van de Vosse, J de Hart, CH van Oijen, D Bessems, TW Gunther, A Segal, BJ Wolters, JM Stijnen, and FPT Baaijens. *Finite-element-based computational methods for cardiovascular fluid-structure interaction*. J Eng Math, 47:335–368, 2003.

[52] W Noh. *CEL: A time-dependent two-space-dimensional coupled Eulerian-Lagrangian code*. In B Alder, S Fernbach, and M Rotenberg, editors, Methods in computational physics, volume 3, pages 117–179. Academic Press, New York, USA, 1964.

[53] TJR Hughes, WK Liu, and TK Zimmerman. *Lagrangian-Eulerian finite element formulation for incompressible viscous flows*. Comp Meth Appl Mech Eng, 29:329–349, 1981.

[54] J Donea. *Arbitrary Lagrangian-Eulerian finite element methods*. In T Belytschko and TJR Hughes, editors, Computational methods for transient analysis. North Holland, Amsterdam, The Netherlands, 1983.

[55] JF Gerbeau and M Vidrascu. *A quasi-newton algorithm based on a reduced model for fluid-structure interaction problems in blood flows*. ESIAM: Math Mod Num Anal, 37(4):631–647, 2003.

[56] HG Matthies and J Steindorf. *Partitioned strong coupling algorithms for fluid-structure interaction*. Comp Struct, 81:805–812, 2003.

[57] S DeParis, M Discacciati, and A Quarteroni. *A Domain Decomposition Framework for Fluid-Structure Interaction Problems*. In C Groth and DW Zingg, editors, Computational Fluid Dynamics 2004. Proceedings of the Third International Conference on Computational Fluid Dynamics, IC-CFD3, Toronto, July 2004, pages 1–18. Springer, Berlin, Deutschland, 2004.

[58] M Fernandez and M Moubachir. *A Newton method using exact jacobians for solving fluid-structure coupling*. Comp Struct, 83:127–142, 2005.

[59] JF Gerbeau, M Vidrascu, and P Frey. *Fluid-structure interaction in blood flows on geometries based on medical imaging*. Comp Struct, 83:155–165, 2005.

[60] S DeParis, M Discacciati, G Fourestey, and A Quarteroni. *Fluid-structure algorithms based on Steklov-Pioncaré operators*. Comp Meth Appl Mech Eng, 195:5797–5812, 2006.

[61] HG Matthies, R Niekamp, and J Steindorf. *Algorithms for strong coupling procedures*. Comp Meth Appl Mech Eng, 195:2028–2049, 2006.

[62] JT Batina. *Unsteady Euler airfoil solutions using unstructured dynamic meshes*. AIAA Journal, 28(8):1381–1388, 1990.

[63] B Palmerio. *Coupling mesh and flow in viscous fluid calculations on unstructured triangular finite elements*. Int J Comp Fluid Dyn, 6(4):275–290, 1996.

[64] K Mer and B Nkonga. *Implicit calculation of an aeroelasticity problem.* Int J Comp Fluid Dyn, 9(2):165–178, 1998.

[65] M Heil. *An efficient solver for the fully coupled solution of large-displacement fluid-structure interaction problems.* Comp Meth Appl Mech Eng, 193:1–23, 2004.

[66] KJ Bathe, H Zhang, and S Li. *Finite element analysis of fluid flows fully coupled with structural interactions.* Comp Struct, 72:1–16, 1999.

[67] J Hron and S Turek. *A monolithic FEM/Multigrid solver for an ALE formulation of fluid-structure interaction with applications in biomechanics.* In HJ Bungratz and M Schäfer, editors, Fluid-structure interaction - Modeling, simulation, optimization, Lecture notes in computational science and engineering. Springer, Berlin, Germany, 2006.

[68] H Zhang, X Zhang, S Ji, G Guo, Y Ledezma, N Elabbasi, and H Decougny. *Recent development of fluid-structure interaction capabilities in the ADINA system.* Comp Struct, 81(8-11):1071–7085, 2003.

[69] Inc. ADINA R&D. *ADINA, The finite element system for structures, heat transfert and CFD*, 2007.

[70] Inc. ANSYS. *Fluid structure interaction solution*, 2007.

[71] Fraunhofer-SCAI. *MpCCI, Mesh-based parallel code coupling interface, version 3.0. Multidisciplinary simulations through coupling*, 2007.

[72] Fraunhofer-SCAI. *MpCCI, Mesh-based parallel code coupling interface, version 3.0.6-9 documentation.* Fraunhofer-SCAI, Sankt Augustin, Germany, 2007.

[73] C Farhat and M Lesoinne. *Two efficient staggered algorithms for the serial and parallel solution of three-dimensional nonlinear transient aeroelastic problems.* Comp Meth Appl Mech Eng, 182:499–515, 2000.

[74] C Föster, WA Wall, and E Ramm. *Artificial added mass instabilities in sequential staggered coupling of nonlinear structures and incompressible viscous flows.* Comp Meth Appl Mech Eng, 196(7):1278–1293, 2007.

[75] P Causin, JF Gerbeau, and F Nobile. *Added-mass effect in the design of partitioned algorithms for fluid-structure interaction problems.* Comp Meth Appl Mech Eng, 194(42-44):4506–4527, 2005.

[76] B Irons and RC Tuck. *A version of the Aitken acceleration for computer implementation.* Int J Num Meth Eng, 1:275–277, 1969.

[77] DP Mok, WA Wall, and E Ramm. *Accelerated iterative substructuring schemes for instationary fluid-structure interaction.* In KJ Bathe, editor, Computational fluid and solid mechanics, pages 1325–1328. Elsevier, 2001.

[78] Y Saad and MH Schultz. *GMRES: A generalized minimal residual algorithm for solving nonsymmetric linear systems*. SIAM J Sci Stat Comp, 7:856–869, 1986.

[79] PN Brown and Y Saad. *Convergence theory of nonlinear Newton-Krylov algorithms*. SIAM J Optim, 4(2):297–330, 1994.

[80] P LeTallec and J Mouro. *Fluid-structure interaction with large structural displacements*. Comp Meth Appl Mech Eng, 190:3039–3067, 2001.

[81] C Farhat, M Lesoinne, and P LeTallec. *Load and motion transfer algorithms for fluid/structure interaction problems with non-matching discrete interfaces: momentum and energy conservation, optimal discretization and application to aeroelasticity*. Comp Meth Appl Mech Eng, 157:95–114, 1998.

[82] A De Boer. *Coupling of non-matching meshes in fluid-structure interaction computations*. Technical report, TU Delft, 19/5/2005 2005.

[83] J Vierendeels, K Dumont, E Dick, and P Verdonck. *Analysis and stabilization of fluid-structure interaction algorithm for rigid-body motion*. AIAA Journal, 43(12):2549–2557, 2005.

[84] S Turek and J Hron. *Proposal for numerical benchmarking of fluid–structure interaction between an Elastic Object and Laminar Incompressible Flow*. In H.-J. Bungartz and M. Schäfer, editors, Fluid–Structure Interaction – Modelling, Simulation, Optimization, volume 53 of *Lecture Notes in Computational Science and Engineering*, pages 371–385. Springer, Berlin, 2006.

[85] Inc. Abaqus. *ABAQUS Analysis user's manual*. Abaqus, Inc., 2006.

[86] D Negrut, R Rampalli, G Ottarsson, and A Sajdak. *On an implementation of the Hilber-Hughes-Taylor method in the context of index 3 differential-algebraic equations of multibody dynamics*. J Comp Nonlin Dyn, 2(1):73–85, 2006.

[87] K Perketold, M Resch, and H Florian. *Pulsatile non-Newtonian flow characteristics in a three-dimensional human carotid bifurcation model*. J Biomech Eng, 113(4):464–475, 1991.

[88] S. Turek and M. Schäfer. *Benchmark computations of laminar flow around a cylinder*. In E.H. Hirschel, editor, Flow simulation with high-performance computers II, volume 52 of *Notes on Numerical Fluid Mechanics*, pages 547–566. Vieweg, 1996.

[89] GJ Langewouters, KH Wesseling, and WJA Goedhard. *The static elastic properties of 45 human thoracic and 20 abdominal aortas in vivo and the parameters of a new model*. J Biomech, 17:425–435, 1984.

[90] M Karamanoglu, DE Gallagher, AP Avolio, and MF O'Rourke. *Functional origin of reflected pressure waves in a multibranched model of the human arterial system*. Am J Physiol - Heart Circ Physiol, 267:H1681–1688, 1994.

[91] N Stergiopulos and N Westerhof. *Evaluation of methods for estimation of total arterial compliance*. Am J Physiol - Heart Circ Physiol, 268(4):H1540–1548, 1995.

[92] P Segers, N Stergiopulos, P Verdonck, and R Verhoeven. *Assessment of distributed arterial network models*. Med & Biol Eng & Comp, 35:729–738, 1997.

[93] SJ Sherwin, V Franke, J Peiro, and K Parker. *One-dimensional modeling of a vascular network in space-time variables*. J Eng Math, 47:217–250, 2003.

[94] JJ Wang and KH Parker. *Wave propagation in a model of the arterial circulation*. J Biomech, 37:457–470, 2004.

[95] A Swillens, L Lanoye, J De Backer, N Stergiopulos, and P Verdonck. *The effect of an abdominal aortic aneurysm on wave reflection in the aorta*. IEEE Trans Biomed Eng, to appear, 2007.

[96] A Quarteroni, S Ragni, and A Veneziani. *Coupling between lumped and distributed models for blood flow problems*. Comput Visual Sci, 4:111–124, 2001.

[97] TJ Pedley. *Mathematical modelling of arterial fluid dynamics*. J Eng Math, 47:419–444, 2003.

[98] ML Raghavan, B Ma, and MF Fillinger. *Non-invasive determination of zero-pressure geometry of arterial aneurysms*. Ann Biomed Eng, 34(9):1414–1419, 2006.

[99] P Segers and PRA Verdonck. *Role of tapering in aortic wave reflection: hydraulic and mathematical model study*. J Biomech, 33:299–306, 2000.

[100] N Westerhof, F Bosman, CJ De Vries, and A Noordergraaf. *Analog studies of the human systemic tree*. J Biomech, 2:121–143, 1969.

[101] T Carew, R Vaishnav, and D Patel. *Compressibility of the arterial wall*. Circulation, 23:61–68, 1968.

[102] P Prendergast, C Lally, S Daly, A Reid, T Lee, D Quinn, and F Dolan. *Analysis of prolapse in cardiovascular stents: a constitutive equation for vascular tissue and finite-element modelling*. ASME J Biom Eng, 125:692–699, 2003.

[103] C Lally, F Dolan, and P Prendergast. *Cardiovascular stent design and vessel stresses: a finite element analysis*. J Biomech, 38:1574–1581, 2005.

[104] C Schulze-Bauer and G Holzapfel. *Determination of constitutive equations for human arteries from clinical data*. J Biomech, 36:165–169, 2003.

[105] DF Young and FY Tsai. *Flow characteristics in models of arterial stenoses*. J Biomech, 6(4):395–410, 1973.

[106] D Berger, J Li, W Laskey, and A Noordergraaf. *Repeated reflection of waves in the systemic arterial system*. Am J Physiol, 264:H269–281, 1993.

[107] N Westerhof, N Stergiopulos, and N Noble. *Snapshots of hemodynamics: An aid for clinical research and graduate education*. Springer Science+Buisiness Media, New York, 2004.

[108] N Westerhof, P Spikema, G Van Den Bos, and G Elzinga. *Forward and backward waves in the arterial system*. Cardiovasc Res, 6(648-656), 1972.

[109] WR Milnor. *Hemodynamics*. Wilkins & Wilkins, Baltimore, MA, USA, 1989.

[110] WW Nichols and MF O' Rourke. *McDonald's blood flow in arteries*. Edward Arnold, London, UK, 3rd edition, 1990.

[111] P Segers and P Verdonck. *Hemodynamics*. In JG Webster, editor, Encyclopedia of medical devices and instrumentation, volume 3. Wiley-Interscience, 2nd edition, 2006.

[112] R Latham, N Westerhof, P Sipkema, B Rubal, P Reuderink, and J Murgo. *Regional wave travel and reflections along the human aorta: a study with six simultaneous micromanometric pressures*. Circulation, 72:1257–1269, 1985.

[113] L Formaggia, F Nobile, A Quarteroni, and A Veneziani. *Multiscale modelling of the circulatory system: a preliminary analysis*. Comput Visual Sci, 2:75–83, 1999.

[114] L Formaggia, JF Gerbeau, F Nobile, and A Quarteroni. *On the coupling of 3D and 1D Navier-Stokes equations for flow problems in compliant vessels*. Comp Meth Appl Mech Eng, 191:561–582, 2001.

[115] I Vignon-Clementel, CA Figueroa, KE Jansen, and CA Taylor. *Outflow boundary conditions for three-dimensional finite element modeling of blood flow and pressure in arteries*. Comp Meth Appl Mech Eng, 195:3776–3796, 2006.

[116] MI Patel, DT Hardman, CM Fischer, and M Appleberg. *Current views on the pathogenesis of abdominal aortic aneurysms*. J Am Coll Surg, 181:371–382, 1995.

[117] CK Zarins, RA White, KJ Hodgson, D Schwarten, and TJ Fogarty. *Endoleaks as a predictor of outcome after endovascular aneurysm repair: AneuRx multicenter clinical trial*. J Vasc Surg, 32(1):90–107, 2000.

[118] The UK Small Aneurysm trial. *Mortality results for randomised controlled trial of early elective surgery or ultrasonographic surveillance of small abdominal aortic aneurysms*. The Lancet, 352(9141):1649–1655, 1998.

[119] FA Lederle, SE Wilson, GR Johnson, DB Reinke, FN Littooy, CW Acher, DJ Ballard, LM Messina, IL Gordon, EP Chute, and CW Krupski. *Immediate repair compared with surveillance of small abdominal aortic aneurysms*. N Eng J Med, 346(19):1437–1444, 2002.

[120] MF Fillinger, ML Raghavan, SP Marra, JL Cronenwett, and FE Kennedy. *In vivo analysis of mechanical wall stress and abdominal aortic aneurysm rupture risk*. J Vacs Surg, 36(3):589–597, 2002.

[121] MF Fillinger, SP Marra, ML Raghavan, and FE Kennedy. *Prediction of rupture risk in abdominal aortic aneurysm during observation: wall stress versus diameter*. J Vasc Surg, 37(4):724–732, 2003.

[122] B Sonesson, T Sandgren, and T Lanne. *Abdominal aortic aneurysm wall mechanics and their relation to risk of rupture*. Eur J Vasc Endovasc Surg, 18:487–493, 1999.

[123] Z Li and C Kleinstreuer. *A new wall stress equation for aneurysm-rupture prediction*. Ann Biomed Eng, 33(2):209–213, 2005.

[124] C Kleinstreuer and Z Li. *Analysis and computer program for rupture-risk prediction of abdominal aorta aneurysms*. BioMed Eng OnLine, 5:contr. 19, 2006.

[125] CM He and MR Roach. *The composition and mechanical properties of abdominal aortic aneurysms*. J Vasc Surg, 20:6–13, 1994.

[126] ML Raghavan, MW Webster, and DA Vorp. *Ex vivo biomechanical behavior of abdominal aortic aneurysm: assessment using a new mathematical model*. Ann Biomed Eng, 24(5):573–582, 1996.

[127] DA Vorp, PC Lee, DHJ Wang, MS Makaroun, EM Nemoto, S Ogawa, and MW Webster. *Association of intraluminal thrombus in abdominal aortic aneurysm with local hypoxia and wall weakening*. J Vasc Surg, 34:291–299, 2001.

[128] JP Vande Geest, DHJ Wang, SR Wisniewski, MS Makaroun, and DA Vorp. *Towards a noninvasive method for determination of patient-specific wall strength distribution in abdominal aortic aneurysms*. Ann Biomed Eng, 34(7):1098–1106, 2006.

[129] WR Mower, WJ Quinones, and SS Gambhir. *Effect of intraluminal thrombus on abdominal aortic aneurysm wall stress*. J Vasc Surg, 26(4):602–608, 1997.

[130] DHJ Wang, MS Makaroun, MW Webster, and DA Vorp. *Effect of intralumbal thrombus on wall stress in patient-specific models of abdominal aortic aneurysm*. J Vasc Surg, 36(3):598–604, 2002.

[131] GWH Schurink, JM van Baalen, MJT Visser, and JH van Bockel. *Thrombus within an aortic aneurysm does not reduce pressure on the aneurysmal wall*. J Vasc Surg, 31:501–506, 2000.

[132] MJ Thubrikar, F Robicsek, M Labrosse, V Chervenkoff, and BL Fowler. *Effect of thrombus on abdominal aortic aneurysm wall dilation and stress*. J Cardiovasc Surg (Torino), 44(1):67–77, 2003.

[133] DA Vorp, WJ Federspiel, and MW Webster. *Does laminated intraluminal thrombus within abdominal aortic aneurysm cause anoxia of the aortic wall?* J Vasc Surg, 23(3):540–541, 1996.

[134] DA Vorp and ML Raghavan. *Mechanical wall stress in abdominal aortic aneurysm: influence of diameter and asymmetry*. J Vasc Surg, 27(4):632–639, 1998.

[135] J Hua and WR Mower. *Simple geometric characteristics fail to reliably predict abdominal aortic aneurysm wall stresses*. J Vasc Surg, 34(2):308–315, 2001.

[136] ML Raghavan, DA Vorp, MP Federle, MS Makaroun, and MW Webster. *Wall distribution on three-dimensionally reconstructed models of human abdominal aortic aneurysm*. J Vasc Surg, 31(4):760–769, 2000.

[137] AK Venkatasubramaniam, MJ Fagan, T Mehta, KJ Mylankal, B Ray, G Kuhan, IC Chetter, and PT McCollum. *A comparative study of aortic wall stress using finite element analysis for ruptured and non-ruptured abdominal aortic aneurysms*. Eur J Vasc Endovasc Surg, 28:168–176, 2004.

[138] EA Finol, ES Di Martino, DA Vorp, and CH Amon. *Fluid-structure interaction and structural analysis of an aneurysm model*. In Summer Bioengineering Conference, pages 75–76, Key Biscane, Florida, USA, 2003.

[139] CM Scotti, AD Shkolnik, SC Muluk, and EA Finol. *Fluid-structure interaction in abdominal aortic aneurysms: effects of asymmetry and wall thickness*. BioMed Eng OnLine, 4:contr 64, 2005.

[140] Z Li and C Kleinstreuer. *Effects of blood flow and vessel geometry on wall stress and rupture risk of abdominal aortic aneurysms*. J Med Eng & Tech, 30(5):283–297, 2006.

[141] BJBM Wolters, MCM Rutten, GWH Schurink, U Kose, J de Hart, and FN van de Vosse. *A patient-specific computational model of fluid-structure interaction in abdominal aortic aneurysms*. Med Eng & Phys, 27:871–883, 2005.

[142] JH Leung, AR Wright, N Cheshire, J Crane, SA Thom, AD Hughes, and Y Xu. *Fluid structure interaction of patient specific abdominal aorta aneurysms: a comparison with solid stress models*. BioMed Eng OnLine, 5:contr 33, 2006.

[143] Y Papaharilaou, JA Ekaterinaris, E Manousaki, and AN Katsamouris. *A decoupled fluid structure approach for estimating wall stress in abdominal aortic aneurysms*. J Biomech, 40:367–377, 2007.

[144] MJ Thubrikar, M Labrosse, F Robicsek, J Al-Soudi, and B Fowler. *Mechanical properties of abdominal aortic aneurysm wall*. J Med Eng & Tech, 25(4):133–142, 2001.

[145] ML Raghavan and DA Vorp. *Toward a biomechanical tool to evaluate rupture potential of abdominal aortic aneurysm: identification of a finite strain constitutive model and evaliuation of its applicability*. J Biomech, 33:475–482, 2000.

[146] ES Di Martino and DA Vorp. *Effect of variation in intraluminal thrombus constitutive properties on abdominal aortic aneurysm wall stress*. Ann Biomed Eng, 31:804–809, 2003.

[147] J Vierendeels, L Lanoye, J Degroote, and P Verdonck. *Implicit coupling of partitioned fluid-structure interaction problems with reduced order models*. Comp & Struct, 85:970–976, 2007.

[148] L Lanoye, J Vierendeels, P Segers, and P Verdonck. *Modeling fluid-structure interaction using Fluent and Abaqus software*. In 7th World Congress on Computational Mechanics, page contr. 1505, Los Angeles, CA, USA, 2006.

[149] ES Di Martino, S Mantero, F Inzoli, G Melissano, D Astore, R Chiesa, and R Fumero. *Biomechanics of abdominal aortic aneurysm in the presence of endoluminal thrombus: experimental characterisation and structural static computational analysis*. Eur J Vasc Endovasc Surg, 15:290–299, 1998.

[150] SP Marra, ML Raghavan, DR Whittaker, MF Fillinger, DT Chen, JM Dwyer, MJ Tsapakos, and FE Kennedy. *Estimation of the zero-pressure geometry of abdominal aortic aneurysms from dynamic magnetic resonance imaging*. In Summer Bioengineering Conference, Vail, CO, USA, 2005.

[151] MS Olufsen, MC Peskin, WY Kim, EM Pedersen, A Nadim, and J Larsen. *Numerical simulation and experimental validation of blood flow in arteries*

with structured-tree outflow conditions. Ann Biomed Eng, 28(11):1281–1299, 2000.

[152] JA Vierendeels, E Dick, and PR Verdonck. *Hydrodynamics of color M-mode Doppler flow wave propagation velocity V(p) : a computer study.* J Am Echocardiogr, 15(3):219–224, 2002.

[153] PR Verdonck, JA Vierendeels, K Riemslagh, and E Dick. *Left ventricular pressure gradients : a computer model simulation.* Med & Biol Eng & Comp, 37(4):511–516, 1999.

[154] JA Vierendeels, K Riemslagh, E Dick, and PR Verdonck. *Computer simulation of intraventricular flow and pressure gradients during diastole.* ASME J Biomech Eng, 122(6):667–674, 2000.

[155] WW Nichols and MF O'Rourke. *McDonald's blood flow in arteries: theoretical, experimental and clinical principles.* Edward Arnold, Kent, 3rd ed. edition, 1990.

[156] I Weber, J Auer, MF O'Rourke, E Kvas, E Lassnig, R Berent, and B Eber. *Arterial stiffness, wave reflections and the risk of coronary heart disease.* Circulation, 109:184–189, 2004.

[157] N Westerhof and MF O'Rourke. *Haemodynamic basis for the development of left ventricular failure in systolic hypertension and for its logical therapy.* J Hypertension, 13:943–952, 1995.

[158] MF O'Rourke. *Mechanical principles. Arterial stiffness and wave reflection.* Pathol Biol, 47:623–633, 1999.

[159] CJH Jones and M Sugawara. *Wavefronts in the aorta - implications for the mechanisms of the left ventricular ejection and aortic valve closure.* Cardiovasc Res, 27:1902–1905, 1993.

[160] AW Khir and KH Parker. *Measurements of wave speed and reflected waves in elastic tubes and bifurcations.* J Biomech, 35:775–783, 2002.

[161] Y Sun, TJ Anderson, KH Parker, and JV Tyberg. *Wave-intensity analysis: a new approach to coronary hemodynamics.* J Appl Physiol, 89:1636–1644, 2000.

[162] RA Bleasdale, KH Parker, and JH Jones. *Chasing the wave. Unfashionable but important new concepts in arterial wave travel.* Heart Circ Physiol, 284:1879–1885, 2003.

[163] JM MacRae, Y Sun, DL Isaac, GM Dobson, C Cheng, WC Little, KH Parker, and JV Tyberg. *Wave intensity analysis: a new approach to left ventricular filling dynamics.* Heart Vessels, 12:53–59, 1997.

[164] AW Khir, A O'Brien, JSR Gibbs, and KH Parker. *Determination of wave speed and wave separation in the arteries*. J Biomech, 34:1145–1155, 2001.

[165] T Shishido, M Sugimachi, O Kawaguchi, H Miyano, T Kawada, W Matsuura, Y Ikeda, and K Sunagawa. *Novel method to estimate ventricular contractility using intraventricular pulse wave velocity*. Am J Physiol, 277(6):2409–2415, 1999.

[166] JJ Wang, KH Parker, and JV Tyberg. *Left ventricular wave speed*. J Appl Physiol, 91:2531–2536, 2001.

[167] A Owen. *A numerical model diastolic filling : importance of intraventricular wave propagation*. Cardiovasc Res, 27(2):255–261, 1993.

[168] J Meisner. *Left atrial role in left ventricular filling : dog and computer studies*. PhD thesis, Yeshiva University, 1986.

[169] RF Janz and AF Grim. *Deformation of the diastolic left ventricle - I. nonlinear elastic effects*. Biophys J, 13:689–704, 1973.

[170] RF Janz, BR Kubert, TF Moriarty, and AF Grim. *Deformation of the diastolic left ventricle - II. nonlinear geometric effects*. J Biomech, 7:509–516, 1973.

[171] E Yellin. *The momentum of mass, the momentum of ideas, and diastolic function*. In N Ingels, G Daughters, J Baan, J Covell, R Reneman, and F Yin, editors, Systolic and diastolic function of the heart. IOS Press, Amsterdam, 1995.

[172] JR Dawson and DG Gibson. *Left ventricular filling and early diastolic function at rest and during angina in patients with coronary artery disease*. Br Heart J, 61(3):248–257, 1989.

[173] E Boersma, ACP Maas, JW Deckers, and ML Simoons. *Early thrombolytic treatment in acute myocardial infarction: reappraisal of the golden hour*. Lancet, 348:771–775, 1996.

[174] K Newby. *Clinical outcomes according to time treatment*. Clin Cardiol, 20:III11–III15, 1997.

[175] DJ Hearse, SM Humphrey, WG Nayler, A Slade, and D Border. *Ultrastructural damage associated with reoxygenation of anoxic myocardium*. J Mol Cell Cardiol, 7:315–324, 1975.

[176] LH Opie. *Reperfusion injury and its pharmacologic modification*. Circulation, 80:1049–1062, 1989.

[177] FB Cerra, TZ Lajos, M Montes, and JH Siegel. *Hemorrhagic infarction : a reperfusion injury following prolonged myocardial ischemic anoxia*. Surgery, 78:95–104, 1975.

[178] K Higo, J Sano, A Karasawa, and K Kubo. *The novel thromboxane A2 receptor antagonist KW-3635 reduces infarct size in a canine model of coronary occlusion and reperfusion*. Arch Int Pharmacodyn Ther, 323:32–49, 1993.

[179] QD Wang, J Pernow, PO Sjoquist, and L Ryden. *Pharmacological possibilities for protection against myocardial reperfusion injury*. Cardiovasc Res, 55:25–37, 2002.

[180] J Zweier and M Talukder. *The role of oxidants and free radicals in reperfusion injury*. Cardiovasc Res, 70:181–190, 2006.

[181] HM Piper, Y Abdallah, and C Schafer. *The first minutes of reperfusion : a window of opportunity for cardioprotection*. Cardiovasc Res, 61:365–371, 2004.

[182] R Kamimura, N Miura, and S Suzuki. *The hemodynamic effects of acute myocardial ischemia and reperfusion in Clawn miniature pigs*. Exp Anim, 52(335-338), 2003.

[183] P Khalil, C Neuhof, R Huss, M Pollhammer, M Khalil, and H Neuhof. *Calpain inhibition reduces infarct size and improves global hemodynamics and left ventricular contractility in a porcine myocardial ischemia/reperfusion model*. Eur J Pharm, 528:124–131, 2005.

[184] C Metzsch, Q Liao, S Steen, and L Algotsson. *Myocardial glycerol release, arrhythmias and hemodynamic instability during regional ischemia-reperfusion in an open chest pig model*. Acta Anaesthesiol Scand, 50:99–107, 2006.

[185] J Baan, ET van der Velde, HG de Bruin, GJ Smeek, J Koops, and AD van Dijk. *Continuous measurement of left ventricular volume in animals and humans by conductance catheter*. Circulation, 70:812–823, 1984.

[186] P Steendijk, ET van der Velde, and J Baan. *Determinants of stroke volume by single and dual excitation of conductance catheter in dogs*. Am J Physiol Heart Circ Physiol, 264:H2198–2207, 1993.

[187] H Suga, A Kitabatake, and K Sagawa. *End-systolic pressure determines stroke volume from fixed and end-diastolic volume in the isolated left ventricle under a constant contractile state*. Circ Res, 44:238–249, 1979.

[188] D Glower, J Spratt, TR Snow, JS Kabas, JW Davis, and C Olsen. *Linearity of the Frank-Starling relationship in the intact heart : the concept of preload recruitable stroke work*. Circulation, 71:994–1009, 1985.

[189] B Lambermont, V D'Orio, P Gerard, P Kolh, O Detry, and R Marcelle. *Time domain method to identify simultaneously parameters of the windkessel model applied to pulmonary circulation*. Arch Physiol Biomech, 106(245-252), 1998.

[190] B Grant and L Paradowski. *Charactarization of pulmonary input impedance with lumped parameter models.* Am J Physiol Heart Circ Physiol, 252:H585–H593, 1987.

[191] K Sagawa, L Maughan, and H Suga. *Cardiac contraction and pressure-volume relationship.* Oxford University Press, New York, 1988.

[192] N Stergiopoulos, JJ Meister, and N Westerhof. *Determinants of stroke volume and systolic and diastolic pressure.* Am J Physiol Heart Circ Physiol, 270(H2050-H2059), 1996.

[193] P Segers, N Steriopoulos, and N Westerhof. *Relation of effective arterial elastance to arterial properties.* Am J Physiol Heart Circ Physiol, 282:1041–1046, 2002.

[194] S Rolin, M Petein, V Tchana-Sato, JM Dogne, P Benoit, and B Lambermont. *BM-573, a dual thromboxane synthase inhibitor and thromboxane receptor antagonist, prevents pig myocardial infarction induced by coronary thrombosis.* J Pharmacol Exp Ther, 306:59–65, 2003.

[195] JM Dogne, S Rolin, M Petein, V Tchana-Sato, A Ghuysen, and B Lambermont. *Characterization of an original model of myocardial infraction provoked by coronary artery thrombosis induced by ferric chloride in pig.* Thromb Res, 116:431–442, 2005.

[196] P Kolh, S Rolin, V Tchana-Sato, M Petein, A Ghuysen, and B Lambermont. *Evaluation of BM-573, a novel TXA2 synthase inhibitor and receptor antagonist, in a porcine model of myocardial ischemia-reperfusion.* Prostaglandins Other Lipid Mediat, 79:53–73, 2006.

[197] D Garcia-Dorado. *Myocardial reperfusion injury : a new view.* Cardiovasc Res, 61:363–364, 2004.

[198] HM Piper, D Garcia-Dorado, and M Ovize. *A fresh look at reperfusion injury.* Cardiovasc Res, 38:291–300, 1998.

[199] F White and C Bloor. *Coronary collateral circulation in the pig : correlation of collateral flow with coronary bed size.* Basic Res Cardiol, 76:189–196, 1981.

[200] W Schaper, G Gorge, B Winkler, and J Schaper. *The collateral circulation of the heart.* Prog Cardiovasc Dis, 31:57–77, 1988.

[201] IM Taylor, NA Shaikh, and E Downar. *Ultrastructural changes of ischemic injury due to coronary artery occlusion in the porcine heart.* J Mol Cell Cardiol, 16:79–94, 1984.

[202] P Kolh, B Lambermont, A Ghuysen, V D'Orio, P Gerard, and P Morimont. *Alternation of left ventriculo-arterial coupling and mechanical efficiency during acute myocradial ischemia.* Int Angiol, 22:148–158, 2003.

[203] P Kolh, B Lambermont, A Ghuysen, V Tchana-Sato, JM Dogne, and J Hanson. *Effects of dobutamine on left ventriculoarterial coupling and mechanical efficiency in acutely ischemic pigs*. J Cardiovasc Pharmacol, 45:144–152, 2005.

[204] M O'Rourke. *Vascular mechanics in biomechanics*. J Biomech, 36:623–630, 2003.

A
Abbreviations and Symbols

1 Abbreviations

AAA	abdominal aortic aneurysm	
ALE	arbitrary Lagrangian-Eulerian	
AV	atrial-ventricular	
BCW	backward compression wave	
BEW	backward expansion wave	
BL	measurements at baseline	
Ca^{2+}	calcium-ion	
$CAX6$	axisymmetrical, biquadratic, triangular elements	
$CAX8RH$	axisymmetrical, biquadratic, rectangular, reduced, hybrid elements	
CFD	computational fluid dynamics	
CHF	congesive heart failure	
CO	cardiac output	$[ml/s]$
Co	Courant number	
CO_2	carbondioxide	
CPU	central processing unit	
CSM	computational solid mechanics	
ECG	electro-cardiogram	
EDP	end-diastolic pressure	$[Pa]$
$EDPVR$	end-diastolic pressure-volume relationship	
EDV	end-diastolic volume	$[ml]$
EF	ejection fraction	$[\%]$
ESP	end-systolic pressure	$[Pa]$

$ESPVR$	end-systolic pressure-volume relationship	
ESV	end-systolic volume	$[ml]$
$EVAR$	endovascular interavention	
FCW	forward compression wave	
FDM	finite difference method	
FEA	finite element analysis	
FEM	finite element method	
FEW	forward expansion wave	
FSI	fluid-structure interaction	
FVM	finite volume method	
$GMRES$	generalized minimal residual method	
$H\&E$	Heamatoxin and Eosin	
HR	heart rate	$[beats/min]$
ILT	intraluminal thrombus	
LA	left atrium	
LAD	left anterior descending	
LDL	low density lipoprotein	
LV	left ventricle	
MAP	mean arterial pressure	$[Pa]$
$NYHA$	New York Heart Association class of disease severity	
$NaCl$	sodium chloride	
LV	left ventricle	
O_2	oxigen	
$PRSW$	preload recruitable stroke work	$[ml]$
PV	pressure-volume	
PVA	pressure-volume area	$[mmHgml]$
RA	right atrium	
Re	Reynolds number	
ROM	reduced order model	
RV	right ventricle	
SA	sino-atrial	
SEF	strain energy function	$[Pa]$
SEM	standard errors on the mean	
SV	stroke volume	$[ml]$
SW	stroke work	$[mmHgml]$
$T60$	measurements after 1 hour	
$T180$	measurements after 3 hours	
$T300$	measurements after 5 hours	
UDF	user defined function	
Wo	Womersley number	

2 Symbols

A	cross-sectional area	$[m^2]$
$\bar{\bar{B}}$	spatial derivative of the shape function tensor	$[m^{-1}]$
c	wave speed	$[m/s]$
C	capacitor in a windkessel model	$[ml/mmHg]$
C_{ij}	coefficients from a strain energy function	$[Pa]$
$\bar{\bar{C}}$	Cauchy-Green strain deformation tensor	$[-]$
D	diameter	$[m]$
$\bar{\bar{d}}$	rate of deformation tensor	$[s^{-1}]$
$\bar{\bar{D}}$	deformation tensor	$[-]$
E	Young's modulus	$[Pa]$
$E(t)$	time-varying elastance	$[mmHg/ml]$
E_a	effective arterial elastance	$[mmHg/ml]$
E_{es}	end-systolic elastance	$[mmHg/ml]$
$\bar{\bar{E}}$	Green-Lagrange strain deformation tensor	$[-]$
$\vec{f}$	volume force vector per unit mass	$[N/kg]$
f	frequency	$[Hz]$
f	root-finding fluid solver	
F	fixed point fluid solver	
$\hat{F}_p$	approximated Jacobian of the fluid solver with respect to p	$[-]$
$\hat{F}_X$	approximated Jacobian of the fluid solver with respect to X	$[Pa/m]$
F_D	drag force	$[N]$
F_L	lift force	$[N]$
$\vec{F}$	force vector	$[N]$
$\bar{\bar{F}}$	deformation gradient tensor	$[-]$
$\vec{g}$	gravity acceleration	$[m/s^2]$
h	wall thickness	$[m]$
$\bar{\bar{H}}$	transformation matrix	$[-]$
I	wave intensity	$[W/m^2]$
$I_i, i = 1, 2, 3$	deviatoric strain invariant	$[-]$
$\bar{\bar{I}}$	unity tensor	$[-]$
J	Jacobian	
k	number of the iteration	$[-]$
K	parameter from the non-linear $A(P)$-relation	$[-]$
$\bar{\bar{K}}$	stiffness matrix	$[N/m]$
$\bar{\bar{l}}$	velocity gradient	$[s^{-1}]$
L	length	$[m]$
L	inductance in a windkessel model	$[mmHgs^2/ml]$
m	mass	$[kg]$
n	number of the time step	$[-]$

$\vec{n}$	normal	$[-]$
$\bar{\bar{N}}$	shape function tensor	$[-]$
p	pressure	$[Pa]$
p_d	end-diastolic pressure	$[Pa]$
p_{vc}	pressure with closed mitral valve	$[Pa]$
$PRSW_o$	intercept of the preload recruitable stroke work curve	$[ml]$
$PRSW_s$	slope of the preload recruitable stroke work curve	$[mmHg]$
Q	flow	$[ml/s]$
r	radius	$[m]$
R	residual function	
R	resistance in a windkessel model	$[mmHgs/ml]$
R_1	characteristic impedance of the windkessel model	$[mmHgs/ml]$
R_2	peripheral resistance	$[mmHgs/ml]$
$\bar{\bar{R}}$	rotation tensor	$[-]$
r, s	local coordinates	$[m]$
$\bar{\bar{s}}$	first Piola-Kirchof stress tensor	$[Pa]$
s	root-finding solid solver	
S	fixed point solid solver	
$\hat{S}_p$	approximated Jacobian of the solid solver with respect to p	$[m/Pa]$
$\hat{S}_X$	approximated Jacobian of the solid solver with respect to X	$[-]$
S	surface	$[m^2]$
t	time	$[s]$
Δt	time step	$[s]$
$\vec{t}$	surface tension	$[Pa]$
$\bar{\bar{T}}$	second Piola-Kirchof stress tensor	$[Pa]$
$\vec{u}$	displacement vector	$[m]$
U	one-dimensional flow velocity	$[m/s]$
$\bar{\bar{U}}$	stretch tensor	$[-]$
$\vec{v}$	flow velocity	$[m/s]$
V	volume	$[ml]$
V_d	dead volume	$[ml]$
$\vec{w}$	vector from the subspace in a GMRES-method	
δW	virtual work	$[Pa.m]$
$\vec{X}$	position vector	$[m]$
z	the coordinate along the symmetry axis	$[m]$
Z	impedance	$[mmHgs/ml]$
Z_{in}	input impedance	$[mmHgs/ml]$
Z_c	characteristic impedance	$[mmHgs/ml]$

3   Greec symbols

α, β, γ	parameters in the Hibler-Hughes-Taylor scheme	$[-]$
β	distensibility	$[1/Pa]$
Γ	reflection coefficient	$[-]$
Γ	fluid-structure interaction interface	
Γ_f	wet side of the interface	
Γ_s	dry side of the interface	
$\bar{\bar{\gamma}}_f$	strain rate tensor	$[s^{-1}]$
$\bar{\bar{\delta}}_f$	dilatation tensor	$[s^{-1}]$
$\bar{\bar{\epsilon}}$	linearized Green-Lagrange strain tensor	$[-]$
φ	phase	
ϕ	parameter	
λ	stretch	$[-]$
λ, μ	Lame constants	$[Pa]$
μ	dynamic viscosity	$[Pa.s]$
ν	Poisson modulus	$[-]$
$\bar{\bar{\sigma}}$	Cauchy stress tensor	$[Pa]$
σ_{VM}	Von Mises stress	$[Pa]$
ρ	density of the fluid	$[kg/m^3]$
ω	underrelaxation factor	$[-]$
Ω_f	fluid domain	
Ω_s	solid domain	
τ	relaxation constant of the myocardial wall	$[s]$
$\bar{\bar{\tau}}$	deviatoric or viscous stress tensor	$[Pa]$

4   Operators

d/dt	total derivative with respect to time	$[s^{-1}]$
	(except chapter 6, see local definition)	
$\cdot$	total derivative with respect to time	
$\partial/\partial t$	partial derivative with respect to time	$[s^{-1}]$
d	infinitesimal difference	
$D_x f$	Jacobian of vector function f with respect to vector variable x	
δ	virtual difference	
Δ	difference	
∇	gradient	$[m^{-1}]$
$\int$	integral	
$\sum$	sum	
$:$	double tensor product	
$^{-1}$	inverse of a tensor	
^{T}	transposition of a tensor	
$^{-T}$	inverse of a transposed tensor	

$\langle , \rangle$ internal vector product

5 Subscripts

Ao	referring to the aorta
BC	referring to the boundary conditions
d	discretized variable
i	referring to the discretized place
k	referring to the number of the iteration
max	referring to the maximal value
o	referring to the undeformed or reference state
$+$	referring to the forward traveling wave
$-$	referring to the backward traveling wave
n	normal part of a surface vector
t	tangential part of a surface vector
t	partial derivative with respect to time
z	partial derivative with respect to the z direction

6 Superscripts

f	referring to the fluid domain
s	referring to the solid domain
n	referring to the number of the time step
n	referring to the nth harmonic in a Fourier decomposition
Γ	referring to the interface
$'$	referring to the applied modification

7 Units

m	meter	
cm	centimeter	$10^{-2}m$
mm	millimeter	$10^{-3}m$
m^3	cubic meter	
l	liter	$10^{-3}m^3$
ml	milliliter	$10^{-6}m^3$
s	second	
min	minute	$60s$
ms	millisecond	$10^{-3}s$
Hz	Hertz	
$beats/min$	beats per minute	$\frac{1}{60}Hz$

Pa	Pascal	
mPa	millipascal	$10^{-3}Pa$
$mmHg$	millimeter Mercury	$133.3Pa$
g	gram	
kg	kilogram	10^3g
mg	milligram	$10^{-3}g$
μg	microgram	$10^{-6}g$
mV	millivolt	
^oC	degrees Celsius	

The end of the beginning

The two adventures were going along. Avon was singing.

"Stop!" cried Edward. "We have reached the end of the branch." With great care the two creatures edged to the very tip.

"The end of the branch," said Avon.

"The beginning of the sky," said Edward.

"Which is it?" asked Avon. "The beginning or the end?"

"It depends on what there is more of, the tree or the sky. Think of all things that get in your way along the branch - leaves, bark, other creatures, a million things to slow you down. Now look at the sky."

Avon looked. "Theres nothing there."

"Exactly. Which means that it will take *longer* to climb the branch. And if it takes longer, the branch must be bigger. And if the branch is bigger than the sky, that means were at the sky's end, but only at the beginning of the branch."

"You mean," asked Avon, quite amazed, "that after all this time, were just beginning? I had now idea how far you have to go before you can start. Almost makes me want to stop."

"You cant do that, either," said Edward severely.

"Why?"

"Can't very well stop if you haven't started, can you?"

"Edward," cried Avon, "I never knew how important it was to start before you begin."

And turning around, they began.

From "The End of the Beginning. Being the Adventures
of a Small Snail (and an Even Smaller Ant)" by AVI.
Found in the airport of New Orleans,
waiting for the flight home
after the American Heart Association Congress november 2004.